USC
UNIVERSIDADE
DE SANTIAGO
DE COMPOSTELA

ÁREA DE ÓPTICA, DEPARTAMENTO DE FÍSICA APLICADA

FACULTAD DE FÍSICA

PhD Thesis

# Active GRIN media for laser beam transformations

---

Ana Isabel Gómez Varela
Santiago de Compostela, noviembre de 2015

# Informe del director

Dña. María del Carmen Bao Varela, Profesora Titular de Universidad del Área de Óptica de la Facultad de Física de la Universidade de Santiago de Compostela,

**INFORMA**

que la presente memoria, titulada “Active GRIN media for laser beam transformations”, ha sido realizada por Dña. Ana Isabel Gómez Varela bajo su dirección y constituye la Tesis que presenta para optar al Grado de Doctor en Fotónica y Tecnologías del Láser.

Santiago de Compostela, 10 de noviembre de 2015

| Vº.Bº. Directora de la Tesis | La Doctoranda |
|---|---|
| María del Carmen Bao Varela | Ana Isabel Gómez Varela |

*A Carlos*

# *Acknowledgements*

Cuando pensaba en cómo sería plasmar todo el trabajo de estos últimos años sobre el papel no imaginaba que los agradecimientos iban a ser algo complicado. Sin el apoyo y el esfuerzo de toda la gente que se ha involucrado de una forma u otra en esta tesis hoy no estaría terminada, por ello sólo espero saber haceros llegar a todos cuánto os agradezco que hayáis estado ahí para mí.

Todo el que me conoce sabe que la primera persona a la que tengo que dar las gracias es al Prof. Carlos Gómez-Reino, que me descubrió el mundo de la investigación. Por ser un gran jefe pero sobre todo una gran persona que ha dejado una huella imborrable en los que hemos tenido la suerte de conocerle. La verdad es que nunca pensé que no estarías aquí para ver el final de nuestro trabajo que es, sin ninguna duda, fruto de tu esfuerzo y buen hacer. Ojalá estés contento con el resultado, jefe. Así que...gracias, gracias y gracias.

Los agradecimientos tienen que seguir ahora necesariamente con Carmen y Maite, por ayudarme a recorrer este camino y estar ahí siempre que lo he necesitado, apoyándome en mi crecimiento como científica. Carmen, gracias por haber dirigido esta tesis, por tus consejos y por tu ayuda para que este trabajo saliera adelante. Maite, gracias por tu ayuda en esta investigación y por haberte preocupado siempre por mí. Y gracias a las dos por vuestra amistad y cariño.

A Dani, porque eres el mejor compañero de trabajo que se puede tener, aunque como amigo eres aún mejor. Hemos pasado muchos momentos buenos pero siempre recordaré que fuiste el primero en venir a ofrecerme ayuda si necesitaba cualquier cosa desde el primer día que empecé a formar parte del grupo, o nuestras escapadas a comer pulpo y churrasco. Aunque mi recuerdo favorito siempre será aquel viaje a Estambul y cómo tuvimos que sortear a los antidisturbios turcos entre gases lacrimógenos. ¡Está claro que la vida contigo no es aburrida!

A todos mis compañeros del Grupo de Microóptica y Óptica GRIN. Paco, muchas gracias por tu ayuda con el sol-gel y con los experimentos de *laser zone melting*.

A Justo, gracias por tu ayuda con Matlab y, por supuesto, por intentar sacarme de la carrera de la rata. ¡Si tú consigues escapar de ella no me olvides y dime cómo se hace! Y a María Montero, ¡simplemente por ser la caña!

A Ana Gargallo y a Héctor, mis compañeros de fatigas con los que he compartido tantos buenos momentos. Espero que nos podamos reunir pronto y celebrar que lo hemos conseguido. Ana, gracias por haber estado siempre ahí y por haberme dado ánimos hasta el último momento, siempre confiando en mí.

A todos mis compañeros del grupo USC-OSA Student Chapter y USC-EPS Young Mind Section (¡¡mis USCOSOS!!).

A Lola y a Rosa, por aceptarme como compañera en sus clases, y a los demás profesores y compañeros de la facultad como Ana Alonso (¡viva el club de las Anas!), María Herrero, Pepe, Manuel, Mossi...entre muchos otros!

Me gustaría agradecer al grupo de Alicia Durán del Instituto de Cerámica y Vidrio que me acogieran para realizar una estancia doctoral. En especial quiero agradecerle a Yolanda Castro todo lo que me ha enseñado y haber estado siempre disponible para ayudarme, incluso mucho después de haber terminado la estancia. También me gustaría agradecerle a Aritz su inestimable ayuda en el laboratorio.

También quiero agradecer al Prof. José Rivas su ayuda para realizar una estancia en el Laboratorio Ibérico Internacional de Nanotecnología (INL). Gracias a Adelaide Miranda por acogerme en su grupo y por haber dedicado su tiempo a ayudarme con mi investigación. Por último, quiero agradecer de corazón a Pieter de Beule su inestimable ayuda tanto en esta tesis como en otros proyectos y por contribuir a formarme como investigadora.

Al Prof. Sushil Kumar Mendiratta por su apoyo y disponibilidad continua junto con Florinda Costa y Jorge Humberto Silva Monteiro. En especial me gustaría dar las gracias a Maria Rute Ferreira André y Paulo S. André por las medidas de elipsometría aportadas a esta investigación.

Muchas gracias a los miembros del Instituto de Ciencia de Materiales de Aragón, principalmente a Germán de la Fuente, Isabel de Francisco y Carlos Estepa por su trabajo en la parte experimental.

Quiero agradecer a la Prof. Rolindes Balda y su grupo por las medidas de fotoluminiscencia presentadas en este trabajo.

A Torsten Pössner y Sandra Gerlach de GRINTECH GmbH, por su colaboración en el desarrollo de materiales GRIN activos.

Por último, pero no menos importante, quiero agradecer a mi familia y amigos. A mis padres, porque siempre están ahí para mí. A mi hermana, por su cariño y preocupación constante. ¡Eres la mejor hermana (y ahora también tía) del mundo! Estoy muy orgullosa de ti. A mi cuñado Santi, porque eres simplemente un crack. A mis padrinos, por ser las personas más buenas y generosas que conozco y por haber dedicado tantos años a cuidarnos. A mis abuelos, por todo el cariño que nos han dado siempre. Y a todo el resto de mi familia.

A mis imprescindibles Quique, Sori (¡y Alonso!), Raquel y Naty, por todos estos años juntos y que espero sean muchísimos más. Y por supuesto, a todos mis amigos, Isa, Paloma, Bea, Álex, Juan...estoy deseando que nos vayamos a cenar al Oasis para celebrarlo! A todos mis compañeros de la Facultad, me habéis hecho pasar los mejores años de mi vida.

He dejado en último lugar a las dos personas en torno a las que gira mi vida. Vera, aún no sabes lo que es una tesis pero tú has vivido esta muy de cerca, gracias por haber tenido tanta paciencia aunque a veces estuviera nerviosa o preocupada, y por haber sido el bebé más bueno del mundo. Gracias por el caos maravilloso que has traído a nuestras vidas, por ser nuestro “milagrito” (¿cómo hemos podido vivir sin ti hasta ahora?). Fabio, no creo que nada de lo que escriba aquí pueda reflejar lo agradecida que estoy por todo lo que haces por nosotras. Espero poder compensarte estos últimos meses en los que has asumido tanta carga para que yo pudiera dedicarme a escribir. Eres una persona excepcional, noble y cariñosa, y yo soy la más afortunada porque hayas querido compartir tu vida conmigo. GRACIAS.

Me gustaría agradecer también la financiación recibida por el Ministerio de Ciencia e Innovación, la Consellería de Cultura de la Xunta de Galicia y al Área de Valorización, Transferencia y Emprendimiento de la Universidade de Santiago de Compostela a través de los proyectos MAT2010-18519, EM2012/019 y dentro del programa "Acelerador de Transferencia". Asimismo, quiero agradecer el apoyo recibido por parte del Ministerio de Educación, Cultura y Deporte mediante una beca para la realización de mis estudios doctorales en el marco del Programa de Formación de Profesorado Universitario y al Banco Santander, gracias al cual puede realizar una estancia de investigación.

A todos, los que estáis en estas páginas y a los que no he podido nombrar, muchas gracias.

# *Summary*

*The number of lasers applications has been constantly increasing since the first laser was born. TEM00 modes, which are described by Gaussian irradiance profiles, are the most common spatial modes provided from a laser source. However, obtaining laser beams with specific irradiance profiles is an important issue for a large number of applications. The process of redistributing the irradiance profile from a laser source in order to obtain a more suitable one for a determined application is commonly known as beam shaping. The irradiance distribution defines the profile of the beam and the phase of the shaped beam determines its propagation properties. A typical example of beam shaping is the conversion of a Gaussian laser beam into a beam with uniform amplitude and constant phase. These uniform beams, that are nominally constant over a specified area, are required in many laser applications, such as laser material processing, lithography, holography, laser fusion, medical purposes, and so on. Beam shapers are the devices employed to transform irradiance and phase of a laser beam. Major challenges for beam shapers are high efficiency and large uniformity.*

*Within this framework, extra-cavity beam shaping by active GRadient-INdex (GRIN) materials for producing distinct beam transformations is studied in this thesis, putting the focus on Gaussian-to-uniform beam conversion. The terms GRadient-INdex or GRaded-INdex are commonly used to refer to an inhomogeneous medium in which the refractive index varies from point to point, whereas the term active implies the capability of an optical material to amplify or attenuate an input light beam or, in other words, a material exhibiting gain or loss effects. In this work, two active GRIN media described by a parabolic and a hyperbolic secant refractive index profile are studied. The expression for the complex refractive index is examined in order to discuss what loss or gain means in terms of the index. The formalism of laser beam propagation in GRIN materials regarded as beam transformers with a Gaussian mask is presented. Moreover, the general conditions for beam transformations by active*

*GRIN materials as a geometrical solution in 2D space of the complex curvature of the input laser beam are obtained and discussed. Application examples of active GRIN media with gain or loss acting as beam transforming systems are performed using MATLAB software. With a view to practical implementation of active GRIN media for laser beam shaping purposes and due to the fact that they are sensitive to deviations from design parameters, a tolerance analysis is presented for a particular laser source.*

*Preliminary research on active GRIN media fabrication is also presented in this work. GRIN materials are typically manufactured by ion-diffusion process, although their fabrication has also been accomplished by ion-stuffing and sol-gel techniques. Sol gel is the first method explored in this work. It provides a low temperature route to film preparation and allows the incorporation of dopants such as rare-earh elements. Different erbium and ytterbium-doped films based on* $SiO_2$*-*$TiO_2$ *and* $SiO_2$ *systems have been prepared. The fabrication and characterization of monolayers with controlled properties is the first step towards the preparation of active GRIN materials by growing successive layers until a multilayer stack with a complex parabolic-like refractive index profile is obtained. The optical constants (refractive index and extinction coefficient), thickness and porosity of selected samples were determined using Spectral Ellipsometry, whereas topographical inspection was conducted by Atomic Force Microscopy. The analysis of luminescence spectra of the erbium sol-gel derived films is also performed, resulting that only the Er-doped silica-titania thin film exhibits significant photoluminescence spectra centered around 1.54* $\mu$*m.*

*The Laser Zone Melting technology feasibility for fabrication of active GRIN media with rotational symmetry is also explored.* $SiO_2$ *rods precursors are coated with a suspension of different inorganic compounds in isopropyl alcohol by dipping and the subsequent sintering process is performed using a* $CO_2$ *laser. The structural properties and chemical composition of the samples are characterized by Scanning Electron Microscopy combined with Energy Dispersive X-ray analysis, revealing the axial and gradual incorporation of dysprosium oxide and lithium niobate within the silica cylinder. Refractive index of a set of samples* *measured by means of Spectral Ellipsometry reveals that a gradient of refractive index profile from the edges to the centre of the rod is promoted with the applied laser zone melting treatment.*

# *Publications*

1. A. I. Gómez-Varela, M. T. Flores-Arias, C. Bao-Varela, X. de la Fuente, and C. Gómez-Reino. “Propagation of gaussian beams through active GRIN materials,” *Journal of Physics: Conference Series*, vol. 274, no. 1, pp. 012124, 2011. ISSN 1742-6596. doi: 10.1088/1742-6596/274/1/012124

2. A. I. Gómez-Varela, M. T. Flores-Arias, C. Bao-Varela, X. de la Fuente, and C. Gomez-Reino. “Beam transformations by active selfoc microlenses,” *Óptica Pura y Aplicada*, vol. 45, no. 2, pp. 215–220, 2012. ISSN 21718814, 00303917. doi: 10.7149/OPA.45.2.215

3. A. I. Gómez-Varela, M. T. Flores-Arias, C. Bao-Varela, and C. Gómez-Reino. “Focusing, collimation and beam shaping by active GRIN rod lenses: Theory and simulation,” *Optics and Lasers in Engineering*, vol. 50, no. 12, pp. 1706–1715, 2012. ISSN 0143-8166. doi: 10.1016/j.optlaseng.2012.07.011

4. A. I. Gómez-Varela, C. Bao-Varela, and M. T. Flores-Arias. “A tolerance analysis on design parameters of parabolic and hyperbolic secant active grin materials for laser beam shaping purposes,” *Laser Physics*, vol. 24, no. 11, pp. 115802, 2014. ISSN 1555-6611. doi: http://dx.doi.org/10.1088/1054-660X/24/11/115802

5. Ana I. Gómez-Varela, Y. Castro, A. Durán, P. A.A. De Beule, M. T. Flores-Arias, and C. Bao-Varela. “Synthesis and characterization of erbium-doped $SiO_2$-$TiO_2$ thin films prepared by sol-gel and dip-coating techniques onto commercial glass substrates as a route for obtaining active gradient-index materials,” *Thin Solid Films*, vol. 583, pp. 115–121, 2015. ISSN 0040-6090. doi: http://dx.doi.org/10.1016/j.tsf.2015.03.028

# *Conference Proceedings Publications*

1. C. Gómez-Reino, A. I. Gómez-Varela, M. T. Flores-Arias, C. Bao-Varela, and X. de la Fuente. “Beam transformations by active GRIN materials,” In Manuel Filipe P. C. Martins Costa, Editor, *Proc. SPIE 8001, International Conference on Applications of Optics and Photonics*, p.p. 80011G–80011G–8, 2011. doi: 10.1117/12.891899

2. C. Bao-Varela, A. I. Gomez-Varela, M. T. Flores-Arias, and C. Gomez-Reino. “Propagation in active GRIN materials: comparison between parabolic and hyperbolic secant complex refractive index profiles,” In Manuel Filipe P. C. Martins Costa, Editor, *Proc. SPIE 8001, International Conference on Applications of Optics and Photonics*, pp. 80012J–80012J–8, 2011. doi: 10.1117/ 12.891912

3. A. I. Gómez-Varela, C. Bao-Varela, and M. T. Flores-Arias. “Design, performance, and tolerances of an active GRIN laser beam shaper,” In Manuel Filipe P. C. Martins Costa, Editor, *Proc. SPIE 8785, 8th Iberoamerican Optics Meeting and 11th Latin American Meeting on Optics, Lasers, and Applications*, vol. 8785, pp. 87854R–87854R–8, 2013. doi: 10.1117/12.2026225

# *Patents*

A. I. Gómez Varela, M. T. Flores Arias, C. Bao Varela, and F. Rey García, "Lente GRIN activa, procedimiento de fabricación y sistema que comprende el uso de la lente (Active GRIN lens, fabrication method and system comprising the use of the lens)," Spanish Patent P201431252, May 22, 2015.

# *Selected Conference Contributions*

1. C. Gomez-Reino, A. I. Gómez-Varela, C. Bao-Varela, M. V. Perez, X. de la Fuente, and M. T. Flores-Arias. “Propagation of Gaussian beams through active GRIN materials,” *RIAO-OPTILAS 2010*, Perú, Lima, September 20-24, 2010. Oral communication.

2. M. T. Flores-Arias, A. I. Gómez-Varela and C. Gómez-Reino. “Laser beam shaping by active GRIN media,” *European Optical Society (EOS) annual meeting*, Paris, France (October 26-29, 2010). Oral communication.

3. C. Gomez-Reino, A. I. Gomez-Varela, M. T. Flores-Arias, C. Bao-Varela and X. de la Fuente. “Beam transformations by active GRIN materials,” *International Conference on Applications of Optics and Photonics*, Braga, Portugal, May 3-7, 2011. Invited talk.

4. C. Bao-Varela, A. I. Gomez-Varela, M.T. Flores-Arias, and C. Gomez-Reino. “Propagation in active GRIN materials: Comparison between parabolic and hyperbolic secant complex refractive index profiles,” *International Conference on Applications of Optics and Photonics*, Braga, Portugal, May 3-7, 2011. Poster communication.

5. A. I. Gómez-Varela, M. T. Flores-Arias, C. Bao-Varela, X. de la Fuente, and C. Gomez-Reino. “Beam transformations by active selfoc microlenses,” $7^{a}$ *Reunión Española de Optoelectrónica, OPTOEL’11*, Santander, Spain, June 28-July 1, 2011. Poster communication.

6. A. I. Gómez-Varela, M. T. Flores-Arias, C. Bao-Varela, X. de la Fuente and C. Gómez-Reino. “Beam shaping and light focusing by active selfoc microlenses,” *8th EOS Topical Meeting on Diffractive Optics*, Delft, The Netherlands, April 18-20, 2012. Poster communication.

7. A. I. Gómez-Varela, M. T. Flores-Arias, C. Bao-Varela, and C. Gómez-Reino. “Theory and simulation of an active GRIN beam shaper,” *ECIO 2012, 16th European conference on integrated optics and*

*technical exhibition*, Sitges, Spain, February 27-March 1, 2012. Poster communication.

8. A. I. Gómez-Varela, M. T. Flores-Arias, C. Bao-Varela, and C. Gómez-Reino. "Estudio comparativo de la condición de transformación de haces Gaussianos en haces uniformes con materiales GRIN activos con perfiles de índice secante hiperbólico y parabólico," *X Reunión Nacional de Óptica*, Zaragoza, Spain, September 4-7, 2012. Poster communication.

9. A. I. Gómez-Varela, M. T. Flores-Arias, and C. Bao-Varela. "Design, performance and tolerances of an active GRIN laser beam shaper," *RIAO/OPTILAS 2013 VIII Iberoamerican Conference on Optics XI Latinamerican meeting on Optics, Lasers and Applications*, Porto, Portugal, July 23-26, 2013. Poster communication.

10. A. I. Gómez-Varela, C. Bao-Varela y M. T. Flores-Arias. "Thickness tolerance of an active GRIN beam shaper with parabolic and hyperbolic secant refractive index profiles," *VIII Reunión Española de Optoelectrónica (OPTOEL)*, Alcalá de Henares, Spain, July 10-12, 2013. Poster communication.

11. A. I. Gómez-Varela, C. Bao-Varela y M. T. Flores-Arias. "Tolerancia de longitud de onda de un conformador de haz GRIN activo," *XXXIV Reunión Bienal de la Real Sociedad Española de Física y* $23^o$ *Encuentro Ibérico de Enseñanza de la Física*, Valencia, España, July 15-19, 2013. Poster communication.

12. A. I. Gómez-Varela, C. Bao-Varela y M. T. Flores-Arias. "Transformación de haces Gaussianos en haces uniformes mediante medios de gradiente de índice activos," *II Encontro da Mocidade Investigadora EDI-USC*, Santiago de Compostela, Spain, January 29-31, 2014. Oral communication.

13. A. I. Gómez-Varela, I. de Francisco, F. Rey-García, R. A. S. Ferreira, P. S. André, C. Bao-Varela, M. T. Flores-Arias, and G. F. de la Fuente. "Parabolic-like refractive index profile active GRIN materials by

Laser Zone Melting method," *II International Conference on Applications of Optics and Photonics*, Aveiro, Portugal, May 26-30, 2014. Poster communication.

14. A. Isabel Gómez-Varela, I. De Francisco, F. Rey-García, V. Lennikov, L. C. Estepa, C. Bao-Varela, and G. F. De la Fuente. "New fabrication method for obtaining optically active GRIN media," *XIII CONGRESO NACIONAL DE MATERIALES*, Barcelona, Spain, June 18-20, 2014. Oral communication.

15. D. Nieto, A. I. Gómez-Varela and M. T. Flores-Arias. "Surface roughness reduction of optical elements by sol-gel coatings," *ICO 2014: Enlightening the future*, Santiago de Compostela, Spain, August 26-29, 2014. Poster communication.

16. A. I. Gómez-Varela, Y. Castro, A. Durán, M. T. Flores-Arias and C. Bao-Varela. "Ellipsometric investigation of sol-gel thin films for active GRIN materials preparation," *ICO 2014: Enlightening the future*, Santiago de Compostela, Spain, August 26-29, 2014. Poster communication.

17. I. de Francisco, A. Gómez-Varela, F. Rey-García, V. Lennikov, L. C. Estepa, C. Bao, and G. F. de la Fuente. "GRIN rod materials obtained by Laser Zone Melting," $5^{th}$ *International Congress on Ceramics (ICC5)*, Beijing, China, August 17-21, 2014. Oral communication.


USC
UNIVERSIDADE
DE SANTIAGO
DE COMPOSTELA

# Contents

# List of Figures


USC
UNIVERSIDADE
DE SANTIAGO
DE COMPOSTELA

# List of Tables


USC
UNIVERSIDADE
DE SANTIAGO
DE COMPOSTELA

# Abbreviations

| | |
|---|---|
| **AFM** | **A**tomic **F**orce **M**icroscopy |
| **Dy** | **Dy**sprosium |
| **EDX** | **E**nergy **D**ispersive **X**-ray |
| **Er** | **Er**bium |
| **GRIN** | **GR**adient-**IN**dex |
| **HS** | **H**yperbolic **S**ecant |
| **LZM** | **L**aser **Z**one **M**elting |
| **MTES** | **M**ethyltriethoxysilane |
| **PL** | **P**hotoluminescence |
| **PSF** | **P**oint **S**pread **F**unction |
| **RE** | **R**are **E**arth |
| **RMS** | **R**oot **M**ean **S**quare |
| **SE** | **S**pectral **E**llipsometry |
| **SEM** | **S**canning **E**lectron **M**icroscopy |
| **TEOS** | **T**etraethoxysilane |
| **TISP** | **T**itanium Isopropoxide |
| **Yb** | **Y**tterbium |


USC
UNIVERSIDADE DE SANTIAGO DE COMPOSTELA

# *Introduction*

Beam shaping is the process of redistributing, in a controlled manner, the irradiance and phase of a beam of optical radiation [1]. The irradiance distribution defines the profile of the beam and the phase of the shaped beam determines its propagation properties. The most common example of beam shaping is the conversion of a Gaussian laser beam into a beam with uniform irradiance distribution and constant phase. In many laser applications a flat-top laser beam is required; while a Gaussian beam would have a energy density peak of double the average, a flat-top beam would be ideally constant over the active area of the beam. Such applications include, for instance, laser processing, laser measuring techniques and laser fusion [2–4]. The methods of producing flat-top beams can be divided into two classes, namely intra- and extra-cavity beam shaping [5, 6]. Intra-cavity beam shaping is based on generating a flat-top beam directly as the cavity output mode. One method to do this is the reverse propagation technique [7, 8]. Other methods based on phase conjugation mirrors at either end of the cavity and on intra-cavity diffractive optics have been developed for mode control and output beam shaping [9, 10]. Extra-cavity beam shaping can be achieved by manipulating the output beam from a laser with suitably chosen amplitude and/or phase elements and has been extensively reviewed to date [1, 6, 11, 12]. Extra-cavity beam shaping techniques can be divided into three basic types: beam attenuation, beam integration and field mapping. In some applications, a combination of two of the three types is used. The first is the beam attenuation. In this case apertures, absorption filters or alternate methods such as polarization effects or ultrasonic waves are used to select a suitable flat portion, to reduce the irradiance across the Gaussian laser beam to that at the edge, to achieve the desired beam by radial variation in polarization or to obtain flat-top beam with two plane ultrasonic waves, propagating in orthogonal direction, through the focus of the laser beam [13–22]. The second technique is the beam integration in which the input beam is broken up into beamlets by a lenslet array and superimposed in the output plane by a lens. The term of multifaceted integrator approach comes from the fact that the output pattern is a sum of diffraction patterns determined by the lenslet apertures. Beam integrators are especially suitable to laser beams with multimode irradiance distribution [23–29]. Several configurations of one or more optical systems are used to uniform lasers by beam integrators. Beam splitting through multiple prisms [30], two segmented cylindrical optical elements with axes perpendicular to each other [31], microlens array in conjunction with a conventional lens [32], a pair of micrograting arrays in orthogonal directions [33] and so on are implemented to give a flat-top laser irradiance distribution with circular, square or rectangular symmetry. The last type is field mapping. Field mappers or beam transformers operate on both phase and amplitude of the input beam to produce a suitable irradiance distribution on the output beam. The field mapping approach to beam shaping is applicable to single mode laser beams [34–41]; there are diffractive [42–45], reflective [46–52] or refractive methods [53–61] or a combination of these methods [62–64]to transform the irradiance and the phase profiles of the input laser beam into distribution better suited for application. Among these optical methods, refractive system has some advantages such as high efficiency, simple structure and less wavelength-dependence which are essential for laser beam shaper systems [41]. The mapping can also be accomplished with non conventional refractive elements, such as passive GRIN (GRadient-INdex) lenses, that are more flexible and compact with respect to beam shaping size [65–68].

GRIN lens has the advantage of combining discrete refraction at the end surfaces with continuos refraction within it [69, 70]. On the other hand, a complex material is an optical material that provides gain or loss to an input light beam. A material that has quadratic gain or loss and refractive index profiles in transverse planes away from the optical axis can be regarded as active GRIN material and light propagation through this material has been widely analyzed in optics [71–76]. However, to our knowledge, no extra-cavity beam shaping by active GRIN material has been reported which enable us to analytically describe general conditions for obtaining, in a controlled manner, uniform light beams and to design beam shapers [77–80]. The theory outlined in this thesis as well as the design are restricted to the problem of producing circular flat-top beams for symmetrical laser beams (for example, fiber lasers, tunable Ti:Sapphire, Nd:YAG or $CO_2$ lasers) by active GRIN materials simply to keep the mathematical analysis as simple as possible. The rectangular beam shaping problem for asymmetrical laser beams (for example, excimer or diode laser) has the same conceptual base, and the all results here may readily be extended to the two dimensional problem.

This thesis is organized in four chapters. Chapter 1 reviews the fundamentals of light propagation in GRIN media from electromagnetic wave perspective in the frame of geometrical optics and introduces basic terminology. The basics of light propagation through GRIN media using the axial and field ray are presented and applied to the study of two GRIN media described by specific refractive index profiles: GRIN media described by a parabolic and hyperbolic secant refractive index distribution. The general description of light propagation in such a media is given by means of a linear integral transform. Chapter 2 describes the theoretical study of Gaussian beam transformations by means of active GRIN materials with gain or loss and parabolic and hyperbolic secant refractive index profiles distribution. The first part of the chapter discusses Gaussian beam propagation in an active GRIN medium having quadratic gain or loss. The guidance behaviour and gain or loss effects on the beam propagation are evaluated through the complex refractive index of the material. The formalism of laser beam propagation in GRIN materials regarded as beam transformers with a Gaussian mask is presented and the expressions governing the radius of curvature and beam waist evolution are obtained. In addition, the general condition for Gaussian-to-flat-top beam transformation by active GRIN media as a geometrical solution in 2D space of the complex curvature of the input laser beam is obtained and the general conditions to generate beam profiles with specific optical functions (focusing and collimation) are also derived. The remainder of the chapter is devoted to planar active GRIN media with hyperbolic secant refractive index profile, where a similar study has been performed. The design of active GRIN media with both parabolic and hyperbolic secant refractive index profiles with gain or loss for Gaussian-to-flat-top beam transformation is discussed in Chapter 3. The chapter also concentrates on the design parameters tolerancing with active GRIN media. Chapter 4 deals with the preliminary exploration of active GRIN media fabrication methods. The fabrication of GRIN optical elements is quite challenging; consequently, addressing the fabrication of GRIN materials with added gain or loss capability supposes an even higher defiance. The chemical route known as Sol-Gel process and Laser Zone Melting technique are the two methods proposed for active GRIN materials preparation. Sol-gel has been demonstrated as a versatile way to generate active films due to the possibility to precisely control the film optical constants and thickness. Besides, a large variety of dopants can be incorporated to the films. In a second part of this chapter, the laser heating procedure known as Laser Zone Melting is introduced and applied to incorporate different inorganic compounds to silica precursors with cylindrical symmetry. The optical and structural characterization of the final samples prepared by both techniques is also presented. Finally, the conclusions and the future work arising from these studies are discussed. Material processing by laser scientists, optical engineers and researches in the field of laser beam shaping will find this thesis of their interest.

USC
UNIVERSIDADE
DE SANTIAGO
DE COMPOSTELA

# Chapter 1

# Light propagation in GRIN media

## 1.1 Introduction

GRadient-INdex materials are inhomogeneous media where the refractive index $n(x, y, z)$ varies from point to point. This local variation of the refractive index in the optical material involves additional capabilities of the material to generate different optical functions. There are different gradient types, comprising axial, radial, one-dimensional and spherical gradients. For axial gradients, the refractive index varies only in the direction of the optical axis $z$, while in perpendicular planes to $z$ the index is constant. In the case of radial gradients, the index is a function of the radial coordinate $r$, which is perpendicular to the optical axis. In one-dimensional or lateral GRIN media, the index depends only on one coordinate, $x$, perpendicular to the optical axis. Spherical gradients exhibit a variation of the index with a spherical radius $R$. Ray tracing in GRadient-INdex media is an essential part on the design of nonuniform lenses, providing an insight in the description and study of how light propagates through such kind of media. In contrast to homogeneous media where light follows rectilinear propagation ("light travels in a straight line"), the direction of the light propagating changes continuously in the GRIN material, depending on the distribution of the refractive index $n(x, y, z)$. The path of rays in a GRadient-INdex media is obtained by solving the ray equation. In general, one has to solve this equation numerically using a standard numerical technique such as the Runge-Kutta method [81] except in some cases where analytical solutions are possible [70, 76].

Light propagation through GRIN media has been extensively studied [69, 70, 76, 82]. The vector wave equations for a pair of vector $\vec{E}$, $\vec{H}$ can be replaced by a simpler equation known as the Helmholtz equation, provided that the refractive index changes very slightly over distances comparable to the wavelength. For waves propagating approximately along the optical axis of inhomogeneous media, the Helmhotz equation reduces to parabolic wave equation.

In this chapter we first review light propagation in GRIN media from electromagnetic wave perspective, given that most optical phenomena are described by electromagnetic vectors satisfying the wave equation. Besides, we will focus in the electromagnetic vectors corresponding to very short wavelengths, i.e., the field that corresponds to the realm of geometrical optics. We will also study the basics of light propagation through GRIN media using the axial and field rays, two linearly independent particular solutions of the paraxial ray equation. Finally, we analyze light propagation through two GRIN media described by particular gradients: GRIN media with parabolic refractive index profile and GRIN media with hyperbolic secant refractive index profile. By GRIN parabolic media we refer to paraxial optical systems with quadratic refractive index profiles. We present a general description of light propagation in these media by means of a linear integral transform, which Kernel can be expressed in terms of the elements of the ray-transfer ABCD matrix. The second medium that we study is a GRIN material characterized by a hyperbolic secant (hereafter HS) refractive index profile. In particular, we analyze Gaussian beam propagation through GRIN materials with parabolic and HS profiles given that Gaussian beams play a very important role in optical lasers and, therefore, in those applications involving their use.

## 1.2 Vector wave equations

It is well-known that the vector wave equations for the electric intensity vector $\vec{E}(\vec{r})$ and the magnetic intensity vector $\vec{H}(\vec{r})$ of a monochromatic field of frequency $w$ (periodic field) in isotropic, inhomogeneous, dielectric, non-magnetic, non-dispersive, and linear media are given by

$$\nabla^2\vec{E} + k^2n^2\vec{E} + \vec{\nabla}\left(\frac{\vec{\nabla}n^2}{n^2}\cdot\vec{E}\right) = 0 \tag{1.1a}$$

$$\nabla^2\vec{H} + k^2n^2\vec{H} + \frac{\vec{\nabla}n^2}{n^2}\times(\vec{\nabla}\times\vec{H}) = 0 \tag{1.1b}$$

where $\nabla^2$, $\vec{\nabla}$ and $\vec{\nabla}\times$ denote Laplacian, gradient and rotational operators, respectively, $n^2$ is the dimensionless dielectric constant (or dimensionless electric permittivity) and $k$ the wavenumber in vacuum

$$k = \frac{w}{c} = \frac{2\pi}{\lambda_0} \tag{1.2}$$

with $\lambda_0$ and $c$ the wavelength and the velocity of light in vacuum.

All the optics of a medium characterized by $n^2$ is studied solving equations (1.1a) and (1.1b). The two first terms in these equations are of equal order of magnitude while the third term may be neglected under the requirement that the relative change of dielectric constant $n^2$ over the distance of the order of the wavelength must be much smaller that unity, that is

$$\frac{\Delta n^2}{n^2} << 1 \tag{1.3}$$

The influence of the term neglected can be evaluated by perturbative methods (WKB analysis).

## 1.3 Scalar wave equation

Vector wave equations have a rather complicated form. Fortunately, for most problems of light propagation in inhomogeneous media condition (1.3) is fulfilled. Under this condition, that specifies a weak inhomogeneous medium, the scalar wave equation or scalar Helmholtz equation

$$\nabla^2\Psi + k^2 n^2 \Psi = 0 \tag{1.4}$$

is approximately satisfied by each component $\Psi(\vec{r})$ of the electric and magnetic field vectors. In other words, in weakly inhomogeneous media the components of the electromagnetic field are uncoupled and the polarization is preserved. Light propagation in this kind of media can therefore be studied by solving the scalar equation.

On the other hand, $\Psi$ can be developed into asymptotic series in $k$ as

$$\Psi(\vec{r}) = \exp\{ikS(\vec{r})\} \sum_{m=0}^{\infty} \frac{\Psi_m(\vec{r})}{(ik)^m} \tag{1.5}$$

where $\Psi_m(\vec{r})$ are real scalar functions of positions.

Substituting equation (1.5) into (1.4) we can derive a set of relations between $\Psi_m$and $S$. In particular, for the first term $(m = 0)$ of the expansion

$$\nabla^2\Psi_0 + ik[\nabla^2 S + 2\vec{\nabla}S \cdot \vec{\nabla}]\Psi_0 + k^2[n^2 - (\vec{\nabla}S)^2]\Psi_0 = 0 \tag{1.6}$$

Due to the real character of $\Psi_0$ and $S$ functions and that they are assumed to be independent of $k$, the real and imaginary parts of equation (1.6) must both vanish. Likewise, for large values of $k$, corresponding to geometrical optics approach $\lambda \to 0$, the first term is much smaller than the last term and may, in general, be neglected. Thus,

$$(\vec{\nabla}S)^2 - n^2 = 0 \tag{1.7a}$$

$$(\nabla^2 S + 2\vec{\nabla}S \cdot \vec{\nabla})\Psi_0 = 0 \tag{1.7b}$$

Equation (1.7a) is the eikonal function. From this equation it follows that surfaces with $S = \mathit{constant}$ are the wavefronts, that is, the locus of points with constant phase. On the other hand, equation (1.7b) is the energy transport equation for the geometrical scalar amplitude $\Psi_0$ along the ray when $k$ is sufficiently large. It can be written as

$$\frac{1}{\Psi_0}\frac{d\Psi_0}{ds} = \frac{d(\ln\Psi_0)}{ds} = -\frac{1}{2}\frac{\nabla^2 S}{n} \tag{1.8}$$

where amplitude $\Psi_0$ is evaluated by introducing the operator

$$n\frac{d}{ds} = \vec{\nabla}S \cdot \vec{\nabla} \tag{1.9}$$

Equation (1.8) can be easily integrated to give

$$\Psi_0(s) = \Psi_0(s_0)\mathrm{exp}\left\{ -\frac{1}{2}\int_{s_0}^{s} \frac{\nabla^2 S}{n} ds' \right\} \tag{1.10}$$

Likewise, substituting equation (1.10) into (1.5) for $m = 0$, $\Psi$ can be expressed as

$$\Psi(s) = \Psi_0(s_0)\mathrm{exp}\left\{ -\frac{1}{2}\int_{s_0}^{s} \frac{\nabla^2 S}{n} ds' \right\}\mathrm{exp}\{ikS\} \tag{1.11}$$

which represents the geometrical scalar field.

## 1.4 Parabolic wave equation

Helmholtz equation can be reduced to a parabolic wave equation making an approximation applicable to waves propagating approximately along the $z$-axis.

We assume, without loss of generality, that the dielectric constant of a GRIN medium can be written as

$$n^2(x,y,z) = n_0^2(z) + \nabla n^2(x,y,z) \tag{1.12}$$

where $\delta n^2/n^2 << 1$ and $n_0$ is an arbitrary function of $z$ that represents the refractive index along the $z$-axis.

Under the above approximation, the scalar field $\Psi$ can be written as

$$\Psi(\vec{r}) = \phi(\vec{r})\exp\left\{ik\int_{z_0}^{z} n_0(z')dz'\right\} \tag{1.13}$$

In this equation we have considered that the variation of $\phi$ with position must be slow within the distance of a wavelength in the $z$-direction. Inserting (1.13) into Helmholtz equation (1.4), and neglecting the second derivative of $\phi$ with respect to $z$, we obtain

$$\nabla_\perp^2\phi + 2ikn_0\frac{\partial\phi}{\partial z} + ik\phi\frac{dn_0}{dz} + k^2(n^2 - n_0^2)\phi = 0 \tag{1.14}$$

where $\nabla_\perp^2$ is the transverse Laplacian operator

$$\nabla_\perp^2 = \nabla^2 - \frac{\partial^2}{\partial z^2} \tag{1.15}$$

Equation (1.14) can be written as

$$\nabla_\perp^2\theta + 2ik\frac{\partial\theta}{\partial\eta} + k^2(n^2 - n_0^2)\theta = 0 \tag{1.16}$$

where the following changes of variable has been introduced

$$\theta(\vec{r}) = n_0^{1/2}(z)\phi(\vec{r}) \tag{1.17a}$$

$$\eta = \int_{z_0}^{z} \frac{dz'}{z'} \tag{1.17b}$$

Equation (1.16) represents the parabolic wave equation with the form of a non-stationary Schrödinger equation, where $\eta$ represents time and $n$ represents potential. it can be rewritten in the operator formulation as

$$2ik\frac{\partial\theta}{\partial\eta} = H\theta = 0 \tag{1.18}$$

where $H$ is the Hamiltonian operator given by

$$H = -\nabla_\perp^2 - k^2(n^2 - n_0^2) \tag{1.19}$$

If we consider a weakly inhomogeneous medium

$$n^2 - n_0^2 \approx 2n_0\Delta n \tag{1.20}$$

equation (1.19) can be written as

$$H \approx -\nabla_\perp^2 - 2k^2 n_0 \Delta n \tag{1.21}$$

where $\Delta n = n - n_0$.

$\Psi$ can be developed in series, where the first term of the expansion corresponds to the geometrical field, given by [83]

$$\Psi(\vec{r}) = \Psi_0^P(\vec{r})\exp\{ikS^P(\vec{r})\} \tag{1.22}$$

where $\Psi_0^P$ and $S^P$ are the parabolic geometrical amplitude and the parabolic eikonal function, respectively.

Equations (1.7a) and (1.7b) can be written as

$$(\nabla S^P)^2 - n^2 = 0 \tag{1.23a}$$

$$\Psi_0^P \nabla_\perp^2 S^P + 2\vec{\nabla}_\perp^P \cdot \vec{\nabla}_\perp \Psi_0^P = 0 \tag{1.23b}$$

where $\vec{\nabla}_\perp$ denotes the transverse gradient operator. We have taken into account that $\Psi_0^P$ and $S^P$ are real functions of position and that they are slowly varying on comparison with the wavelength in the $z$-direction, so that $\partial^2 S^P/\partial^2 z$ and $\partial S^P/\partial z \cdot \partial \Psi_0^P/\partial z$ can be neglected.

Finally, the geometrical field can be obtained by integrating equation (1.23b) as

$$\Psi_0(\vec{r}) = \Psi_0^P(\vec{r}_0)\exp\bigg\{-\frac{1}{2}\int_{z_0}^{z}\frac{\nabla_\perp^2 S^P}{n_0}dz'\bigg\}\exp\{ikS^P\} \tag{1.24}$$

where equation (1.22) and

$$\vec{\nabla}_\perp S^p \cdot \vec{\nabla}_\perp = n_0 \frac{d}{dz} \tag{1.25}$$

have been used.

Equations (1.11) and (1.24) represent the propagation of the geometrical complex amplitude between two arbitrary points joined by all possible rays and the are the elliptic and parabolic solutions for the scalar field. They become the Kernel functions of the integral equation used to find the complex amplitude distribution on an arbitrary surface if the scalar field at the initial surface is known in both approximations.

## 1.5 Ray equation in a GRIN medium

Light propagation in GRadient INdex media with a nonuniform index distribution $n(x, y, z)$ can be described by means of the vector ray equation. It can be derived from the Fermat's principle [84], which asserts that 'the light between two points is the curve for which the optical path attains an extreme value". Taking this into account, we can obtain the ray equation as an extreme condition. According to Fermat's principle

$$S = \int_{P_0}^{P_1} L\left((x, y, z)\frac{dx}{ds}, \frac{dy}{ds}, \frac{dz}{ds}, s\right) ds = extremum \tag{1.26}$$

where $S$ is the eikonal funtion (optical path length) and $ds$ is a diferential arc length along a ray trajectory between $P_0$ and $P_1$. Equation (1.26) is formally equivalent to Hamilton's principle in classical mechanics, where $s$ denotes time.

$$ds = \sqrt{dx^2 + dy^2 + dz^2} \tag{1.27}$$

In equation (1.26), $L$ is the optical Lagrangian [70], given by

$$L = n(x, y, x)\left[\left(\frac{dx}{ds}\right)^2 + \left(\frac{dy}{ds}\right)^2 + \left(\frac{dz}{ds}\right)^2\right]^{1/2} \tag{1.28}$$

The extremum condition of the optical path length is expressed as

$$\delta S = 0 \tag{1.29}$$

and the solution to this variational problem is obtained by substituting equation (1.28) in the Euler-Lagrange's equation.

Hence, the vector ray equation describing ray propagation in media with nonuniform index distribution in vectorial form is [70]

$$\frac{d}{ds}\left(n\frac{d\vec{r}}{ds}\right) = \nabla\vec{n} \tag{1.30}$$

where $\nabla\vec{n}$ is the gradient of $n$, $\vec{r}$ is the ray's position in the GRIN medium and equation (1.28) has been used.

The differential equation of rays can be written in Cartesian coordinates by taking one variable as an independent one [76]. Commonly, the z-coordinate is chosen to coincide with the axis of the optical system. Now, the Euler's equations become

$$\frac{d}{dz}\left(\frac{\partial L}{\partial \dot{x}}\right) = \frac{\partial L}{\partial x} \tag{1.31a}$$
$$\frac{d}{dz}\left(\frac{\partial L}{\partial \dot{y}}\right) = \frac{\partial L}{\partial y} \tag{1.31b}$$

and $L$ and $S$ can be written as

$$L(x,y,\dot{x},\dot{y};z) = n(x,y,z)(1+\dot{x}^2+\dot{y}^2)^{1/2} \tag{1.32}$$
$$S = \int_{z_0}^{z_1} L dz \tag{1.33}$$

where dot denotes derivative with respect to $z$.

Using equation (1.32) we can rewrite equations (1.31a) and (1.31b) as

$$\frac{d}{dz}\left(\frac{n\dot{x}}{\sqrt{1+\dot{x}^2+\dot{y}^2}}\right) = \sqrt{1+\dot{x}^2+\dot{y}^2}\frac{\partial n}{\partial x} \tag{1.34a}$$
$$\frac{d}{dz}\left(\frac{n\dot{y}}{\sqrt{1+\dot{x}^2+\dot{y}^2}}\right) = \sqrt{1+\dot{x}^2+\dot{y}^2}\frac{\partial n}{\partial y} \tag{1.34b}$$

Considering the optical direction cosines with respect to the $x$-, $y$- and $z$- axis

$$p = n\cos\alpha = n\frac{dx}{ds} = \frac{n\dot{x}}{\sqrt{1+\dot{x}^2+\dot{y}^2}} \tag{1.35a}$$

$$q = n\cos\beta = n\frac{dy}{ds} = \frac{n\dot{y}}{\sqrt{1+\dot{y}^2+\dot{y}^2}} \tag{1.35b}$$

$$l = n\cos\gamma = n\frac{dz}{ds} = \frac{n}{\sqrt{1+\dot{x}^2+\dot{y}^2}} \tag{1.35c}$$

it follows that the equations (1.34a) and (1.34b) can be expressed as [76]

$$n\frac{\partial l}{\partial p}\frac{\partial n}{\partial z} + p\dot{l} = 0 \tag{1.36a}$$

$$n\frac{\partial l}{\partial q}\frac{\partial n}{\partial z} + q\dot{l} = 0 \tag{1.36b}$$

From these expressions we can see that in radial GRIN media with only transverse variation of the refractive index the optical direction cosine with respect to the $z$-axis is invariant along any ray

$$\frac{\partial n}{\partial z} = 0 \tag{1.37}$$

Ray equations (1.36a)-(1.36b) are not easy to solve, so it is necessary to assume some conditions as, for instance, that ray propagates very close to the $z$-optical axis (paraxial approximation) and that the optical direction cosines of the ray, $p$ and $q$, are small.

## 1.6 Gaussian beams

The output modes of most laser sources can be simply described by Hermite-Gaussian or Laguerre-Gaussian functions. Therefore, the analysis of the propagation of laser beams through a particular optical system can be simplified by studying propagation of Gaussian beams through such a system. Gaussian beams are the most commonly beams obtained from all stable optical resonators where the laser radiation is produced. In this section we will introduce the characteristic parameters of Gaussian beams, since we are interested in the study of the propagation and transformation of Gaussian beams in active GRIN materials, namely in planar GRIN media with hyperbolic secant refractive index profile and GRIN media with parabolic refractive index profile.

### 1.6.1 Characteristic parameters of Gaussian beams

Gaussian beams present maximum irradiance value on the axis and decreases as a Gaussian function with distance from the axis. The most basic beam is the $TEM_{00}$ with a parabolic phase distribution at the transmitter located at $z = 0$. The complex amplitude distribution of a Gaussian laser beam can be written as [71, 85]

$$\Psi(r,z) = A_0 \frac{w_0}{w(z)} \exp\left\{ i \left[ k\left( z + \frac{r^2}{2R(z)} \right) - \varphi(z) \right] \right\} \exp\left\{ -\frac{r^2}{w^2(z)} \right\} \tag{1.38}$$

where

$$r = (x^2 + y^2)^{1/2} \tag{1.39}$$

is the square of the distance of the point $x, y$ from the axis of propagation.

Equation (1.39) describes the behaviour of the Gaussian beam amplitude as a function of the transversal dimension $r$ and the axial coordinate $z$. $A_0$ is a complex constant, $k = \frac{2\pi}{\lambda}$ is the wave number, with $\lambda$ the wavelength at the material where the beam propagates. The functions $w(z)$, $R(z)$ and $\varphi(z)$ represent the width or beam waist, the radius of curvature and a phase shift factor, respectively, and deserve special attention.

The function $w(z)$ describes the evolution along the propagation direction of the points having a decrease of $1/e$ in amplitude, or $1/e^2$ in irradiance with respect to the amplitude at the propagation axis $z$. This dependence is obtained from the evolution of the amplitude distribution [86–88] and takes the form of

$$w^2(z) = w_0^2 \left[ 1 + \left( \frac{\lambda z}{\pi w_0^2} \right)^2 \right] \tag{1.40}$$

where $w_0$ is the beam waist at $z = 0$ (see Figure 1.1). From this expression we can see that $w(z)$ reaches a minimum at $z = 0$, this being the minimum value of $w_0$.

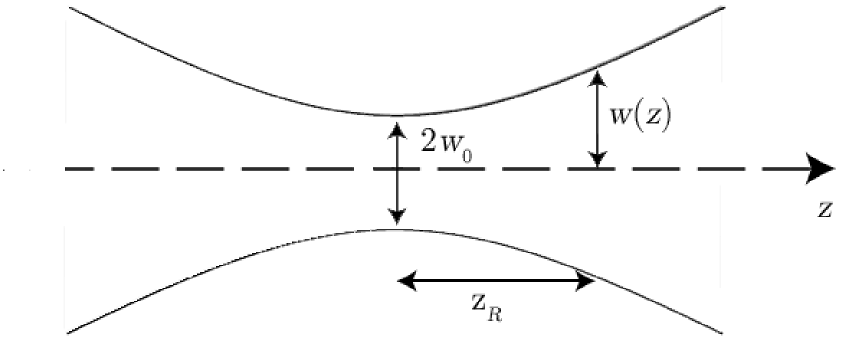

FIGURE 1.1: Gaussian beam width $w(z)$ as a function of the distance $z$ along the beam; $w_0$ is the beam waist and $z_R$ is Rayleigh range.

The radius of curvature $R(z)$ dependence with $z$ is given by

$$R(z) = z \left[ 1 + \left( \frac{\pi w_0^2}{\lambda z} \right)^2 \right] \tag{1.41}$$

The radius of curvature tends to infinity at the beam waist position, meaning that at the beam waist, the wavefront is plane. On the other hand, when $z$ tends to infinity, it shows a linear variation with $z$ that is typical of a spherical wavefront originated at $z = 0$ or, in other words, coming from a point source at this plane.

The third parameter $\varphi(z)$ is known as the Guoy phase shift and is described by

$$\varphi(z) = tan^{-1} \left( \frac{\lambda z}{\pi z} \right) \tag{1.42}$$

This phase factor represents a $\pi$ phase shift when the wavefront crosses the beam waist region [85].

The irradiance distribution of Gaussian beams is proportional to the modulus-square of the complex amplitude in equation (1.38)

$$I(r,z) = |\Psi(r,z)|^2 = \frac{|A_0|^2 w_0^2}{w^2(z)} \exp\left\{-2\frac{r^2}{w^2(z)}\right\} = \frac{\exp\left\{-2\frac{r^2}{w^2(z)}\right\}}{1+\left(\frac{z}{z_R}\right)^2} \tag{1.43}$$

where equation (1.40) has been used and $z_R = \frac{\pi w_0^2}{\lambda}$ is a parameter known as the Rayleigh range of the Gaussian beam. Its physical meaning is related to the behaviour of the beam along a propagation distance. The width at a plane $z = z_R$ is $\sqrt{2}$ larger than in the waist, that is, $\sqrt{2}w_0$, and the irradiance drops to half of its maximum value, where $I^{max} = I_0 = |A_0|^2$.

Gaussian beam theory was popularized by Kogelnik [89], who studied the passage of Gaussian beams through different optical systems as lenses and lenslike media. He introduced a complex beam parameter for which the transformation of Gaussian beams by any given optical structure can be expressed as a bilinear transformation (ABCD formalism). Kogelnik rewrote equation (1.38) as

$$\Psi(r,z) = A_0 \frac{w_0}{w(z)} \exp\{i\varphi(z)\} \exp\left\{i\frac{\pi}{\lambda}U(z)r^2\right\} \tag{1.44}$$

where the complex curvature of the beam is defined as

$$U(z) = \dot{q}(z)q^{-1}(z) = \frac{1}{R(z)} + \frac{i\lambda}{\pi w^2(z)} \tag{1.45}$$

where

$$q(z) = q_R + iq_I \tag{1.46}$$

is the complex beam parameter and $q_R$ and $q_I$ its real and imaginary parts, respectively. At the same time, $q(z)$ is solution of the paraxial ray equation in the medium considered and the same happens for $q_R$ and $q_I$ [83, 87]

where

$$\ddot{q}_{\binom{R}{I}} + g^2(z)q_{\binom{R}{I}} = 0 \tag{1.47}$$

satisfying the $z-$invariant condition

$$q_R\dot{q}_I - \dot{q}_R q_I = \frac{1}{k_0} \tag{1.48}$$

or equivalently

$$q^*\dot{q} - q\dot{q}^* = 2i(q_R\dot{q}_I - \dot{q}_R q_I) = \frac{2i}{k_0} \tag{1.49}$$

In the above expressions $k_0$ is the wavenumber in free space. Inserting equation (1.47) into equation (1.45) and separating into real and imaginary parts we can relate the main characteristic parameters of Gaussian beams in terms of the complex ray

$$w^2(z) = \frac{qq^*}{[k_0(q_R\dot{q}_I - \dot{q}_R q_I)]} = qq^* \tag{1.50}$$

$$\frac{1}{R(z)} = \frac{1}{2}\frac{dw}{dz}w^{-2} = \frac{1}{|q|}\frac{d|q|}{dz} = \frac{d}{dz}ln|q| \tag{1.51}$$

$$\varphi(z) = k_0 z - \frac{1}{2}phase[q(z)] \tag{1.52}$$

### 1.6.2 ABCD matrix formalism

Within the framework of the paraxial approach, matrix optics provides a modular transformation describing the effect on an optical system as the cascade operation of its components, where each simple optical system is given by its matrix representation. Hence, light propagation through different optical systems can be described using the formalism known as *ray transfer analysis* or *ABCD law* [90]. It allows to simplify and systematize light propagation within the paraxial approach by relating the position $x$ and slope $\dot{x}$ of any ray at the output of a given optical system with its corresponding position $x(0)$ and slope $\dot{x}(0)$ at the input of the system [71, 91]

$$\begin{pmatrix} x \\ \dot{x} \end{pmatrix} = M \begin{pmatrix} x(0) \\ \dot{x}(0) \end{pmatrix} \tag{1.53}$$

where

$$M = \begin{pmatrix} A & B \\ C & D \end{pmatrix} \tag{1.54}$$

and because of reciprocity the determinant of the matrix ray $M$ is the unity when the optical system is immersed in air.

For Gaussian illumination the complex beam parameter $q(z)$ and its derivative with respect to $z$, $\dot{q}(z)$, are the equivalent to the position and slope of a light beam in geometrical optics. Hence, propagation of Gaussian beams through an optical systems can be described by the following matrix representation

$$\begin{pmatrix} q(z) \\ \dot{q}(z) \end{pmatrix} = \begin{pmatrix} A & B \\ C & D \end{pmatrix} \begin{pmatrix} q(0) \\ \dot{q}(0) \end{pmatrix} \tag{1.55}$$

which provides the relationship between the complex rays at its corresponding derivatives at any plane $z$ within the optical system and with the input plane $z = 0$.

From equation (1.55) we can define all the characteristic parameters of the Gaussian beam. According to Kogelnik [71] the evolution of a Gaussian through an optical system can be described using the ABCD formalism and the evolution of the complex curvature as

$$U(z) = \frac{AU(0) + B}{CU(0) + D} \tag{1.56}$$

where $U(0)$ is the value of the complex curvature at $z = 0$.

ABCD matrix formalism can be applied to the study of Gaussian beam propagation through GRIN media, as we will see in the next section, when the ray transfer matrix of the media and the complex ray are known.

## 1.7 GRIN media with parabolic refractive index profile

In this section we summarize the mathematical basis of light propagation through a particular GRIN media with parabolic variations of its refractive index profile.

### 1.7.1 Ray equation and ABCD law

As we have mentioned in section 1.6.2, ray equations, in general, can not be solved exactly and approximate solutions can be derived. We will consider a weakly inhomogeneous medium with rotational symmetry where $\triangle n/n << 1$ for distances of $\lambda$ order, where $\lambda$ is the wavelength in free space, $n$ is the refractive index and $\triangle n$ is the diference between the refractive index at the axis at any transverse direction to it. The refractive index can be expressed as a McLaurin power series expansion with respect to cylindrical coordinates as

$$n^2(x,y,z) = n_0^2(z) \pm |n_{1z}^2|(x^2+y^2) \pm \frac{1}{2}|n_{2z}^2|(x^2+y^2)^2 \pm \dots \tag{1.57}$$

where $n_0^2$, $n_{1z}^2$ and $n_{2z}^2$ represent the dielectric constants along the optical axis and the first and the second derivatives of $n^2$ with respect to $z$ evaluated at $x = y = 0$, respectively. Under paraxial approximation, the refractive index for GRIN media with rotational symmetry to a first-order approximation is given by

$$n(x,y,z) = n_0(z)\left[1 \pm \frac{g^2(z)}{2}(x^2+y^2)\right] \tag{1.58}$$

where

$$g^2(z) = \frac{n_{1z}^2(z)}{n_0^2(z)} > 0 \tag{1.59}$$

is a slowly varying function with $z$ that characterizes the dielectric constant or refractive index distributions [76].

In general, analytical solutions of the ray equation are difficult to determine and need to be solved numerically by, for instance, the Runge-Kutta method. However, under paraxial approximation and considering meridional rays (rays that propagate in planes that include the optical axis), the ray equation is reduced to a simpler expression. Taking also under consideration $p, q$ small quantities which the rays bends slightly with respect to $z$-axis, we can rewrite equations (1.35a) and (1.35b) as

$$p = n_0(z)\dot{x} \tag{1.60a}$$

$$q = n_0(z)\dot{y} \tag{1.60b}$$

and equations (1.34a) and (1.34b) can be expressed under paraxial approximation as

$$\dot{p} = \frac{d}{dz}[n_0(z)\dot{x}] \tag{1.61a}$$

$$\dot{q} = \frac{d}{dz}[n_0(z)\dot{y}] \tag{1.61b}$$

Equations (1.60) and (1.61) are called paraxial equations and their solutions are paraxial rays that can be considered as approximations of the exact light rays in the neighborhood of the optical axis. We are going to consider only one set of equations $x, p$ as our GRIN medium is symmetric in $x, y$ and $p, q$, so equations for $y, q$ follow from analogy. Taking this into account, equation (1.61a) can be rewritten as

$$\ddot{x} + \frac{\dot{n}_0(z)}{n_0(z)}\dot{x} \pm g^2(z)x = 0 \tag{1.62}$$

Taking into account that $n_0$ as a constant we have

$$\ddot{x} \pm g^2(z)x = 0 \tag{1.63}$$

Considering the negative sign in equation (1.58), equation (1.63) has solutions with an infinite number of zeros within the interval $(0, \infty)$, i.e., it has oscillatory solutions. On the contrary, assuming a positive sign in (1.58) the solutions to the second order differential equation (1.63) are non-oscillatory [92]. So, in order to study the optical properties (namely, imaging and transforming) in GRIN media, we are going to consider the particular GRIN medium surrounded by vacuum of thickness $d$, described by a refractive index distribution that can be, under a second order approximation as

$$n(r, z) = n_0\left[1 - \frac{g^2(r, z)}{2}r^2\right] \quad \text{for} \quad r = \sqrt{x^2 + y^2} \tag{1.64}$$

with $n_0$ being the refractive index at the $z$-optical axis and $g(z)$ the gradient parameter, which describes the evolution of the transverse parabolic-index distribution along the $z$-axis.

Besides, equation (1.60a) and (1.63) can be written as

$$p = n_0 \dot{x} \tag{1.65a}$$

$$\ddot{x} + g^2(z)x = 0 \tag{1.65b}$$

The general solutions to equations (1.65a) and (1.65b) provide the position $x(z)$ and the optical cosine direction $p(z)$ of the paraxial ray at a point $P$ in the GRIN medium. These solutions can be written as a linear combination of two independent particular solutions, which are the axial, $H_a$, and field, $H_f$, rays defined by Luneburg [69]. The axial ray is the solution

$$x_a = H_a(z) \tag{1.66a}$$

$$p_a = n_0 \dot{H}_a(z) \tag{1.66b}$$

that, at $z = 0$ satisfies the boundary conditions

$$H_a(0) = 0 \tag{1.67a}$$

$$p_a(0) = n_0 \Longrightarrow \dot{H}_a(0) = 1 \tag{1.67b}$$

that is, the axial ray is a paraxial ray that originates at a point of the optical axis with slope of value 1 as depicted in figure 1.2.

The second solution, the field ray, is given by

$$x_f = H_f(z) \tag{1.68a}$$

$$p_f = n_0 \dot{H}_f(z) \tag{1.68b}$$

with the boundary conditions

$$H_f(0) = 1 \tag{1.69a}$$

$$p_f(0) = 0 \Longrightarrow \dot{H}_f(0) = 0 \tag{1.69b}$$

Hence, the field ray is a paraxial ray that leaves the reference plane parallel to the axis with slope zero (figure 1.2).

In the above expressions $\dot{H}_a$ and $\dot{H}_f$ are the slopes of the axial and field rays, respectively.

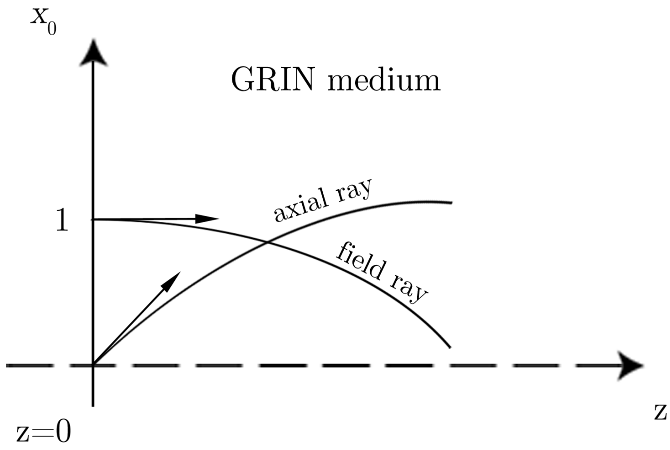

FIGURE 1.2: Axial and field rays in a GRIN medium and the corresponding boundary condtitions.

Any paraxial ray in the GRIN medium can be expressed in the general form as [76]

$$x(z) = H_f(z)x(0) + \frac{H_a(z)}{n_0}\dot{x}(0) \tag{1.70a}$$

$$p(z) = p_f(z)x(0) + p_a(z)\frac{p(0)}{n_0} = n_0\dot{H}_f(z)x(0) + \dot{H}_a(z)p(0) \tag{1.70b}$$

We can write these equations for the position and slope of the ray as

$$x(z) = H_f(z)x(0) + H_a(z)\dot{x}(0) \tag{1.71a}$$

$$\dot{x}(z) = \dot{H}_f(z)x(0) + \dot{H}_a(z)\dot{x}(0) \tag{1.71b}$$

with $\dot{x}(0)$ being the slope of the ray at the plane $z = 0$.

Two paraxial rays $x_1, p_1$ and $x_2, p_2$ are related by Lagrange's invariant at any transverse plane $z$ as

$$p_1(z)x_2(z) - p_2(z)x_1(z) = constant \tag{1.72}$$

that is, the Wronskian is a constant.

So, for the axial and field ray we have that

$$p_a(z)H_f(z) - H_a(z)p_f(z) = n_0 \tag{1.73a}$$

$$\dot{H}_a(z)H_f(z) - H_a(z)\dot{H}_f(z) = 1 \tag{1.73b}$$

The linear algebraic nature of equations (1.70a), (1.70b), (1.71a) and (1.71b) allows as to use matrices that *describe the paraxial propagation of light through a GRIN medium*, that is

$$\begin{pmatrix} x(z) \\ p(z) \end{pmatrix} = M'(z) \begin{pmatrix} x(0) \\ \dot{x}(0) \end{pmatrix} = \begin{pmatrix} H_f(z) & H_a(z)/n_0 \\ n_0\dot{H}_f(z) & \dot{H}_a(z) \end{pmatrix} \begin{pmatrix} x(0) \\ p(0) \end{pmatrix} \tag{1.74}$$

$$\begin{pmatrix} x(z) \\ \dot{x}(z) \end{pmatrix} = M(z) \begin{pmatrix} x_0 \\ \dot{x}_0 \end{pmatrix} = \begin{pmatrix} H_f(z) & H_a(z) \\ \dot{H}_f(z) & \dot{H}_a(z) \end{pmatrix} \begin{pmatrix} x_0 \\ \dot{x}_0 \end{pmatrix} \tag{1.75}$$

such that

$$|M'(z)| = |M(z)| = 1 \tag{1.76}$$

$M$ and $M'$ are known as ray-transfer or ABCD matrices and characterize the light propagation in the GRIN medium completely. In this ray matrix formalism, the ABCD elements of $M$ and $M'$ matrices are

$$A = H_f(z); \quad B = H_a(z); \quad C = \dot{H}_f(z); \quad D = \dot{H}_a(z) \tag{1.77a}$$

$$A' = A; \quad B' = \frac{B}{n_0}; \quad C = n_0C; \quad D' = D \tag{1.77b}$$

Since $H_a$ and $H_f$ are two linearly independent solutions of equations (1.65a) and (1.65b), they can be expressed as [93, 94]

$$H_a(z) = [g_0 g(z)]^{-1/2} \sin\left[\int_0^z g(z')dz'\right] \tag{1.78a}$$

$$H_f(z) = \left[\frac{g_0}{g(z)}\right]^{1/2} \cos\left[\int_0^z g(z')dz'\right] \tag{1.78b}$$

where $g_0$ is the value of the gradient parameter $g(z)$ at $z = 0$.

Inserting above equations in (1.65b) we obtain

$$\ddot{g}g - \frac{3}{2}\dot{g}^2 = g^3\left[\frac{g}{2}{\frac{\dot{g}}{g^2}}^2 + \frac{d}{dz}\frac{\dot{g}}{g^2}\right] = 0 \tag{1.79}$$

that is, axial and field rays satisfy (1.65b) only approximately. For small variations of $g(z)$ over distances on the order of the wavelength

$$\frac{|\dot{g}|}{g^2(z)} << 1 \tag{1.80}$$

equation (1.79) is almost zero and the slope of the axial and field rays can be written as

$$\dot{H}_a(z) = \left[\frac{g(z)}{g_0}\right]^{1/2} \cos\left[\int_0^z g(z')dz'\right] \tag{1.81a}$$

$$\dot{H}_f(z) = -[g_0 g(z)]^{1/2} \sin\left[\int_0^z g(z')dz'\right] \tag{1.81b}$$

and the oscillatory rays preserve the boundary conditions as well as satisfy the Lagrange's invariant.

For the particular case of a self-focusing GRIN medium, where $g(z) = g_0 =$ *constant*, the axial and field ray position and slope reduce to

$$H_a(z) = \frac{\sin(g_0 z)}{g_0}; \quad H_f(z) = \cos(g_0 z) \tag{1.82a}$$

$$\dot{H}_a(z) = \cos(g_0 z); \quad \dot{H}_f(z) = -g_0 \sin(g_0 z) \tag{1.82b}$$

### 1.7.2 The Kernel function

We have treated the propagation of light through first-order systems in the scalar and paraxial approximation. These first-order optical systems are described in scalar diffraction theory by a canonical integral transform, which can be introduced in three ways: as an integral transform, through a matrix representation, and as a linear transformation of the Wigner function. The identity between these transforms has been well establish in literature [95–100].

Let $\Psi(x_0, y_0; 0)$ be the complex amplitude of a parabolic scalar field at a transverse plane $z = 0$. Hence, the field $\Psi$ at any plane $z > 0$ is given by the integral transform or generalized Fresnel transform [101]

$$\Psi(x, y, z) = \int_{\mathbb{R}^2} K(x_0, y_0, x, y; z)\Psi(x_0, y_0; 0)dx_0 dy_0 \tag{1.83}$$

with $K$ being the kernel of the linear transformation known in optics as the impulse response or Point Spread Function (PSF).

The kernel is the Green's function of the parabolic wave equation with the boundary condition [76, 102]

$$K(x_0, y_0, x, y; z) \to \delta(x - x_0, y - y_0) \quad as \quad z \to 0 \tag{1.84}$$

where $\delta$ is the two-dimensional Dirac delta function.

The complex amplitude distribution at any arbitrary transverse plane can be obtained from equation (1.83) with the aid of the kernel, if the field at a reference plane is known.

Now we will consider a GRIN medium whose refractive index is given by equation (1.64). Taking into account that the the geometrical field in equation (1.24) represents the propagation of the complex amplitude of the parabolic field between two arbitrary points located at two transverse planes and joined by all classical rays, that is, by rays that minimize the optical path. Therefore, equation (1.24) becomes the kernel satisfying the parabolic equation (1.18) and the condition (1.84). Hence, the kernel function can be rewritten as

$$K(x_0, y_0, x, y; z) = K_0 \mathrm{exp}\left\{ -\frac{1}{2n_0}\int_0^z \nabla_\perp^P S^P dz' \right\} \mathrm{exp}\{ikS^P\} \tag{1.85}$$

where $K_0$ is a constant determined by equation (1.84).

The eikonal function for parabolic approximation can be expressed as

$$S^P = \int_0^z L^P dz' \tag{1.86}$$

where equation (1.33) has been used, and $L^P$ is the parabolic optical Lagrangian.

Taking into account that this parabolic approximation (or in the paraxial region), the ray slopes are

$$\dot{x} << 1, \quad \dot{y} << 1 \tag{1.87}$$

the paraxial Lagrangian can be written as

$$L^P = n_0\left[1 - \frac{g^2(z)}{2}(x^2+y^2) + \frac{\dot{x}^2+\dot{y}^2}{2}\right] \tag{1.88}$$

where equation (1.64) has been used and all higher orders have been neglected.

Inserting equation (1.88) into (1.86) we have that the eikonal function for parabolic approximation can be written as

$$S^P = n_0 z + \frac{n_0}{2}\int_0^z [\dot{x}^2 + \dot{y}^2 - g^2(z')(x^2+y^2)]dz' \tag{1.89}$$

Considering equation (1.63), the integral in the above expression becomes

$$\int_0^z [\dot{x}^2 + \dot{y}^2 - g^2(z')(x^2+y^2)]dz' = \int_0^z \frac{d}{dz'}[x\dot{x} + y\dot{y}]dz' \tag{1.90}$$

Thus, equation (1.89) reduces to

$$S^P = n_0 z + \frac{n_0}{2}(x\dot{x} + y\dot{y})|_0^z \tag{1.91}$$

which can be rewritten as function of the axial and field rays using equations (1.71a)-(1.71b) and (1.73b)

$$S^P = n_0 z + (x_0^2+y_0^2)H_f(z)\dot{H}_f(z) + (\dot{x}_0^2+\dot{y}_0^2)H_a(z)\dot{H}_a(z) + 2(x_0\dot{x}_0+y_0\dot{y}_0)H_a(z)\dot{H}_f(z) \tag{1.92}$$

where $(x_0, y_0)$, $(\dot{x}_0, \dot{y}_0)$ are the position and slope of any paraxial at $z = 0$ and, in terms of the ray position at the two reference planes, as

$$S^P = n_0 z + \frac{n_0}{2H_a(z)}[(x^2+y^2)\dot{H}_a(z) + (x_0^2+y_0^2)H_f(z) - 2(x_0x + yy_0)] \quad (1.93)$$

since from equation (1.71a) it follows that the ray slope at $z = 0$ can be expressed in terms of the ray position at both planes as

$$\begin{pmatrix} \dot{x}_0 \\ \dot{y}_0 \end{pmatrix} = \frac{\begin{pmatrix} x \\ y \end{pmatrix} - \begin{pmatrix} x_0 \\ y_0 \end{pmatrix} H_f(z)}{H_a(z)} \quad (1.94)$$

On the other hand, substituting equation (1.93) into the amplitude of the kernel function and integrating we obtain

$$\exp\left\{ -\frac{1}{2n_0}\int_0^z \nabla_\perp^2 S dz' \right\} = \frac{1}{H_a(z)} \quad (1.95)$$

Since, the kernel function becomes

$$\begin{aligned} K(x_0, y_0, x, y; z) =& \frac{K_0}{H_a(z)} \exp(ikn_0z) \exp\left\{ i\frac{kn_0}{2H_a(z)} \cdot \right. \\ & \left. \cdot\, [(x^2+y^2)\dot{H}_a(z) + (x_0^2+y_0^2)H_f(z) - 2(x_0x + y_0y)] \right\} \end{aligned} \quad (1.96)$$

$K_0$ can be determined using condition (1.84). By using the property

$$\int_{\mathbb{R}} \delta(x - x_0, y - y_0) dx dy = 1 \quad (1.97)$$

where

$$\delta(x - x_0, y - y_0) = \lim_{z \to 0}(x_0, y_0, x, y; z) \quad (1.98)$$

$K_0$ results

$$K_0 = \frac{kn_0}{i2\pi} \quad (1.99)$$

Taking this into account, the Kernel function can be written as

$$\begin{aligned}K_0(x_0,y_0,x,y;z) =&\frac{kn_0}{i2\pi H_a(z)}\exp(ikn_0z)\cdot\\&\cdot\exp\left\{i\frac{kn_0}{2H_a(z)}[(x^2+y^2)\dot{H}_a(z)+\right.\\&\left.+(x_0^2+y_0^2)H_f(z)-2(x_0x+y_0y)]\right\}\end{aligned}\tag{1.100}$$

or, equivalently,

$$\begin{aligned}K_0(x_0,y_0,x,y;z) =&\frac{kn_0}{i2\pi H_a(z)}\exp(ikn_0z)\exp\left\{i\frac{kn_0\dot{H}_f(z)}{2H_f(z)}(x^2+y^2)\right\}\cdot\\&\cdot\exp\left\{i\frac{kn_0H_f(z)}{2H_a(z)}\left[\left(x_0-\frac{x}{H_f(z)}\right)^2+\left(y_0-\frac{y}{H_f(z)}\right)^2\right]\right\}\end{aligned}\tag{1.101}$$

We can also express equations (1.100)-(1.101) in terms of the ray-transfer matrix relating positions and slopes of a ray at two transverse planes as

$$\begin{aligned}K_0(x_0,y_0,x,y;z) =&\frac{kn_0}{i2\pi B}\exp(ikn_0z)\cdot\\&\cdot\exp\left\{i\frac{kn_0}{2B}[(x^2+y^2)D+(x_0^2+y_0^2)A-2(x_0x+y_0y)\right\}\end{aligned}\tag{1.102}$$

or

$$\begin{aligned}K_0(x_0,y_0,x,y;z) =&\frac{kn_0}{i2\pi B}\exp(ikn_0z)\exp\left\{i\frac{kn_0C}{2B}(x^2+y^2)\cdot\right.\\&\cdot\exp\left\{\exp\left\{i\frac{kn_0A}{2B}\left[\left(x_0-\frac{x}{A}\right)^2+\left(y_0-\frac{y}{A}\right)^2\right]\right\}\right.\end{aligned}\tag{1.103}$$

where equation (1.77a) has been used.

Equations (1.100) and (1.101) can also be parametrized in terms of the ray-transfer matrix connecting positions and optical direction cosines of a ray at two transverse planes. So, using equation (1.77b), equation (1.100) is given by

$$\begin{aligned} K_0(x_0, y_0, x, y; z) =& \frac{kn_0}{i2\pi B'}\exp(ikn_0 z)\cdot \\ & \cdot \exp\left\{ i\frac{k}{2B'}(x^2+y^2)D' + \right. \\ & \left. + (x_0^2 + x_0^2)A' - 2(x_0 x + y_0 y)] \right\} \end{aligned} \tag{1.104}$$

In the above equations, we have the following relation

$$AD - BC = A'D' - B'C' = 1 \tag{1.105}$$

where equations (1.77a)-(1.77b) have been used.

It is important to remark that an important particular case of the canonical integral transform is the Fresnel transform, which describes diffraction in free space. Hence, when $n_0 = 1$, $H_a(z) = z$, $\dot{H}_a(z) = 1$, $H_f(z) = 1$, and $\dot{H}_f(z) = 0$, equations (1.100) and (1.101) define the well-known point spread function of Fresnel diffraction. It corresponds to the canonical integral transform parametrized by the transfer matrix with $A = D = 1$, $C = 0$, and $B = z$

### 1.7.3 Gaussian beam propagation

Since the realization of the first laser by Maiman in 1960 [103] they have become ubiquitous, playing an important role on development of applications including optical communications, life sciences, microelectronics, medical therapeutics and industrial, among others. In most laser applications it is necessary to know the propagation characteristics of laser beam. In general, laser beam propagation can be approximated by assuming that the laser beam has an ideal Gaussian intensity profile, a widespread model in laser optics.

We consider a GRIN medium surrounded by air with rotational symmetry around the $z-$axis, semiaperture $a$ and thickness $d$ with a parabolic refractive index distribution given by

$$\begin{cases} n^2(x,y,z) = n_0^2[1-g^2(z)r^2] \text{ for } r=(x^2+y^2)^{1/2} \leq a & \text{and} \quad 0 \leq z \leq d \\ 1 & \text{rest} \end{cases} \tag{1.106}$$

Figure 1.3 shows the refractive index profile variations and the geometry of a GRIN medium. The passage of a Gaussian beam through this GRIN medium is described by the ABCD law [104]

$$\begin{pmatrix} q(z) \\ n_0\dot{q}(z) \end{pmatrix} = \begin{pmatrix} H_f(z) & \frac{Ha(z)}{n_0} \\ n_0\dot{H}_f(z) & \dot{H}_a(z) \end{pmatrix} \begin{pmatrix} q(0) \\ n_0\dot{q}(0) \end{pmatrix} \tag{1.107}$$

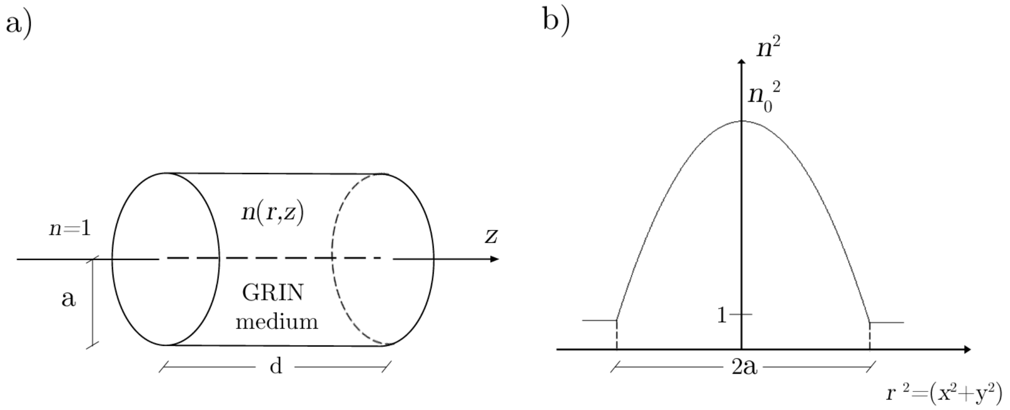

FIGURE 1.3: GRIN lens: a) geometry of a cylindrical GRIN material of radius $a$ and thickness $d$ surrounded by free space and b) transverse parabolic refractive index profile distribution.

where $q(0)$ and $\dot{q}(0)$ are the position and the slope of the complex ray at the input plane.

The expressions for the complex ray $q$ and its slope $\dot{q}$ for any $z > 0$ can be obtained from the above matrix equation. Considering now (1.107) and (1.45) we can write

$$q(z) = q(0)\alpha(z) \tag{1.108a}$$

$$\dot{q}(z) = q(0)\dot{\alpha}(z) \tag{1.108b}$$

where

$$\alpha(z) = H_f(z) + U(0)\frac{H_a(z)}{n_0} \tag{1.109a}$$

$$\dot{\alpha}(z) = \dot{H}_f(z) + U(0)\frac{\dot{H}_a(z)}{n_0} \tag{1.109b}$$

and $U(0)$, the complex curvature at the input plane, is given by

$$U(0) = U_R(0) + iU_I(0) = \frac{1}{R(0)} + i\frac{\lambda}{\pi w^2(0)} \tag{1.110}$$

with $U_R$ and $U_I$ being the real and imaginary parts of $U$. $R(0)$ and $w(0)$ are the radius of curvature and the beam half-width at the input plane, respectively. These beam parameters, assuming that the beam waist of diameter $2w_0$ is located at a distance $d_1$ from the input plan of the GRIN medium (see figure 1.4) are defined as

$$R(0) = d_1\left[1 + \left(\frac{\pi w_0^2}{\lambda d_1}\right)^2\right] \tag{1.111}$$

$$w^2(0) = w_0^2\left[1 + \left(\frac{\lambda d_1}{\pi w_0^2}\right)^2\right] \tag{1.112}$$

On the other hand, the complex curvature of the Gaussian beam, given by (1.110), can also be expressed in terms of the complex rays as

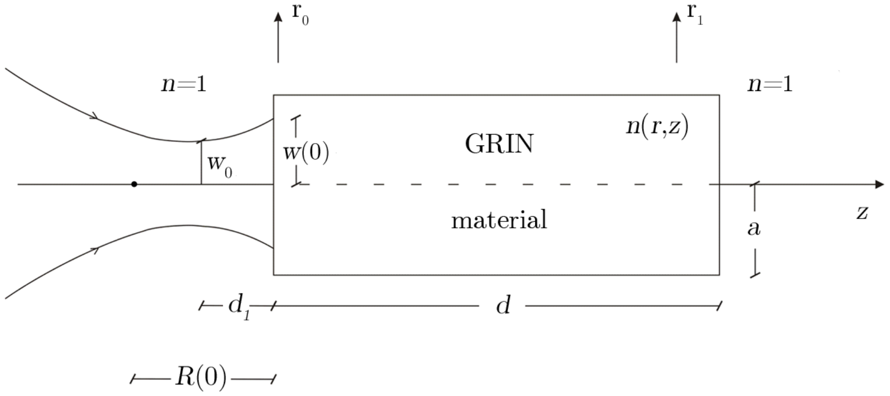

FIGURE 1.4: Illustration for a Gaussian beam with parameters $R(0)$ and $w(0)$ at the input face of a GRIN material of radius $a$ and thickness $d$ surrounded by free space.

$$U(0) = n_0\dot{q}(0)q^{-1}(0) \tag{1.113}$$

where the position and the slope of the complex ray at the input plane are defined as

$$q(0) = w_0 + i\frac{\lambda d_1}{\pi w_0} \tag{1.114}$$

$$\dot{q}(0) = \frac{i\lambda}{\pi n_0 w_0} \tag{1.115}$$

In above equations, dot denotes derivative with respect to $z$ evaluated at z=0.

Inserting equations (1.108a), (1.108b), (1.109a) and (1.109b) into (1.45) and (1.50), we obtain that the complex curvature can be expressed as

$$U(z) = n_0\dot{\alpha}(z)\alpha^{-1}(z) = n_0\dot{q}(z)q^{-1}(z) \tag{1.116}$$

and the beam waist

$$w^2(z) = w^2(0)|\alpha(z)|^2 \tag{1.117}$$

As an application example of the above formalism we consider a plane Gaussian beam ($d_1 = 0, w^2(0) = w_0^2$ ) impinging on the input face of a GRIN selfoc medium, that is, with $g(z) = g_0 = constant$, and described by the refractive index profile distribution of equation (1.106). By substitution of the initial conditions of the beam

$$q(0) = w_0 \tag{1.118a}$$

$$\dot{q}(0) = \frac{i\lambda}{\pi n_0 w_0} \tag{1.118b}$$

and the axial and field ray

$$H_a(z) = \frac{\sin(g_0 z)}{g_0} \tag{1.119a}$$

$$H_f(z) = \cos(g_0 z) \tag{1.119b}$$

into (1.109a), (1.109b) and (1.117), the beam waist of an input plane Gaussian beam in the self-focusing GRIN medium can be written as

$$w^2(z) = w_0 \left[ \cos^2(g_0 z) + \left( \frac{\lambda}{\pi n_0 g_0 w_0^2} \right)^2 \sin^2(g_0 z) \right] \tag{1.120}$$

We can rewrite the above expression as function of the beam waist of the fundamental mode $w_{fm}$ for the selfoc medium [101]

$$w_{fm} = \sqrt{\frac{\lambda}{\pi n_0 g_0}} \tag{1.121}$$

as follows

$$w^2(z) = w_0 \left[ \cos^2(g_0 z) + \left( \frac{w_{fm}}{w_0} \right)^4 \sin^2(g_0 z) \right] \tag{1.122}$$

From equation (1.122) we can analyze the evolution of the beam half-width for Gaussian plane illumination in the GRIN medium. For the $z-$lengths in the material verifying

$$z = \frac{m\pi}{g_0} \quad (m = 0, 1, 2, 3...) \tag{1.123}$$

the beam waist is equal to the beam half-width of the input plane Gaussian beam, while for lengths of the GRIN medium

$$z = \frac{(2m+1)\pi}{2g_0} \quad (m = 0, 1, 2, 3...) \tag{1.124}$$

the beam waist results

$$w^2 = \frac{w_{fm}^4}{w_0^2} \tag{1.125}$$

Consequently, for these $z$ positions in the lens we have that $w > w_0$ for $w_{fm} > w_0$, while $w < w_0$ if $w_{fm} < w_0$. It is interesting to note that when $w_{fm} = w_0$, from (1.122) it follows that $w(z) = w_{fm}$. Now the beam propagates as the fundamental mode, and there is an adiffractional Gaussian beam inside the selfoc material. The evolution of the beam waist of the input plane Gaussian beam for these three cases, i.e.,$w_{fm} < w_0$, $w_{fm} > w_0$ and $w_{fm} = w_0$ is shown in figure 1.5.

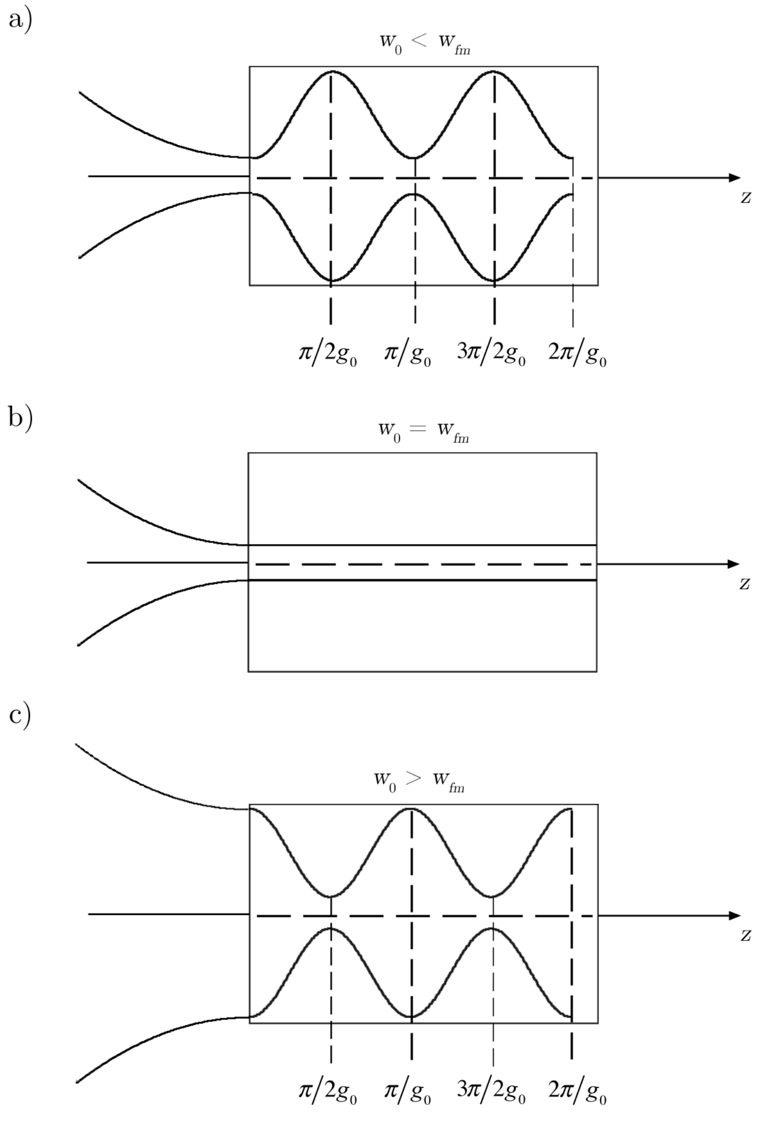

FIGURE 1.5: Propagation of a plane Gaussian beam into a GRIN selfoc medium for a) $w_0 < w_{fm}$, b) $w_{fm} = w_0$, and c) $w_0 > w_{fm}$.

## 1.8 Planar GRIN media with complex hyperbolic secant refractive index profile

Light propagation in GRIN media described by a different gradient index profiles has been analyzed in order to use their ability to implement optical functions as, for instance, focusing and collimation, in integrated optics, fiber optics or optical sensing. The simplest GRIN medium able to carry out those optical operations is the parabolic one, where the ray equation can be solved analytically in the paraxial region. However, there is another transverse GRIN medium with focusing and collimation properties that is characterized by a hyperbolic secant (HS) refractive index profile. It provides a stigmatic image without the need for carrying out the paraxial approximation and is of significant practical interest. In particular, the hyperbolic secant refractive index profile presents some advantages in comparison to the parabolic one: i) is a more general profile, given that the parabolic function can be considered as the first-order approximation of the Taylor expansion series of the HS function; ii) the equation governing light propagation can be solved analytically without carrying out any type of approximation; and iii) the medium is free of aberrations for meridional rays. Fabrication of GRIN media with such index profiles has already been demonstrated [105, 106].

### 1.8.1 Ray equation and ABCD law

In this section we consider a GRIN planar waveguide with a hyperbolic secant (HS) transverse refractive index profile along the $x$-axis is given by

$$n^2(x) = n_0^2 sech^2(gx) \tag{1.126}$$

In equation (1.126) $n_0$ is the refractive index along the optical axis $z$ and $g$ is the gradient parameter. The reciprocal of the gradient parameter, $g^{-1}$ is the half-width of the profile, i.e., the distance in transverse direction at which the

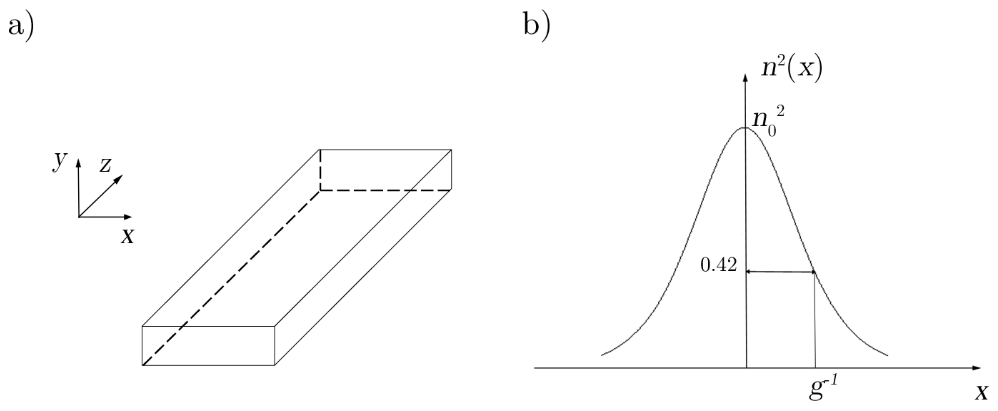

FIGURE 1.6: a) Planar waveguide and b) hyperbolic secant refractive index profile distribution.

refractive index profile decays to 0.42 of its maximum value, as shown in Figure 1.6.

As in this case the third optical direction cosine is invariant along the GRIN medium, given that $\partial n/\partial z = 0$, and taking into account (1.126) we have that

$$l = l_0 = n(x)\frac{\partial z}{\partial s} = \frac{n(x)}{\sqrt{1+\dot{x}^2}} = constant \tag{1.127}$$

Equation (1.127) can be rewritten as

$$dz = \frac{l_0}{\sqrt{n(x)^2 - l_0^2}}dx \tag{1.128}$$

Substituting the expression of the transverse refractive index profile given by equation (1.126) in equation (1.128) we have

$$dz = \frac{\cosh(gx)}{\sqrt{A^2 - \sinh^2(gx)}}dx \tag{1.129}$$

where

$$A^2 = \frac{n_0^2 - l_0^2}{l_0^2} \tag{1.130}$$

Thus, from equation (1.129) we have that the ray trajectory in the GRIN medium between any two points located at $z = 0$ and $z > 0$ can be expressed as

$$z = \int_{x_0}^{x} \frac{\cosh(gx)}{\sqrt{A^2 - \sinh^2(gx)}} dx \tag{1.131}$$

We can solve this equation in a hyperbolic space of coordinates $(u, z)$ where $u$ is given by the transformation

$$u = \sinh(gx) \tag{1.132}$$

This new variable determines the position of the ray in the new coordinate system. Inserting equation (1.132) into (1.131) and performing the integration with respect to $u$ we obtain that the ray trajectory in the hyperbolic secant GRIN medium is

$$z = \frac{1}{g}\left[\sin^{-1}\left(\frac{u}{A}\right) - \sin^{-1}\left(\frac{u_0}{A}\right)\right] \tag{1.133}$$

with $u_0$ being the value of $u$ at $z = 0$, i.e., $u_0 = \sinh(gx_0)$.

Equation (1.133) can be rewritten as

$$u(z) = A\sin(\tau) \tag{1.134}$$

where

$$\tau = \sin^{-1}\left(\frac{u_0}{A}\right) + gz \tag{1.135}$$

Equation (1.134) indicates the ray position at any point within the medium and its derivative with respect to $z$, $\dot{u}(z)$ represents the ray slope in the coordinate system $(u, z)$ as follows

$$\dot{u}(z) = g\dot{x}\cosh(gx) = Ag\cos(\tau) \tag{1.136}$$

The ray equation for position and slope (1.134) and (1.136) can also be expressed as

$$u(z) = A\left\{\frac{u_0}{A}\cos(gz) + \cos\left[\sin^{-1}\left(\frac{u_0}{A}\right)\right]\sin(gz)\right\} \tag{1.137a}$$

$$\dot{u}(z) = gA\left\{\cos\left[\sin^{-1}\left(\frac{u_0}{A}\right)\right]\cos(gz) - \frac{u_0}{A}\sin(gz)\right\} \tag{1.137b}$$

and

$$\cos\left[\sin^{-1}\left(\frac{u_0}{A}\right)\right] = \cos(\tau_0) = \frac{\dot{u}_0}{gA} \tag{1.138}$$

with $\tau_0$ and $\dot{u}_0$ being the respective values of $\tau$ and $\dot{u}$ at $z = 0$.

Hence, equations (1.137a) and (1.137b) become

$$u(z) = u_0\cos(gz) + \dot{u}_0\frac{\sin(gz)}{g} \tag{1.139a}$$

$$\dot{u}(z) = -u_0 g\sin(gz) + \dot{u}_0\cos(gz) \tag{1.139b}$$

If we introduce now the axial $H_a$ and field $H_f$ ray, defined by Luneburg [69] as particular solutions of the ray equation, we have

$$H_a(z) = \frac{\sin(gz)}{g} \tag{1.140a}$$

$$\dot{H}_a = \cos(gz) \tag{1.140b}$$

$$H_f(z) = \cos(gz) \tag{1.140c}$$

$$\dot{H}_f = -g\sin(gz) \tag{1.140d}$$

where the initial conditions for these rays are

$$H_a(0) = \dot{H}_f(0) = 0 \tag{1.141a}$$

$$\dot{H}_a(0) = H_f(0) = 1 \tag{1.141b}$$

and Lagrange's invariant relating $H_a$ and $H_f$ as follows

$$\dot{H}_a(z)H_f(z) - H_a(z)\dot{H}_f(z) = 1 \tag{1.142}$$

In this manner, equations (1.139a) and (1.139b) result

$$u(z) = u_0 H_f(z) + \dot{u}_0 H_a(z) \tag{1.143a}$$

$$\dot{u}(z) = u_0 \dot{H}_f(z) + \dot{u}_0 \dot{H}_a(z) \tag{1.143b}$$

Equations (1.143a) and (1.143b) present the same form that the paraxial ray equation in (1.71a) and (1.71a) for a parabolic GRIN medium but in this case the solution to the ray equation has been obtained for a new coordinate system $(u, z)$, without using any approximation, verifying that the hyperbolic secant refractive index profile is free of aberrations for meridional rays.

Light propagation in the planar waveguide, expressed by equations (1.143a) and (1.143b), can also be described using a 2x2 matrix representation (ABCD law)

$$\begin{pmatrix} u(z) \\ \dot{u}(z) \end{pmatrix} = \begin{pmatrix} H_f(z) & H_a(z) \\ \dot{H}_f(z) & \dot{H}_a(z) \end{pmatrix} \begin{pmatrix} u(0) \\ \dot{u}(0) \end{pmatrix} \tag{1.144}$$

Real trajectories can be obtained undo the change of coordinates given by (1.132), that relates the position and the slope of a ray at any plane of the GRIN medium with the position at the input face of the material but in the hyperbolic space of coordinates.

### 1.8.2 Gaussian beam propagation

We consider a plane Gaussian beam whose waist is located at the input face of a HS medium with length $d$ and study its evolution inside the GRIN material. As we saw in the previous section, light propagation in this material can be analyzed solving the ray equation in a hyperbolic space of coordinates $(u, z)$ where $u$ is given by the transformation (1.132). Taking into account that for a Gaussian beam the complex ray $q(z)$ plays the role of the real ray $x(z)$, it follows that in the HS medium, a complex ray in the hyperbolic space can be defined as the position $q_h(z)$ and the slope $\dot{q}_h(z)$ as [107]

$$q_h(z) = \sinh[gq(z)] = q_{hR} + iq_{hI} \tag{1.145}$$

where $q_{hR}$ and $q_{hI}$ represent the real and imaginary part of $q_h$ and are given by

$$q_{hR}(z) = \sinh[gq_R(z)]\cos[gq_I(z)] \tag{1.146a}$$

$$q_{hI}(z) = \cosh[gq_R(z)]\sin[gq_I(z)] \tag{1.146b}$$

with $q_R$ and $q_I$ the real and imaginary part of the complex ray $q(z)$.

On the other hand

$$\dot{q}_h(z) = \frac{dq_h(z)}{dz} = g\dot{q}(z)\cosh[gq(z)] = \dot{q}_{hR} + i\dot{q}_{hI} \tag{1.147}$$

where $\dot{q}_{hR}$ and $\dot{q}_{hI}$ represent the real and imaginary part of $\dot{q}_h$

$$\dot{q}_{hR}(z) = g[\dot{q}_R(z)c(z) - \dot{q}_I(z)s(z)] \tag{1.148a}$$

$$\dot{q}_{hI}(z) = g[\dot{q}_R(z)s(z) + \dot{q}_I(z)c(z)] \tag{1.148b}$$

being

$$c(z) = \cosh[gq_R(z)]cos[gq_I(z)] \tag{1.149a}$$

$$s(z) = \sinh[gq_R(z)]\sin[gq_I(z)] \tag{1.149b}$$

We can express $q_h(z)$ and $\dot{q}_h(z)$ as function of the initial values $q_h(0)$ and $\dot{q}_h(0)$ taking into account that the transformation given by equations (1.145) and (1.147) by means of the matrix equation [108]

$$\begin{pmatrix} q_h(z) \\ \dot{q}_h(z) \end{pmatrix} = \begin{pmatrix} H_f(z) & H_a(z) \\ \dot{H}_f(z) & \dot{H}_a(z) \end{pmatrix} \begin{pmatrix} q_h(0) \\ \dot{q}_h(0) \end{pmatrix} \tag{1.150}$$

Equivalently, we can write

$$\begin{pmatrix} q_{hR}(z) + iq_{hI}(z) \\ \dot{q}_{hR}(z) + i\dot{q}_{hI}(z) \end{pmatrix} = \begin{pmatrix} H_f(z) & H_a(z) \\ \dot{H}_f(z) & \dot{H}_a(z) \end{pmatrix} \begin{pmatrix} q_{hR}(0) \\ \dot{q}_{hI}(0) \end{pmatrix} \tag{1.151}$$

where $q_{hR}(0)$, $q_{hI}(0)$, $\dot{q}_{hR}(0)$ and $\dot{q}_{hI}(0)$ are the real and imaginary parts of $q_h(0)$ and $\dot{q}_h(0)$, respectively.

From equation (1.151) it follows that

$$q_{hR}(z) = H_f(z)q_{hR}(0) + H_a(z)\dot{q}_{hR}(0) \tag{1.152a}$$

$$q_{hI}(z) = H_f(z)q_{hI}(0) + H_a(z)\dot{q}_{hI}(0) \tag{1.152b}$$

$$\dot{q}_{hR}(z) = \dot{H}_f(z)q_{hR}(0) + \dot{H}_a(z)\dot{q}_{hR}(0) \tag{1.152c}$$

$$\dot{q}_{hI}(z) = \dot{H}_f(z)q_{hI}(0) + \dot{H}_a(z)\dot{q}_{hI}(0) \tag{1.152d}$$

Now, if we solve $\cos[gq_I(z)]$ from (1.146a) and substitute in (1.146b)

$$\sinh^4[gq_R(z)] + (1 - q_{hR}^2 - q_{hI}^2)\sinh^2[gq_R(z)] - q_{hR}^2 = 0 \tag{1.153}$$

and insert the following change of variable

$$t = \sinh^2[g q_R(z)] \tag{1.154}$$

we have that expression (1.153) can be written as a quadratic equation which solution is given by

$$t = \frac{1}{2}\left\{(q_{hR}^2 + q_{hI}^2 - 1) + \sqrt{(1 - q_{hR}^2 - q_{hI}^2) + 4q_{hR}^2}\right\} \tag{1.155}$$

Hence, the real part of $q(z)$ is

$$q_R(z) = \frac{1}{g}\sinh^{-1}[\sqrt{t}] \tag{1.156}$$

and the imaginary part $q_I(z)$

$$q_I(z) = \frac{1}{g}\cos^{-1}\left[\frac{q_{hR}(z)}{\sqrt{t}}\right] \tag{1.157}$$

Following the same procedure, we can obtain $\dot{q}_R$ and $\dot{q}_I$ from the system of equations formed by (1.148a) and (1.148b). The solutions of this system can be written as

$$\dot{q}_R(z) = \frac{1}{s^2(z) + c^2(z)}\left[\dot{q}_{hR}\frac{c(z)}{g} + \dot{q}_{hI}\frac{s(z)}{g}\right] \tag{1.158}$$

$$\dot{q}_I(z) = \frac{1}{s^2(z) + c^2(z)}\left[\dot{q}_{hI}\frac{c(z)}{g} - \dot{q}_{hR}\frac{s(z)}{g}\right] \tag{1.159}$$

In this manner, from equations (1.156)-(1.159) we know the expressions for the real and imaginary part of the complex ray and its derivative, in the real space, for any length of the HS medium. The substitution of the previous equations in (1.45) and (1.50) allows us to determine the evolution of the beam waist and the complex curvature inside the HS material.


USC
UNIVERSIDADE
DE SANTIAGO
DE COMPOSTELA

## Chapter 2

# Gaussian beam propagation and beam transformations in active GRIN media

### 2.1 Introduction

In the previous chapter Gaussian beam propagation in passive GRIN media exhibiting neither gain or loss was discussed. However, light beams do experience gain or loss effects when propagating in most dielectric media, which are considered as complex materials. These effects of gain or loss in GRIN materials can be phenomenologically studied from expressions for passive (lossless) GRIN media if the real refractive index profile is extended to a complex-valued function by analytical continuation [71, 72, 86]. On the other hand, the output modes of most laser sources can be simply described by Hermite-Gaussian or Laguerre-Gaussian functions. Therefore, the analysis of the propagation of laser beams through a particular optical system can be simplified by studying propagation of Gaussian beams through such a system.

As we pointed out in the previous chapter, the study of GRIN media described by different refractive index profiles has great interest due to their capability to perform specific optical functions as imaging and Fourier transform, which are specially important in applications as integrated optics, microoptics or optical sensing, among others.

In this chapter we study some optical functions that can be implemented with active GRIN media described by a parabolic and hyperbolic secant transverse refractive index profiles and determine the general conditions that must be fulfilled, in a controlled manner, to produce focusing and beam shaping and for simulating beam transformer devices. We are specially interested in the use of active GRIN media as beam homogenizers with the added capability of amplification or attenuation of a Gaussian beam. With this objective in mind, we first examine the expressions for the parabolic and HS refractive indices to evaluate the guidance behaviour and gain or loss effects of the active media on Gaussian beam propagation. Laser propagation within both active media regarded as a Gaussian mask is also studied. The expressions governing the radius of curvature and beam waist evolution are derived. Besides, the irradiance distribution of the Gaussian beam within both active GRIN media is determined.

## 2.2 Active GRIN media with parabolic refractive index profile

### 2.2.1 Complex parabolic-like refractive index profile

We refer to active GRIN materials as those GRIN media exhibiting gain or loss effects. The equations describing light propagation in passive GRIN materials can be used for active GRIN materials by simply replacing the real refractive index profile by a complex refractive index in expressions for passive (or lossless) GRIN media case.

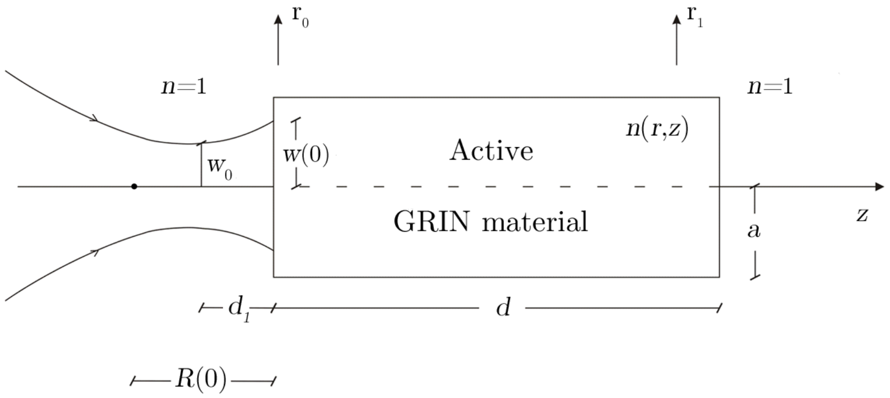

FIGURE 2.1: Active GRIN material of radius $a$ and thickness $d$ surrounded by free space and illuminated by a Gaussian with beam parameters $R(0)$ and $w(0)$ at the input face of the GRIN medium.

We consider an active GRIN material, with rotational symmetry around the $z$ axis, of thickness $d$ and semiaperture $a$ limited by plane parallel faces (see Figure 2.1) whose refractive index can be written as a parabolic transverse gain or loss profile

$$n(r) = n_0\left[1 - \frac{g^2(z)}{2} r^2\right], \text{for } r = (x^2 + y^2)^{1/2} \le a \text{ and } 0 \le z \le d \tag{2.1}$$

whereby $n_0$ and $g(z)$ represent the on-axis complex refractive index and the gradient parameter, respectively, given by

$$n_0 = n_{0R} + in_{0I} \tag{2.2}$$

$$g(z) = g_R(z) + ig_I(z) \tag{2.3}$$

with $n_{0R}, n_{0I}$ being real constants.

Inserting equations (2.2) and (2.3) into equation (2.1) the real, $n_R$, and imaginary, $n_I$, parts of the refractive index can be expressed as

$$n_R = Re[n(r,z)] = n_{0R}\left[1 - \frac{G_R^2(z)}{2}r^2\right] \tag{2.4}$$

$$n_I = Im[n(r,z)] = n_{0I}\left[1 - \frac{G_I^2(z)}{2}r^2\right] \tag{2.5}$$

where

$$G_R^2 = \frac{Re[n_0 g^2(z)]}{n_{0R}} = g_R^2 - g_I^2 - \frac{2n_{0I}g_R(z)g_I(z)}{n_{0R}} \tag{2.6}$$

$$G_I^2 = \frac{Im[n_0 g^2(z)]}{n_{0I}} = g_R^2 - g_I^2 + \frac{2n_{0R}g_R(z)g_I(z)}{n_{0I}} \tag{2.7}$$

Using equations (2.4) and (2.5), active GRIN materials with gain or loss can be classified [86]. The real part of the refractive index determines the guidance behaviour of the active material in such a way that if $G_R^2(z) > 0$, $n_R$ decreases as radial distance increases and the active material presents a normal guidance behaviour; however, if $G_R^2(z) < 0$, $n_R$ increases with radial distance and anomalous guidance occurs. On the other hand, the gain or loss in active medium is determined by the sign of the imaginary part of the refractive index $n_I$. The material has loss if $n_I > 0$ and it experiences gain if $n_I < 0$. On-axis loss or gain is obtained as $n_{0I} > 0$ and $n_{0I} < 0$, respectively. If $G_I^2(z) > 0$ and $Im[n_0 g^2(z)] > 0$, loss decreases as distance from axis increases, turning to gain at transverse distance

$$\tilde{r} > \frac{\sqrt{2}}{G_I(z)} \tag{2.8}$$

This behaviour is typical for unstable light propagation. On the other hand, If $G_I^2(z) < 0$, and for $n_{0I} > 0$ and $Im[n_0 g^2(z)] < 0$, loss increases with increasing radial distance, meaning that stable light propagation occurs. In the case that $G_I^2(z) < 0$ and for $n_{0I} < 0$ and $Im[n_0 g^2(z)] > 0$, gain increases with the transverse direction provoking light unstable propagation. If $G_I^2(z) > 0$, with $n_{0I} < 0$ and $Im[n_0 g^2(z)] < 0$, gain effects decrease along the transverse direction, turning into losses on the irradiance distribution of the propagating beam from the radial distance indicated by (2.8). The latter is summed up in Table 2.1. Likewise, the real part $g_R$ of gradient parameter determines the transverse parabolic profile and the imaginary part $g_I$ is related to the effect of gain or loss on this parabolic profile.

TABLE 2.1: Classification of light propagation behaviour in active GRIN materials.

| **$G_R^2 > 0$** **NORMAL GUIDANCE** | **$G_R^2 < 0$** **ANOMALOUS GUIDANCE** |
|---|---|
| $n_R$ *decreases with r*<br>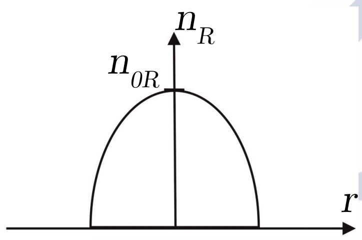<br> | $n_R$ *increases with r*<br>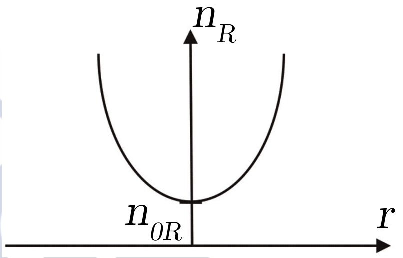<br> |
| **$G_I^2 > 0$** | |
| $n_{0I} > 0,\ Im[n_0 g^2(z)] < 0$ | **STABLE PROPAGATION**<br>*Loss increases with r*<br>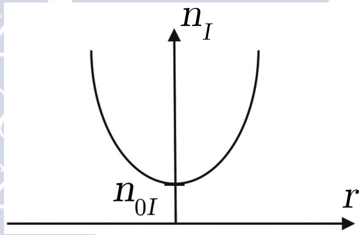<br> |
| $n_{0I} < 0,\ Im[n_0 g^2(z)] > 0$ | **UNSTABLE PROPAGATION**<br>*Gain increases with r*<br>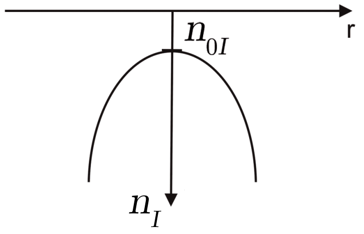<br> |

**$\underline{G_I^2 < 0}$**

$n_{0I} > 0,\ Im[n_0 g^2(z)] > 0$ **STABLE PROPAGATION**

*Loss if* $r < \tilde{r}$

*Gain if* $r > \tilde{r}$

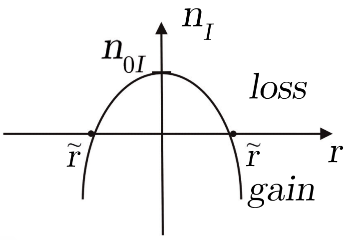

$n_{0I} < 0,\ Im[n_0 g^2(z)] < 0$ **UNSTABLE PROPAGATION**

*Gain if* $r < \tilde{r}$

*Loss if* $r > \tilde{r}$

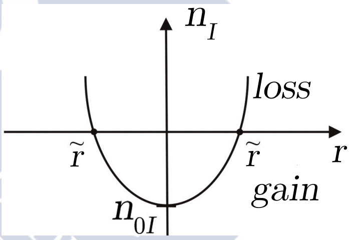

### 2.2.2 Light propagation and beam parameters

In this section the propagation of Gaussian beams in active GRIN materials is studied. The active GRIN medium is illuminated by a monochromatic wave with wavelength $\lambda$ and beam waist of diameter $2w_0$ located at distance $d_1$ from the input face, described by a Gaussian profile (see the schematic representation in Figure 2.1). The complex amplitude distribution corresponding to a Gaussian beam at the input plane of the active GRIN material can be written in the paraxial region, apart from complex constant, as

$$\Psi(x_0, y_0; 0) = \frac{w_0}{w(0)} \exp\left\{ i \frac{\pi U(0)}{\lambda} (x_0^2 + y_0^2) \right\} \tag{2.9}$$

where $U(0)$ is the complex curvature at the input plane given by (1.110).

The propagation of this complex field through the active GRIN medium is described by the parabolic wave equation for a complex refractive index.

$$2ik(n_{0R} + in_{0I}) \frac{\partial \Psi}{\partial z} = H\Psi \tag{2.10}$$

with $H$ the Hamiltonian given by

$$H = k^2(x^2 + y^2)(n_{0R} + in_{0I})^2 [g_R(z) + ig_i(z)]^2 - \nabla_\perp^2 \tag{2.11}$$

Note that, in this case, the Hamiltonian is a non-Hermitian operator.

As we said, the active medium operating in the paraxial domain with complex refractive index given by equation (2.1) can be regarded as an active first-order system. If finite aperture size of the material and non-linear effects are neglected, the complex amplitude distribution at any plane $z = z_1$, for $0 \leq z_1 \leq d$, Gaussian beam propagation through this medium can be described by a linear integral transformation given by equation (1.83)

$$\Psi(x_1, y_1; z_1) = \int_{R^2} K(x_0, y_0, x_1, y_1; z_1) \Psi(x_0, y_0; 0) dx_0 dy_0 \tag{2.12}$$

but, in this case, $K$ is the Point Spread Function of the active material, which can be expressed, in paraxial region, as

$$K(x_0,y_0,x_1,y_1;z_1) =$$
$$= \begin{cases} \frac{kn_0}{i2\pi H_a(z_1)}\exp\{i\frac{kn_0}{2H_a(z_1)}[(x_0^2+y_0^2)H_f(z_1)+(x_1^2+y_1^2)\dot{H}_a(z_1)-2(x_0x_1+y_0y_1)]\} \\ \text{for } H_a(z_1)\neq 0 \\ \frac{1}{H_f(z_1)}\exp\{i\frac{kn_0\dot{H}_f(z_1)}{2Hf(z_1)}(x_1^2+y_1^2)\}\delta(x_0-\frac{x_1}{H_f(z_1)}, y_0-\frac{y_1}{H_f(z_1)}) \\ \text{for } H_a(z_1)=0 \end{cases} \tag{2.13}$$

with $k$ being the wavenumber in free space and $\delta$ is the 2-D Dirac delta function. $H_a$ and $\dot{H}_a$ represent the position and the slope of the complex axial ray at $z_1$ and $H_f$ and $\dot{H}_f$ are the position and the slope of the complex field ray at $z_1$ [69]. Both complex rays can also be expressed in terms of their real and imaginary parts in a compact form as

$$\overset{(\cdot)}{H}_f(z_1) = \overset{(\cdot)}{H}_{fR}(z_1) + i\overset{(\cdot)}{H}_{fI}(z_1) \tag{2.14}$$

$$\overset{(\cdot)}{H}_a(z_1) = \overset{(\cdot)}{H}_{aR}(z_1) + i\overset{(\cdot)}{H}_{aI}(z_1) \tag{2.15}$$

Equation (2.13) is derived from equation (1.101). Taking into account that the axial and field rays for the active GRIN medium are also complex functions, equation (2.13) can be written in a simplified form using the real and imaginary parts of the axial and field rays as

$$\begin{aligned} K(x_0,y_0,x_1,y_1;z_1) = \frac{kn_0}{i2\pi H_a(z_1)}&\exp(-kn_{0I})\exp\left\{-\frac{k}{2}\theta(x_0,y_0,x_1,y_1;z_1)\right\}\cdot \\ &\cdot\exp(ikn_{0R}z_1)\exp\left\{i\frac{k}{2}\Omega(x_0,y_0,x_1,y_1;z_1)\right\} \end{aligned} \tag{2.16}$$

where

$$\begin{aligned}\theta(x_0, y_0, x_1, y_1; z_1) = \frac{1}{|H_a(z_1)|^2} \{ & Im[n_0 H_a^*(z_1) \dot{H}_a(z_1)](x_1^2 + y_1^2) + \\ & + Im[n_0 H_a^*(z_1) H_f(z_1)](x_0^2 + y_0^2) + \\ & - 2Im[n_0 H_a^*(z_1)](x_0 x_1 + y_0 y_1)\end{aligned} \tag{2.17}$$

$$\begin{aligned}\Omega(x_0, y_0, x_1, y_1; z_1) = \frac{1}{|H_a(z_1)|^2} \{ & Re[n_0 H_a^*(z_1) \dot{H}_a(z_1)](x_1^2 + y_1^2) + \\ & + Re[n_0 H_a^*(z_1) H_f(z_1)](x_0^2 + y_0^2) + \\ & - 2Re[n_0 H_a^*(z_1)](x_0 x_1 + y_0 y_1)\end{aligned} \tag{2.18}$$

It follows from (2.16) that the amplitude of the PSF is modulated by a Gaussian function and, therefore, an active GRIN material acts as a quadratic phase transformer with a Gaussian mask induced by its complex refractive index. Besides, inserting (2.9) and (2.13) into (2.12), the complex amplitude distribution at $z_1$ can be evaluated to obtain

$$\Psi(x_1, y_1; z_1) = \frac{w_0 e^{-k n_{0I} z_1} e^{i k n_{0R} z_1}}{w(0) \alpha(z_1)} e^{\frac{i\pi U(z_1)}{\lambda}(x_1^2 + y_1^2)} \tag{2.19}$$

where

$$\alpha(z_1) = H_f(z_1) + \frac{U(0)}{(n_0)} H_a(z_1) \tag{2.20}$$

and $U(z_1)$ is the complex curvature at $z_1$ given, in terms of axial and field complex rays, by

$$\begin{aligned}U(z_1) &= n_0 \frac{n_0 \dot{H}_f(z_1) + U(0) \dot{H}_a(z_1)}{n_0 H_f(z_1) + U(0) H_a(z_1)} = \\ &= n_0 \frac{d}{dz} \{ ln[n_0 H_f(z) + U(0) H_a(z) \} \big|_{z=z_1}\end{aligned} \tag{2.21}$$

The matrix formulation for ray propagation through an active GRIN material, which relates the complex ray at the input plane to the complex ray at any plane $z_1$ in the material, provides the expression of the complex curvature in terms of the complex ray. The complex matrix equation for ray propagation, in this case, is expressed as follows

$$\begin{pmatrix} q(z_1) \\ n_0\dot{q}(z_1) \end{pmatrix} = \begin{pmatrix} H_f(z_1) & H_a(z_1)/n_0 \\ n_0\dot{H}_f(z_1) & \dot{H}_a(z_1) \end{pmatrix} \begin{pmatrix} q(0) \\ n_0\dot{q}(0) \end{pmatrix} \tag{2.22}$$

Equation (2.22) is basically the same as (1.107) with complex axial and field rays. From equation it follows that any other complex ray into the active GRIN material can be expressed as a linear combination of the complex field and axial rays. Likewise, the complex ray position and slope can be written as

$$q(z_1) = \alpha q(0) \tag{2.23}$$

$$\dot{q}(z_1) = \dot{\alpha} q(0) \tag{2.24}$$

where (1.113), (2.20) and

$$\dot{\alpha}(z_1) = \dot{H}_f(z_1) + \frac{U(0)}{(n_0)}\dot{H}_a(z_1) \tag{2.25}$$

have been used.

The modulus of the position and the slope of the complex ray at $z_1$ in terms of $\alpha$ and $\dot{\alpha}$ functions can be expressed as

$$|q(z_1)| = w(0)\,|\alpha(z_1)| \tag{2.26}$$

$$|\dot{q}(z_1)| = w(0)\,|\dot{\alpha}(z_1)| \tag{2.27}$$

The complex curvature amplitude at any plane $z_1$ in the material can be also expressed by the position and the slope of the complex ray as

$$U(z_1) = n_0\dot{q}(z_1)q^{-1}(z_1) \tag{2.28}$$

Equation (2.28) can be used for evaluating beam parameters at $z_1$ by the complex ray since the complex curvature in terms of the radius of curvature and beam half-width says

$$U(z_1) = U_R(z_1) + iU_I(z_1) = \frac{1}{R(z_1)} + i\frac{\lambda}{\pi w^2(z_1)} \tag{2.29}$$

Comparing equations (2.28) and (2.29), the beam parameters at $z_1$ can be obtained as

$$\begin{aligned} R(z_1) =& \frac{|q(z_1)|^2}{Re[n_0\dot{q}(z_1)q^*(z_1)]} \\ =& \frac{|q(z_1)|^2}{n_{0R}[q_R(z_1)\dot{q}_R(z) + q_I(z_1)\dot{q}_I(z_1)] - n_{0I}[q_R(z_1)\dot{q}_I(z) - q_I(z_1)\dot{q}_R(z_1)]} \end{aligned} \tag{2.30}$$

$$\begin{aligned} w^2(z_1) =& \frac{\lambda|q(z_1)|^2}{\pi Im[n_0\dot{q}(z_1)q^*(z_1)]} = \\ =& \frac{|q(z_1)|^2}{\pi\{n_{0R}[q_R(z_1)\dot{q}_I(z_1) - q_I(z_1)\dot{q}_R(z_1)] + n_{0I}[q_R(z_1)\dot{q}_R(z_1) + q_I(z_1)\dot{q}_I(z_1)]} \end{aligned} \tag{2.31}$$

where $^*$ denotes the complex conjugate value and $Re$ and $Im$ represent the real and the imaginary part, respectively.

Finally, the irradiance of the beam at a given plane $z_1$ within the medium can be determined inserting equations (2.30) and (2.31) into (2.29) and this into (2.19). Hence, the irradiance results

$$I(x_1, y_1, z_1) = |\Psi(x_1, y_1, z_1)|^2 = I_0\frac{\exp(-2kn_{0I}z_1)}{|\alpha(z_1)|^2}\exp\left\{\frac{-2(x_1^2 + y_1^2)}{w^2(z)}\right\} \tag{2.32}$$

where $I_0 = w_0^2/w^2(0)$.

According to equation (2.32), a Gaussian irradiance profile is obtained at $z_1$ with on-axis loss or gain determined by the sign of the imaginary part $n_{0I}$ of the refractive index along $z_1$ axis. If $w^2$ is positive, the Gaussian beam irradiance is maximum at axis and decreases with radial distance. On the contrary, if $w^2$ is negative, the irradiance of the Gaussian beam is a minimum along the $z_1$-axis and increases with radial distance. Then, light concentration or light spread around the $z_1$-axis occurs as $w^2$ is positive or negative, respectively.

### 2.2.3 Beam transformations by parabolic-like active GRIN media

The active GRIN materials under study in this thesis can be used as beam transforming systems and implement different functions as collimation of light, focusing of light, beam uniformization and imaging. In this sense, the aim of this section is to determine the general conditions that must be satisfied for a parabolic-like active GRIN medium in order to carry out such functions.

#### 2.2.3.1 Condition for uniform beam shaping operation

The active GRIN medium can act as a beam shaper system when the denominator in equation (2.31) is equal to zero, that is, the beam half-width tends to infinite at the output face of the material of thickness $d$. Regarding this, the condition for uniform beam shaping by a parabolic-like active GRIN medium takes the form of

$$Im[n_0\dot{q}(d)q^*(d)] = 0 \Longrightarrow w(d) \to \infty \tag{2.33}$$

The active medium is regarded as a beam shaping system to generate uniform laser beams: a spherical Gaussian beam is turned into a uniform divergent or convergent wavefront as the radius of curvature $R(d)$ is negative or positive, respectively. Such cases are illustrated in Figure 2.2.

Propagation of Gaussian beams can be graphically represented on a circle diagram [69, 109]. Rewriting equation (2.33) we obtain

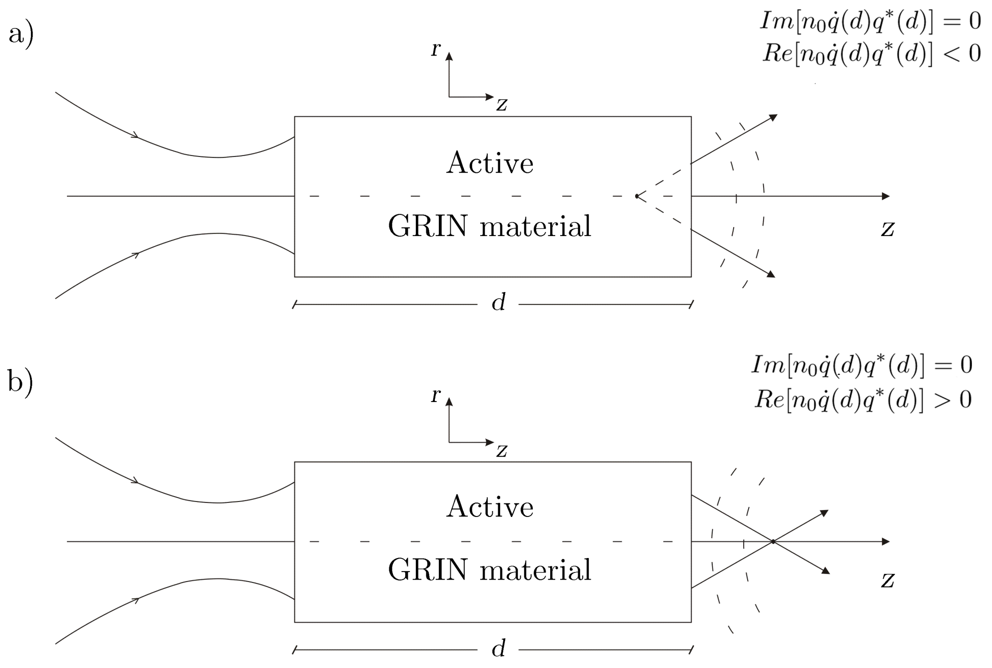

FIGURE 2.2: Beam shaping by active GRIN materials: transformation of an input spherical Gaussian beam into a uniform (a) diverging $R(d) < 0$ and (b) converging $R(d) > 0$ wavefront.

$$[U_R(0) - C_R]^2 + [U_I(0) - C_I]^2 = h^2 \tag{2.34}$$

This equation describes a circle in the complex $2-D$ space with cartesian axes the real and the imaginary parts of the complex curvature of the Gaussian beam at the input plane, as shown in 2.3. The radius $h$ and the center $C(C_R, C_I)$ of the circle corresponding to the uniform spherical wavefront condition are given by

$$h^2 = \frac{|n_0|^4}{4Im^2[n_0 H_a^*(d)\dot{H}_a(d)]} \tag{2.35}$$

$$C_R = -\frac{Im[n_0^2 \dot{H}_f(d) H_a^*(d)]}{2Im[n_0 H_a^*(d)\dot{H}_a(d)]} \tag{2.36}$$

$$C_I = -\frac{|n_0 H_f(d)|^2 - Re[n_0^2 \dot{H}_f(d) H_a^*(d)]}{2Im[n_0 H_a^*(d) \dot{H}_a(d)]} \tag{2.37}$$

More detail on the calculus is provided in Appendix section A.1.

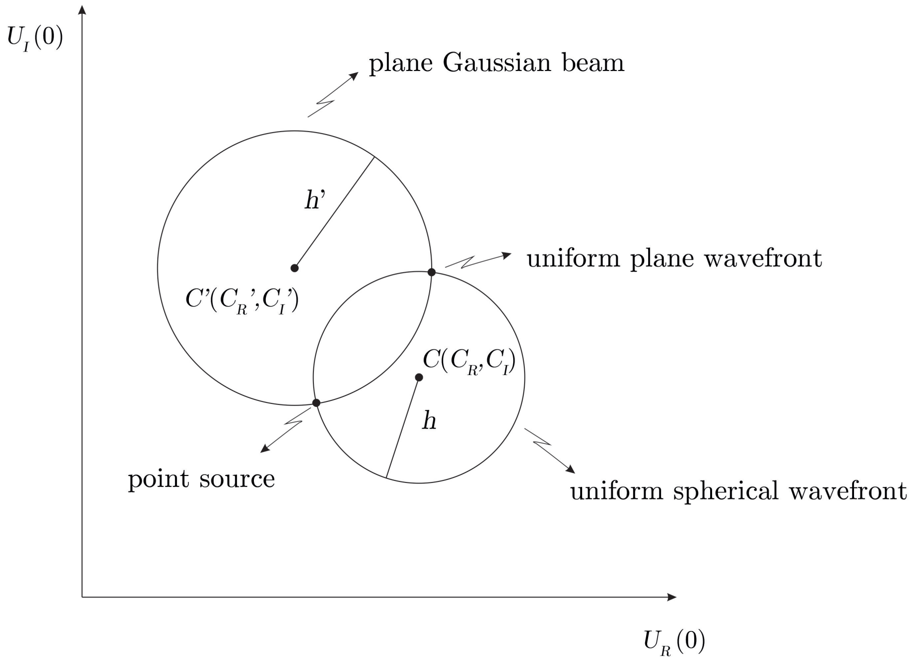

FIGURE 2.3: Circle diagrams for the study of transformations of Gaussian beams by an active GRIN material in the 2-D complex space of the real and imaginary parts of the complex curvature of an input spherical Gaussian beam.

Furthermore, for the Gaussian to uniform beam conversion condition, the complex amplitude distribution at the output of the GRIN medium becomes

$$\begin{aligned}\Psi(x_1, y_1; d) =& \frac{w_0 e^{-kn_{0I}d} e^{ikn_{0R}d}}{|q(d)|} \exp\left\{ - itan^{-1}\left\{ \frac{Im[\alpha(d)]}{Re[\alpha(d)]} \right\} \right\} \cdot \\ & \cdot \exp\left\{ i\frac{\pi}{\lambda R(d)}(x_1^2 + y_1^2) \right\}\end{aligned} \tag{2.38}$$

Apart from complex constant factors, the above equation represents an uniform spherical wave of curvature radius

$$R(d) = \frac{|q(d)|^2}{Re[n_0\dot{q}(d)q^*(d)]} \tag{2.39}$$

The radius of curvature $R(d)$ is positive if $Re[n_0\dot{q}(d)q^*(d)] > 0$, that is, a converging wave, and negative if $Re[n_0\dot{q}(d)q^*(d)]z_0$, that is, diverging wave.

Hence, and considering equation (2.39), the irradiance of the emergent uniform spherical wave is given by

$$I(x_1, y_1; d) = \frac{w_0^2}{|q(d)|^2} e^{(-2kn_{0I}d)} = \frac{w_0^2}{R(d)Re[n_0\dot{q}(d)q^*(d)]} e^{(-2kn_{0I}d)} \tag{2.40}$$

In this case, at the output face of the active GRIN medium we have that the incident Gaussian beam has been turned into a beam with an uniform irradiance distribution.

#### 2.2.3.2 Condition for plane Gaussian beam transformation

Another optical function that can be implemented with active GRIN media is the conversion of an input spherical Gaussian beam into a plane Gaussian beam. In order to have this transformation the condition that must be fulfilled is

$$Re[n_0\dot{q}(d)q^*(d)] = 0 \Longrightarrow R(d) \rightarrow \infty \tag{2.41}$$

that is, the radius of curvature of the beam at the output tends to infinite, as illustrated in figure 2.4.

The mathematical relation between the complex curvature and the input beam, related to the complex refractive index of the active GRIN material and the complex axial and field ray, can be achieved by rewriting equation (2.41) as

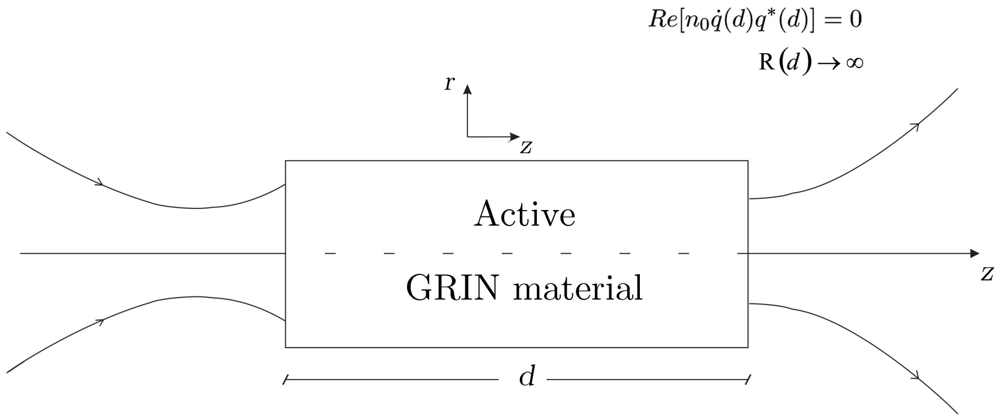

FIGURE 2.4: Plane Gaussian beam transforming system: transformation of an input spherical Gaussian beam into an output plane Gaussian beam by an active GRIN material.

$$[U_R(0) - C'_R]^2 + [U_I(0) - C'_I]^2 = h'^2 \tag{2.42}$$

A plane Gaussian beam at the output face of the active GRIN medium will be obtained when real and imaginary parts of the complex curvature must be solution of the circle given by equation (2.42). In this case, the radius $h'$ and the center $C'(C'_R, C'_I)$ are (see appendix section A.2)

$$h'^2 = \frac{|n_0|^4}{4Re^2[n_0 H_a^*(d)\dot{H}_a(d)]} \tag{2.43}$$

$$C'_R = -\frac{|n_0 H_f(d)|^2 + Re[n_0^2 \dot{H}_f(d) H_a^*(d)]}{2Re[n_0 H_a^*(d)\dot{H}_a(d)]} \tag{2.44}$$

$$C'_I = -\frac{Im[n_0^2 \dot{H}_f(d) H_a^*(d)}{2Re[n_0 H_a^*(d)\dot{H}_a(d)]} \tag{2.45}$$

Thus, the complex amplitude distribution at the output face of an active GRIN media of thickness $d$ results

$$\begin{aligned}\Psi(x_1, y_1; d) = &\frac{w_0 e^{-kn_{0I}d} e^{ikn_{0R}d}}{|q(d)|} \exp\left\{ - i tan^{-1} \left\{ \frac{Im[\alpha(d)]}{Re[\alpha(d)]} \right\} \right\} \cdot \\ &\cdot \exp\left\{ \frac{-}{x_1^2 + y_1^2} w^2(d) \right\}\end{aligned} \tag{2.46}$$

Equation (2.46) represents a plane Gaussian beam whose waist at $z = d$ is

$$w^2(d) = \frac{\lambda |q(d)|^2}{\pi Im[n_0 \dot{q}(d) q^*(d)]} \tag{2.47}$$

and irradiance given by

$$I(x_1, y_1; d) = \frac{w_0^2}{|q(d)|^2} \exp(-2kn_{0I}d) \exp\left\{ - \frac{2(x_1^2 + y_1^2)}{w^2(d)} \right\} \tag{2.48}$$

#### 2.2.3.3 Condition for beam collimation

Figure 2.3 depicts the geometrical solutions for transformations suffered by input Gaussian beams by active GRIN media. Relationships between the real and imaginary parts of the input spherical Gaussian beams that can be turned into a uniform spherical Gaussian beam or at a plane Gaussian beam are mapped as circles defined in a $2 - D$ space with Cartesian axis $U_R(0)$ and $U_I(0)$. Both circumferences always intersect at two points since the following condition is fulfilled

$$(C_R - C_R')^2 + (C_I - C_I')^2 < (h + h')^2 \quad \text{for} \quad |n_0| > 0 \tag{2.49}$$

The intersecting points provide the limiting cases for which the complex curvature of the output beam tends to zero or infinite. Common solutions from equations (2.34) and (2.42) are the two mutual intersection points of the circumferences, where one of them corresponds to the case of zero complex curvature at the output

$$U(d) \to 0 \Longrightarrow R(d) \quad \text{and} \quad w(d) \to \infty \tag{2.50}$$

In this situation, the real and imaginary parts of the input complex curvature are given by

$$U_R(0) = -\frac{Re[n_0 \dot{H}_f(d) \dot{H}_a^*(d)]}{|\dot{H}_a(d)|^2} \tag{2.51}$$

$$U_I(0) = -\frac{Im[n_0 \dot{H}_f(f) \dot{H}_a^*(d)]}{|\dot{H}_a(d)|^2} \tag{2.52}$$

The input spherical Gaussian beam is turned into a uniform plane wave at the output of the active GRIN material as illustrated in figure 2.5. Therefore, the medium can be regarded as an optical collimator system.

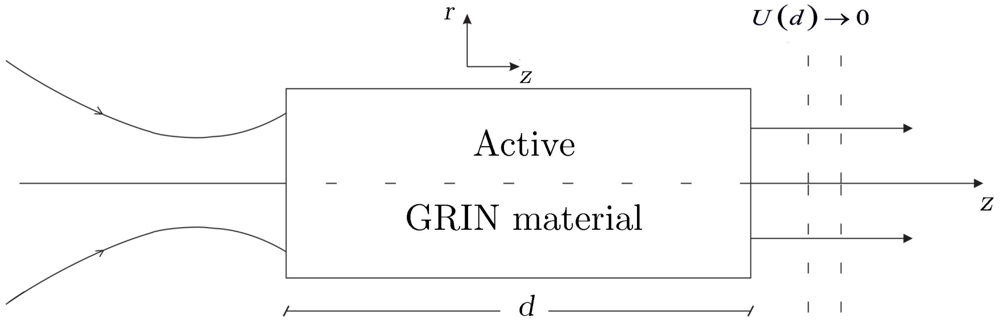

FIGURE 2.5: Collimator system: transformation of an input spherical Gaussian beam into an output uniform plane wavefront by an active GRIN material.

The complex amplitude distribution for the case of zero complex curvature at the output reduces to

$$\Psi(x_1, y_1; d) = \frac{w_0 e^{-kn_{0I}d} e^{ikn_{0R}d}}{|q(d)|} \exp\left\{ - itan^{-1}\left\{ \frac{Im[\alpha(d)]}{Re[\alpha(d)]} \right\}\right\} \tag{2.53}$$

that is, a uniform plane wave of amplitude

$$\frac{w_0}{|q(d)|} \exp(-kn_{0I}d) \tag{2.54}$$

and irradiance

$$I(x_1, y_1; d) = \frac{w_0^2}{|q(d)|^2} \exp(-2kn_{0I}d) \tag{2.55}$$

#### 2.2.3.4 Beam focusing by active GRIN media

In the previous section we have seen that the intersection points of circumferences in figure 2.3 correspond to the limiting cases for which the complex curvature of the output beam tends to zero or infinite. Now we consider the case of infinite complex curvature at the output, that is

$$U(d) \to \infty \Longrightarrow R(d) \quad \text{and} \quad w(d) \to 0 \tag{2.56}$$

for which the real and imaginary parts of the complex curvature can be expressed as

$$U_R(0) = -\frac{Re[n_0 H_f(d) H_a^*(d)]}{|H_a(d)|^2} \tag{2.57}$$

$$U_I(0) = -\frac{Im[n_0 H_f(f) H_a^*(d)]}{|H_a(d)|^2} \tag{2.58}$$

The active GRIN material of a given thickness $d$ operates as a beam focuser system turning an input spherical Gaussian beam into a point source on its output face (see figure 2.6).

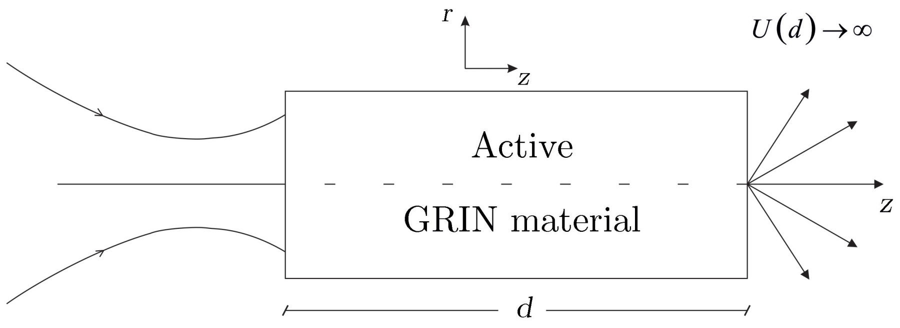

FIGURE 2.6: Focuser system: transformation of an input spherical Gaussian beam into an output point source by an active GRIN material.

Table 2.2 collects the conditions that an active GRIN medium must obey for each optical function.

TABLE 2.2: Gaussian beam transformations by active GRIN materials.

| | **Condition** |
|---|---|
| **Uniform shaping** | $Im[n_0\dot{q}(d)q^*(d)] = 0 \Longrightarrow w(d) \to \infty$ |
| **Non-uniform collimating** | $Re[n_0\dot{q}(d)q^*(d)] = 0 \Longrightarrow R(d) \to \infty$ |
| **Uniform collimating** | $U(d) \to 0 \Longrightarrow w(d)$ and $R(d) \to \infty$ |
| **Focusing** | $U(d) \to \infty \Longrightarrow w(d)$ and $R(d) \to 0$ |

### 2.2.3.5 Special cases

The circumferences in equations (2.34) and (2.42) exhibit a particular behaviour as the position and the slope of the complex axial ray vanish at the output of the active GRIN material. If $H_a(d) = 0$, both circumferences degenerate into two perpendicular straight lines

$$U_R(0) = -\frac{1}{Re[H_f^*(d)\dot{H}_a(d)]}\{Im[H_f^*(d)\dot{H}_a(d)]U_R(0) + Im[n_0 H_f^*(d)\dot{H}_f(d)]\} \tag{2.59a}$$

$$U_I(0) = \frac{1}{Im[H_f^*(d)\dot{H}_a(d)]}\{Re[H_f^*(d)\dot{H}_a(d)]U_R(0) + Re[n_0 H_f^*(d)\dot{H}_f(d)]\} \tag{2.59b}$$

which mutually cut each other at a point, given by equations (2.51) and (2.52), common solution of the two lines and corresponding to the transformation of the input Gaussian beam into a uniform plane wavefront (collimator system). On the other hand, if $\dot{H}_a(d) = 0$ the circles become two perpendicular straight lines

$$U_R(0) = \frac{1}{Re[n_0^2\dot{H}_f(d)H_a^*(d)]}\{Im[n_0^2\dot{H}_f(d)H_a^*(d)]U_R(0) + |n_0|^2 Im[n_0 H_f^*(d)\dot{H}_f(d)]\} \tag{2.60a}$$

$$U_I(0) = -\frac{1}{Im[n_0^2\dot{H}_f(d)H_a^*(d)]}\{Re[n_0^2\dot{H}_f(d)H_a^*(d)]U_R(0) + |n_0|^2 Im[n_0 H_f^*(d)\dot{H}_f(d)]\} \tag{2.60b}$$

which cut each other at a point, given by equations (2.57) and (2.58), common solution of the two lines and corresponding to the transformation of an input spherical Gaussian beam into a point source (focuser system).

## 2.3 Hyperbolic secant planar active GRIN medium with gain or loss

### 2.3.1 Complex hyperbolic secant refractive index profile

In this section we will study light propagation through an Hyperbolic Secant (HS) active GRIN medium. This medium is described by a hyperbolic secant transverse gain or loss profile given by

$$n(x,z) = n_0 \mathrm{sech}[g(z)x] \quad \text{for} \quad 0 \leq z \leq d \tag{2.61}$$

where $g(z)$ and $n_0$ are the complex gradient parameter and the refractive index along the $z$-optical axis, respectively. We assume that $n_0$ and $g(z)$ can be expressed, by means of their real and imaginary parts as in equations (2.2) and (2.3). The real part of $g(z)$ determines the HS profile while the imaginary part is related to effect of gain or loss on the profile. Taking those equations into account we have that the real and imaginary part of the refractive index are written as

$$n_R = Re[n(x,z)] = \frac{n_{0R}\cosh[g_R(z)x]\cos[g_I(z)x] + n_{0I}\sinh[g_R(z)x]\sin[g_I(z)x]}{\cosh^2[g_R(z)x] - sin^2[g_I(z)x]} \tag{2.62}$$

$$n_I = Im[n(x,z)] = \frac{-n_{0R}\sinh[g_R(z)x]\sin[g_I(z)x] + n_{0I}\cosh[g_R(z)x]\cos[g_I(z)x]}{\cosh^2[g_R(z)x] - sin^2[g_I(z)x]} \tag{2.63}$$

As happened in section 2.2.1, the real $n_R$ part of the refractive index determines the guidance behaviour of the active material. When $n_R$ decreases with the transverse coordinate $x$, the material shows a normal guidance behaviour, that is

$$\frac{n_{0R}g_I + n_{0I}g_R}{n_{0R}g_R - n_{0I}g_I} > \frac{\tanh(g_R x)}{\tan(g_I x)} \frac{\cosh^2(g_R x) + \sin^2(g_I x)}{\cos^2(g_I x) - \sinh^2(g_R x)} \tag{2.64}$$

while if $n_R$ increases with the transverse coordinate $x$ the material shows an anomalous guidance behaviour

$$\frac{n_{0R}g_I + n_{0I}g_R}{n_{0R}g_R - n_{0I}g_I} < \frac{\tanh(g_R x)}{\mathrm{tang}_I(x)} \frac{\cosh^2(g_R x) + \sin^2(g_I x)}{\cos^2(g_I x) - \sinh^2(g_R x)} \tag{2.65}$$

The effect of gain or loss is determined by the sign of the imaginary part $n_I$ in such a way that we will be in presence of a gain or loss material if $n_I < 0$ or $n_I > 0$, respectively. On the other hand, on-axis gain or loss occurs when $n_{0I} < 0$ or $n_{0I} > 0$. Therefore, taking into account equation (2.63) and that the denominator in this expression is always positive, the HS active GRIN medium will present loss effect when $Im[n(x,z)] > 0$, so

$$\frac{n_{0I}}{n_{0R}} > \tanh(g_R x)\tan(g_I x) \tag{2.66}$$

When loss increases with increasing transverse distance $x$ we will have stable light propagation. However, if loss decreases as distance with optical axis increases we will have unstable light propagation. On the contrary, if $Im[n(x,z)] < 0$, the HS active GRIN medium will present gain effect

$$\frac{n_{0I}}{n_{0R}} < \tanh(g_R x)\tan(g_I x) \tag{2.67}$$

having stable light propagation within the material if gain decreases with along the transverse direction, while unstable light propagation happens if gain increases along the transverse direction.

### 2.3.2 Light propagation in hyperbolic secant active GRIN medium and beam parameters

We consider now an active GRIN medium described by the HS refractive index profile of equation (2.61). In section 1.8.2 we saw that ray trajectories in a GRIN medium with HS transverse refractive index profile can be obtained by solving the ray equation in a hyperbolic space of coordinates $(u, z)$ where $u$ is given by the transformation (1.132).

Extending the known expressions for passive media to complex-valued refractive index function and taking into account that for a Gaussian beam the complex ray plays the role of the coordinate $x$, the position $q_h$ and the slope $\dot{q}_h$ of the hyperbolic complex ray can be written as

$$q_h(z) = \sinh[g(z)q(z)] = q_{hR}(z) + iq_{hI}(z) \tag{2.68}$$

$$\dot{q}_h(z) = [g(z)\dot{q}(z) + \dot{g}(z)q(z)]\cosh[g(z)q(z)] = \dot{q}_{hR}(z) + i\dot{q}_{hI}(z) \tag{2.69}$$

We want to obtain the complex curvature of a Gaussian beam after propagation a given distance $z = z_1$ within the HS GRIN material. Taking into account equations (2.68) and (2.69), and the gradient parameter written as a complex-valued function as defined in (2.3), the position and the slope of the hyperbolic complex ray can be written as

$$q_{hR}(z_1) = sinh[\zeta(z_1)]cos[\eta(z_1)] \tag{2.70}$$

$$q_{hI}(z) = cosh[\zeta(z)]sin[\eta(z)] \tag{2.71}$$

$$\dot{q}_{hR}(z) = [g_R(z)C(z) - g_I(z)S(z)]\dot{q}_R - [g_I(z)C(z) + g_R(z)S(z)]\dot{q}_I \tag{2.72}$$

$$\dot{q}_{hI}(z) = [g_I(z)C(z) + g_R(z)S(z)]\dot{q}_R + [g_R(z)C(z) - g_I(z)S(z)]\dot{q}_I \tag{2.73}$$

being

$$\zeta(z) = g_R q_R(z) - g_I(z)q_I(z) \tag{2.74}$$

$$\eta(z) = g_I q_R(z) + g_R(z) q_I(z) \tag{2.75}$$

$$C(z) = cosh[\zeta(z)] cos[\eta(z)] \tag{2.76}$$

$$S(z) = sinh[\zeta(z)] sin[\eta(z)] \tag{2.77}$$

We can know the expression of the hyperbolic complex rays within this active GRIN medium from their initial values at the input face of the material $z = 0$, i.e., $q_h(0)$ and $\dot{q}_h(0)$. Writing the matrix formulation for the ray propagation in an analogous manner to equation (1.144) we have

$$\begin{pmatrix} q_h(z) \\ n_0 \dot{q}_h(z) \end{pmatrix} = \begin{pmatrix} H_f(z) & H_a(z)/n_0 \\ n_0 \dot{H}_f(z) & \dot{H}_a(z) \end{pmatrix} \begin{pmatrix} q_h(0) \\ \dot{q}_h(0) \end{pmatrix} \tag{2.78}$$

where the complex axial $H_a$ and the field $H_f$ rays, and the respective derivatives $\dot{H}_a$ and $\dot{H}_f$, are those defined in equation (1.107) but with complex gradient parameter $g$.

Now that we know the expression for complex ray in the hyperbolic space, we can obtain these expressions in the real space of coordinates $(x, z)$. So, the real and imaginary of the position of the complex ray for the HS active GRIN material are

$$q_R(z) = \frac{1}{g_R(z)} \left\{ \sinh^{-1}[\sqrt{t(z)}] + g_I(z) q_I(z) \right\} \tag{2.79}$$

$$q_I(z) = \frac{1}{|g(z)|^2} \left[ g_R(z) \cos^{-1} \left\{ \frac{q_{hR}(z)}{\sqrt{t(z)}} \right\} - g_I(z) \sinh^{-1}[\sqrt{t(z)}] \right\} \tag{2.80}$$

where

$$t(z) = \sinh^2[\zeta(z)] = \frac{1}{2} \left\{ [q_{hI}^2(z) + q_{hR}^2(z) - 1] + \sqrt{[1 - q_{hI}^2(z) - q_{hR}^2(z)]^2 + 4 q_{hR}^2(z)} \right\} \tag{2.81}$$

The real and imaginary parts of the slope of the complex ray can also be obtained by solving the equations system given by equation (2.72) and (2.73) and taking into account equations (2.74)-(2.77). Thus, we have that in the real space of coordinates $(x, z)$ for the HS active GRIN material $\dot{q_R}(z)$ and $\dot{q}_I(z)$ take the form

$$\begin{aligned}\dot{q}_R(z) =&\frac{1}{|g(z)|^2[C^2(z)+S^2(z)]}\Big\{[g_R(z)C(z)-g_I(z)S(z)]\dot{q}_{hR}(z)+\\&+[g_R(z)S(z)+g_I(z)C(z)]\dot{q}_{hI}(z)-A(z)\Big\}\end{aligned}\tag{2.82}$$

$$\begin{aligned}\dot{q}_I(z) =&\frac{1}{|g(z)|^2[C^2(z)+S^2(z)]}\{[g_R(z)C(z)-g_I(z)S(z)]\dot{q}_{hI}(z)+\\&-[g_R(z)S(z)+g_I(z)C(z)]\dot{q}_{hR}(z)-B(z)\Big\}\end{aligned}\tag{2.83}$$

where

$$\begin{aligned}A(z) =&[C^2(z)+S^2(z)]\Big\{-[g_R(z)\dot{g}_I(z)-g_I(z)\dot{g}_R(z)]q_I(z)+\\&+[g_I(z)\dot{g}_I(z)+g_R(z)\dot{g}_R(z)]q_R(z)\Big\}\end{aligned}\tag{2.84}$$

$$\begin{aligned}B(z) =&[C^2(z)+S^2(z)]\Big\{[g_R(z)\dot{g}_I(z)-g_I(z)\dot{g}_R(z)]q_R(z)+\\&+[g_I(z)\dot{g}_I(z)+g_R(z)\dot{g}_R(z)]q_I(z)\Big\}\end{aligned}\tag{2.85}$$

It is interesting to remark that the Gaussian beam does not satisfy the $z-$invariant condition (1.48) when considering propagation through an active HS GRIN medium, that is

$$q_R\dot{q}_I-\dot{q}_Rq_I\leq cte \quad for \quad 0<z<d \tag{2.86}$$

and the absolute square of the complex ray is

$$|q(z)|^2 = \frac{1}{|g(z)|^2}\left\{\left\{\sinh^{-1}\left[\sqrt{t(z)}\right]\right\}^2 + \left\{\cos^{-1}\left[\frac{q_{hR}(z)}{\sqrt{t(z)}}\right]\right\}\right\} \tag{2.87}$$

The radius of curvature and the beam waist of the beam in the active HS GRIN medium can be written as function of the complex ray as in expressions (2.30) and (2.31). Taking this into account and inserting equations (2.82)-(2.85) we have

$$R(z) = \frac{|g(z)|^2|q(z)|^2[C^2(z) + S^2(z)}{\Gamma} \tag{2.88}$$

$$w^2(z) = \frac{\lambda}{\pi}\frac{|g(z)|^2|q(z)|^2[C^2(z) + S^2(z)]}{\chi} \tag{2.89}$$

where

$$\begin{aligned}\Gamma =& [g_R(z)C(z) - g_I(z)S(z)]\{n_{0R}[q_R(z)\dot{q}_{hR}(z) + q_I(z)\dot{q}_{hI}(z) + \\ & - n_{0I}[q_R(z)\dot{q}_{hI}(z) - q_I(z)\dot{q}_{hR}(z)]\} + \\ & + [g_I(z)C(z) + g_R(z)S(z)]\{n_{0R}[q_R(z)\dot{q}_{hI}(z) - q_I(z)\dot{q}_{hR}(z)] + \\ & + n_{0I}[q_R(z)\dot{q}_{hR}(z) + q_I(z)\dot{q}_{hI}(z)\} + \\ & - [C^2(z) + S^2(z)]|q(z)|^2\{n_{0R}[g_R(z)\dot{g}_R(z) + g_I(z)\dot{g}_I(z)] + \\ & - n_{0I}[g_R(z)\dot{g}_I(z) - g_I(z)\dot{g}_R(z)]\}\end{aligned} \tag{2.90}$$

$$\begin{aligned}\chi =& [g_R(z_1)C(z_1) - g_I(z_1)S(z_1)]\{n_{0R}[q_R(z_1)\dot{q}_{hI}(z_1) - q_I(z_1)\dot{q}_{hR}(z_1) + \\ & + n_{0I}[q_R(z_1)\dot{q}_{hR}(z_1) + q_I(z_1)\dot{q}_{hI}(z_1)]\} + \\ & - [g_I(z_1)C(z_1) + g_R(z_1)S(z_1)]\{n_{0R}[q_R(z_1)\dot{q}_{hR}(z_1) + q_I(z_1)\dot{q}_{hI}(z_1)] + \\ & - n_{0I}[q_R(z_1)\dot{q}_{hI}(z_1) - q_I(z_1)\dot{q}_{hR}(z) + \\ & - [C^2(z_1) + S^2(z_1)]|q(z_1)|^2\{n_{0R}[g_R(z_1)\dot{g}_I(z_1) - g_I(z_1)\dot{g}_R(z)] + \\ & + n_{0I}[g_R(z_1)\dot{g}_R(z_1) + g_I(z_1)\dot{g}_R(z_1)]\}\end{aligned} \tag{2.91}$$

We can rewrite the expression of the complex curvature of the beam within the HS active GRIN medium as

$$U(z_1) = n_0\frac{\dot{q}(z_1)}{q(z_1)} = \frac{1}{R(z_1)} + i\frac{\lambda}{\pi w^2(z_1)} = \frac{1}{|q(z)|^2[C^2(z)+S^2(z)}(\Gamma + i\chi) \quad (2.92)$$

Therefore, the irradiance can be expressed as follows

$$I(x_1, z_1) = |\Psi(x_1, z_1)|^2 = \frac{I_0}{|\alpha(z_1)|^2}\exp(-2kn_{0I})\exp\left[\frac{-2x_1^2}{w^2(z_1)}\right] \quad (2.93)$$

where $\alpha(z_1)$ is given by (2.20) and $I_0 = \frac{w_0^2}{w^2(0)}$.

The Gaussian beam transformations conditions that can be carried out by the HS active GRIN medium are those gathered in table 2.2.

## Chapter 3

# Design and tolerance analysis of active GRIN beam shapers

### 3.1 Introduction

Beam shaping is the process of redistributing, in a controlled manner, the irradiance and phase of a beam of optical radiation. Shortly after first lasers operation in the early 1960s, beam shapers systems to tailor Gaussian laser beams into beams with uniform irradiance profiles started to be developed. In many applications an uniform or flat-top beam is more desirable than a Gaussian beam, comprising photolithography, material processing, cutting and drilling, entertainment, alignment, targeting, and many others. This chapter addresses the design of active GRIN beam shapers using materials described by a parabolic and hyperbolic secant complex refractive index profiles by providing particular numerical examples to the systems discussed in the previous chapter. Uniform beam profiles can optimize the application by either enhancing system performance or providing source properties. The main problem with beam uniformization devices is that waist much of the original available energy in the laser beam and that suffer from alignment problems because they are formed by several compounds. For instance, a traditional way to produce such profiles consists on expanding the laser beam and selecting the central part. At this region the irradiance is approximately flat; however, much of the energy of the beam is lost. Advantageously, the active GRIN beam shapers with gain or loss proposed in this work consist of a single element, which may minimize the complexity of current available shaper systems. Besides, both active GRIN parabolic and HS shaper can provide amplified or attenuated uniform beams. It is possible to obtain beam shapers with different specifications by simply modifying the design parameters. For instance, active GRIN shapers with diverse shaping length can be fabricated varying the active GRIN material parameters such as the real and imaginary refractive index of the medium.

Tolerance analysis is very important when designing active GRIN beam shapers as they are sensitive to design parameters deviation, such as thickness and laser working wavelength. As these elements are designed to redistribute intensity, a fraction of deviation in laser source parameters can have noticeable effect on the desired target intensity distribution.

In this chapter we study the active GRIN parabolic and HS as beam homogenizers. Numerical examples using media with gain or loss are presented. The examples in this chapter intend to show that the active media, when designed with a proper complex gradient, can transform an input laser beam into a uniform beam. Section 3.2 examines the complex refractive indices of parabolic and HS media to evaluate the guidance behaviour and gain on loss effects. In the parabolic case, the evolution of laser beam parameters within the medium is studied and the length where the medium fulfills the beam shaping condition is determined. Likewise, simulations of the relative irradiance against distance propagation in the active material with gain or loss are presented. A comparative study between active GRIN parabolic and HS complex refractive index profiles and laser beam propagation is also presented. Finally, in section 3.3 we analyze the sensitivity of active GRIN parabolic and HS beam shaper systems to medium thickness and laser wavelength. To evaluate the flatness quality of the shaped beams we use the root mean square (RMS) and determine the interval where they can still be considered nearly uniform beams for practical purposes.

The parameters of examples are calculated with MATLAB code developed (MATLAB R2011a).

## 3.2 Design and numerical studies of Gaussian beams propagation in active GRIN media for laser beam shaping purposes

In this chapter beam shaping by both active GRIN parabolic and HS materials is illustrated by applying the results obtained in the previous sections. Hereinafter we are going to consider an active self-focusing (selfoc) GRIN medium where the complex gradient parameter $g_0$ is constant and given by

$$g_0 = g_{0R} + ig_{0I} \tag{3.1}$$

The real and imaginary parts of the position and the slope of the complex axial and field rays are written in terms of hyperbolic and trigonometric functions as

$$H_{aR}(z_1) = \frac{1}{|g_0|^2}[g_{0R}\mathrm{sin}(g_{0R}z_1)\mathrm{cosh}(g_{0I}z_1) + g_{0I}\mathrm{cos}(g_{0R}z_1)\mathrm{sinh}(g_{0I}z_1)] \tag{3.2}$$

$$H_{aI}(z_1) = \frac{1}{|g_0|^2}[g_{0R}\mathrm{cos}(g_{0R}z_1)\mathrm{sinh}(g_{0I}z_1) - g_{0I}\mathrm{sin}(g_{0R}z_1)\mathrm{cosh}(g_{0I}z_1)] \tag{3.3}$$

$$H_{fR}(z_1) = \dot{H}_{aR}(z_1) = \mathrm{cos}(g_{0R}z_1)\mathrm{cosh}(g_{0I}z_1)] \tag{3.4}$$

$$H_{fI}(z_1) = \dot{H}_{aI}(z_1) = -\mathrm{sin}(g_{0R}z_1)\mathrm{sinh}(g_{0I}z_1)] \tag{3.5}$$

$$\dot{H}_{fR}(z_1) = -g_{0R}\mathrm{sin}(g_{0R}z_1)\mathrm{cosh}(g_{0I}z_1) + g_{0I}\mathrm{cos}(g_{0R}z_1)\mathrm{sinh}(g_{0I}z_1) \tag{3.6}$$

$$\dot{H}_{fI}(z_1) = -[g_{0I}\mathrm{sin}(g_{0R}z_1)\mathrm{cosh}(g_{0I}z_1) + g_{0R}\mathrm{cos}(g_{0R}z_1)\mathrm{sinh}(g_{0I}z_1) \tag{3.7}$$

The remainder of this chapter focuses on the numerical design of active GRIN beam shapers utilizing media with parabolic and HS refractive indices profiles. All the simulations have been done with values corresponding to commercial available laser sources and GRIN lenses. The flow diagram shown in figure 3.1 illustrates the steps followed to obtain the thickness of the active GRIN material where the input non-uniform beam is turned into one with a uniform irradiance distribution: i) selecting the complex refractive index and aperture of the active GRIN material; ii) determining the value of the complex gradient parameter and plotting of the real and imaginary part of $n$; iii) evaluating the evolution of the beam half-width square in the active medium to obtain the beam shaping length (equation (2.33)); and iv) simulating the beam irradiance propagation in the material to investigate the Gaussian to flat-top beam transformation.

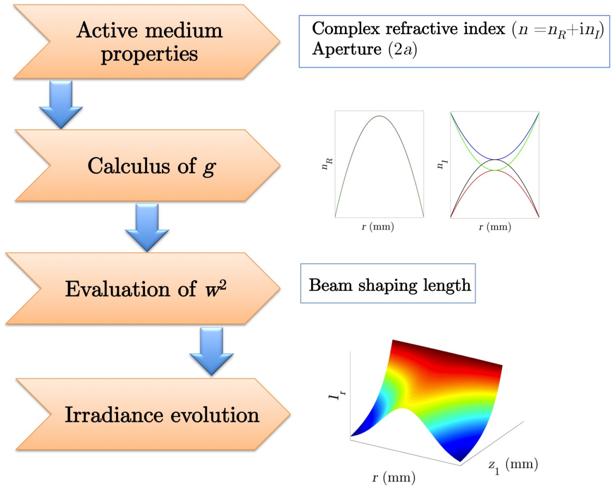

FIGURE 3.1: Flow chart for the obtaining of the beam shaping distance.

### 3.2.1 Parabolic active GRIN media

In this section we present several application examples of active GRIN media for beam shaping purposes. In particular, we are going to consider an active GRIN material with rotational symmetry around the $z$-axis, thickness $d$ and limited by plane parallel faces whose refractive index is given by the parabolic transverse gain or loss profile of equation (2.1).

#### 3.2.1.1 Complex refractive index and Gaussian beam propagation

The parabolic behaviour of the real $n_R$ and imaginary $n_I$ part of the complex refractive index for an active GRIN parabolic medium of semiaperture $a = 1.5$ mm is depicted in figure 3.2. $n_{0R} = 1.62$, $n_R(a) = 1.60$, $n_{0I} = |0.00001|$ and $n_I(a) = |0.0001|$. $n_R(a)$ and $n_I(a)$ stand for the real and imaginary part of the refractive index at the edges of the material, respectively. Whether the material exhibits gain or loss is determined only by the sign of the imaginary part of its refractive index. Hence, four different cases have been considered: the medium exhibits loss ($n_{0I}, n_I(a) > 0$), blue line), gain ($n_{0I}, n_I(a) < 0$), red line), on-axis loss and gain at the edges ($n_{0I} > 0, n_I(a) < 0$, black line) and on-axis gain and loss at the edges ($n_{0I} < 0, n_I(a) > 0$, green line). In all cases $n_R$ decreases with increasing radial distance (see figure 3.2a), so the medium presents normal guidance propagation. Regarding the imaginary part of the refractive index, in the four cases considered a parabolic behaviour occurs (figure 3.2b)). The material has loss when $n_{0I}$ is positive no matter what the sign of $g_{0I}$ is. In the loss case we have that $n_{0I} > 0$ and that the value of the imaginary part of the complex gradient parameter is negative. As we can see in the figure, $n_I$ increases from the center to the edges of the material. Therefore, loss increases with increasing radial distance and stable light propagation takes place in the material [86]. In the on-axis loss case, $n_{0I} > 0$ and $g_{0I} > 0$, loss decreases with increasing distance from the optical axis, turning to gain to the transverse distance $r = |0.4959|$ mm, given by equation (2.8). This behaviour is typical for unstable light propagation. On the contrary,when $n_{0I} < 0$ the material exhibits gain regardless of the sign of $g_{0I}$. In the gain case, $n_{0I} < 0$ and $g_{0I} > 0$, gain increases with increasing distance from the axis. This is the unstable case. Finally, in the on-axis gain case both $n_{0I}$ and $g_{0I}$ are positive and gain decreases as distance from axis increases, turning to loss at $r = |0.4959|$ mm, meaning that stable light propagation occurs.

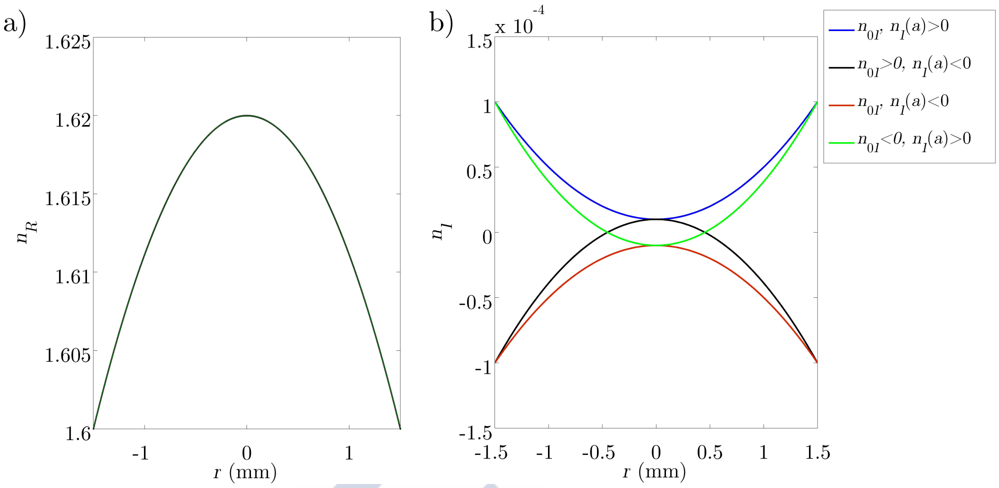

FIGURE 3.2: Profiles of (a) real and (b) imaginary part of the refractive index across an active GRIN parabolic medium of semiaperture $a = 1.5$ mm exhibiting loss (blue line), gain (red line), on-axis loss and gain at the edges (black line) and on-axis gain and loss at the edges (green line).

Table 3.1 summarizes the numerical values used for the design of the active GRIN parabolic medium.

TABLE 3.1: Numerical values for the design of the active GRIN parabolic beam shaper.

| $\mathbf{n_{0R}}$ | $\mathbf{n_R(a)}$ | $\mathbf{n_{0I}}$ | $\mathbf{n_I(a)}$ | $\mathbf{g_{0R}}$ **(mm$^{-1}$)** | $\mathbf{g_{0I}}$ **(mm$^{-1}$)** | **Case** |
|---|---|---|---|---|---|---|
| 1.62 | 1.60 | $10^{-5}$ | $10^{-4}$ | 0.10476 | -0.00024 | Loss |
| 1.62 | 1.60 | $-10^{-5}$ | $-10^{-4}$ | 0.10476 | 0.00024 | Gain |
| 1.62 | 1.60 | $10^{-5}$ | $-10^{-4}$ | 0.10476 | -0.00029 | On-axis loss |
| 1.62 | 1.60 | $-10^{-5}$ | $10^{-4}$ | 0.10476 | 0.00029 | On-axis gain |

We analyze now the irradiance distribution in an active GRIN parabolic medium with the specifications of table 3.1. The material is illuminated by a laser beam operating at 1064 nm and beam waist of radius 1.25 mm located at 1.5 mm from the input face of the material. First, we consider the loss case. Figures 3.3a) and b) depict the evolution of the beam half-width square $w^2$ and the radius of curvature $R$ in the active medium. $w^2$ is positive and decreases slowly down to the shaping length, where it reaches its peak value. As discussed in section 2.2.3, the active GRIN medium can act as a beam shaper system when the beam half-width tends to infinite at the output face of the material. From the figure we have that the shaping length is $z_{shaping} = 2.779$ mm. At this plane $w^2$ changes its sign, being negative above the shaping length. On the other hand, the radius of curvature is negative along the propagation distance in the active material, increasing up very rapidly at the input face of the material. As the propagation of the beam in the medium continues, the trend changes and the radius of curvature slowly increases towards the optical axis.

The relative irradiance evolution against propagation in the material with loss is plotted in figure 3.4. The active GRIN parabolic material works as a Gaussian to uniform beam shaper transforming system with loss; irradiance increases with propagation and beam radius becomes wider (diverging Gaussian beam) until the shaping length is reached. Consequently, the input beam is reshaped into a uniform beam of aperture 3 mm with constant irradiance distribution. In addition, we find that the beam has suffered from attenuation after propagating in the active material: the on-axis irradiance measured at the beam shaping plane has decreased by 21.5%. $I_r$ represents the relative irradiance distribution $I/I_0$

The evolution of the beam parameters and of the relative irradiance with propagation distance in the active material for the gain case are shown in figures 3.5 and 3.6. In this case, the shaping length is $z_{shaping} = 2.787$ mm and, as in the loss case, $w^2$ is positive below shaping length, reaches its maximum value at $z_{shaping}$ and then changes its sign to negative. The radius of curvature is negative along the propagation of the beam in the material. The behaviour of the relative irradiance is similar to the loss case: the input Gaussian beam is turned into a beam with uniform irradiance distribution in the active material of thickness 2.787 mm (shaping length). However, an amplified uniform beam is obtained at the output face of the parabolic medium due to the gain effects (figure 3.6). In this case, the on-axis relative irradiance at the shaping plane

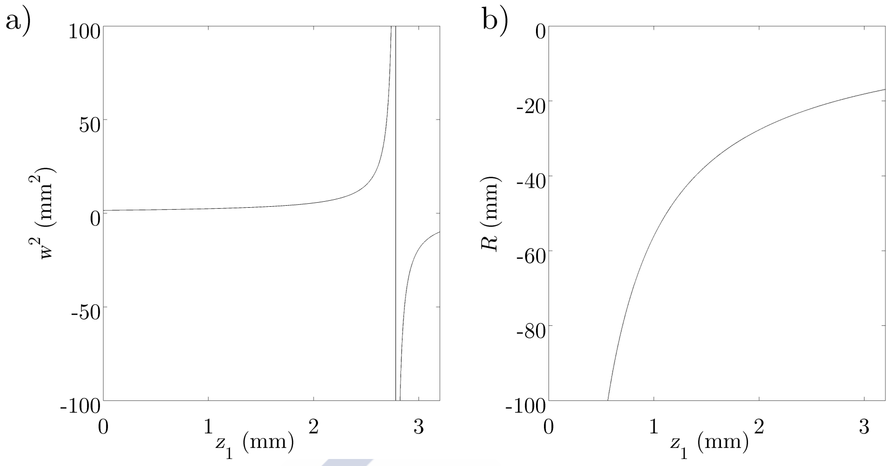

FIGURE 3.3: Beam parameters evolution within the active GRIN medium with loss illuminated by a laser beam with $\lambda = 1064$ nm and $w_0 = 1.25$ mm: a) beam half-width square, and b) radius of curvature.

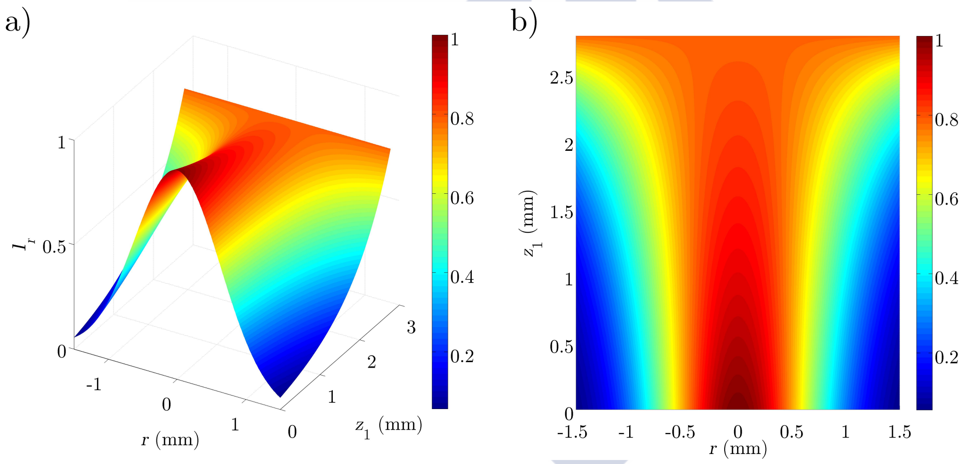

FIGURE 3.4: Gaussian to flat-top beam conversion by a parabolic active GRIN material with loss: a) relative irradiance evolution versus propagation distance, and b) top-view of beam propagation within the active material. Parameter values: $n_{0I} = 0.00001, n_I = 0.0001, g_{0R} = 0.10476$ mm$^{-1}$, $g_{0I} = -0.00024$ mm$^{-1}$. The design shaping length is $z_{shaping} = 2.779$ mm.

increases significantly by 51.5% with respect to the on-axis irradiance at the input face of the material

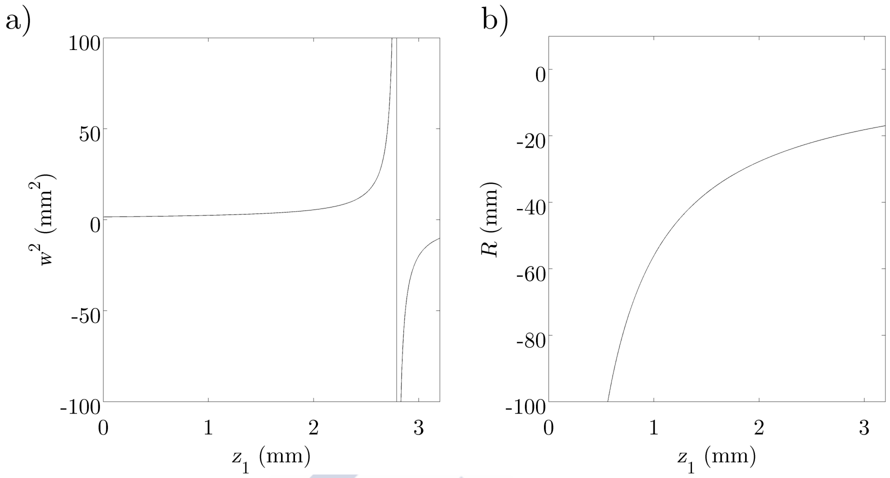

FIGURE 3.5: Beam parameters evolution within the active GRIN medium with gain illuminated by a laser beam with $\lambda = 1064$nm and $w_0 = 1.25$ mm: a) beam half-width square, and b) radius of curvature.

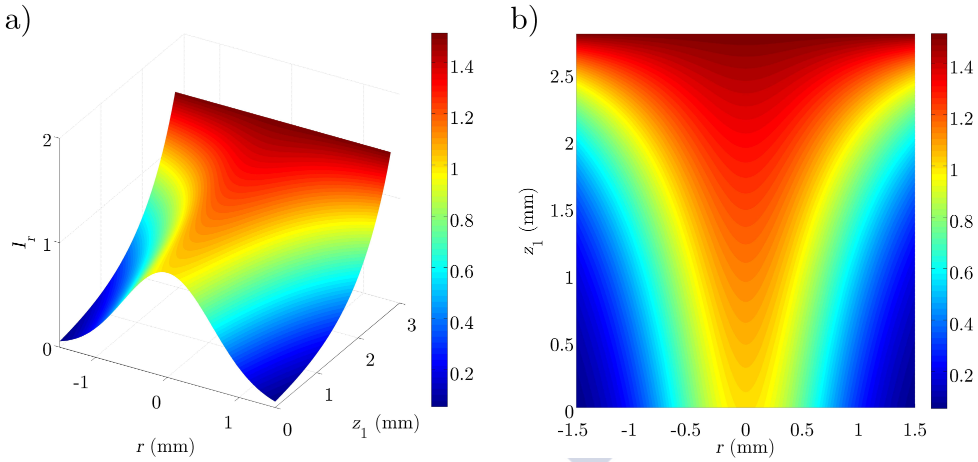

FIGURE 3.6: Gaussian to flat-top beam conversion by a parabolic active GRIN material with gain. Parameter values: $n_{0I} = -0.00001, n_I = -0.0001, g_{0R} = 0.10476$ mm$^{-1}$, $g_{0I} = 0.00024$ mm$^{-1}$. The design shaping length is $z_{shaping} = 2.787$ mm.

We consider now the on-axis loss and on-axis gain cases. Figures 3.7 and 3.9 plot beam parameters $w^2$ and $R$ against propagation distance in the on-axis loss case and on-axis gain case, respectively. From the figures we can see that beam parameters evolution within the active medium is the same than in the loss and gain cases. However, there is a shift to the left at the plane where $w^2$ changes its sign from positive to negative. As can be seen in the representations of $w^2$, the shaping length is 2.258 mm in the on-axis loss case and 2.263 mm in the on-axis gain case. This means that the beam propagates shorter distances in the active material and that beam attenuation (figure 3.8) and amplification (figure 3.10) is smaller than in the loss and gain cases. The on-axis irradiance at the output face of the materials decreases by 19.0% in the on-axis loss case and increases by 38.2% in the on-axis gain case.

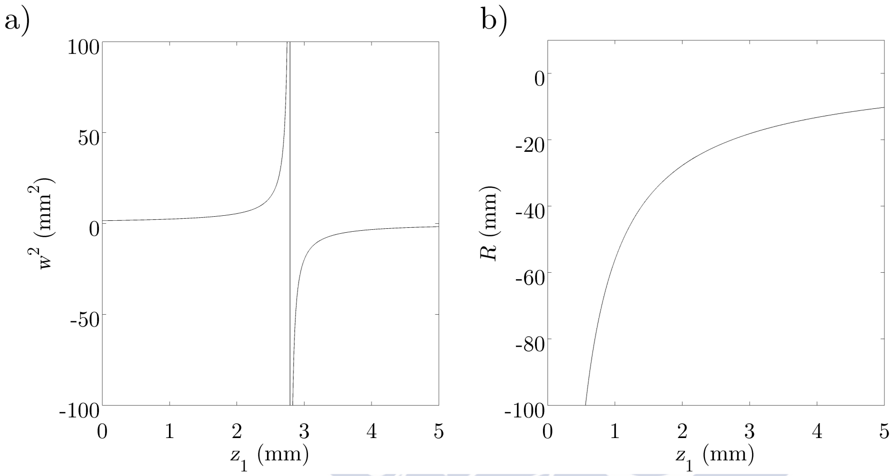

FIGURE 3.7: Beam parameters evolution within the active GRIN medium with on-axis loss and gain at the edges of the material illuminated by a laser beam with $\lambda = 1064$ nm and $w_0 = 1.25$ mm: a) beam half-width square and b) radius of curvature.

#### 3.2.1.2 Influence of input Gaussian beam parameters on the shaping length design

The design of active GRIN beam shapers strongly depends on the value of the input beam parameters, namely the wavelength, beam waist and distance from the beam waist to the input face of the material. The value of these parameters determines the shaping length $z_{shaping}$ that the active material should have in

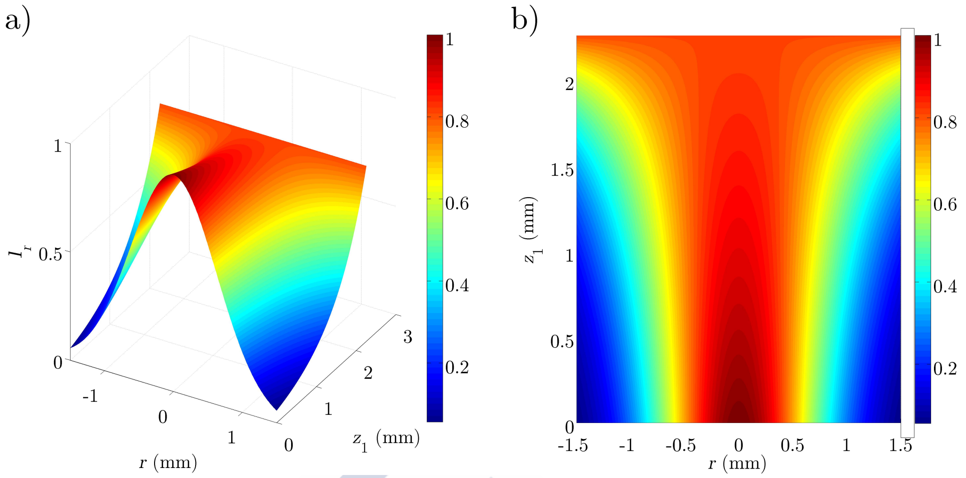

FIGURE 3.8: Gaussian to flat-top beam conversion by a parabolic active GRIN material exhibiting on-axis loss and gain at the edges: a) relative irradiance evolution versus propagation distance, and b) top-view of the beam propagation within the active material. Parameter values: $n_{0I} = 0.00001, n_I = -0.0001, g_{0R} = 0.10476\text{mm}^{-1}, g_{0I} = 0.00024\text{mm}^{-1}$. The design shaping length is $z_{shaping} = 2.258$ mm.

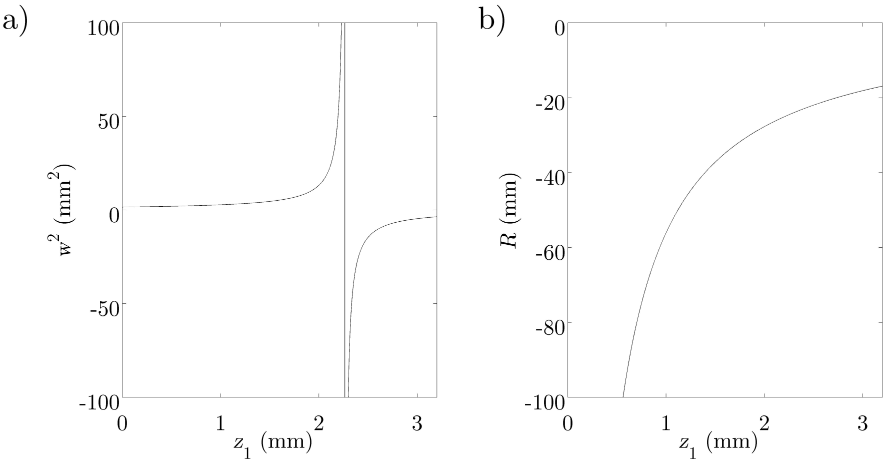

FIGURE 3.9: Beam parameters evolution within the active GRIN medium with on-axis gain and loss at the edges of the material illuminated by a laser beam with $\lambda = 1064$ nm and $w_0 = 1.25$ mm: a) beam half-width square, and b) radius of curvature.

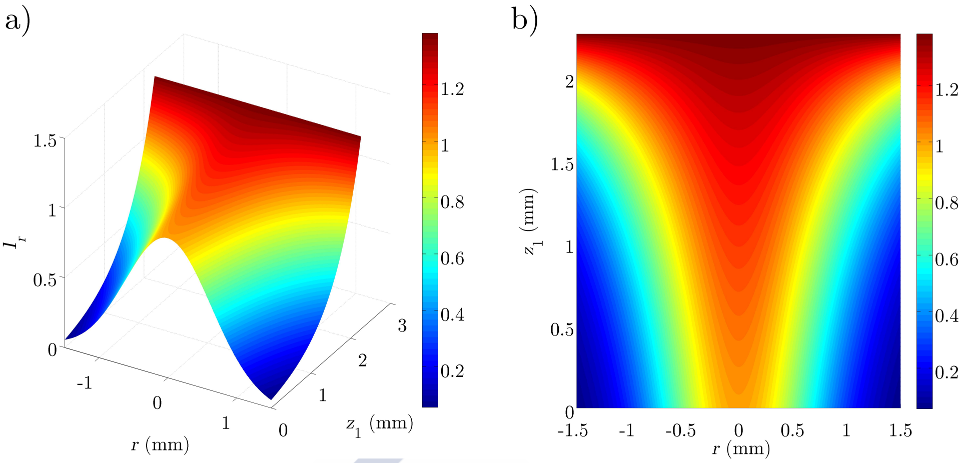

FIGURE 3.10: Gaussian to flat-top beam conversion by a parabolic active GRIN material exhibiting on-axis gain and loss at the edges: a) relative irradiance evolution versus propagation distance, and b) top-view of the beam propagation within the active material. Parameter values: $n_{0I} = -0.00001, n_i = 0.0001, g_{0R} = 0.10476\text{mm}^{-1}, g_{0I} = -0.00024\text{mm}^{-1}$. The design shaping length is $z_{shaping} = 2.263$ mm.

order to be able to operate as a Gaussian beam shaper. In this section we are going to study the influence of the input beam parameters in the active GRIN medium with gain and semiaperture $a = 1.5$ mm described by the refractive index profile of figure 3.2.

- *Wavelength*

  We consider now four Gaussian beams impinging on the active GRIN parabolic medium of different wavelengths. Figure 3.11 shows the evolution of the beam half-width square with propagation in the active GRIN parabolic medium with gain of Gaussian beams with increasing wavelengths $\lambda = 830$ nm (black line), $\lambda = 1064$ nm (red line), $\lambda = 1330$ nm (blue line) and $\lambda = 1550$ nm (green line). As we can see in the graph, the beam half-width square presents the same behaviour in all cases; $w^2$ decreases with propagation distance up to the uniform shaping length, where it reaches a peak value, and changes its sign from positive to negative above the shaping length. However, the design shaping length is different for each wavelength and increases its value with $\lambda$. Hence, we have that for $\lambda = 830$ nm, $\lambda = 1064$ nm, $\lambda = 1330$ nm and $\lambda = 1550$ nm the beam shaping condition is fulfilled at 2.14 mm, 2.78 mm, 3.54 mm and 4.20 mm, respectively.

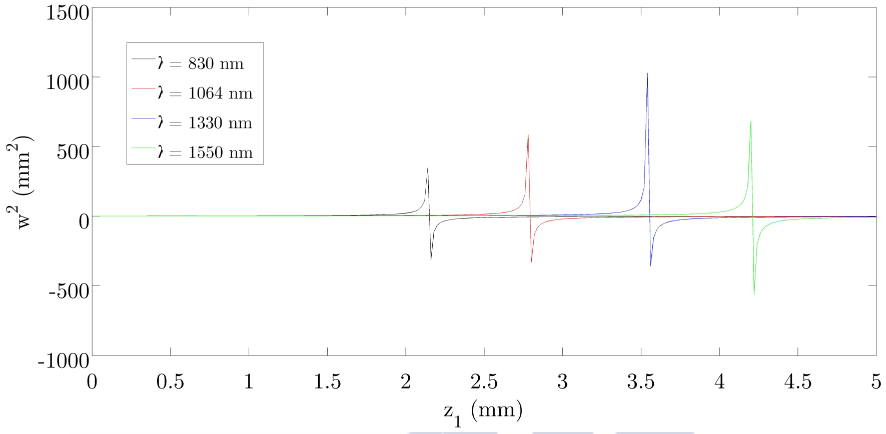

FIGURE 3.11: Evolution of the beam half-width square in an active GRIN parabolic medium with gain of a laser beam with $\lambda = 830$ nm (black line), $\lambda = 1064$ nm (red line), $\lambda = 1330$ nm (blue line) and $\lambda = 1550$ nm (green line). The design shaping lengths are 2.14 mm, 2.78 mm, 3.54 mm and 4.20 mm, respectively. Parameter values: $a = 1.5$ mm, $w_0 = 1.25$ mm, $n_{0I} = -0.00001, n_I = -0.0001, g_{0R}$=0.10476 mm$^{-1}$, $g_{0I}$=0.00024 mm$^{-1}$.

To illustrate these results, simulations of irradiance evolution with propagation distance in the active parabolic medium with gain were performed (see figure 3.12. The active material works as a beam shaper that tailors and amplifies the input Gaussian beam into a beam with uniform irradiance distribution of aperture 3 mm at the output face. The differences in the shaping length result in significant differences in the value of the relative irradiance at the output face of the material (from 45% up to 72% irradiance increase for the shorter and the larger shaping length). Thus, the increase in relative irradiance can be contributed to larger propagation distances.

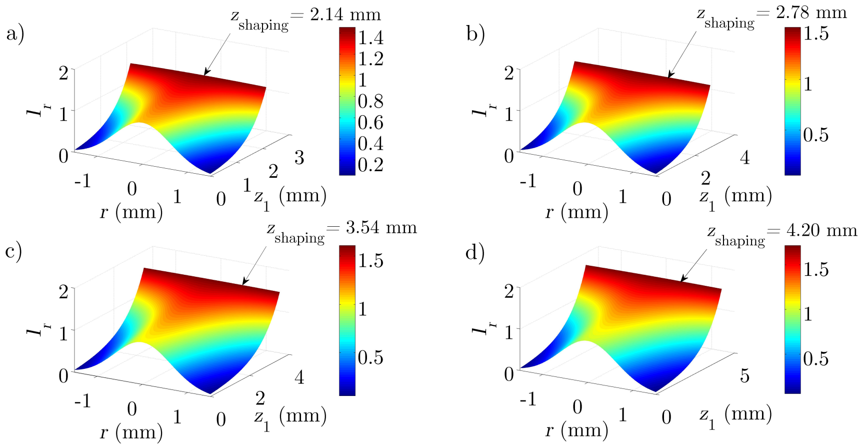

FIGURE 3.12: Gaussian to flat-top beam conversion by a parabolic active GRIN material exhibiting gain for incident beam wavelength: a) $\lambda = 830$ nm, b) $\lambda = 1064$ nm, c) $\lambda = 1330$ nm, and d) $\lambda = 1550$ nm.

- *Beam waist*

The influence of the input beam waist on the design thickness of the active GRIN parabolic beam shaper is shown in figure 3.13. The numerical analysis is performed for a laser beam operating at $\lambda = 1064$ nm and beam waist 1 mm, 1.25 mm, 1.5 mm and 1.75 mm. Shaping length rapid falls when increasing the value of the beam waist. The behaviour of $w^2$ is the same in all cases; it is positive below the shaping length, where it reaches its maximum value, then it changes its sign to negative above the shaping length. For visual representation of the evolution of the irradiance in the active material the reader is referred to figure 3.14. For shorter values of $w_0$ the beam propagates a larger distance in the active material; therefore the irradiance at the out face of the medium reaches higher values.

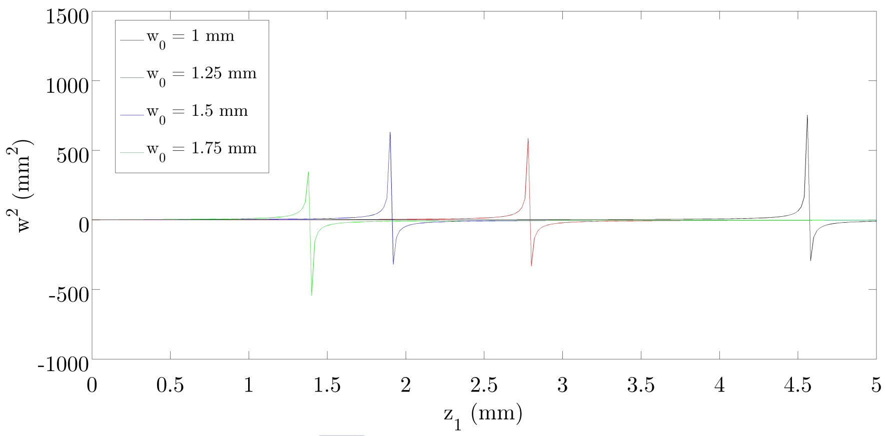

FIGURE 3.13: Evolution of the beam half-width square in an active GRIN parabolic medium with gain of a laser beam with $w_0 = 1$ mm (black line), $w_0 = 1.25$ nm (red line), $w_0 = 1.5$ nm (blue line) and $w_0 = 1.75$ nm (green line). The design shaping lengths are 4.56, 2.78, 1.90 and 1.38 mm, respectively. Parameter values: $a = 1.5$ mm, $\lambda = 1064$ nm, $n_{0I} = -0.00001, n_I = -0.0001, g_{0R}$=0.10476 mm$^{-1}$, $g_{0I}$=0.00024 mm$^{-1}$.

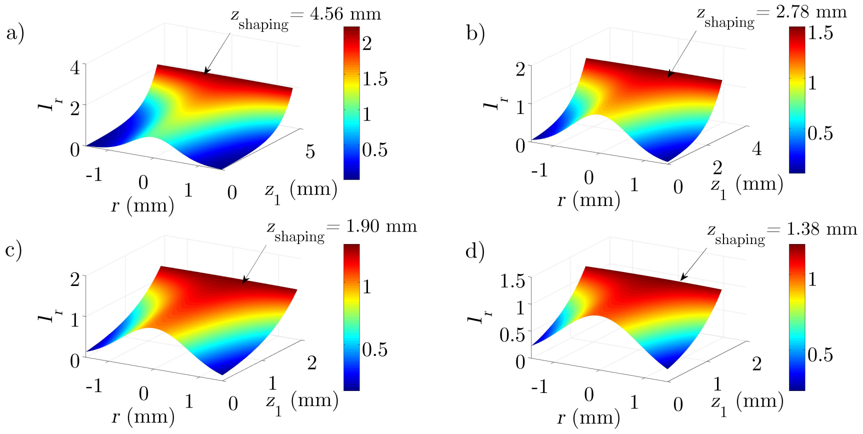

FIGURE 3.14: Gaussian to flat-top beam conversion by a parabolic active GRIN material exhibiting gain for input beam waist: a) $w_0 = 1$ mm and $z_{shaping} = 4.56$ mm, b)$w_0 = 1.25$ mm and $z_{shaping} = 2.78$ mm, c) $w_0 = 1.5$ mm and $z_{shaping} = 1.9$ mm, and d) $w_0 = 1.75$mm and $z_{shaping} = 1.38$ mm.

- *Distance from the beam waist to the input face of the material*

  We focus now on the analysis of the influence of distance from the Gaussian beam waist to the input face of the material $d_1$ (figure 2.1). In this case, $d_1$ has to change its value considerably in order to affect the beam shaping distance. Figure 3.15 gives an example of this situation. When $d_1 = 1.5$ mm (black line) the shaping length is $z_{shaping} = 2.78$ mm. Values of $d_1$ of the same order of magnitude barely influences the shaping length and values three orders of magnitude larger have to be used to find significant changes on the shaping length. In this way, for distances of 1 m, 2 m, and 3 m shaping lengths of 2.64 mm, 2.32 mm and 1.38 mm are obtained. $w^2$ evolves within the active medium in the same way as described in the case of $\lambda$ and $w_0$.

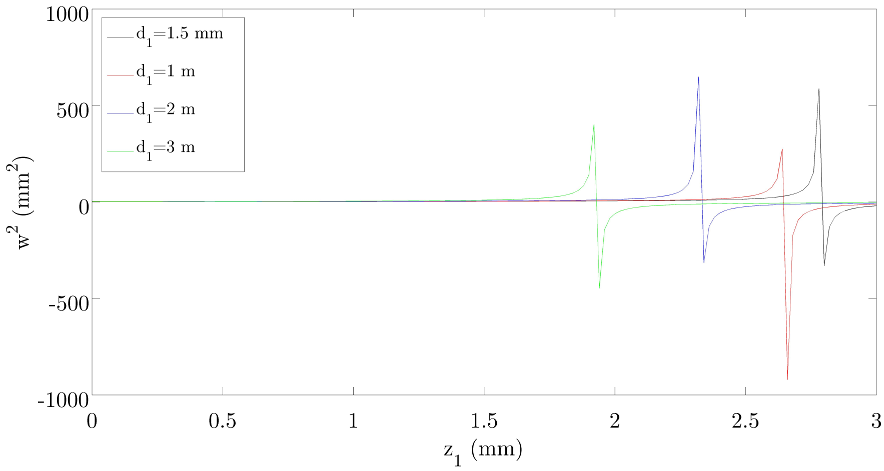

FIGURE 3.15: Evolution of the beam half-width square in an active GRIN parabolic medium with gain of a laser beam with $d_1 = 1.5$ mm (black line), $d_1 = 1$ m (red line), $d_1 = 2$ m (blue line) and $d_1 = 3$ m (green line). The corresponding design shaping lengths are 2.78, 2.64, 2.32 and 1.38 mm, respectively. Parameter values: $a = 1.5$ mm, $\lambda = 1064$ nm, $n_{0I} = -0.00001, n_I = -0.0001, g_{0R}$=0.10476 mm$^{-1}$, $g_{0I}$=0.00024mm$^{-1}$.

The evolution of the relative irradiance is shown in figure 3.16. The graph indicates that the Gaussian beam is turned into a uniform beam at the corresponding shaping lengths and that the relative irradiance at the output face of the material declines as $d_1$ gets larger values.

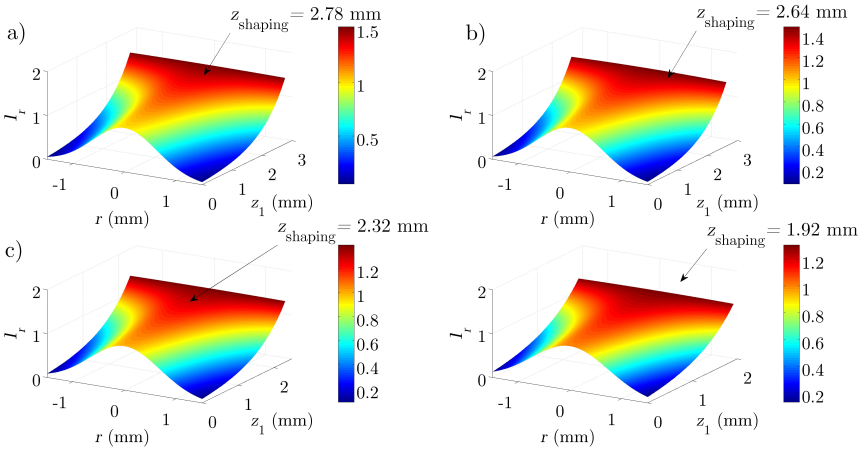

FIGURE 3.16: Gaussian to flat-top beam conversion by an active GRIN parabolic material exhibiting gain for different distances of the incident beam waist to the material: a) $d_1 = 1.5$ mm and $z_{shaping} = 2.78$ mm, b) $d_1 = 1$ m and $z_{shaping} = 2.64$ mm, c) $d_1 = 2$ m and $z_{shaping} = 2.32$ mm, and d) $d_1 = 3$m and $z_{shaping} = 1.92$ mm.

### 3.2.2 Comparison between GRIN parabolic and hyperbolic secant complex refractive indices

In section 3.2.1 we have studied the active GRIN parabolic medium and demonstrated that it can be designed as Gaussian beam uniformization system. Media with a refractive index profile given by a hyperbolic secant distribution (equation (2.61)) can also operate as beam shapers. The HS distribution is a more general profile because the parabolic transverse distribution is considered as the first-order approximation to the Taylor's expansion series of the HS profile. In this section we compare the parabolic and HS complex refractive index profiles with gain and loss in terms of their real and imaginary parts. Gaussian beam propagation in both media is also analyzed.

#### 3.2.2.1 Complex refractive index profiles

The profiles of real and imaginary parts of the HS refractive active index medium of semiaperture $a = 0.5$ mm, $n_{0R} = 1.57$, $n_{0I} = |0.00001|$ are presented in figure 3.17. Four different cases regarding if the material has loss or gain have been considered: the medium exhibits loss ($n_{0I}, n_I(a) > 0$), blue line), gain ($n_{0I}, n_I(a) < 0$), red line), on-axis loss and gain at the edges ($n_{0I} > 0, n_I(a) < 0$, black line) and on-axis gain and loss at the edges ($n_{0I} < 0, n_I(a) > 0$, green line). The simulations show that a similar behaviour to the parabolic case (3.2a) takes place for $n_R$, decreasing with increasing radial distance (figure 3.17a). It thus reveals that the medium presents normal guidance propagation. $n_I$ versus transverse distance is represented in figure 3.17a) in the four cases considered. In the loss case, the value of $n_I$ is positive and has its lowest value on axis and increasing values at increasing distance from the axis, therefore stable light propagation occurs. On the contrary, unstable light propagation happens in the on-axis loss case, where loss decreases with increasing distance from the optical axis, turning to gain to the transverse distance $r = |0.151|$ mm. In the gain case, $n_{0I} < 0$ and $n_I$ has its highest value on-axis and decreases to the edges of the material, so stable light propagation is obtained. In contrast, for the on-axis gain case, gain decreases with increasing distance from the axis, turning to loss at $r = |0.151|$ mm meaning that unstable light propagation occurs. Table 3.2 collects the numerical values used for the design of the active GRIN HS medium.

TABLE 3.2: Numerical values for the design of the active GRIN HS beam shaper.

| $\mathbf{n_{0R}}$ | $\mathbf{n_R(a)}$ | $\mathbf{n_{0I}}$ | $\mathbf{n_I(a)}$ | $\mathbf{g_{0R}}$ **(mm$^{-1}$)** | $\mathbf{g_{0I}}$ **(mm$^{-1}$)** | **Case** |
|---|---|---|---|---|---|---|
| 1.57 | 1.55 | $10^{-5}$ | $10^{-4}$ | 0.31924 | -0.00072 | Loss |
| 1.57 | 1.55 | $-10^{-5}$ | $-10^{-4}$ | 0.31924 | 0.00072 | Gain |
| 1.57 | 1.55 | $10^{-5}$ | $-10^{-4}$ | 0.31924 | -0.00088 | On-axis loss |
| 1.57 | 1.55 | $-10^{-5}$ | $10^{-4}$ | 0.31924 | 0.00088 | On-axis gain |

We are interested on the study of the evolution of $n_R$ and $n_I$ with aperture of the active GRIN parabolic and HS media. Such cases are depicted in the figures

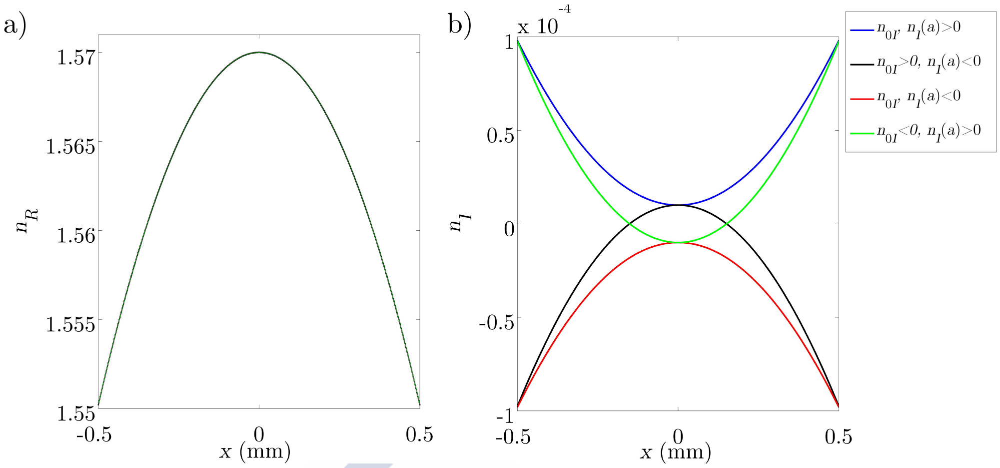

FIGURE 3.17: Profiles of (a) real and (b) imaginary part of the refractive index across an active GRIN HS medium of semiaperture $a = 0.5$ mm and $n_{0R} = 1.57$ exhibiting loss (blue line), gain (red line), on-axis loss and gain at the edges (black line) and on-axis gain and loss at the edges (green line). The imaginary part of the refractive index at the optical axis is $n_{0I} = |0.00001|$.

3.18 and 3.19. As follows from these figures, the parabolic and HS profiles of the real part of the complex refractive index are very similar. Nonetheless, the parabolic distribution shows a better coincidence with the HS distribution in the paraxial region (figure 3.18a)) and the difference between them rises with increasing aperture. Regarding the imaginary part of the refractive index, we can observe the same behaviour. In the region closer to the optical axis ($a = 0.5$ mm) the resemblance among both profiles is clear. In contrast, as the aperture of the medium increases, the parabolic and hyperbolic distributions start to separate. The most evident differences can be observed when semiaperture is equal to 5 mm and 10 mm (figures 3.19c) and 3.19d)).

Figure 3.20 shows an example of how, for a semiaperture of 5 mm, $n_R$ decreases as distance from axis increases, revealing that normal guidance takes place in both active GRIN parabolic and HS media. This happens regardless the sign of $n_{0I}$ and $n_I(a)$. However, $n_I$ behaves in a different manner; as can be seen from figure 3.21, both profiles has the same values close to the optical axis and they split as distance from the axis climbs in all cases but now, the sign of $n_{0I}$ and

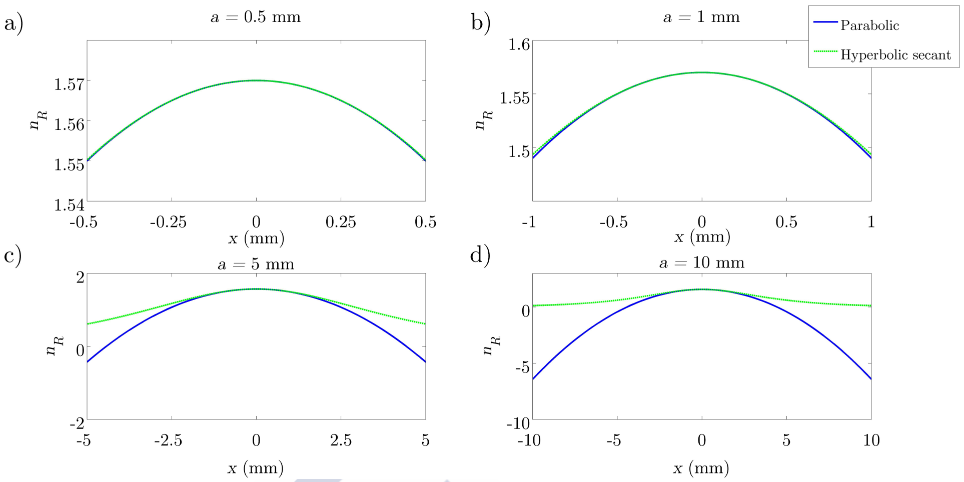

FIGURE 3.18: Profiles of real part of the refractive index across an active GRIN parabolic and HS medium of semiaperture: a) $a = 0.5$ mm, b) $a = 1$ mm, c) $a = 5$ mm, and d) $a = 10$ mm exhibiting gain.

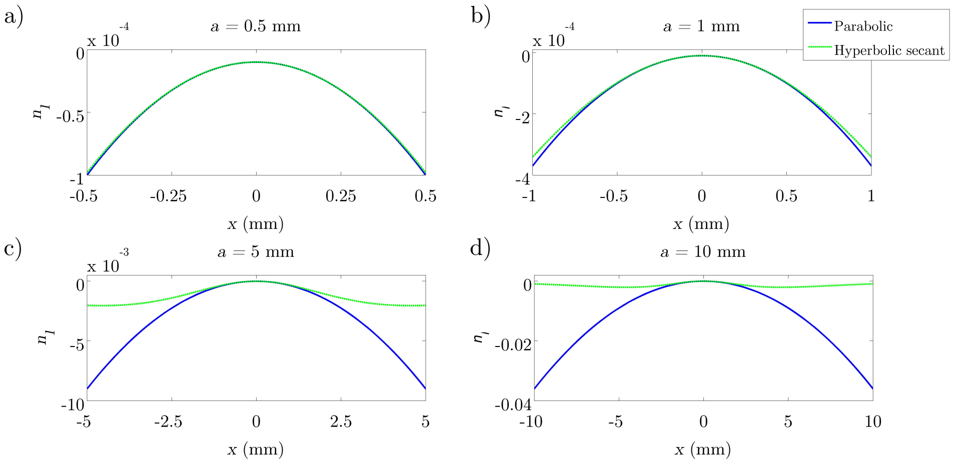

FIGURE 3.19: Profiles of imaginary part of the refractive index across an active GRIN parabolic and HS medium of semiaperture: a) $a = 0.5$ mm, b) $a = 1$ mm, c) $a = 5$ mm, and d) $a = 10$ mm exhibiting gain.

$n_I(a)$ influence the vertex position in the ordinate axis of both distributions, as expected. For both figures representing $n_R$ and $n_I$, the HS distribution separates the same distance from the parabolic distribution, notwithstanding the gain or loss case considered.

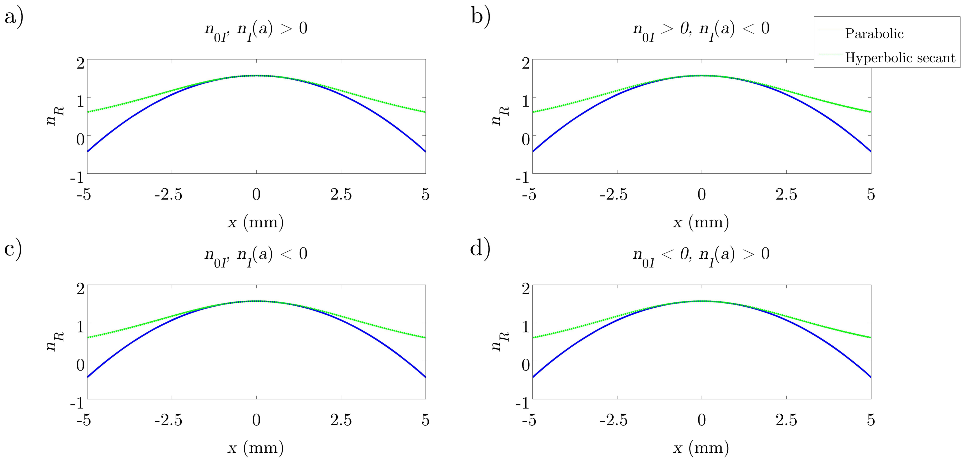

FIGURE 3.20: Evolution of the real part of the complex refractive index with semiaperture 5 mm in: a) loss case, (b) on-axis loss and gain at the edges, c) gain, and d) on-axis gain and loss at the edges for active GRIN parabolic and HS media. Simulations have been done for parameter values shown in table 3.2.

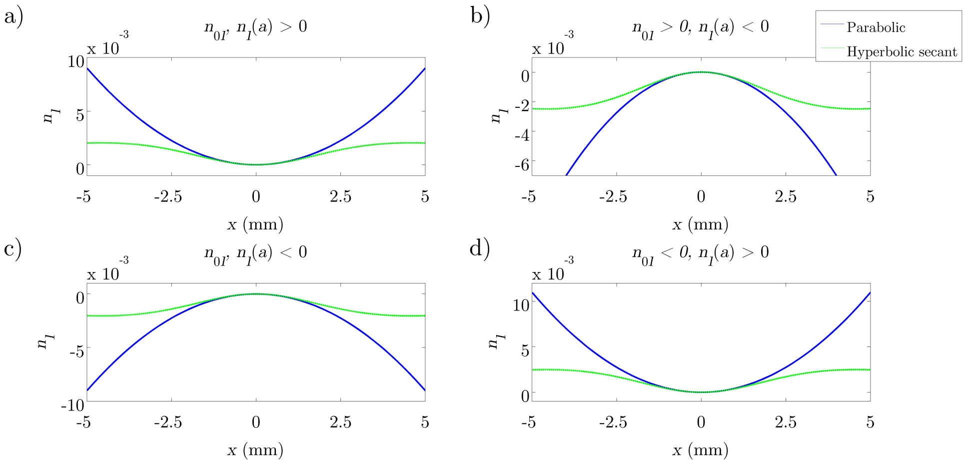

FIGURE 3.21: Evolution of the imaginary part of the complex refractive index with semiaperture in: a) loss case, (b) on-axis loss and gain at the edges, c) gain, and d) on-axis gain and loss at the edges for active GRIN parabolic and HS media. Simulations have been done for parameter values shown in table 3.2.

#### 3.2.2.2 Ray tracing

We consider now a plane Gaussian beam whose waist is located at the input face of an active GRIN parabolic and hyperbolic secant medium with constant complex gradient parameter (see equation (3.1)). The complex ray position and slope at the input are given by

$$q(z=0) = q_0 = w_0 \tag{3.8}$$

$$\dot{q}(z=0) = \dot{q}_0 = \frac{i\lambda}{\pi n_0 w_0} \tag{3.9}$$

It is important to remember that, as shown in section 2.3.2, the complex curvature of a Gaussian beam propagating a distance $z$ within an active GRIN HS medium with position and slope of the complex ray in the (x,z) space of coordinates must be obtained by the inverse transform given by (2.68). For the HS medium, the position and slope of the hyperbolic complex ray at the input are given by

$$q(z=0) = q_{hR0} + iq_{hI0} = \sinh(g_{0R}w_0)\cos(g_{0I}w_0) + i\cosh(g_{0R}w_0)\sin(g_{0I}w_0) \tag{3.10}$$

$$\begin{aligned}\dot{q}(z=0) &= \dot{q}_{hR0} + i\dot{q}_{hI0} = \\ &\{[-g_{0I}\cosh(g_{0R}w_0)\cos(g_{0I}w_0) - g_{0R}\sinh(g_{0R}w_0)\sin(g_{0I}w_0)]+ \\ &+ i[[g_{0R}\cosh(g_{0R}w_0)\cos(g_{0I}w_0) - g_{0I}\sinh(g_{0R}w_0)\sin(g_{0I}w_0]]\}\frac{\lambda}{\pi n_0 w_0}\end{aligned} \tag{3.11}$$

Inserting equations (3.10) and (3.11) into (2.3.2) and also considering that the real and imaginary parts of position and slope of the axial and field rays can be written as in equations (3.2)-(3.7), all the Gaussian beam parameters in the active medium can be obtained.

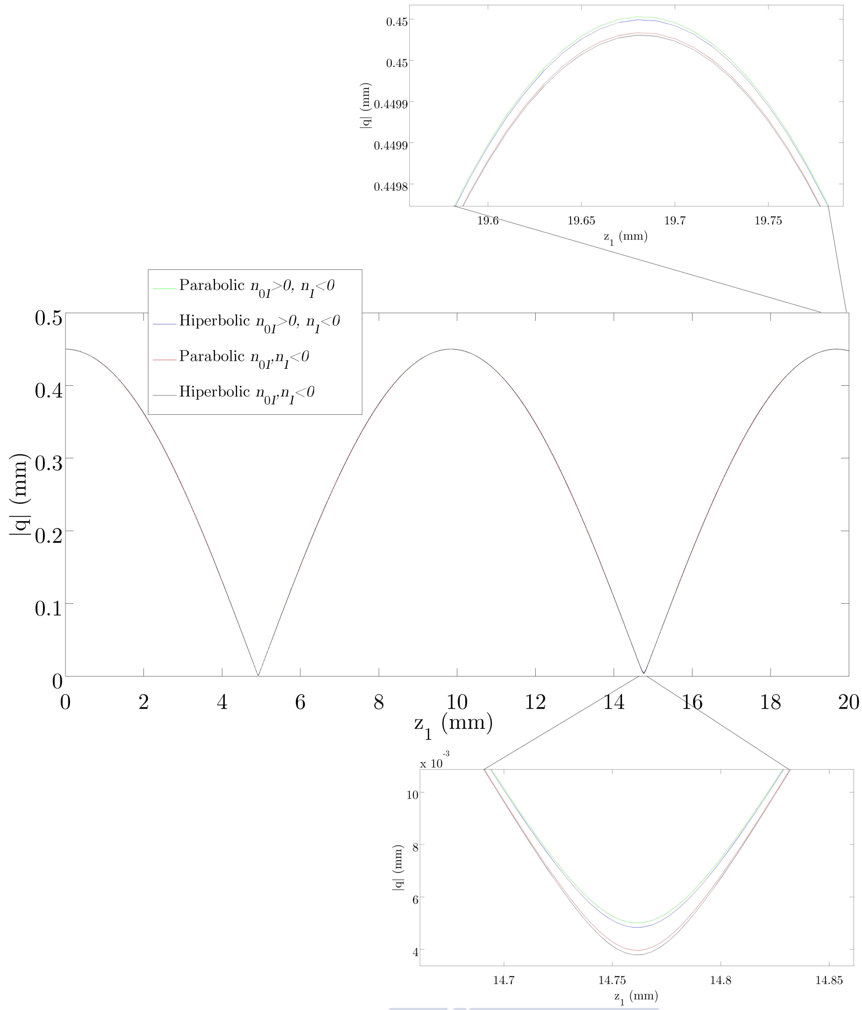

FIGURE 3.22: Evolution of the complex ray in an active gain and on-axis loss GRIN medium with parabolic and HS refractive index profile. Calculations have been made for parameter values of table 3.2. Input beam: $\lambda$ = 575 nm and $w_0$ = 0.45 mm.

Figure 3.22 depicts the evolution of the magnitude of the position of the complex ray for the active parabolic and HS media for gain and on-axis loss cases. Calculations have been performed using the numerical values collected in table 3.2 and considering an input beam with $\lambda$=575 nm and $w_0$=0.45 mm. From this figure it follows that the ray trajectory never cuts the optical axis of the media.

The amplitude of the oscillations is not constant along the beam propagation due to the gain or loss effects. Besides, the oscillation amplitude decreases as distance propagation increases. In addition, we have that the valleys appear closer to the optical axis in the gain case (black and red line for HS and parabolic media, respectively); on the contrary, for the on-axis loss case (green and blue line for HS and parabolic media, respectively) we have that crests of oscillations take a higher value. It is also interesting to note that the difference among parabolic and HS active media increases with propagation distance and is larger at valleys that at crests.

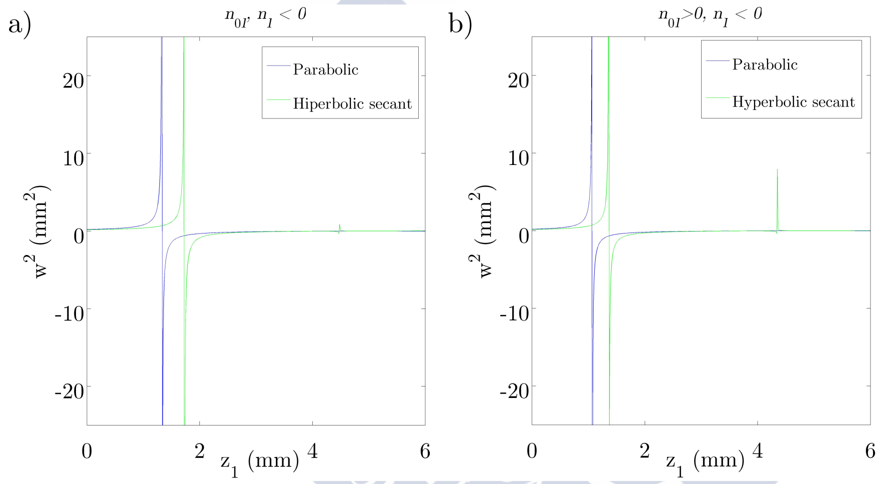

FIGURE 3.23: Evolution of the beam half-beam square in an active (a) gain and (b) on-axis loss GRIN medium. The beam shaping condition is fulfilled at a shorter propagation distance in the parabolic medium (blue line) compared to the HS medium (green line). Input beam: $\lambda$=575 nm and $w_0$=0.45 mm.

Beam-half width square evolution within the parabolic and HS active media with gain and on-axis loss is presented in figure 3.23a) and 3.23b), respectively. Both graphs indicate a very similar evolution in both cases with the exception of the those regions where $w^2$ changes its sign from positive to negative or, in other words, where the input Gaussian beam is turned into a beam with an uniform irradiance distribution. The beam shaping length is shorter in the parabolic medium (blue line) than in the HS medium (green line), for both gain and on-axis loss case. In addition, we can see in the plots that the HS medium has a second shaping length, which also occurs after a shorter propagation of the beam in the gain case.

## 3.3 Tolerance analysis on design parameters of parabolic and hyperbolic secant active GRIN media

When designing an active GRIN beam shaper one should take into account that it must meet requirements within a reasonable tolerance. Beam shapers devices are sensitive to deviations from design parameters, so it is important to determine the tolerance interval of these parameters to ensure the quality of the output uniform beam irradiance profile. We have shown in the previous sections that an active GRIN medium with parabolic or HS refractive index profile can be designed to operate as a Gaussian beam shaper. In this section we analyze a particular case of Gaussian to flat-top conversion by active parabolic and HS media with gain where the media thickness does not correspond to the exact shaping length due to, for example, fabrication errors. Influence of wavelength fluctuations from the design value on the output beam irradiance profiles is also studied. We evaluate the flatness quality of the beam using the root mean square (RMS). Most of commercial beam shapers manufacturers establish as acceptable flat-top beams those with RMS values under 10% or 15%, depending on the application [110]; therefore, we also establish these values as tolerance criteria for beam shapers designed with active GRIN materials. We evaluate the output irradiance profiles considering different values of the material thickness and the input Gaussian beam wavelength, over and below the design parameters. We calculate the RMS to determine the values defining the interval where the output beam can be still considered a nearly uniform beam, for practical purposes. In this way, we have designed two active GRIN beam shapers with parabolic and HS refractive index profile with gain, that transforms a plane Gaussian beam of wavelength 575 nm and beam half-width 0.45 mm into a 1 mm width flat-top beam. For visualization of numerical values corresponding to the gain case used to perform the simulations the reader is referred to table 3.2

Figure 3.24 plots the relative irradiance evolution versus propagation distance in an active GRIN parabolic medium with gain. From this figure it can be seen that the active medium reshapes the input Gaussian beam into a nearly flat-top beam of aperture and amplifies the on-axis irradiance by 61%. The shaping condition, given by equation (2.33), is fulfilled at $z_{shaping} = 1.33$ mm. As the active medium has gain, the output beam is amplified at the output face of the material.

We analyze now the tolerances of the active GRIN parabolic beam shaper. The specifications of the medium are shown in table 3.2 (gain case). Consider figure 3.25a); when the medium is 1.56 mm thick (17.3% superior to the design shaping length) the uniformity on the output beam profile drops, and higher irradiance values at the centre than at the edges are achieved. Conversely, when the material is 1.10 mm thick (a 17.3% inferior to the design shaping length), the uniformity on the output beam profile declines and narrow peaks appears at the edges instead of the targeted flat-top beam. For this thickness tolerance, RMS value stays below 15%.

Figure 3.26 depicts the cross sections of the beam irradiance profiles at the output face of the active GRIN parabolic medium when the thickness fluctuation from the design value (exact shaping length) is ±17.3%. At shaping length, the input plane Gaussian beam (solid line) is turned into a uniform beam at the output face of the material (dotted line). If the input beam propagates in the active GRIN parabolic medium a distance 17.3% shorter than the design one, the uniformity of the output beam profile diminishes, with higher irradiance values at the axis (dashed line). In contrast, if the propagation distance is 17.3% larger that the design one, the uniformity of the output flat-top profile is also deteriorated, but now the irradiance increases gently as we move from the axis towards the edges of the medium (dashed-dotted line).

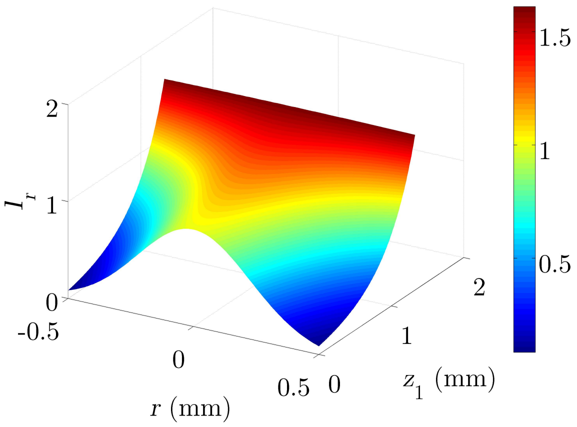

FIGURE 3.24: Gaussian to uniform beam conversion by an active GRIN parabolic medium. Input beam parameters: $\lambda = 575$ nm and $w_0 = 0.45$ mm.

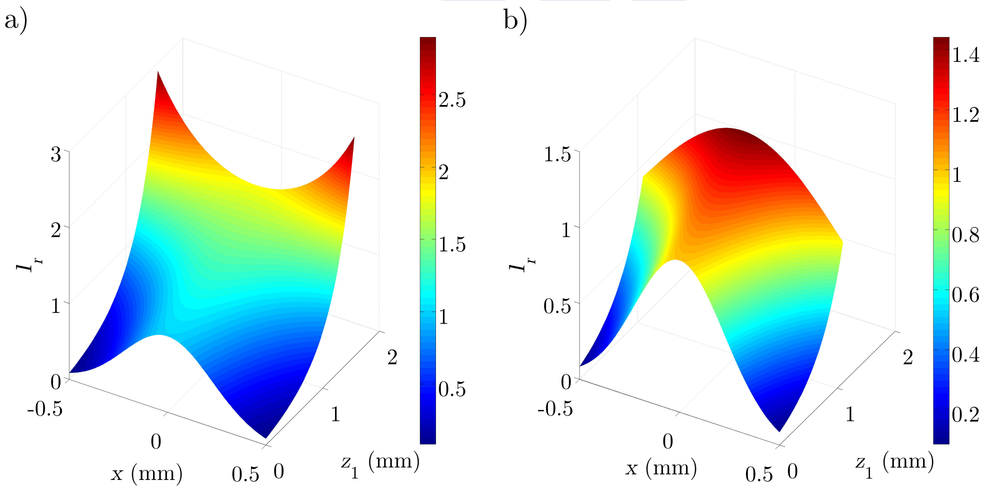

FIGURE 3.25: Simulated irradiance evolution of the input plane Gaussian beam propagating through the parabolic active GRIN beam shaper up to a certain distance (a) above and (b) below the exact the shaping length. The thickness tolerance is 17.3%.

Figure 3.27 represents the evolution of $I_r$ with propagation distance in the active material when the working wavelength deviates from the design one. When

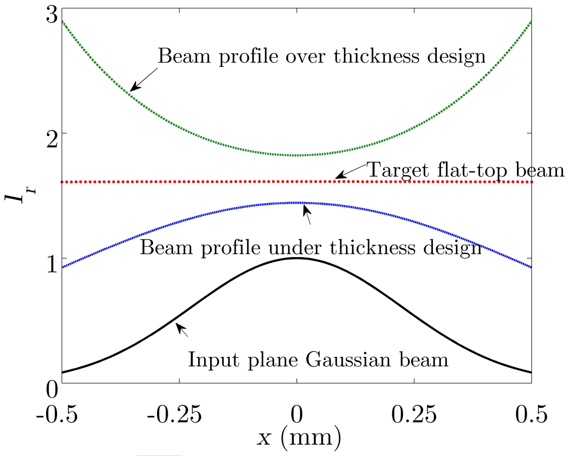

FIGURE 3.26: Cross sections of the input and output beams profiles in the active GRIN parabolic medium: input plane Gaussian beam (solid line), target uniform beam at the exact shaping length (dotted line), beam at a propagation distance 17.3% larger (dotted-dashed line) and shorter (dashed line) than shaping length.

this happens, the output beam profile uniformity drops, which can result in an unsuitable profile for the desired application. The wavelength tolerance in this case is 13.5% (RMS values below 15%). For the exact shaping length, a wavelength 13.5% superior to the design one means a noticeable deviation from an uniform irradiance profile as shown in figure 3.27a). The output beam profile quality deteriorates and the output uniform beam profile obtained in figure 3.24 becomes a non-uniform beam profile whose irradiance is higher at the axis than at the edges. On the contrary, if laser wavelength is 13.5% inferior to the design one narrow peaks appear at the edges of the material figure. This is illustrated in figure 3.24b). Relative irradiance versus distance from axis of the active medium is depicted in figure 3.28. Here, cross sections corresponding to the input Gaussian beam, target flat-top beam and beam profiles over and below the design wavelength considering a 13.5% wavelength tolerance are represented.

The active GRIN beam shaper is designed for a specific laser wavelength and its thickness must fulfill the beam shaping condition. When these parameters deviate from the design values, the flat-top quality deteriorates. In Figure 3.29a)

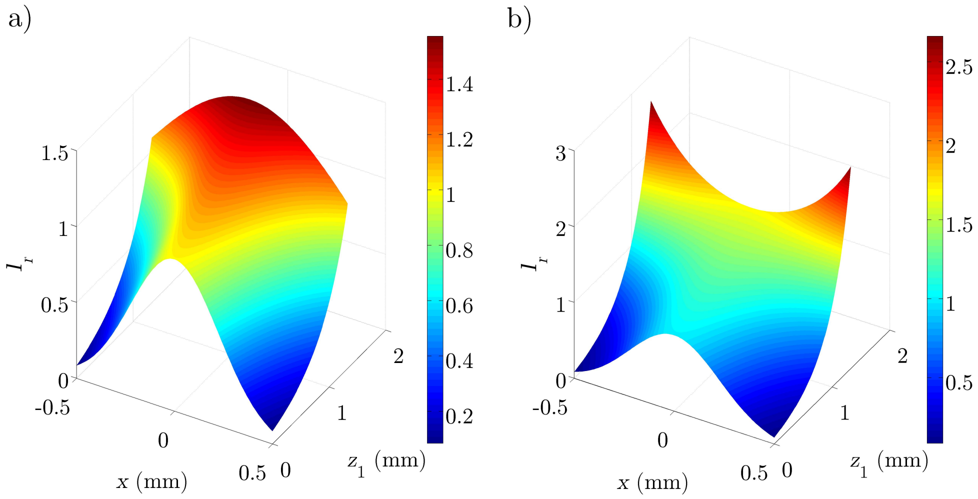

FIGURE 3.27: Simulated irradiance evolution of the input plane Gaussian beam through the active GRIN parabolic beam shaper for a 13.5% deviation from the design working wavelength: a) $\lambda = 652.6$ nm and b) $\lambda = 497.4$ nm.

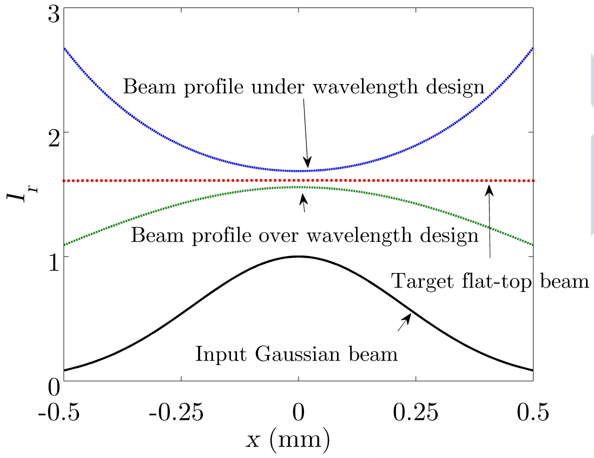

FIGURE 3.28: Study of wavelength tolerance: cross sections of the input and output beams profiles of the input plane Gaussian beam (solid line), the desired flat-top beam at the shaping length (dotted line), the beam profile over (dotted-dashed line) and below (dashed line) than the design wavelength.

thickness deviation and b) wavelength deviation from design parameters of 17.3% and 13.5%, respectively, are shown. When the shaper thickness changes from

1.10 mm to 1. 56 mm, RMS values are below 15%. For wavelengths among 497 nm and 653 nm, RMS values vary from 14.6% to 10.6%.

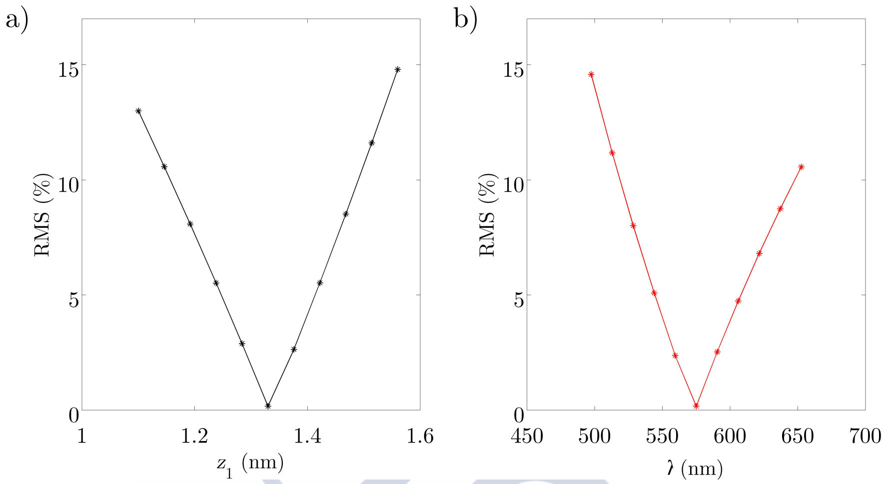

Figure 3.29: RMS versus deviations from a) the design thickness and b) the working wavelength of an active GRIN parabolic beam shaper.

Consider now an active GRIN HS with gain medium specially designed to reshape the plane Gaussian beam under study in this work. The relative irradiance evolution $I_r$ of the input Gaussian beam versus propagation in the active GRIN hyperbolic secant material with gain is depicted in Figure 3.30. The specifications of the active medium are shown in table 3.2. At exact shaping length, $z_{shaping} = 1.73$ mm, the plane Gaussian beam is turned into a large uniform beam doubling the on-axis relative irradiance of the input beam. The more significant gain effects compared to parabolic case seem to be due to the fact that the beam shaping condition is fulfilled at a larger distance in the active HS medium than in the parabolic one (figure 3.23).

Figure 3.31 shows the relative irradiance evolution of the input laser beam in the active GRIN HS material for 13% thickness tolerance. The behaviour of $I_r$ is similar to GRIN parabolic beam shaper case (see figure 3.25). As confirmed by figure 3.32, where cross sections of the output beam profiles are presented, if the input beam propagates in the active medium a distance shorter or larger from the exact beam shaping length, the shape of the profiles at the output face of

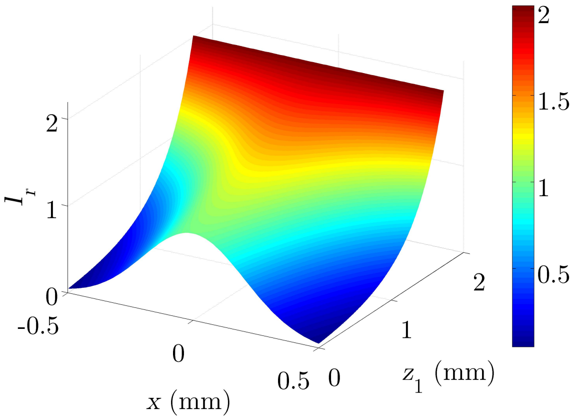

FIGURE 3.30: Gaussian to flat-top beam conversion by a HS active GRIN medium. Input beam parameters: $\lambda = 575$ nm and $w_0 = 0.45$ mm.

the medium suffers a significant degradation on profile uniformity. On the other hand, when the beam shaping condition is fulfilled a beam with large uniformity is obtained.

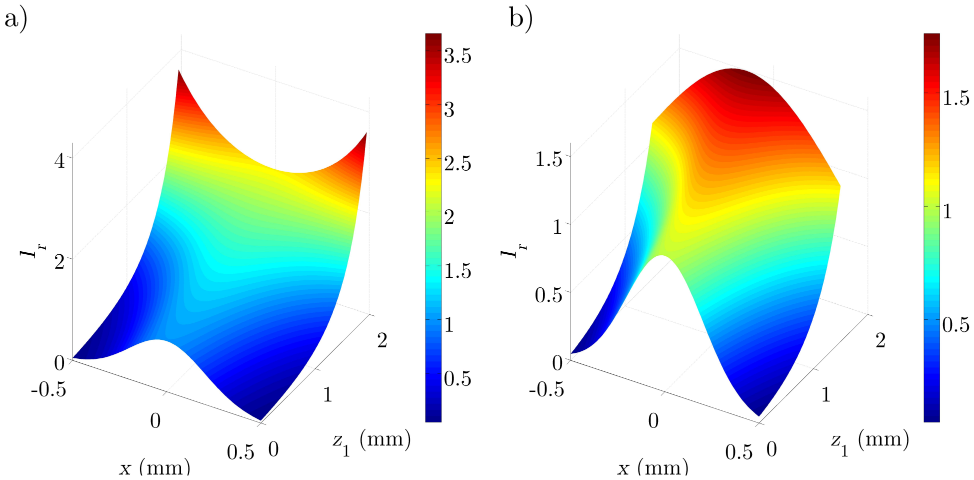

FIGURE 3.31: Simulated irradiance evolution of the input plane Gaussian beam through the active GRIN HS beam shaper when (a) the thickness of the medium is 13% greater than shaping length and (b) 13% shorter than shaping length.

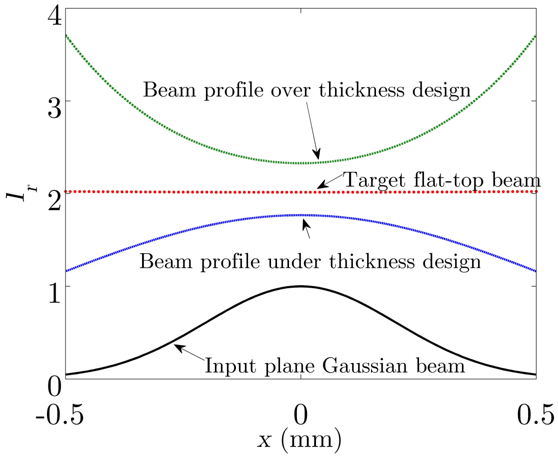

FIGURE 3.32: Cross sections of the input and output beams profiles corresponding to the active GRIN HS material considering a ±13% thickness tolerance: input plane Gaussian beam (solid line), target uniform beam at the exact beam shaping length (dotted line), non-uniform profile above (dashed line) and below (dashed-dotted line) shaping length.

The active GRIN HS beam shaper is designed for a specific laser wavelength. If for some reason this wavelength deviates from the design value, the targeted flat-top beam is transformed into a beam with essentially non-uniform irradiance profile. In this case, the wavelength tolerance is 9.9% and over a wavelength range from 518 to 632 nm, RMS values are below 15%. $I_r$ evolution in the medium is represented in figure 3.33 and the output transverse irradiance profiles are shown in figure 3.34. The input plane Gaussian beam (solid line) is turned into a flattened profile at the exact beam shaping length (dotted line) while deviations from the design wavelength provoke that the desired flattened profile turns into a beam with essentially non-uniform irradiance profile (dashed and dashed-dotted lines).

The overall specifications of the active GRIN beam shapers proposed are summarized in table 3.3.

Figure 3.35 plots RMS versus a) thickness deviation and b) wavelength deviation from design parameters of 13% and 9.9%, respectively. When the HS shaper thickness changes from 1.51 mm to 1.95 mm, RMS values are below 15%.

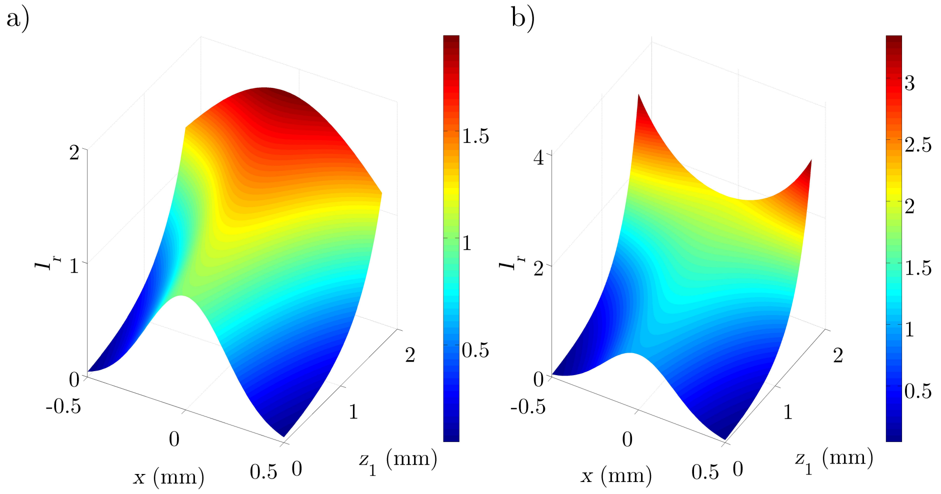

FIGURE 3.33: Simulated irradiance evolution of the input plane Gaussian beam through the active GRIN HS beam shaper for a 9.9% deviation from the design wavelength: a) $\lambda = 632$ nm and b) $\lambda = 518nm$.

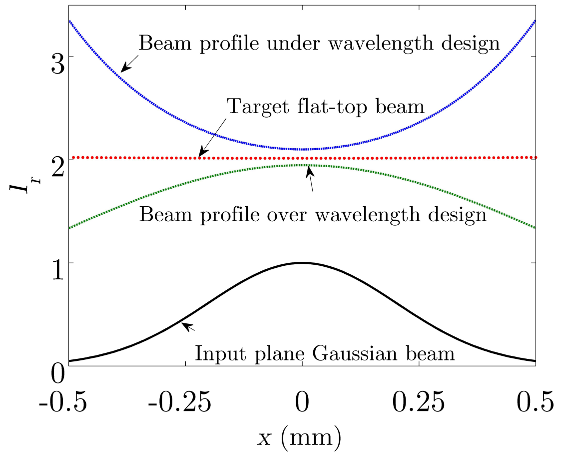

FIGURE 3.34: Effect of variations in the wavelength from the design value on the output irradiance profile of a plane Gaussian beam, after propagating in the HS active GRIN material. The input plane Gaussian beam (solid line) is shaped into a large uniform beam at the design wavelength and shaping length (dotted line), while non-uniform beam is obtained below (dashed line) and above (dotted-dashed line) the design wavelength.

TABLE 3.3: Active GRIN beam shaper specifications.

| **Parameter** | **Parabolic** | **Hyperbolic secant** |
|---|---|---|
| Wavelength | 575 nm | 575 nm |
| Beam waist | 0.45 mm | 0.45 mm |
| Aperture | 1 mm | 1 mm |
| Output beam | flat-top, 1 mm width | flat-top, 1 mm width |
| Output beam thickness tolerance | ±17.3% | ±13.5% |
| Output beam wavelength tolerance | ±13% | ±9.9% |

Furthermore, we find that when the wavelengths cover a range between 518 nm and 632 nm, RMS values also stay below 15%.

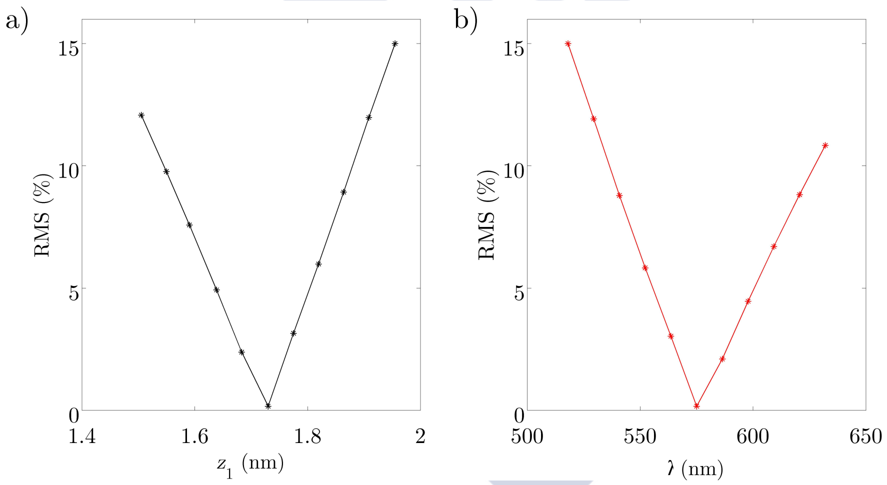

FIGURE 3.35: RMS versus deviations from a) the design thickness and b) the working wavelength of an active GRIN HS beam shaper.

## Chapter 4

# Active GRIN media fabrication methods

## 4.1 Introduction

This chapter addresses the exploration of two methods for active GRIN media fabrication: Sol-gel process and Laser Zone Melting (LZM) technique. Conventional methods for GRIN materials development [111] are neutron irradiation [112], chemical vapor deposition (CVD) [113], partial polymerization [114], and ion exchange. The latter technique [115, 116] is the main technology used for large-scale production of GRIN lenses.

In this work, we first explore the possibility of using the chemical route known as sol-gel process for active GRIN media preparation. The sol-gel route has been demonstrated as an alternative for the preparation of glasses and ceramic materials at considerably lower temperatures compared to conventional techniques, being a cost effective method that can be deposited on substrates with different shapes [117]. GRIN lenses prepared by sol-gel process have also been reported [118, 119]. Some of the advantages of this method include the possibility to precisely control the stoichiometry, producing multicomponent homogeneous systems not previously available and obtaining of high-purity materials for electronics and optics [120]. In particular, sol-gel is a versatile way for thin film manufacturing which permits to control the refractive index and thickness of the coatings [121]. Furthermore, optical properties of rare-earth (RE) doped materials prepared via sol-gel have been widely investigated for photonic applications where optical activity through the use of RE dopants is a key requirement due to the ease of introducing a wide variety of dopants [122–125]. In this thesis we have prepared erbium and ytterbium-doped films prepared by sol-gel and using dip coating technique in order to evaluate the feasibility of applying the sol-gel process in the fabrication of active GRIN media. Optical constants and thickness of the final films have been analyzed using Spectral Ellipsometry (SE) whereas topographical features have been inspected by Atomic Force Microscopy (AFM). Photoluminescence spectra versus erbium concentration have also been studied.

The second technique that we have explored is the Laser Zone Melting method, a technique used to process thermal shock sensitive materials [126, 127]. Preliminary experiments were initiated to determine the feasibility of LZM to develop active GRIN materials. LZM is a laser heating method which causes high temperature gradients in relatively small controlled areas, thus promoting local melting of the materials at the vicinity of the treated area with an uniform distribution within the melt region [128]. LZM is used for a variety of materials including metals, oxides, and semiconductors. In the present thesis, LZM technique was used to produce erbium, ytterbium, dysprosium, and lithium niobate-doped $SiO_2$ glass rods with a $CO_2$ laser source. Structural properties and chemical composition of the samples have been characterized by Scanning Electron Microscopy (SEM) combined with Energy Dispersive X-ray (EDX), while refractive index has been obtained by means of Spectral Ellipsometry.

The remainder of this chapter is organized as follows. In section 4.2 we present a short introduction to physical and chemical principles of the sol-gel process and to the so-called wet immersion-techniques for coating deposition. In this section, the basis of the LZM process are also introduced. Section 4.3

describes the precursors and substrates selected in the experimental part of this thesis. Characterization techniques and experimental procedure are described in sections 4.4 and 4.5. Finally, section 4.6 presents and discusses the main research results.

## 4.2 Fabrication methods

### 4.2.1 Sol-gel process

The sol-gel process [129] is a powerful and versatile method for producing numerous kinds of materials with interesting optical and photonic properties, for instance GRadient-INdex elements. A large number of optical elements encompassing bulk optics, active waveguides, solid lasers, materials for nonlinear optics, gradient refractive index materials and chemical and biological sensors have been prepared by sol-gel methods [130–132]. The sol-gel process offers some unique opportunities for the synthesis of optical materials over existing production methods including control of composition and low processing temperature. The process gives excellent control of purity and composition since it starts with pure materials. It also allows to deposit films and coatings on different surfaces, enabling a flexibility that is not possible with other conventional techniques. Particular advantages of sol-gel coating are shown in table 4.1. In addition, sol-gel techniques allow the obtaining of hybrid coatings by incorporating organic molecules. The greatest limitation of the sol-gel process is that the cost of the raw materials, especially of the alcoxides, can be high. In addition, sol-gel has a long process duration, the synthesis of monoliths presents some difficulties and the process has to be performed under very controlled conditions in order to obtain the correct properties of the structure control and reproducibility [133].

The sol-gel route is a method especially suitable for preparation of GRIN materials due to the possibility of tuning the refractive index profile in accordance to the requirements of the application. In particular, fabrication of radial GRIN media, where the index profile varies continuously from the optical axis to the periphery along the transverse direction in such a way that the surfaces of constant index are concentric cylinders about the optical axis, by sol-gel have been reported by two different methods. These techniques are based in partial leaching of index-modifying cations from an alcoxy-derived wet gel and interdifussion of index-modifying cations in the liquid phase of a wet gel [118, 134–136].

In this work we have prepared and characterized rare earth-doped silica and silica-titania thin films as a preliminary step for growing layer stacks with progressively different complex refractive indices, where the final complex index of the structure is characterized by a parabolic-like distribution. The planar active GRIN material can be obtained by consecutive deposition on the glass substrate of sol-gel coatings with different complex refractive indices $n_1, n_2, \ldots, n_m$ ($m$ is an integer) as shown in figure 4.1a). Hence, a final multilayer GRIN structure, characterized by a complex refractive index with a parabolic-like profile distribution for both its real and imaginary part (see figure 4.1b)), can be generated. The properties of thin films processed by sol-gel such as its refractive index can be tailored by modifying the different parameters involved in the process as, for instance, selecting the type of the precursors, molar ratios between the reactants, and the synthesis temperature, among others [133].

TABLE 4.1: Advantages of sol-gel coating.

| **Term** | **Remark** |
|---|---|
| Low-temperature processing | Coating of glasses, integrated electronic, and optical devices, among others, is possible |
| Small thickness | Very thick coatings are possible |
| High optical quality | Transparent films are possible |
| Great control of chemical composition | Different refractive indices can be obtained |
| Easy coating of large surfaces | Very attractive for industry |

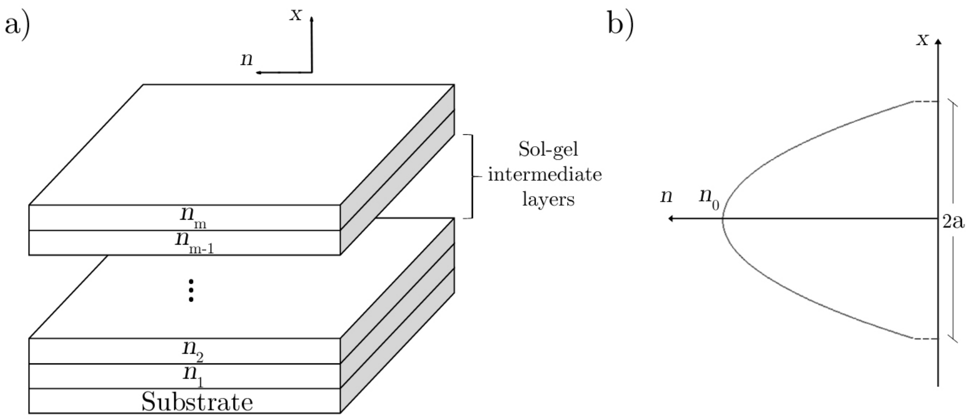

FIGURE 4.1: Geometry of the planar active GRIN material: a) sol-gel coatings with different complex refractive indices are progressively grown onto the glass substrate to generate a final structure characterized by b) a parabolic-like profile distribution for both the real and imaginary part of the complex refractive index.

#### 4.2.1.1 Sol-gel chemistry

Sol-gel route was first proposed for production of optical materials by M. Ebelmen in 1845 [137]. This process basically involves the evolution of inorganic networks through the formation of a colloidal suspension (sol) and its gelation to form a network in a continuous liquid phase (gel) [121, 138]. A colloid is a suspension in which the dispersed phase is so small ($1 \sim 1000$ nm) that gravitational forces are negligible and interactions are dominated by short-range forces, such as Van der Waals attraction and surface charges. The reactions implicated in the sol-gel chemistry are based on the hydrolysis and condensation of the starting materials or precursors, which normally consist of alkoxides and inorganic solutions to produce silicates, alumina and zirconia, among others [139]. Hydrolysis is a reaction in which metal alkoxide $(M - \mathrm{O}R)$ react with water to form metal hydroxide $(M - \mathrm{OH})$. Condensation is a reaction which occurs when two metals hydroxides $(M - \mathrm{O}H + \mathrm{OH} - M)$ combine to give a metal oxyde species $(M - \mathrm{O} - M)$. A gel consists of sponge like, three-dimensional solid network whose pores are filled with another substance (usually the original solvent of the sol). Basically, the sol-gel process comprises the following steps: (i) preparation of a homogeneous solution of easily purified precursor(s); (ii) transformation of this solution into a sol form by treatment with a suitable reagent as, for instance, water with HCl for oxide ceramics; (iii) allowance/induction of the sol to change into a gel (or viscous sol) by polycondensation; (iv) shaping the gel to the finally desired form or shape as thin film, fiber, etc. and (v) application of a thermal treatment (sintering) to convert the shaped gel to the desired material.

Two kinds of sol are considered depending on the type of precursors employed: (i) inorganic sols, where precursors are purely inorganic compounds and (ii) hybrid sols, where a mixture of hybrid and inorganic precursors exist. Sol-gel processing consists mostly of two groups of reactions, hydrolysis and condensation reactions of organic and inorganic precursors, in order to obtain spatial networks covalently attached. Usually, alkoxides are used as starting precursors. An example is the formation of silica glass from tetraethoxysilane (TEOS).

1. *Hydrolisis*: In this stage precursors are hydrolized, e.g. TEOS form Si-OH. The most important parameters that affect the hydrolysis rate are pH and $H_2O$/alkoxide ratio. They influence the type of catalyst and/or complex agents that have to be employed. Hydrolysis can be performed by acid or basic catalysis:

$$\mathrm{Si(OC_2H_5)_4} + 4\mathrm{H_2O} \rightarrow \mathrm{Si(OH)_4} + 4\mathrm{C_2H_5OH} \tag{4.1}$$

2. *Condensation*: Where the hydrolyzed species are associated forming covalently linked networks, e.g. building bridges -Si-O-Si- .

$$\mathrm{Si(OH)_4} \rightarrow \mathrm{SiO_2} + 2\mathrm{H_2O} \tag{4.2}$$

The overall reaction is

$$Si(OC_2H_5)_4 + 2H_2O \rightarrow SiO_2 + 4C_2H_5OH \tag{4.3}$$

The two moles of water are the minimum necessary amount to completely convert one mole of TEOS.

The reactions that take place in sol-gel processes depend on a series of parameters, including compositions and concentrations of precursors and solvent used, the amount of added water, catalysts, further additives, sequence in which the components are added, time schedule of mixing of the components, further conditions of mixing (e.g. atmosphere, ultrasonics agitation or mixing efficiency) and temperature.

#### 4.2.1.2 Film deposition

Sol-gel method is one of the simplest technique to manufacture thin films. Wet chemical sol-gel technologies are the most versatile and easiest ones to get coatings using a liquid deposition for a variety of inorganic and hybrid and nanocomposite materials. Such techniques involve the application of a liquid precursor film on a substrate that is then converted to the desired coating material by a series of subsequent post-treatment steps. There exist several coating sol-gel methods [121, 140], which are summarized below, that allow coating a wide variety of substrates and complex geometries.

- *Dip coating*

  In dip coating technique, the substrate to be coated is immersed in a liquid and subsequently withdrawn at a constant withdrawal speed. The process takes place under well-controlled temperature and atmospheric conditions. The schematics of the dip coating process is briefly represented in figure 4.2. As shown in the figure, the film formation involves several steps, but nevertheless the underlaying physical and chemical processes are mostly overlapping. To obtain the final film normally a thermal treatment is necessary. The densification temperature depends on the composition.

As schematically represented in the figure, the process starts with the immersion of the substrate in the coating bath. Next, the liquid film is entrained on removal of the substrate from the liquid, which then consolidates by drying and accompanying chemical reactions. The consolidation step represents the sol-gel transition with concomitant processes of draining, evaporation and hydrolysis.

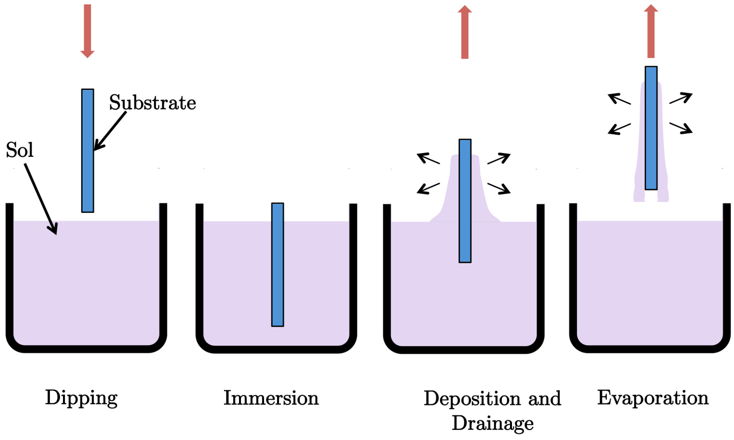

Figure 4.2: Film deposition by dip coating: dipping and immersion of the substrate into the sol, formation of the layer by withdrawing the substrate and gelation of the layer by solvent evaporation.

The sequential stages of sol-gel dip coating [141] are illustrated in figure 4.3. The substrate is vertically withdrawn from the coating sol at a constant speed $U_0$. From a physical view, the process that leads to the formation of the film on the substrate is based on a fluid mechanical equilibrium between the entrained film and the receding coating sol. The two regimes are separated by a stagnation line, above which the coating liquid is entrained by the substrate whereas the liquid below is retained in the bath. Since the inorganic species are progressively concentrated by evaporation, leading to aggregation, gelation and final drying stage to form a type of dry gel or xerogel.

The equilibrium is mainly governed by the viscous drag ($\propto U_0/h$), the gravity force ($\rho g h$) and the liquid-vapour surface tension ($\gamma_{LV}$), although other forces like the inertial force or the disjoining pressure play also an important role. When the substrate speed and liquid viscosity $h$ are low, which normally occurs for sol-gel deposition, the final film thickness $h_0$ is given by the Landau-Levich equation [142]:

$$h_0 = 0.94 \frac{(\eta U_0)^{2/3}}{{\gamma_{LV}}^{1/6} (\rho g)^{1/2}} \tag{4.4}$$

where $\rho$ is the liquid density and $g$ is the acceleration of gravity.

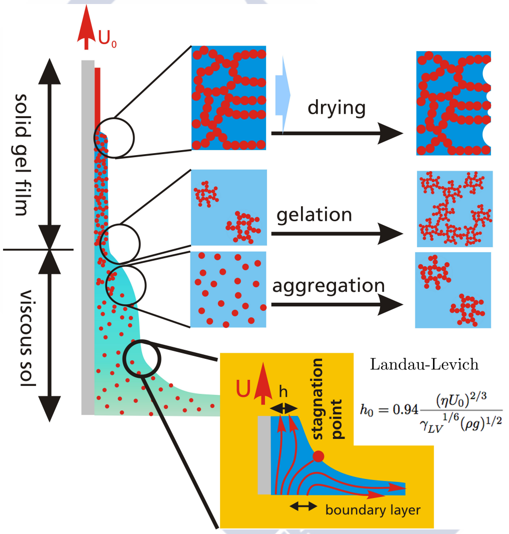

FIGURE 4.3: Details of sol-gel dip coating process [143].

- *Spin coating process*

Spin coating technique is a simple process to deposite thin films onto relatively flat surfaces. In this technique, the substrate spins around an axis that should be perpendicular to the coating area. The process can be basically described as follows: the sol is deposited on the substrate, spin up, spin off and gelation by solvent evaporation. Spin coating and dip coating are two basic techniques used to deposit sol-gel coatings but in spin coating is the physics of the rotation of the substrate which leads to the film formation. The deposited film become thin by the centrifugal draining, and tend to be uniform due to the balance of the rotational accelerations by the viscous drag felt within the solution. A major difference between dip coating and spin coating is that the latter produces a one-sided coating, while dip coating yields a double-sided coating. The quality of the final coating depends on the rheological parameters (rheology is a complex parameter that depends on particle shape, temperature, solvent, concentration and particle interaction) of the sol, along with the Reynolds number of the surrounding atmosphere.

- *Spray coating techniques*

  Spray coating methods are widely used in industry for organic lacquers, being also feasible for coating irregularly shaped glass forms. Spray coating techniques are normally limited to special cases and smaller substrates sizes than dip coating techniques. The main advantage of the dip coating method for large area application is that the coating thickness can be very precisely controlled by controlling the viscosity and the withdrawal speed. Nevertheless, it presents some disadvantages [144]:

  1. A high volume of sol is normally needed. Furthermore, the sol can be “contaminated” when the substrate is dipped several times in the sol (leaching) and by the environment (dust). This can affect the repeatability of the process and its quality.
  2. The withdrawal speeds are in the range of a few cm/min, which implies that long processing times may be required for large substrates.

  The preparation of optical coatings by spraying offers therefore several advantages compared to dip coating technique, since the so far realized processing speed of 1 (mol/L)/min is already 10 times faster and offers better throughput as it requires less sol volume. Coating sols with rather short pot lives can be used and the coating step is suitable for establishing an in-line process. One more advantage is that it uses "fresh" sol each time the coating is applied with a spray. With the spray coating method optical coating with controlled thickness in the range of about 200 nm can be obtained.

Processes similar to spray coating, where very fine droplets are produced like the pyrosol-process, in general lead to very homogeneous coatings on hard substrates, but the coating material does not hit the surface in form of liquid droplets but more or less in form of dried small particles in the nanometer range [144]. Due to the high reactivity of these particles when reaching the hot surface, a continuous glass film can be formed.

- *Flow coating methods*

  In the flow coating process the liquid coating system is directly poured over the substrate. In this case, the resulting film thickness depends on the angle of inclination of the substrate, the coating liquid viscosity and the solvent evaporation rate. A variation of this process involves the spinning of the substrate after coating; this can result useful in order to obtain more homogeneous coatings. If no spinning process is applied, the film thickness increases from the top to the bottom of the substrate [144].

- *Capillary coating*

  Capillary coating or laminar flow coating designates the deposition of a wet film developed by Floch [145, 146] and Thomas [147]. It combines the high optical quality produced by dip coating with the advantage that all the coating sol can be used. In this technique substrates are coated in an horizontal upside-down position using a vacuum-chuck for substrate carriage. The process can be described as follows: the sol is pumped into a slot applicator tube, flows out in a laminar motion to the surface through the slot and forms a continuos and homogeneous films on the outside. The liquid can be recycled by draining it into a collector trough and returned to a container. There is no physical contact between the applicator tube and the substrate; however, a close interval allowing the creation of a narrow meniscus and, at the time a laminar regime during deposition is achieved, an homogeneous coating is generated on the surface. In capillary technique, the fluid dynamics controlling the entrained film thickness is almost identical to those for dip coating. Britten [148] addressed the fluid dynamic of capillary coating in 1993 and establish the dependence of the entrained film thickness on the substrate translation rate, viscosity of the coating media, geometry and falling film flowrate. Britten's model results are in good agreement with optical coatings measurements for films deposited from Newtonian coating fluids. Most of the precautions that must be considered in dip coating processes apply to capillary coating including cleanliness, vibration damping and smooth motion of the substrate or applicator tube assembly. A particular problem that can arise with the capillary method is the particle contamination due to the thick film or dripe line that can build up at the point where the meniscus cuts and detaches from the substrate. This problem is critical for multilayer deposition and can be minimized by cleaning the substrate edges at intervals during the coating runs.

- *Roll-to-roll (R2R) coating*

  Roll coating is another wet coating technique by which thin liquid film is formed on a continuously moving web or substrate using two (or more) rotating cylinders, the surfaces of which move either in the same direction (forward) or opposite direction (reverse). Part of the liquid passes through the gap between the rolls and splits downstream into two thin films, each coating one of the rolls [140]. This technique is used in the painting, photographic, photovoltaics and tape-recording industries for covering a large surface area with one or several uniform layers [149].

### 4.2.2 Laser Zone Melting

"In-situ" Laser Zone Melting designates a method developed to process thermal shock sensitive materials with a $CO_2$ laser scanner combined with simultaneous external heating of the substrate and its uniform movement [150–153]. The application of the laser beam on a surface causes high temperature gradients in relatively small controlled areas, promoting local melting of the materials at the vicinity of the treated area. It is also an interesting alternative to conventional synthesis techniques of rare-earth active optical materials, as sol-gel and solid-sate methods, allowing the incorporation of the doping ions in the glass substrate by diffusion processes [128, 154]. LZM technique permits consolidating mixtures of glass and polycristalline phases with high melting points at the same time that the substrate is maintained at significantly lower temperatures. Stress derived from thermal shock is thus substantially reduced or completely avoided. A major advantage of LZM method over sol-gel process is that shorter fabrication times are required allowing cost minimization. The LZM device used in this work is illustrated in figure 4.4. The beam of a $CO_2$ laser is displaced along the longitudinal direction of the substrate with a galvanometer mirror system. The beam is focused on the glass rod while it rotates at constant speed in an orthogonal direction to the laser line focus.

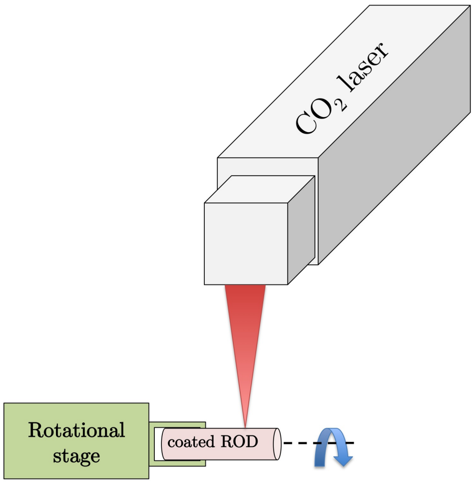

FIGURE 4.4: Laser Zone Melting setup: the $CO_2$ laser is equipped with a galvanometer mirror system which precisely position the laser beam onto the substrate. The sample is maintained under constant speed of rotation during the process.

The laser source used in this technique was a $CO_2$ laser operated at the wavelength of 10.6 $\mu$m. The first $CO_2$ laser was built and demonstrated at Bell Telephone Laboratories by C. Kumar N. Patel in 1964. This type of lasers are continuous or pulsed high power gas lasers and are capable to provide high power efficiency in the infrared region. $CO_2$ laser produces a beam in the infrared region of the spectrum at numerous discrete output wavelengths that can be selected between 9 and 11 microns with the use of isotopes in the laser gas mixture. As most materials absorb efficiently at these wavelengths, $CO_2$ lasers are widely employed in science and industrial applications, including laser cutting, welding, drilling, and surface treatment [155, 156].

The active medium of $CO_2$ lasers is composed by a mixture of carbon dioxide ($CO_2$), Nitrogen ($N_2$) and Helium (He) [157]. The laser pumping is achieved by an electrical gas discharge. The $N_2$ molecules are excited by the electrical discharge and transfer their excitation energy to $CO_2$ molecules by colliding with them. The $CO_2$ plays the role of light emitter in the laser. On the other hand, helium function is "depopulate" the lowest laser level, i.e., helps carbon dioxide molecules to drop from the lower laser levels to ground state, thus keeping the population inversion necessary for laser operation. Besides, helium aids to remove the heat from the system.

## 4.3 Precursors and substrates

In this work we have explored the sol-gel method and the LZM technique to produce planar and cylindrical active GRIN media, respectively. In both cases we have chosen $SiO_2$ host matrices, since glassy hosts are highly attractive material for development of optic and photonic devices mainly due to high glass transition temperature, chemical stability and low thermal expansion coefficient [158, 159]. Besides, oxide glasses are well known as excellent hosts for rare-earth ions. Lanthanides or RE ions are characterized by $[Xe].4f^{12}.6s^2$ electronic configuration. They have became key materials in photonics field as they can provide optical gain. For instance, erbium and ytterbium (alone or together) in glass are widely used in photonic systems [128, 160, 161]. Erbium (Er) is specially relevant in the optical communication field because it presents a photoluminescence peak at a wavelength around 1.5 $\mu$m, inside the third window of fibre communication system, whereas ytterbium (Yb) is one of the most important gain media for lasers.

Preparation of optical material using sol-gel process present several advantages compared to conventional methods [129]. Sol-gel route allows flexible chemistry along with low process temperatures. The latter is important to prepare active photonic devices by incorporating rare earth ions, as they have low solubility in silica glass, thus a non-equilibrium low temperature process is necessary to have RE ions in host matrix with atomic level homogeneity [162, 163]. Sol-gel process also permits minimal formation of clusters of RE ions for high doping level of such ions [164]. RE elements as erbium and ytterbium can be incorporated into sol-gel films and monoliths [165–167]. The optical and luminescence properties of sol gel silica glasses with incorporated RE ions has been widely reported [168, 169], which makes them a promising route for preparation of active GRIN media.

For developing active GRIN media it is important to have tunable complex refractive indices over a range as large and continuos as possible. With this objective in mind, we have prepared three sol systems doped with erbium using $SiO_2$-$TiO_2$ and $SiO_2$ as host matrices. Ytterbium-doped films have also been prepared for the $SiO_2$-$TiO_2$ system.

1. MTES/TISP sol

   Erbium and ytterbium-doped $SiO_2$-$TiO_2$ thin films have been produced by the sol–gel method. $SiO_2$ and $TiO_2$ are commonly used in optics and photonics applications due to the wide spectral region of transparency from visible to near infrared, their chemical durability, thermal stability and low cost. $SiO_2$-$TiO_2$ was selected as host matrix, where $TiO_2$ co-doping has been used to control the refraction index as the variation of $SiO_2/TiO_2$ molar ratios allows to obtain optical layers with intermediate refractive index between the $SiO_2$ and $TiO_2$ ($n = 1.45$ and $n = 2.5$, respectively, at wavelength of 632.8 nm). In particular, $70SiO_2/30TiO_2$ composition was selected taking into account that we are interested on coatings with refractive indices in the interval (1.5-1.65). In addition to this, the incorporation of dopants such as erbium and ytterbium to this system is possible [123, 132, 170].

In this instance, the sol was prepared using methyltriethoxysilane (MTES) and titanium isopropoxide (TISP) as silicon dioxide and titanium dioxide precursors. Erbium-doped films containing different Er concentration have been fabricated. In addition, ytterbium-doped thin films has been prepared to compared the optical constants and thickness to that of non-doped and erbium-doped $SiO_2$-$TiO_2$films. There exist a wide variety or erbium and ytterbium-bearing compounds. But some of them as, for instance, erbium oxide, hydroxide and carbonate are insoluble in alcohol, while erbium chloride is weak solubly. On the contrary, erbium nitrate is highly soluble and allows to form heavy doped solutions [171]. Besides, erbium alkoxides result easily hydrolized, requiring of processing under $N_2$ atmosphere. For these reasons, Er and Yb nitrates where used as erbium and ytterbium precursors, respectively.

2. MTES/TEOS sol

   A MTES/TEOS sol in the molar ratio 60/40 was prepared using tetraethylorthosilane (TEOS) and methyltriethoxysilane (MTES) as a mixed silica precursor in order to obtain films with lower complex refractive index than those prepared only with TEOS as a silica precursor. Erbium nitrate was used as erbium precursor.

3. TEOS sol

   In this case, erbium-doped silica films were fabricated using tetraethoxysilane (TEOS) and erbium nitrate as silica and erbium precursors, respectively.

The thin films prepared by sol-gel method were deposited onto commercial soda-lime slides of about 75 by 25 mm$^2$ and 1 mm thick. Soda lime glass is widely used in commercial and consumer products and processes. In addition, the utilization of glass substrates allows cost minimization due to their reduced prices and that the fabrication process can be performed at low temperatures.

For Laser Zone Melting process, the substrates used were $SiO_2$ glasses with cylindrical symmetry with respect to the optical axis with 1, 2 and 4.6 mm of diameter. Commercial raw powders of $Er_2O_3$, $Dy_2O_3$, $Yb_2O_3$ and $LiNbO_3$ were used as dopant elements to prepare suspensions in isopropyl alcohol. LZM has been proven as a suitable technique for surface modification and production of inorganic compounds coatings. Dysprosium (Dy) is normally not used for laser operation, although several studies have reported their use for laser action [172, 173]. It is a very interesting material as co-dopant for quenching the population in certain energy levels by energy transfer processes [174]. On the other hand, Lithium Niobate ($LiNbO_3$) has become a dielectric material used in a variety of applications including optical communications, electro-optic modulation and Q-switching of infrared wavelength [175–178].

## 4.4 Characterization techniques

In this section, the characterization techniques used in this work are shortly introduced. Thin films prepared by the sol-gel method were optically characterized by Spectroscopic Ellipsometry (SE) in order to determine their optical constants, thickness and porosity. The topography of selected films was conducted by means of Atomic Force Microscopy (AFM). Additionally, photoluminescence spectra from the $Er^{3+}$-doped films at room temperature were also measured. The doped glass rods prepared by LZM technique were analyzed by Scanning Electron Microscopy while the investigation of the refractive index profile across the transverse section was performed with Spectral Ellipsometry.

### 4.4.1 Spectral Ellipsometry

Ellipsometry is an optical and non-destructive technique that can provide significant insight into film structures. It is an accurate and powerful method that characterizes light reflection (or transmission) from samples [179–181] by measuring the change in polarized light upon light reflection (or light transmission). Ellipsometry was first developed by Drude in 1887 [182]. After Drude there was not much literature on ellipsometry mainly due to it was a very time consuming process and another characterization techniques was preferred instead. It was in the 1970s and 1980s when ellipsometry data acquisition became an automate process and its resolution was increased notably. Nowadays, ellipsometers are widely used in different research fields. They are commonly employed to characterize thin film optical constants, that is refractive index ($n$) and extinction coefficient ($k$), and thickness, as the response measure by the ellipsometer depends on optical properties and thickness of the sample. Nevertheless, it is also used to determine crystallinity, roughness, composition and other material properties associated with changes in light response from a material. Spectroscopic ellipsometry area of application has been expanded lately, as it has proven to be a process diagnosis tool on the atomic scale from real-time observation [183, 184]. However, ellipsometry measurements have two general restrictions, as surface roughness of samples has to be low, and the measurement must be performed at oblique incidence [181].

Ellipsometry presents important advantages as, for instance, that samples do not require any special preparation or environment and that are unaffected by the measurement process. Furthermore, it is a very exact and reproducible measuring method with very high thickness sensitivity ($\sim$ 0.1 Å), allows fast thin film thickness mapping and comprises a wide application area. The main disadvantages of ellipsometry measurements is that data analysis requires of an optical model defined by the optical constants and layer thicknesses of the sample and that the spatial resolution of the measurement provided because the spot size of a light beam used as measurement probe is typically several millimeters.

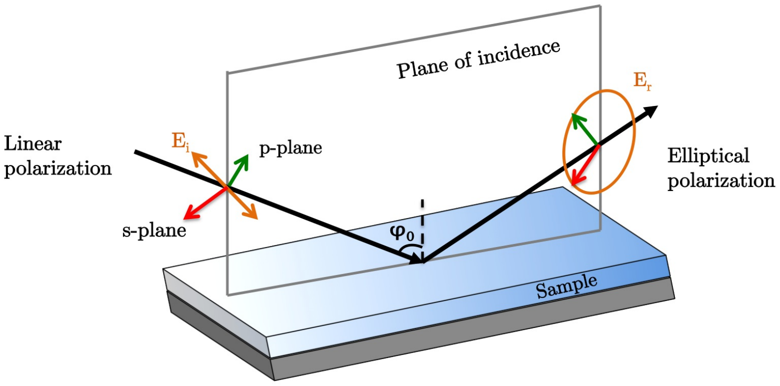

FIGURE 4.5: Schematic illustration of principle of ellipsometry.

Ellipsometry is therefore an indirect method for film characterization as it uses incident light of known polarization and measures changes in polarization of the reflected light. The polarization state is usually decomposed in a system of two orthogonal basis vectors $(p, s)$. The $p$-component oscillates parallel to the plane of incidence while the $s$-component oscillates parallel to the surface of the sample (see figure 4.5). Incident light used for ellipsometry measurements is usually linearly polarized and the reflected light presents elliptical polarization.The data acquired by the ellipsometer only yield the value of the sample of the two ellipsometric angles $\Psi$ and $\Delta$. These variables represent the polarization change experienced upon light reflection by the components of the electric vector parallel and perpendicular to the plane of incidence. $\Psi$ and $\Delta$ denote the amplitude ratio and phase difference between $p$- and $s$-polarized light waves. The ellipsometric angles are defined by the following relation (fundamental equation of the ellipsometry):

$$\rho = \frac{r_p}{r_s} = tan\Psi e^{i\Delta} \tag{4.5}$$

whereby $r_p$ and $r_s$ are the complex Fresnel reflection coefficient corresponding to the $p$- and $s$-polarized light waves, respectively.

As indicated before, ellipsometry does not directly measures thickness or optical constants, thus for data analysis is necessary to build up an optical model and fit the experimental data. The general steps for data analysis using ellipsometry is depicted in figure 4.6: i) measurement of experimental ellipsometric angles $\Delta$ and $\Psi$; ii) definition of an optical model defined by the optical constants and layer thicknesses of the sample; iii) fitting to measured $(\Psi,\Delta)$ spectra; and iv) generation of the final results.

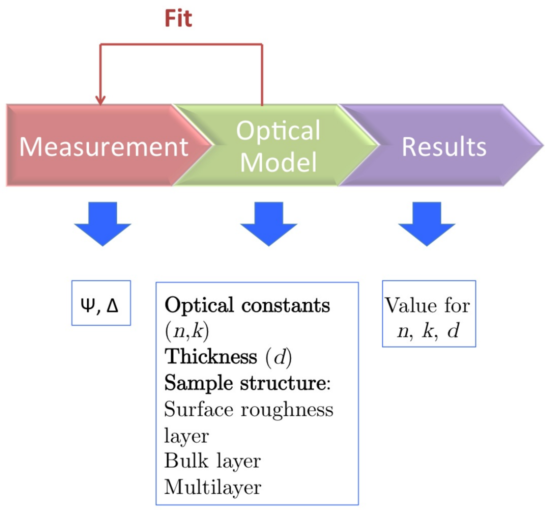

FIGURE 4.6: Ellipsometric data acquisition and analysis flow chart.

### 4.4.2 Atomic Force Microscopy

Atomic Force Microscopy is a characterization technique which allows to measure local properties, such as height, friction, magnetism, with a probe. The atomic force microscope is one kind of scanning probe microscopes (SPM). An AFM is rather different from optical or electron microscopes, because it does not form an image by focusing light or electrons onto a surface: to acquire an image, the AFM measures force between a probe (normally, a sharp tip) and the sample surface. An imaging microscope measures a two-dimensional projection of the surface of the material, which does not provide height information. Thus, with a traditional microscope such information must be inferred from the image or rotate the sample to see feature heights [185]. The AFM reaches a resolution far below the diffraction limit offered by the optical microscopy as light is not involved in recording the image. Its resolution is limited only by the tip radius and the spring constant of the cantilever. Though the lateral resolution of AFM is low ($\sim$ 30 nm) due to the convolution, the vertical resolution can be up to 0.1 nm. Basically, AFMs perform image acquisition by measuring the vertical and lateral deflections of the cantilever by using the optical lever. The optical lever consists of a laser diode beam that is focused on the back of the cantilever and bounces off reaching a position-sensitive photodetector photodetector consisting of four-quadrant photo-detector. The differences between the quadrants of signals indicate the position of the laser spot on the detector and thus the angular deflections of the cantilever.

AFM is very often compared to electron beam techniques such as the Scanning Electron Microscope (SEM) or Transmission Electron Microscope (TEM). On the one hand, AFM is able to image the sample in an ambient atmosphere and with no need of a prior treatment of the sample, while TEM and SEM require of a conductive sample (thus electrically insulating samples are usually coated with a thin layer of conducting material before imaging). These facts make AFM scanning quicker and in addition, artifacts introduced by vacuum drying or during the coating procedure can be avoided. However, AFM image recording is usually slower than at SEM, so if a large number of features on one sample are required, AFM may be considerably slower than SEM for the same sample. These techniques have a dimensional range rather similar, with SEM (usually) having a somewhat lower resolution to AFM, while the ultimate resolution of TEM is quite similar to that of AFM.

AFM can not only measure images as it has become an enabling technology for the measurement and manipulation of samples on the nanoscale. Other advantages of AFM technique are its high sensitivity and that its integration with other techniques is very simple. A powerful area of development for AFM is its combination with optical microscopy [186]. When AFM is combined with optical microscopy, a more complete study of biological samples can be done allowing a better comprehension of structure-function relationships. AFM has been integrated with different optical imaging techniques, including Confocal Laser Scanning Microscopy (CLSM) [187], Total Internal Reflection Microscopy (TIRFM)[188], Fluorescence Lifetime Imaging Microscopy (FLIM) [189], Reflection Interference Contrast Microscopy (RICM) [190, 191], Stimulated Emission Depletion Microscopy (STED) [192, 193], and Photo-Activated Light Microscopy (PALM) [194].

### 4.4.3 Photoluminescence

Photoluminescence (PL) can be defined as the spontaneous emission of light from a material under optical excitation. When incident light on a material has enough sufficient energy, photons are absorbed and electronic excitations are created. Eventually, the electrons return to the ground state if this relaxation is radiative, the emitted light is the photoluminescence signal [168]. PL is a non-destructive, simple and highly sensitive method to characterize materials that requires very little sample manipulation or environmental control. The instrumentation required for PL investigations basically consists on an optical source and an optical power meter or spectrophotometer. The radiation emitted by the sample is collected and dispersed by a monochromator and measured by a suitable detector, which transfers the signal for amplification and processing.

Photoluminescence in solid materials can be classified in two fundamental types, intrinsic and extrinsic PL[195]. The first type is an inherent property of the material, whereas in the second one the luminescent properties are due to dopants or impurities, generally denominated activators, incorporated to the material. Rare-earth elements are typical activators used in doped-glasses that can be investigated by PL techniques. As pointed out in section 4.3, Erbium is widely used in photonics devices and specially in optical communications due to its photoluminescence peak at ca. 1.5 $\mu$m. Figure 4.7 shows the Stark level manifolds of trivalent erbium ions and some common pump transitions and the corresponding laser transitions.

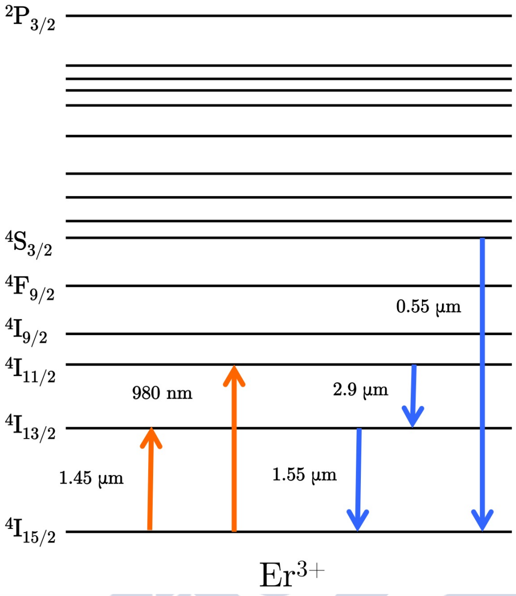

FIGURE 4.7: Energy level diagram for $Er^{3+}$ and common pump transitions (orange) and the corresponding laser transitions (blue).

### 4.4.4 Scanning Electron Microscopy

Scanning Electron Microscopy is an instrumental technique for high-resolution imaging of surfaces. It is widely used for both research and routine evaluation in materials science, the semiconductor industry, nanotechnology, and the biological and medical sciences, among other fields. Basically, the scanning electron microscopy method consists on focusing beam of high-energy electrons to generate a variety of signals at the surface of the target sample [196, 197]. The signals resulting from electron-sample interaction reveal a bunch of information about the properties of a sample, including external morphology (texture), chemical composition, and crystalline structure and orientation of materials making up the sample. As a result of the interaction of the primary electrons with the sample surface a number of different particles or waves are emitted (secondary electrons, back-scattered electrons (BSE), X-rays, Auger electrons. . . ). SEM microscopy detects and processes secondary electrons, the backscattered electrons and the X-rays. The secondary electrons emerge from the sample with an energy below 50 eV. The BSE are primary electrons that have been scattered by sample atoms and scape from the sample with energy similar to that of the incident electron stream. X-ray generation is produced by inelastic collisions of the incident electrons with electrons in discrete orbitals of atoms in the samples. The probed depth in Energy-Disperive X-ray analysis (EDX) is around 1-3 $\mu$m. The secondary and backscattered electrons are used for imaging samples: secondary electrons provide morphology and topography on samples while BSE are more valuable to illustrate contrasts in composition in multiphase samples. On the other hand, the X-rays give characteristic chemical information of the emitting atoms: yield X-rays with a characteristic wavelength, produced for each element in the sample that is excited by the incident electron beam.

In most applications, data are collected over a selected area of the surface of the sample, and a 2-dimensional image is generated that displays spatial variations in these properties. Areas ranging from approximately 1 cm to 5 microns in width can be imaged in a scanning mode using conventional SEM techniques [198]. The SEM is also capable of performing analyses of selected point locations on the sample; this approach is especially useful in qualitatively or semi-quantitatively determining chemical compositions, crystalline structure, and crystal orientations. Typically, a SEM has resolution of 5 nm.

SEM is a key characterization technique in the materials science and technology fields. Sample preparation depends on the nature of the samples and the data required and many applications require minimal preparation of the sample. Some limitations of SEM are that the target sample has to fit into the SEM chamber and some accommodation to prevent charge build-up on electrically insulating samples has to be performed. Electrically insulating samples are usually coated with a thin layer of conducting material, commonly carbon, gold, or some other

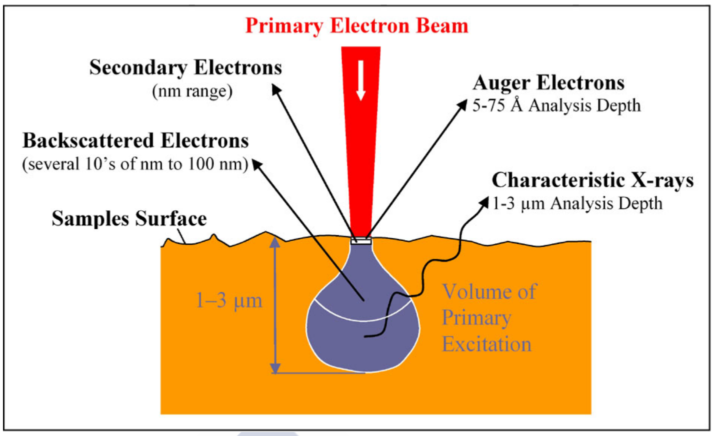

FIGURE 4.8: Interaction diagram of a stream of electrons focused at a material [199].

metal or alloy, depending on the data to be acquired. Carbon is most desirable if elemental analysis is a priority, while metal coatings are most effective for high resolution electron imaging applications. Alternatively, there exist instruments capable of "low vacuum" operation, which enables the analysis of electrically insulating samples without the need of conductive coating.

## 4.5 Experimental procedure and active GRIN media characterization

The following section describes the preparation of the doped sol-gel films and LZM glass rods. The technical description of the characterization performance for both fabrication process is also presented.

## 4.5.1 Thin film preparation by sol-gel process

### 4.5.1.1 Sol preparation

- *70MTES/30TISP sol*

A series of $Er^{3+}$-doped $70SiO_2$-$30TiO_2$ sols in the range 0–2.0 at.% of Er were prepared using methyltriethoxysilane (MTES, $CH_3Si(OCH_2CH_3)_3$, 98%, ABCR) and titanium isopropoxide (TISP, $Ti[OCH(CH_3)_2]_4$, 97%, ABCR) (precursors for silica and titanium, respectively) in acid environment. The preparation process was identical for all sols and conducted in two steps. Initially MTES was pre-hydrolyzed in the presence of HCl (0.1N) with ethanol as solvent. Then, this mixture was stirred for one hour. On the other hand, titanium isopropoxide was dissolved in ethanol and complexed by adding glacial acetic acid (AcH). After stirring for one hour, the two parts were then and distilled water was added drop by drop until hydrolysis is completed. Finally, erbium nitrate pentahydrate ($Er(NO_3)_3\cdot\ 5H_2O$, 99.9%, ABCR) is also added to the mixture, and maintained under stirring for one more hour. The sol was synthetised at ambient atmosphere and room temperature. The molar ratios used for the preparation of the sol with final concentration of 100 g/l are shown in table 4.2.

Table 4.2: Composition of the 70MTES/30TISP sol.

| **Composition** | **Molar ratios** |
|---|---|
| MTES/TISP | 70/30 |
| $H_2O$/Alcoxides | 1.5 |
| Alkoxides/AcH = 1 | 1 |

The same procedure was utilized to process $Yb^{3+}$-doped $70SiO_2/30TiO_2$ thin films with doping element nominal concentrations of 0, 0.3, and 1.0 at.%. In this case, ytterbium nitrate pentahydrate ($Yb(NO_3)_3\cdot\ 5H_2O$, 99.9%, ABCR) has been used as ytterbium precursor.

The synthesis route followed for the preparation of $Er^{3+}$ and $Yb^{3+}$-doped silica-titania layers is shown in figure 4.9.

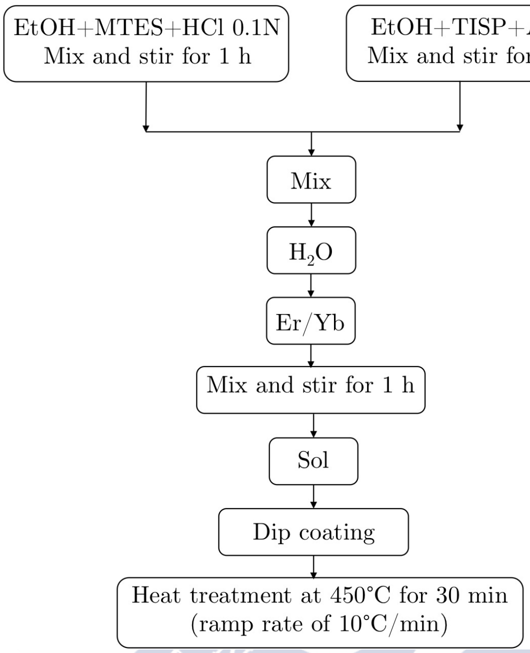

FIGURE 4.9: Flow chart of the preparation process for $Er^{3+}$ and $Yb^{3+}$-doped $SiO_2$-$TiO_2$ thin films.

- *60MTES/40TEOS sol*

$Er^{3+}$-doped silica glasses were prepared by sol gel technique with 0.3 and 1.0 weight percentage of the RE in the silica matrix. A two-step sol is prepared by adding water and acetic acid to the refluxed sol–gel process using tetraethoxysilane (TEOS, $Si(OCH_2CH_3)_4$, 99%, ABCR) and methyltriethoxysilane (MTES, $CH_3Si(OCH_2CH_3)_3$, 98%, ABCR) as silica precursors for the preparation of silica sol by hydrolysis and condensation reaction. First, TEOS and MTES was mixed with absolute ethanol and acidulated water (0.1 M AcH) was added drop by drop. Next, distilled water was incorporated to the solution. The sol was then refluxed in a water bath at 40°C under continuous stirring for 2 h. All steps were carried out under ambient atmosphere. The molar composition of the sol with final concentration 180 g/l is listed in table 4.3 and the flow chart followed for the preparation of $Er^{3+}$-doped silica films is illustrated in figure 4.9.

Table 4.3: Composition of 60MTES/40TEOS sol.

| **Composition** | **Molar ratios** |
|---|---|
| MTES/TEOS | 60/40 |
| $H_2O$/Alcoxides | 1.8 |
| Alcoxides/AcH = 1 | 4 |

Figure 4.10 represents the synthesis route followed for the preparation of $Er^{3+}$-doped silica layers using MTES ad TEOS as silica precursors.

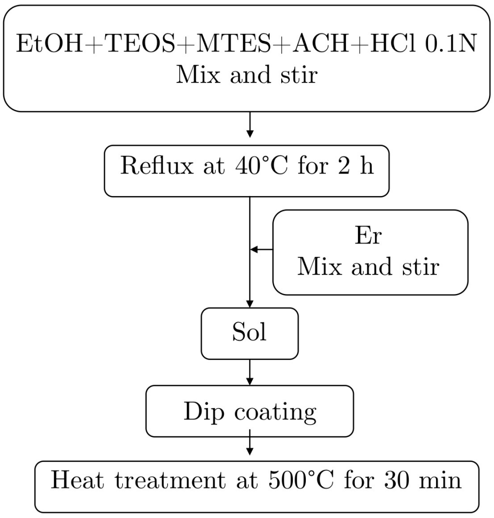

Figure 4.10: Flow chart of the preparation process for $Er^{3+}$-doped $SiO_2$ thin films using MTES and TEOS.

- *TEOS sol*

Tetraethoxysilane (TEOS, $Si(OCH_2CH_3)_4$, 99%, ABCR) was used as the precursor for the silica support. The two-step sol was prepared by mixing TEOS with pure ethanol (solvent) and stirred. In this first stage HCl

(0.1N) was added drop by drop. The acidic solution was stirred vigorously at 60°C under reflux for 90 min. Then, in the second stage of the preparation process HCl (0.1N) was added, drop by drop, and the sol was maintained at 40°C under reflux for 60 min. The sol was finally subjected to aging process for 48 h under stirring. Molar ratio HCl/TEOS = 4/1 was employed. The synthesis route followed for the preparation of $Er^{3+}$-doped silica layers using TEOS as silica precursor is depicted in figure 4.10.

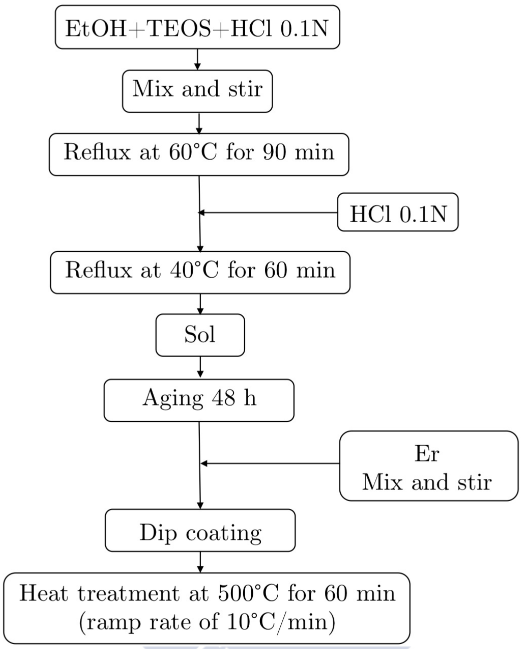

FIGURE 4.11: Flow chart of the preparation process for $Er^{3+}$-doped $SiO_2$ thin films using TEOS.

### 4.5.1.2 Film deposition by dip coating

Substrates were first washed in distilled water, dried and finally washed in ethanol. Films were deposited on well-cleaned commercial glass slides by dip coating technique using a withdrawal rate of 10, 20, 30, 40 and 50 cm/min. The dip coater equipment used to apply the range of coatings is shown in figure 4.12.

The deposited coatings were allowed to dry for several minutes before being removed for further thermal processing. After drying, the samples prepared with the 70MTES/30TISP sol were heat treated at 450°C for 30 minutes using a ramp rate of 10°C/min in air atmosphere. For MTES/TEOS sol, the coated samples were sintered at 500°C for 30 min, while those coatings prepared with the TEOS sol were sintered at 500°C for 60 minutes using a ramp rate of 10°C/min in air atmosphere. With sol-gel process coatings with high optical quality using low sintering temperature can be obtained. The decrease of the sintering temperature compared to conventional manufacturing process is crucial with a view to future industrial application.

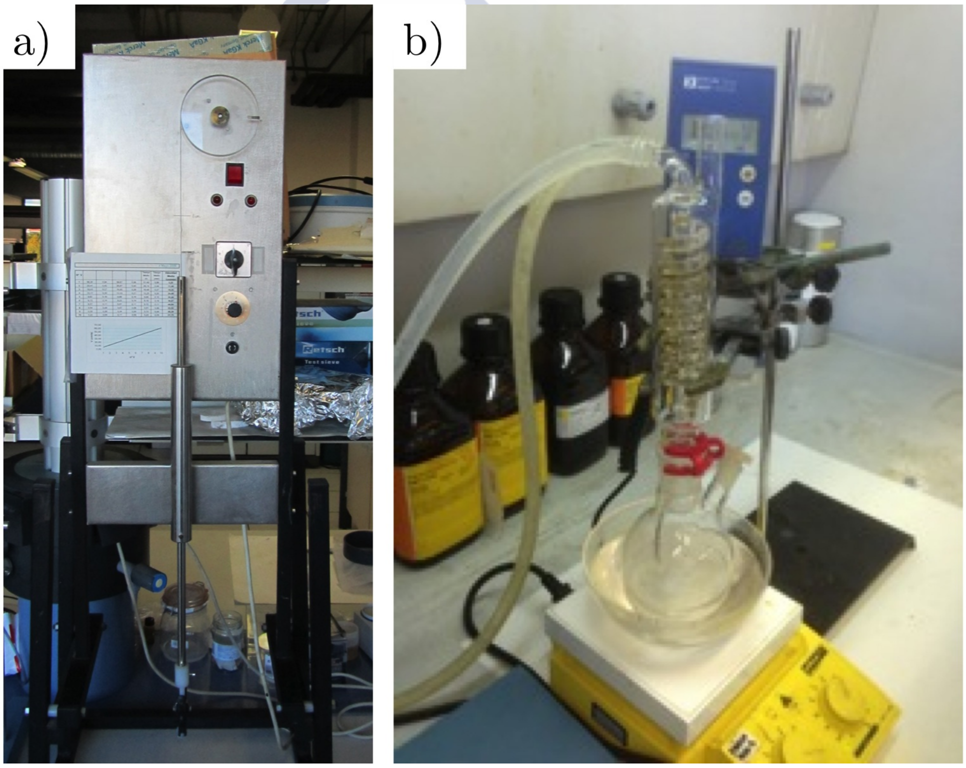

Figure 4.12: a) Dip coating system at *Instituto de Cerámica y Vidrio* (ICV-CSIC) and b) reflux setup.

### 4.5.2 Sample characterization

#### 4.5.2.1 Spectral ellipsometry

Ellipsometry measurements were performed using a Spectral Ellipsometer (M-2000UTM, J.A. Co., Woollam) shown in figure 4.13 at the *Instituto de Cerámica y Vidrio* (ICV) to characterize the films deposited onto commercial glass-slides. The spectra were taken in the wavelength range of 400 and 1000 nm at incident angles of 65, 70, and 75 degrees. All measurements were realized at the center of the samples. Here we will deal with the components of the complex index of refraction expressed as

$$N = n + ik \tag{4.6}$$

where $n$ is the real part of the refractive index, $i$ is the imaginary operator and $k$ is the imaginary part of the refractive index or the extinction coefficient. Hereafter, $n$ will denote the refractive index although that is, of course, acceptable only in case of loss-free or passive materials. The ellipsometric data were fitted using the WVASE32 software and Cauchy dispersion model [181, 200]. From the fitting of ellipsometric spectra, the optical constants $(n, k)$, and thickness $(d)$ of the sol-gel derived coatings were derived.

#### 4.5.2.2 Atomic force microscopy

The thin films obtained by dip coating immersion technique were examined by Atomic Force Microscopy (AFM). The experiments were performed using a Bruker Dimension Icon® Atomic Force Microscope, at the *International Iberian Nanotechology Laboratory* (INL). The microscope was operated under intermittent contact mode, also referred to as tapping mode, in air at a line scan rate of 1-2 Hz. The cantilever tip had a height of 10-15 $\mu$m and a radius of 10 nm. Typical cantilever resonance frequency varied between 350 and 367 kHz at

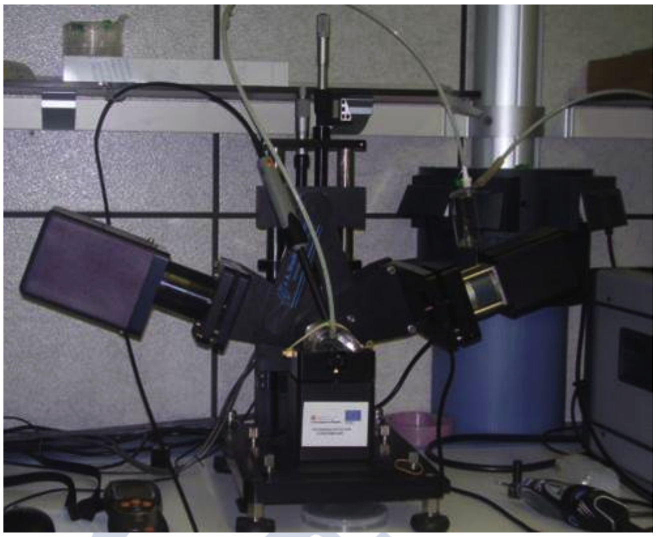

FIGURE 4.13: Spectral Ellipsometer (M-2000UTM, J.A. Co., Woollam) at the *Instituto de Cerámica y Vidrio* (ICV-CSIC).

a force constants between 20 to 80 Nm$^{-1}$. The images acquired were analyzed using Gwyddion software.

#### 4.5.2.3 Photoluminescence

Luminescence measurements of Er$^{3+}$-doped films were performed at room temperature with a single grating monochromator (focal length: 0.22 m), an infrared Hamamatsu H10330A-75 photomultiplier and standard lock-in techniques. The films were excited at 980 nm with a tunable Ti-sapphire ring laser, and the incident beam formed a 25 angle with the sample normal. The emitted light was collected along the direction perpendicular to the film. The measurements were carried out at the *Departamento de Física Aplicada I, Escuela Técnica Superior de Ingeniería de Bilbao, Universidad del País Vasco UPV-EHU.*

## 4.5.3 Laser Zone Melting

### 4.5.3.1 Sample preparation

Different inorganic compounds have been used as coating precursors in LZM process. In particular, $Er_2O_3$ (Metall, 99.9%), $Yb_2O_3$ (Metall, 99.9%), $Dy_2O_3$ (Aldrich, 99.9%) and and $LiNbO_3$ (Alfa Aesar, pureza 99,9995%) were used as starting materials and liquid suspensions media were prepared with isopropyl alcohol (PANREAC, chemical purity) with a solid content of 60% in weight. The coating of commercial $SiO_2$ rods was carried out by dip coating immersion technique utilizing a withdrawal rate of 7 mm/s.

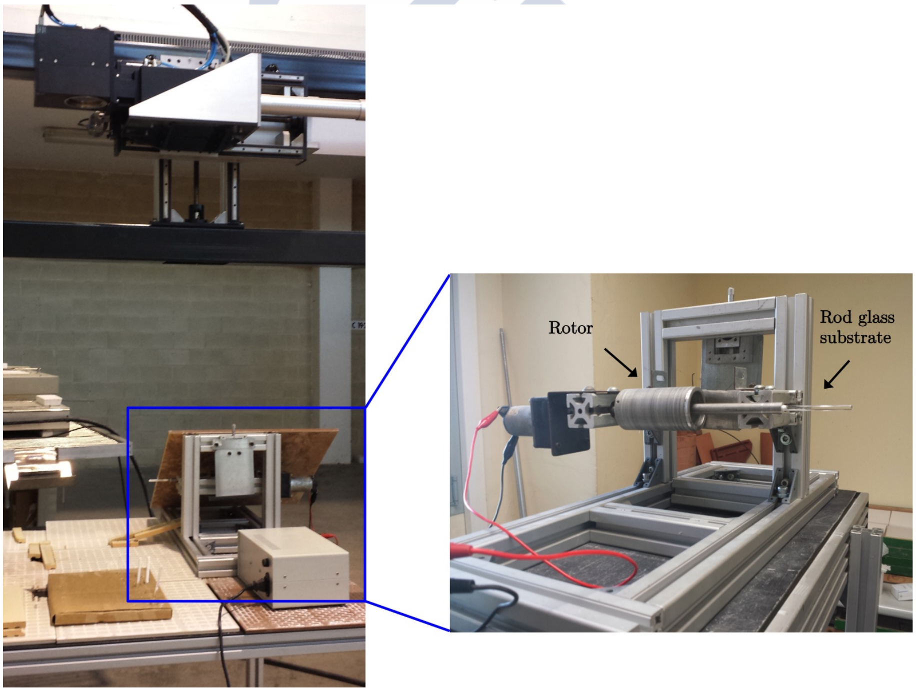

FIGURE 4.14: Experimental setup of the Laser Zone Melting process.

The coated samples were placed onto a rational stage moving at constant speed of rotation $\omega$ and irradiated at normal incidence using two types of $CO_2$ laser sources operating at 10.6 $\mu$m, as illustrated in figure 4.4. The output beam laser is displaced along the $SiO_2$ rod precursors with a galvanometer mirror system. LZM experimental setup is shown in figure 4.14. The laser power and rotation rate parameters were maintained constant during the process. Once the laser treatment was finished, the samples were allowed to cool down while rotating before their removal from the rotational stage.

Three different laser treatments were performed in order to realize a first evaluation of the most suitable precursors and processing parameters for the gradual diffusion of the doping elements in the glass rods. The processing parameters used for LZM are shown in tables 4.4, 4.5 and 4.6, where $w$, $v$, $d$, $I$, and $J$ are the rotation speed, the scanning speed, the laser line width, the irradiance and the fluence, respectively. The turns are the complete rotations of the rod. In the first and second treatment (LZM1 and LZM2) laser processing was carried out at ambient temperature ($T_a$), while for the third treatment (LZM3) the rotating rods were pre-heated in order to prevent failure due to thermal shock and assist the incorporation of the dopants on the substrate. LZM3 treatment was only performed for $LiNbO_3$-coated rods. For LZM1 and LZM3 a ROFIN-Sinar 350W SLAB-type laser source operated in Q-switched mode at 20 kHz was used, while a ROFIN DC025 SLAB $CO_2$ 2000W laser source operating in continuos mode with laser power fixed at 2 kW was used for all of the samples in LZM2.

Table 4.4: Processing parameters for LZM first treatment (LZM1) applied to 4.6 mm in diameter $SiO_2$ rods.

| **Process** | **T (°C)** | **$\omega$ (r.p.m)** | **v (mm/s)** | **d (mm)** | **Turns** | **I (MW/cm$^2$)** | **F (J/cm$^2$)** |
|---|---|---|---|---|---|---|---|
| LZM1.1 | $T_a$ | 3.33 | 17270 | 60 | 1 | 81.4 | 2.03 |

Table 4.5: Processing parameters for LZM second treatment (LZM2) applied to 1 and 2 mm in diameter $SiO_2$ rods.

| **Process** | **T (°C)** | **$\omega$ (r.p.m)** | **v (mm/s)** | **d (mm)** | **Turns** | **I (MW/cm$^2$)** | **F (J/cm$^2$)** |
|---|---|---|---|---|---|---|---|
| LZM2.1 | $T_a$ | 3.33 | 25000 | 388 | 2 | 5 | 2.39 |
| LZM2.2 | $T_a$ | 3.33 | 25000 | 388 | 2 | 10 | 4.78 |

TABLE 4.6: Processing parameters for LZM third treatment (LZM3) applied to 4.6 mm in diameter $LiNbO_3$-coated $SiO_2$ rods.

| **Process** | **T (°C)** | **$\omega$ (r.p.m)** | **v (mm/s)** | **d (mm)** | **Turns** | **I (MW/cm$^2$)** | **F (J/cm$^2$)** |
|---|---|---|---|---|---|---|---|
| LZM3.1 | 120 | 6.96 | 17320 | 170 | 10 | 90.35 | 2.259 |
| LZM3.2 | 120 | 6.96 | 17248 | 120 | 10 | 90.48 | 2.262 |
| LZM3.3 | 120 | 6.96 | 17170 | 80 | 10 | 90.62 | 2.266 |
| LZM3.4 | 120 | 6.96 | 12372 | 80 | 10 | 100.43 | 2.511 |
| LZM3.5 | 120 | 6.96 | 9825 | 60 | 10 | 106.55 | 2.664 |
| LZM3.6 | 120 | 6.96 | 9825 | 40 | 10 | 106.55 | 2.664 |

#### 4.5.3.2 SEM\EDX analysis

Microestructural characterization of the final samples prepared by LZM method was made in a scanning electron microscope (SEM, JEOL JSM 6400) equipped with an energy dispersive spectroscopy (EDX) system, at the *Aragón Materials Science Institute (ICMA-CSIC).*

#### 4.5.3.3 Spectral ellipsometry characterization

The spectroscopic ellipsometry measurements were performed with an AutoSE ellipsometer (HORIBA Scientific) at the *Departamento de Física, laboratório Associado CICECIO – Aveiro Institute of Materials e Instituto de Telecomunicações, Universidade de Aveiro.* For the data acquisition a total of 218 points in the wavelength interval from 450 to 850 nm, an incidence angle of 70° and a signal quality of 50 ms per point and an average of 20 measurements per point were considered. A measurement spot area of 250x250 $\mu m^2$ was used. Twenty measurements were performed along the sample radial direction. In figure 4.16 images of the sample surface for the selected measurement positions indicated in figure 4.15 are shown. The measurement area corresponds to the white squares in the image.

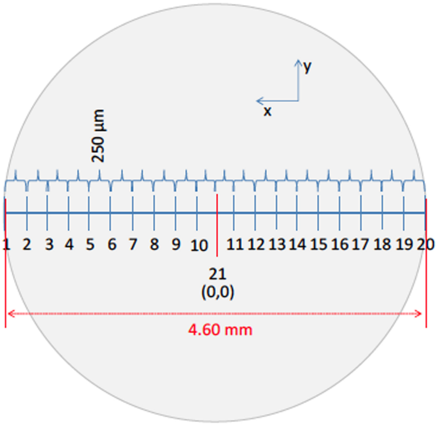

FIGURE 4.15: Scheme of the measurement points for determination of the refractive index along the glass rods radial distance.

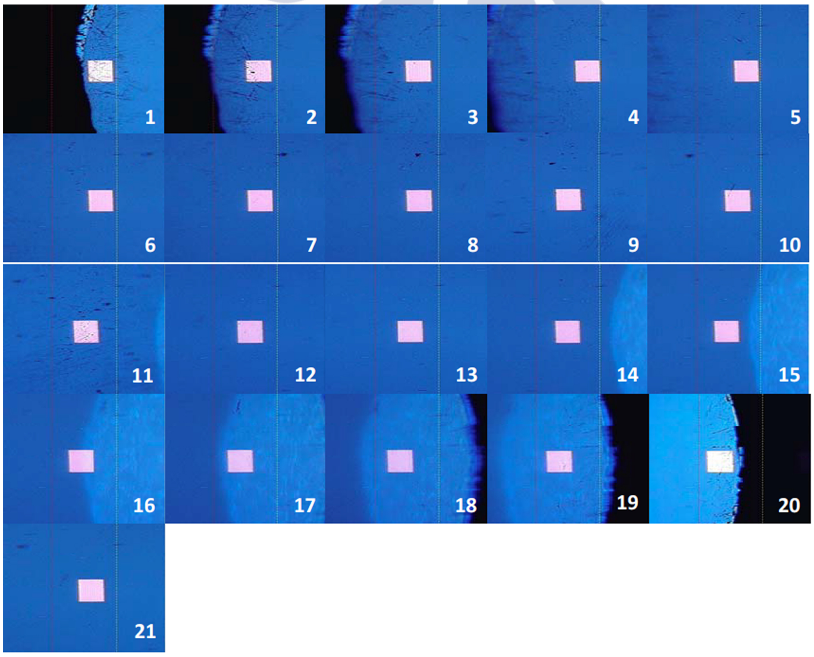

FIGURE 4.16: Images of the $LiNbO_3$-doped commercial silica rod sample surface for different positions. The measurement area corresponds to the white squares in the image (250x250 $\mu m^2$).

## 4.6 Results and discussion

The present section deals with the main findings obtained in this work. Selected samples prepared by sol-gel process and LZM technique are characterized in terms of their optical, morphological and compositional properties.

### 4.6.1 Sol-gel process

#### 4.6.1.1 Optical constants and porosity by Spectral Ellipsometry

The thickness of the undoped and Er and Yb-doped silica-titania films as function of the dopant nominal concentration derived from spectral ellypsometry measurements is shown in figures 4.17 and 4.18, respectively. As expected, the film thickness increases with the withdrawal speed in all cases, i.e. faster withdrawal speed yields thicker layers. Furthermore, the film thickness increases with increasing doping concentration. This effect was observed by Bruynoogue *et al.* in 1997 [201] and attributed to the increase of the sol viscosity with increasing Erbium concentration. Measured coating thicknesses are presented in table 4.7.

TABLE 4.7: Thickness of the Erbium and Ytterbium-doped films (in nm) as function of the withdrawal speed.

| **v(cm/min)** | **$SiO_2 - TiO_2$** | **0.3 at.%-Er** | **1 at.%-Er** | **0.3 at.%-Yb** | **1 at.%-Yb** |
|---|---|---|---|---|---|
| 10 | 175.5511 | 233.42 | 261.8382 | 257.8178 | 299.2726 |
| 20 | 253.0274 | 383.4222 | 405.9374 | 353.0033 | 386.3899 |
| 30 | 333.3354 | 504.4552 | 536.4889 | 421.4963 | 458.1186 |
| 40 | 388.5397 | 641.0907 | 666.3358 | 5196666 | 530.0701 |
| 50 | 438.4412 | 752.5503 | 802 | 576.4415 | 609.2828 |

The evolution of the refractive index with the wavelength of the undoped and Er-doped silica-titania films is presented in figure 4.19a). The representatives films selected for their study were deposited using a withdrawal rate of 20 cm/min

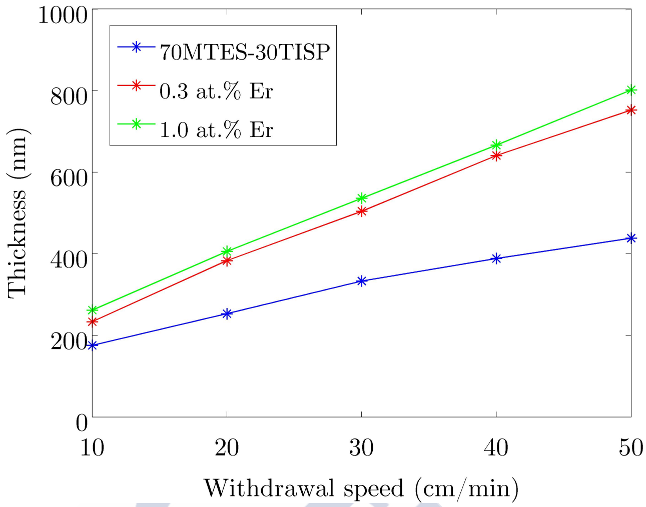

Figure 4.17: Thickness of the dip-coated Er-doped 70MTES/30TISP thin films versus withdrawal speed obtained with SE.

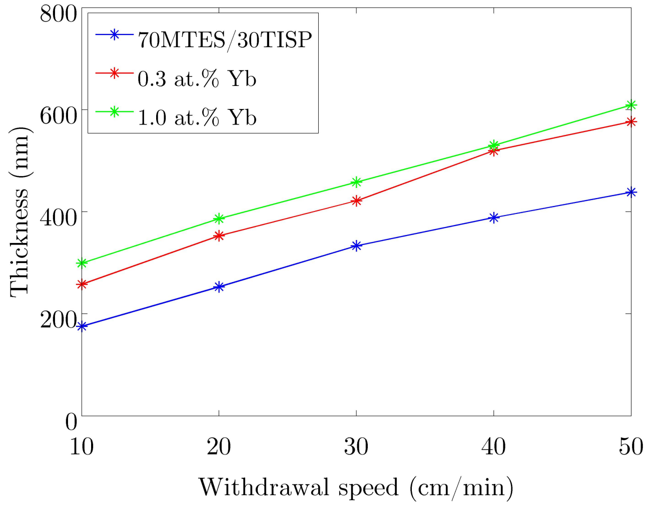

Figure 4.18: Thickness of the dip-coated Yb-doped 70MTES/30TISP thin films versus withdrawal speed obtained with SE.

for $SiO_2$-$TiO_2$ coatings and 10 cm/min for Er-$SiO_2$-$TiO_2$ coatings. Table 4.8 lists the different atomic percentage of erbium precursor used. The refractive index significantly decreases with increasing Er concentration but remains below to undoped $SiO_2$-$TiO_2$ film. This fact suggests that the porosity of the coating enhances with dopant concentration. At $\lambda = 633$ nm, refractive indexes of 1.612, 1.597, 1.571 and 1.529 were obtained for samples A, B, C and D, respectively.

TABLE 4.8: Erbium nominal concentration (at.%) in the 70MTES/30TISP sol.

| **Sample** | **Er (at.%)** |
|---|---|
| A | 0 |
| B | 0.3 |
| C | 1.0 |
| D | 2.0 |

Based on measured refractive index $n$, and assuming that the pores of the layer are filled up solely with air, their porosity percentage $\Pi$ can be determined using the following equation [202, 203],

$$\Pi = 1 - \frac{n_p^2 - 1}{n_p^2 + 2} / \frac{n_b^2 - 1}{n_b^2 + 2} \tag{4.7}$$

where $n_p$ and $n_b$ correspond to the refractive index of the reference film (the non-doped film in this study) and the refractive index of the erbium-doped film, respectively. Thus, porosity values of 2.0%, 5.4% and 11.25%, were determined as a function of dopant concentration for samples B, C and D.

The spectral dependence of extinction coefficient is represented in 4.19b). Positive values of $k$ in the wavelength range from 400 nm to 1000 nm are obtained, which are suitable for fabrication of an active GRIN media with loss by multilayering deposition. The behaviour of $k$ is similar for samples A, B and C. Nevertheless, a significant difference is evidenced for sample D, with the highest value of the extinction coefficient along the whole spectral range, which is most likely due to the disparity of the surface morphology compared to the other deposited samples.

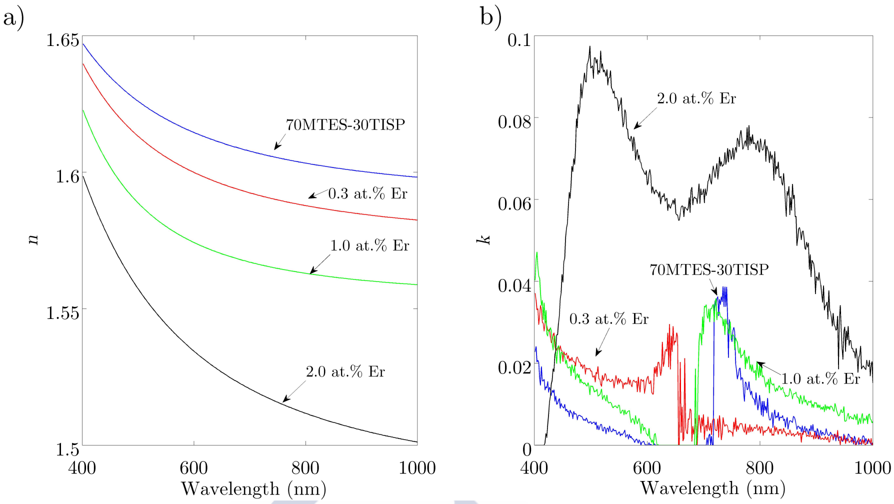

FIGURE 4.19: Ellipsometric measurements of the deposited sol-gel erbium-doped thin films compared to non-doped $SiO_2$-$TiO_2$ coatings: a) refractive index and b) extinction coefficient.

We analyze now the 0.3 and 1.0 at.% Yb-doped $SiO_2$-$TiO_2$ layers prepared by dip coating using a withdrawal rate of 10 cm/min (table 4.9). The pure silica coating has been deposited with a withdrawal rate of 20 cm/min. Ellipsometric measurements indicate that the thicknesses of the non-doped and Yb-doped samples are in the range from 230 to 300 nm. The refractive index decrease with wavelength is depicted in figure 4.20a). Besides, the refractive index diminishes with the increase of the dopant percentage, as happened with the Er-doped films. Results show that slightly lower refractive indexes are obtained with Yb dopant element, thus we have more porous films that in the Er-doped films. At $\lambda = 633$ nm refractive indexes of 1.579 and 1.547 were obtained for samples doped with a nominal concentration of ytterbium of 0.3 and 1.0 at.%, respectively. The relative porosity values of the films obtained as a function of dopant concentration was 5% and 10% for samples E and F, respectively. On the other hand, the extinction coefficient as function of wavelength and ytterbium concentration is illustrated in figure 4.20b). For the stronger doped film (sample F), $k$ is close to zero along the measuring wavelength interval, achieving its maximum value around 650 nm. The behaviour of the extinction coefficient is similar for the silica-titania film (sample A) and the 0.3 at.% Yb-doped silica film (sample F). For sample A $k$ reaches its maximum value at ca. 750 nm and it is slightly shifted to the right for sample F, reaching a maximum at approximately 800 nm.

TABLE 4.9: Ytterbium nominal concentration (at.%) in the 70MTES/30TISP sol.

| **Sample** | **Yb (at.%)** |
|---|---|
| E | 0.3 |
| F | 1 |

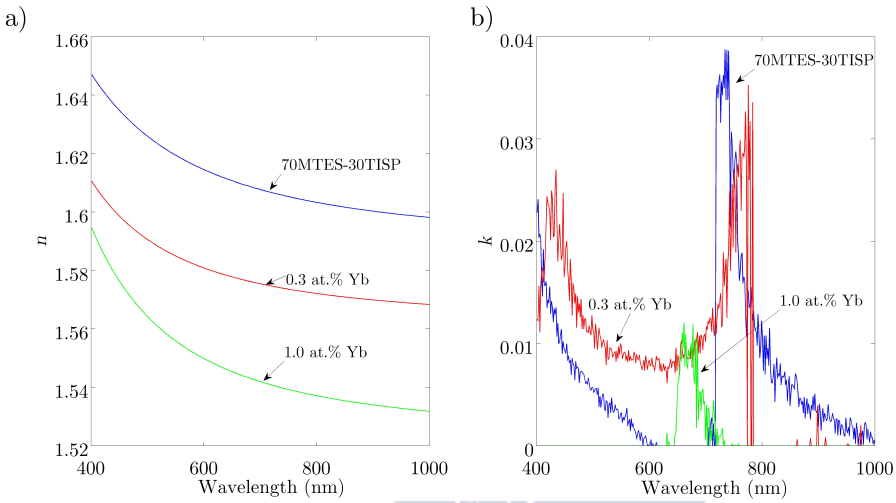

FIGURE 4.20: Ellipsometric measurements of the deposited sol-gel ytterbium-doped thin films compared to non-doped $SiO_2$-$TiO_2$ coatings: a) refractive index and b) extinction coefficient.

The thickness of the dip-coated layers prepared with 60MTES/40TEOS sol and TEOS sol as function of the withdrawal rate are given by figures 4.21 and 4.22, respectively. As follows from the figures, thickness increased linearly with increasing withdrawal rate at dip coating process. The maximum thickness values are obtained for the 1.0 at.% Er-doped 60MTES/T40EOS and TEOS sol-gel film. The difference in thickness among 0.3 and 1.0 at.% Er-doped 60MTES/40TEOS oscillates approximately between 200-300 nm; for

Er-doped TEOS coatings the values of the thickness are very close for both Er concentrations being the maximum difference in thickness almost 50 nm. 60MTES/40TEOS sol-gel coatings allows to obtain thicker doped films (from 700 to 2000 nm) than those prepared with TEOS (from 135 to 310 nm) and 70MTES/30TISP sol (from 175 to 800 nm).

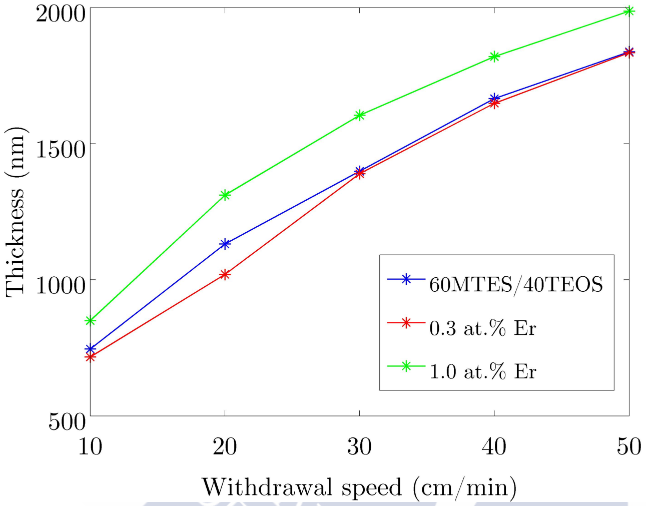

FIGURE 4.21: Thickness of the Er-doped 60MTES/40TEOS thin films versus withdrawal speed obtained with SE.

The refractive index as function of the wavelength of 0.3 and 1.0 at.% erbium-doped films prepared with 70MTES/30TISP, 60MTES/40TEOS and TEOS sols is depicted in figure 4.23. Er-doped 60MTES/40TEOS and TEOS films were deposited by dip coating using a withdrawal rate of 10 (table 4.10) and 40 cm/min (table 4.11), respectively. The graph shows that different refractive indexes can be prepared depending on the sol system and the concentration of the dopant. Er-doped silica films with refractive indices ca. 1.45 has been achieved using the TEOS as silicon dioxide precursor. Coatings with a low refractive index can be obtained via acid-catalyzed two-step sol-gel process using TEOS and MTES as silica precursors, while higher refractive indices are provided by the 70MTES/30TISP sol where the titania precursor was used to

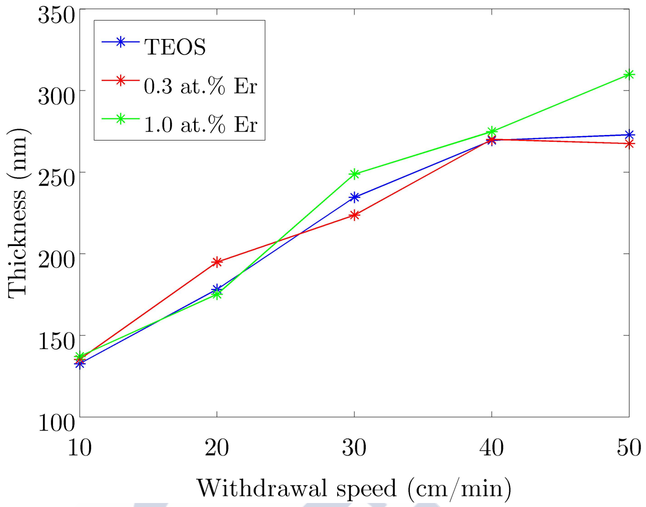

FIGURE 4.22: Thickness of the Er-doped TEOS thin films versus withdrawal speed obtained with SE.

increase the refractive index of the material. In all the systems considered higher erbium-dopant concentration yields to lower refractive indexes. The value of $n$ measured at $\lambda = 633$ nm for erbium concentration and sol system investigated is listed in table 4.12.

TABLE 4.10: Erbium nominal concentration (at.%) in the 60MTES/40TEOS sol.

| **Sample** | **Er (at.%)** |
|---|---|
| G | 0.3 |
| H | 1 |

TABLE 4.11: Erbium nominal concentration (at.%) in the TEOS sol.

| **Sample** | **Er (at.%)** |
|---|---|
| I | 0.3 |
| J | 1 |

TABLE 4.12: Thin films refractive indices at $\lambda = 633$ nm for the Er-doped sols.

| | **70MTES/30TISP** | | **60MTES/40TEOS** | | **TEOS** | |
|---|---|---|---|---|---|---|
| **Er (at.%)** | 0.3 | 1 | 0.3 | 1 | 0.3 | 1 |
| **n** | 1.597 | 1.571 | 1.337 | 1.334 | 1.443 | 1.432 |

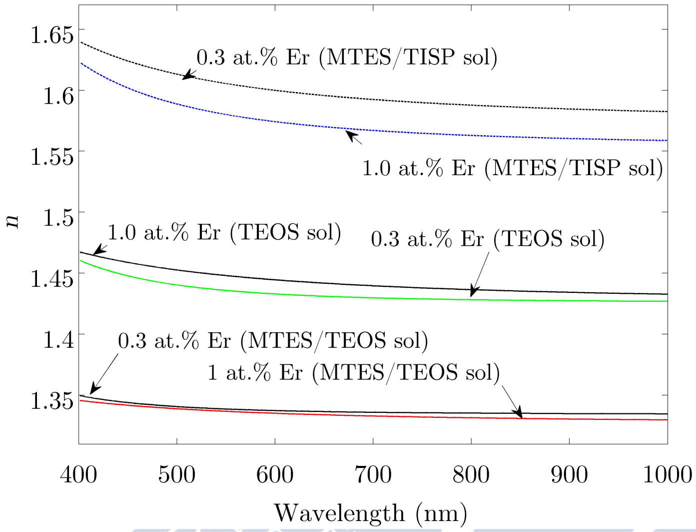

FIGURE 4.23: Refractive index of the Er-doped films prepared with 70MTES/30TISP, 60MTES/40TEOS and TEOS sols as function of the wavelength.

The extinction coefficients of the Er-doped films prepared with 60MTES/40TEOS and TEOS systems measured by SE are shown in figure 4.24a) and 4.24b), respectively. Nonzero $k$ values are obtained for the Er-doped 60MTES/40TEOS films. Both G and H samples show similar behaviour with important and almost alternate peaks and troughs. On the contrary, the Er-doped TEOS films have an extinction coefficient of zero except for the wavelength range from approximately 500 up to 700 nm, where light suffers from absorption.

The three systems studied indicate that a wide variety of RE-doped thin films

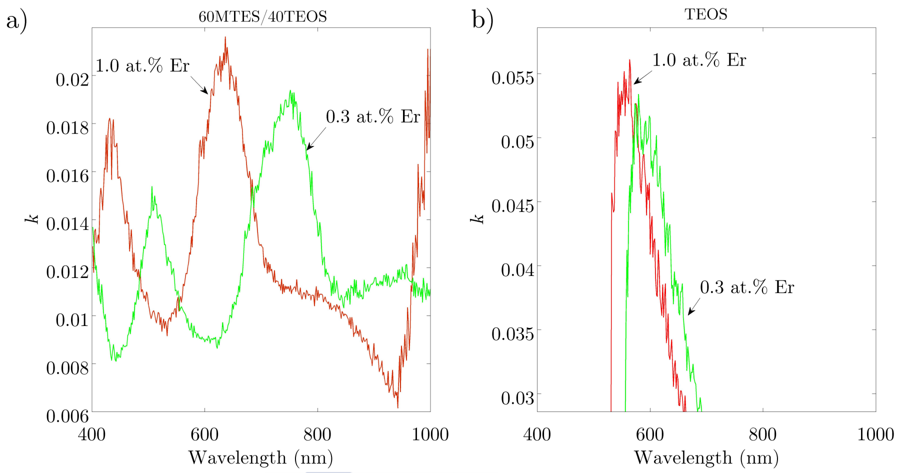

FIGURE 4.24: Extinction coefficient of the Er-doped films prepared with 60MTES/40TEOS and TEOS sols as function of the wavelength.

can be obtained by sol-gel chemical route. The main advantage of this process regarding active GRIN media preparation is the possibility to tailor the thickness and the optical constants of the films by modifying the parameters involved in sol-gel technique. The deposition of several consecutive layers are expected to yield to thicker custom-made structures with controlled complex refractive index for laser beam shaping.

#### 4.6.1.2 AFM morphological analysis of $Er^{3+}$ doped $SiO_2$-$TiO_2$ thin films

The topography of selected erbium-doped samples was studied using AFM technique. In particular, AFM images of non-doped and erbium-doped monolayers in atomic percentages in the range 0.3 to 2.0 at.%, deposited onto commercial glass slides by sol-gel dip coating and after annealing at 450°C, are shown in figures 4.25, 4.26, 4.27, and 4.28. From the topographical data, the most common roughness parameters, the arithmetic roughness ($R_a$) and the root mean square roughness ($R_q$ or $R_{rms}$), were evaluated [185]. Both parameters have a positive correlation, i.e., higher values mean greater topographical variation. While $R_a$ and $R_q$ describe the magnitude of the roughness-larger values correspond to rougher, surfaces-skewness ($R_{sk}$) and kurtosis ($R_{sk}$) describe the distribution of the sample height. Skewness ($R_{sk}$) is a measure of the average of the first derivative of the surface, i.e. the departure of the surface from symmetry. A negative value of this parameter indicates that the surface is composed of valleys, whereas a surface with a positive skewness is said to contain mainly peaks and asperities. Therefore, a negatively skewed surface is good for lubrication purposes. On the other hand, kurtosis describes the sharpness of profile peaks. A distribution with high kurtosis would have a small number of extreme heights (i.e. a few very high peaks or very low valleys), as opposed to many moderate height features (which will give lower, or negative kurtosis values).

The numerical values obtained for the scan samples have been listed in table 4.13, showing that smooth surfaces are obtained. The smallest surface roughness values were obtained for sample A (4.8). No significant change in the topography of the films from no-doped, 0.3% and 1.0%Er-$SiO_2$-$TiO_2$ films was observed during the visual inspection of AFM images. In general, the topography shows irregular granules of different shapes, sizes and separations. However, the doped film with 2.0% at. erbium (sample D) shows significant structural changes with respect to the other films. The AFM image shows a surface topography such as honeycomb structured porous. The pore size diameter was estimated to 250 nm. As a general feature exposed by AFM analysis, it can be appreciated that valleys, mountains and island clusters become higher as erbium concentration increases. In the latter figure we can see that the size and number of porous in sample D has notably increased in relation to samples A, B and C. This in good agreement with the SE results, where porosity of the coating enhancement with dopant concentration was observed.

In table 4.13 we can see that both the arithmetic roughness and root-mean-square have larger values as erbium concentration increases. $R_a$ and $R_q$ values also increase as function of the inspected scan area of the sample. For samples A, B and C, skewness has mostly positive values close to zero, which indicates a

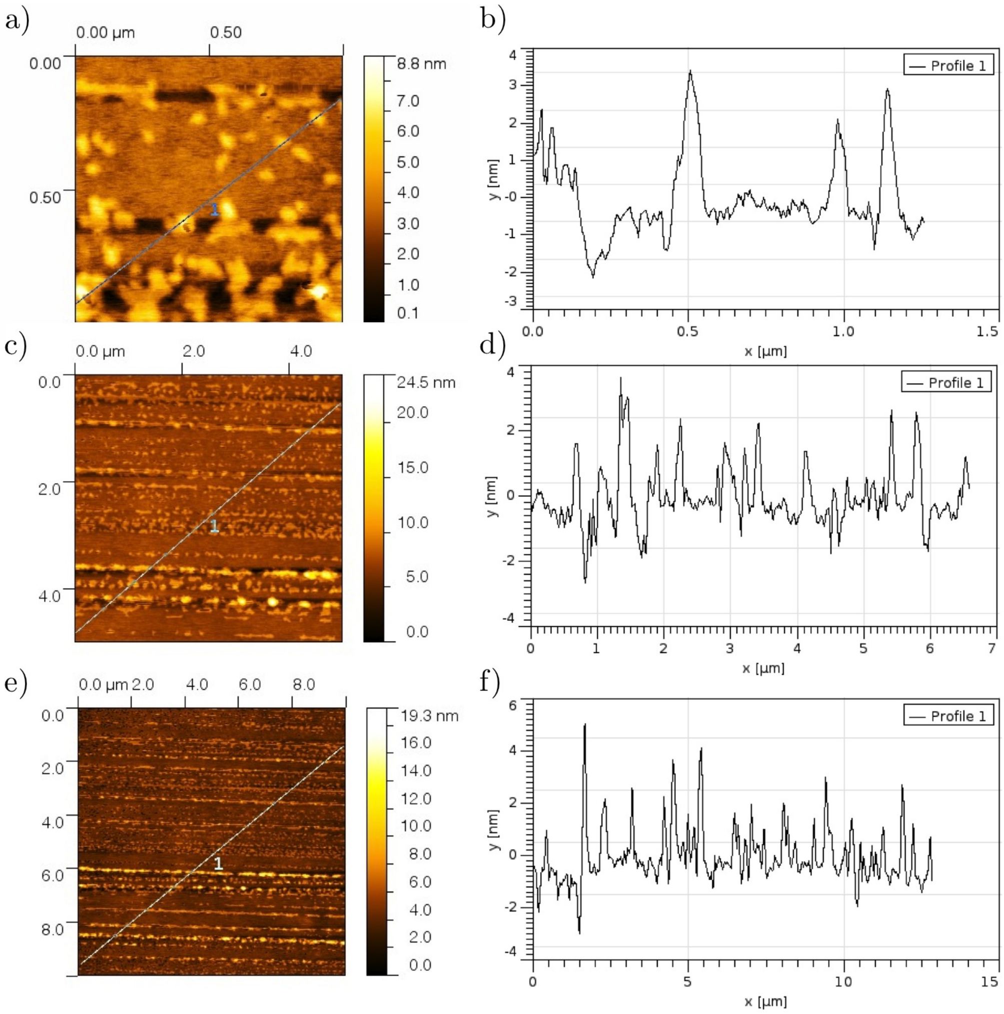

FIGURE 4.25: 2-D tapping mode in air AFM images of $SiO_2$-$TiO_2$ thin film prepared onto a commercial glass substrate by sol-gel dip coating for scan areas of 1 $\mu$m a), 5 $\mu$m c) and 10 $\mu$m e), and section profiles recorded along the grey line indicated b), d) and f).

surface with no accentuated protruding features. On the contrary, sample D has a negative skewness for all scan areas, meaning that there are pits or depressions in the surface. Kurtosis values provided are higher for samples A and D, showing that the surfaces have a small number of extreme heights, while samples B and

C have lower kurtosis values, meaning that there are moderate height features.

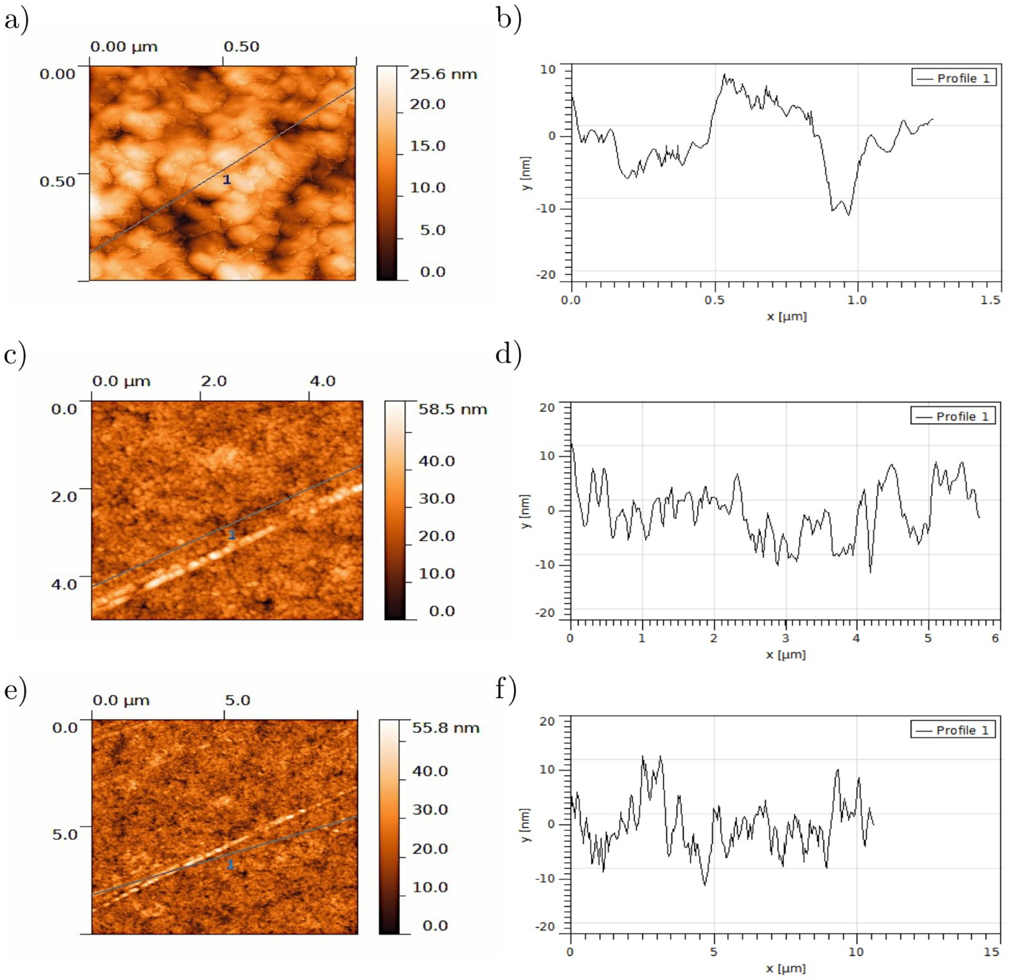

FIGURE 4.26: 2-D tapping mode in air AFM images of 0.3%-Er $SiO_2$-$TiO_2$ thin film prepared onto glass substrate by sol-gel dip coating for scan areas of 1 $\mu$m a), 5 $\mu$m c) and 10 $\mu$m e), and section profiles recorded along the grey line indicated b), d) and f).

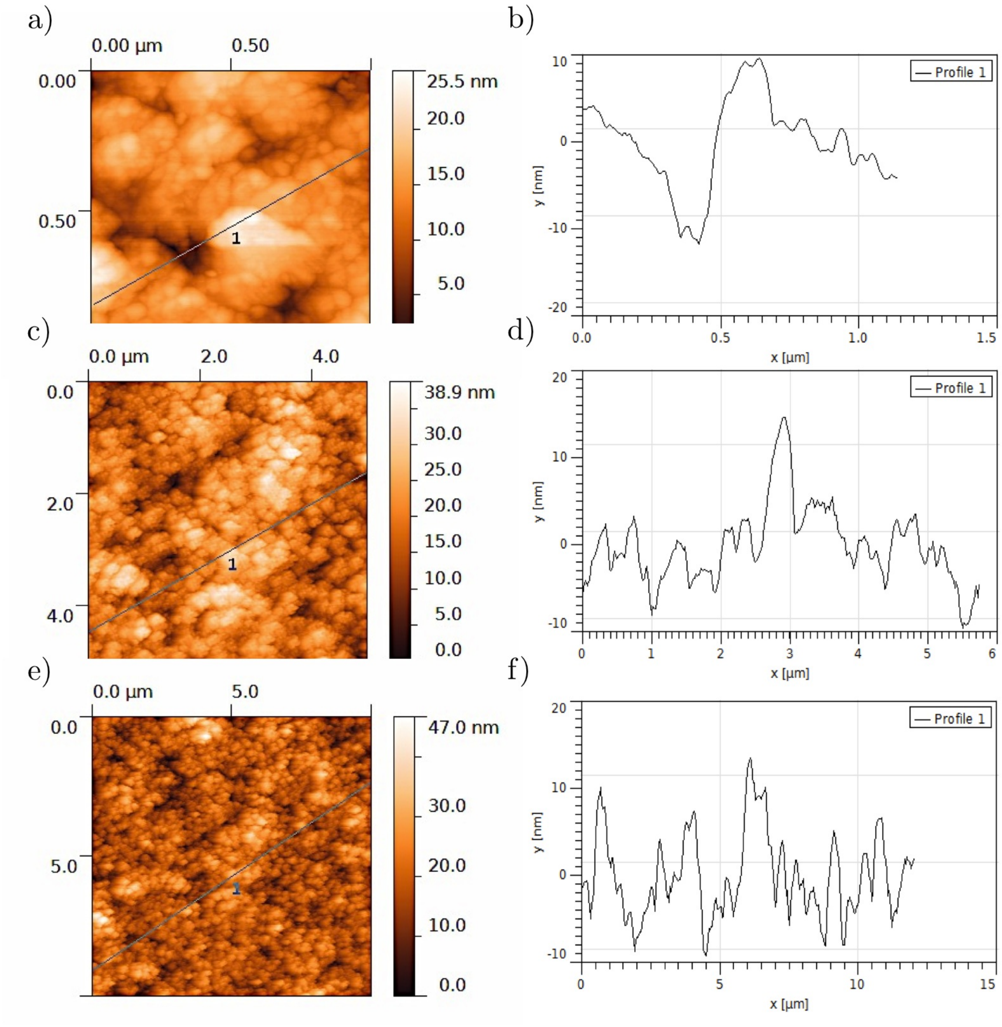

FIGURE 4.27: 2-D tapping mode in air AFM images of 1.0%-Er $SiO_2$-$TiO_2$ thin film prepared onto glass substrate by sol-gel dip coating for scan areas of 1 $\mu$m a), 5 $\mu$m c) and 10 $\mu$m e), and section profiles recorded along the grey line indicated b), d) and f).

The topographical features of representative erbium-doped silica films prepared with 60MTES/40TEOS and TEOS sols were also analyzed by AFM. Such cases are depicted in figures 4.29 and 4.30, respectively. Surface roughness of samples F and G was of $\sim$ 0.8 nm and $\sim$ 6 nm (arithmetic and RMS roughness data

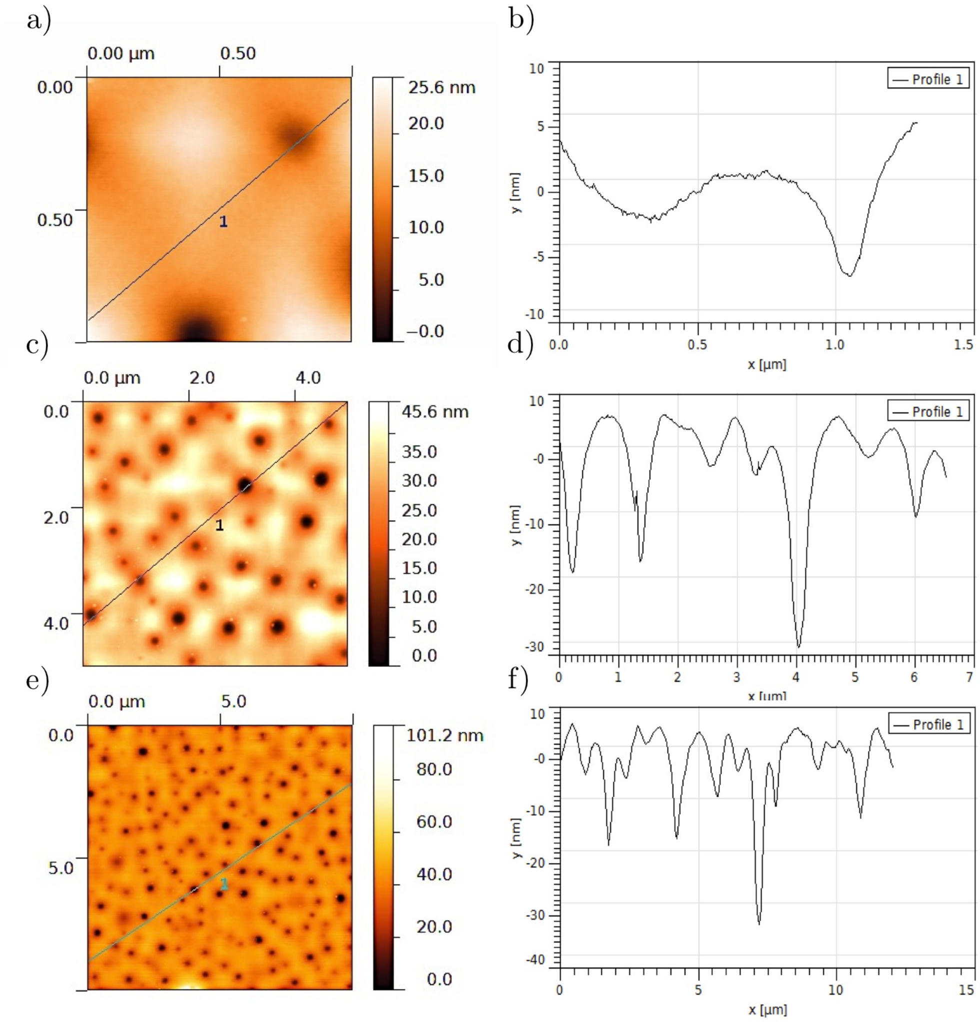

FIGURE 4.28: 2-D tapping mode in air AFM images of 2.0%-Er $SiO_2$-$TiO_2$ thin film prepared onto glass substrate by sol-gel dip coating for scan areas of 1 $\mu$m a), 5 $\mu$m c) and 10 $\mu$m e), and section profiles recorded along the grey line indicated b), d) and f).

listed in table 4.14 and shown in figure 4.29). Low kurtosis values have been obtained for both films, thus their surfaces present moderate height features. On the other hand, the small skewness values determined indicate that there are not prominent surface features. From visual inspection of AFM images we

Table 4.13: AFM arithmetic roughness ($R_a$), root-mean-square roughness ($R_q$), skew ($R_{sk}$), and kurtosis ($R_{ku}$) of the Er-doped $SiO_2$-$TiO_2$ films.

| **Er at.%** | **Scan size ($\mu$m)** | **Ra (nm)** | **Rq (nm)** | **Rsk** | **$R_{ku}$** |
|---|---|---|---|---|---|
| 0 | 1 | 0.702 | 1.008 | 0.432 | 1.99 |
|  | 5 | 0.82 | 1.28 | 2.41 | 11.7 |
|  | 10 | 1.11 | 1.55 | 1.57 | 6.91 |
| 0.3 | 1 | 3.16 | 3.90 | -0.103 | -0.261 |
|  | 5 | 3.88 | 5.25 | 0.818 | 2.96 |
|  | 10 | 3.53 | 4.67 | 0.548 | 2.28 |
| 1 | 1 | 2.6 | 3.46 | -0.168 | 0.61 |
|  | 5 | 4.19 | 5.31 | 0.121 | 0.027 |
|  | 10 | 4.06 | 5.25 | 0.42 | 0.908 |
| 2 | 1 | 2.15 | 3.08 | -0.991 | 3.59 |
|  | 5 | 4.10 | 5.74 | -1.55 | 3.93 |
|  | 10 | 4.14 | 5.81 | -1.36 | 5.57 |

can see that there exist an important structural change in sample G. In sample F different particle sizes (varying approximately between 20 and 40 nm) almost homogeneously distributed across the sample surface and somewhat spheroidal in form, but not completely spherical, are observed. On the contrary, in sample G larger particles are evidenced by AFM scan, reaching up $\sim 0.7\ \mu$m large when measured across the horizontal axis in figure 4.29.

Table 4.14: AFM data of the Er-doped $SiO_2$ films prepared with 60MTES/40TEOS sol.

| **Er at.%** | **Ra (nm)** | **Rq (nm)** | **Rsk** | **$R_{ku}$** |
|---|---|---|---|---|
| 0.3 | 0.779 | 1.036 | 1.43 | 2.62 |
| 1 | 5.97 | 8.03 | 0.951 | 0.795 |

Samples H and I correspond to 0.3 and 1.0%-doped silica coatings prepared with TEOS sol (table 4.11). In this case, surface roughness was of $\sim 0.2$ nm and $\sim 1$ nm (arithmetic and RMS roughness data listed in table 4.15 and shown in figure 4.30). The surface roughness is significantly lower than for Er-doped 60MTES/40TEOS coatings and relatively smooth, which is desirable for low surface scattering loss applications. The highest roughness values correspond to Er-doped 70MTES/30TISP films (samples C and D in tables 4.26 and 4.27).

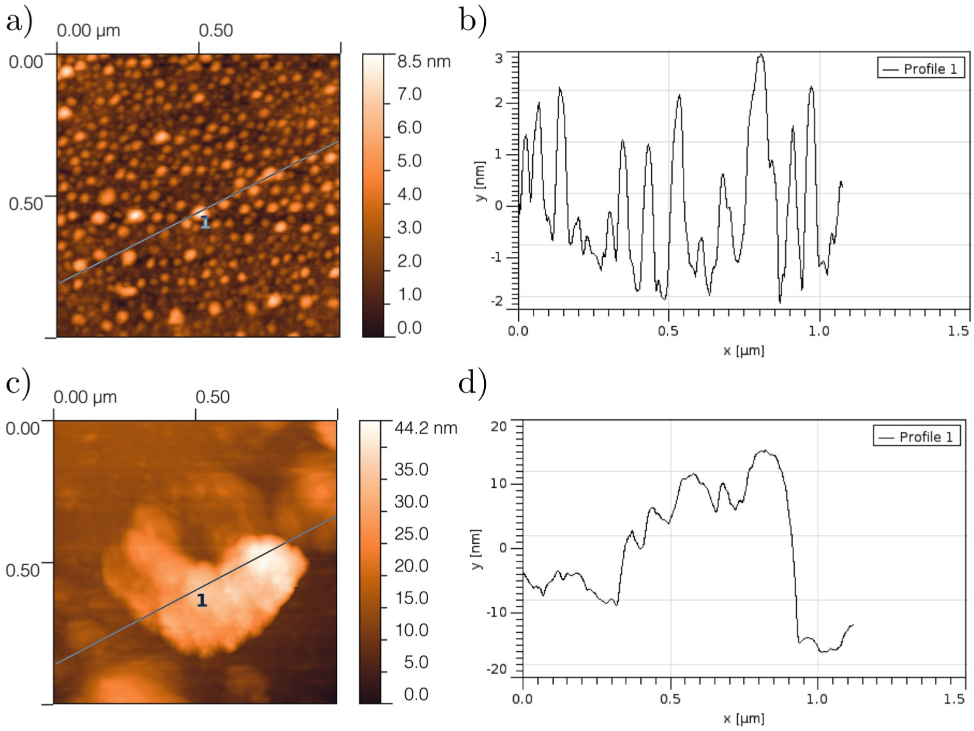

FIGURE 4.29: 2-D tapping mode in air AFM images of the 0.3 % (top) and 1.0%-Er (bottom) $SiO_2$ thin films prepared onto glass substrates with 60MTES/40TEOS sol for scan area of 1 $\mu$m. Section profiles recorded along the grey line are shown in b) and d) images.

The positive values of $R_{sk}$ for both samples suggest that the peaks and asperities are predominant over valleys. The most remarkable result corresponds to the large $R_{ku}$ value of sample H. This is due to the inclusion of particles of $\sim$ 90 nm size in the mostly homogeneous and smooth surface of the sample.

From the topographical analysis of the samples it can be concluded that in both erbium-doped 60MTES/40TEOS and TEOS sol systems roughness increases with RE concentration. The same trend is observed in samples prepared with the Er-doped 70MTES/30TISP sol system.

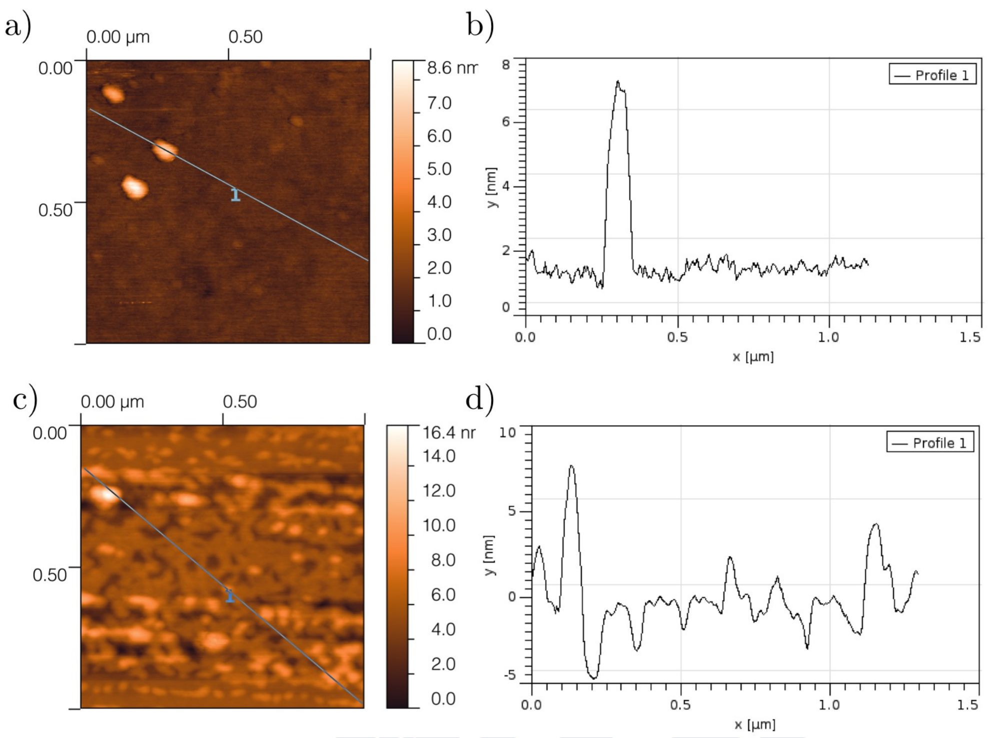

FIGURE 4.30: 2-D tapping mode in air AFM images of the 0.3 (top) and 1.0 at.%Er (bottom) $SiO_2$ thin films prepared onto glass substrates with TEOS sol for scan area of 1 $\mu$m. Section profiles recorded along the grey line are shown in b) and d) images.

TABLE 4.15: AFM data of the Er-doped $SiO_2$ films prepared with TEOS sol.

| **Er at.%** | **Ra (nm)** | **Rq (nm)** | **Rsk** | **$R_{ku}$** |
|---|---|---|---|---|
| 0.3 | 0.249 | 0.466 | 5.05 | 47.2 |
| 1 | 1.02 | 1.44 | 0.758 | 3.46 |

#### 4.6.1.3 Photoluminescence study of $Er^{3+}$ doped $SiO_2$-$TiO_2$ thin films

The normalized photoluminescence spectra of erbium-doped films (samples B, C, D, G, H, I and J) prepared using sol-gel process are shown in figure 4.31. The spectra were acquired using a excitation wavelength of 980 nm at room temperature. The $Er^{3+}$ emission bands in the infrared region at around 1.54 $\mu$m were assigned to the intra 4-$f$ transition (see figure 4.7) from the first excited state to the ground state ($^4I_{13/2} \rightarrow {}^4I_{15/2}$). The larger peak corresponds to the 2.0 at.% erbium-doped $SiO_2$-$TiO_2$ film. However, high pump power (600 mW) was required to acquire the PL spectra of the samples, even for the most prominent peak, indicating that emission signal is very weak.

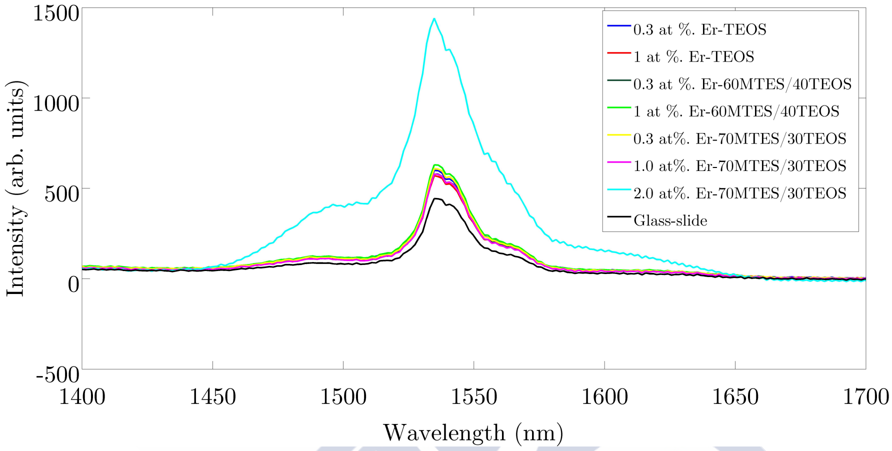

FIGURE 4.31: Photoluminescence spectra of $SiO_2$-$TiO_2$ and $SiO_2$ thin films with varying erbium concentrations. The excitation wavelength was 980 nm at a pump power of 600 mW.

Rather short luminescence lifetimes were observed during data acquisition for all samples. This problem is due to a combined effect of high energy exchanges between $Er^{3+}$ ions and high OH content [204]. One possible solution to this question is to increase the annealing temperature to reduce the number of OH impurities, yielding to enhanced luminescence lifetimes. It has also been reported that intensity of the PL in erbium-doped silica films can be increased by increasing the film thickness [205], whereas larger luminescence lifetime can be obtained if annealing is performed in vacuum [166].

### 4.6.2 Laser Zone Melting

#### 4.6.2.1 SEM\EDX characterization

The transverse cross sections of several $CO_2$ laser surface treated $SiO_2$ rods substrates of diameter 4.6 mm have been observed by SEM/EDX technique in order to evaluate their microstructure, chemical compatibility and compositional profile. The micrographs shown in figures 4.32-4.35 correspond to selected samples obtained with the processing parameters listed in table 4.4. These samples have been treated using a ROFIN-Sinar 350W SLAB-type $CO_2$ in Q-switch mode and a ROFIN DC025 SLAB $CO_2$ 2000W laser sources, operating at 10.6 $\mu$m. Two distinct regions can be appreciated in figure 4.32, where dysprosium dioxide was used as dopant-element: i) the Dy-coated outer part of thickness ca. 17 $\mu$m and ii) the inner part which corresponds to the unaffected core of the glass cylinder. The latter is basically the $SiO_2$ rod precursor. In this case, no diffusion of Dy within the rod substrate has been achieved. Some cracks appear close to the coating-substrate interface due to the laser heating process while within the original cylinder precursor several scratches can also be observed. Te latter is due to the polishing process of the samples performed after the LZM process and before their SEM/EDX characterization.

Similar results have obtained for Er and Yb as shown in figures 4.33 and 4.34. The incorporation of the dopant element has neither been achieved and micro-cracks have been generated with the LZM treatment. Now the thickness of the resulting coating has considerably increased as measured thickness is ca. 60 $\mu$m for the Er-coating and ca. 140 $\mu$m for the Yb-coating. It is important to note that the analysis of the compositional profile reveals the existence of the silicon (Si) element in the coating for the erbium case, meaning that there are diffusion from the substrate towards the coating (see figure 4.33). However, a different result is observed for $LiNbO_3$ as it has been incorporated within the silica cylinder precursor up ca. 50 $\mu$m. Cracking is still critical in the outer treated part and in the coating-substrate interface.

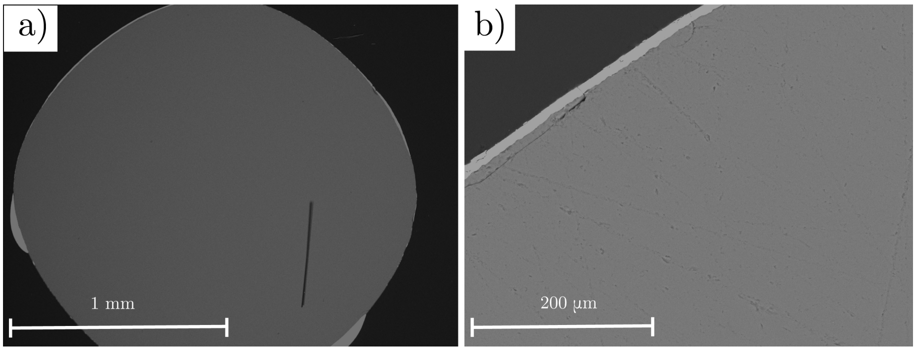

FIGURE 4.32: SEM micrographs obtained on a transverse cross section of $SiO_2$ rod coated with a suspension of $Dy_2O_3$ in isopropyl alcohol. The laser treatment was performed with a $CO_2$ laser operating in Q-switch mode at 20 kHz and room temperature (see data corresponding to LZM1 in table 4.4).

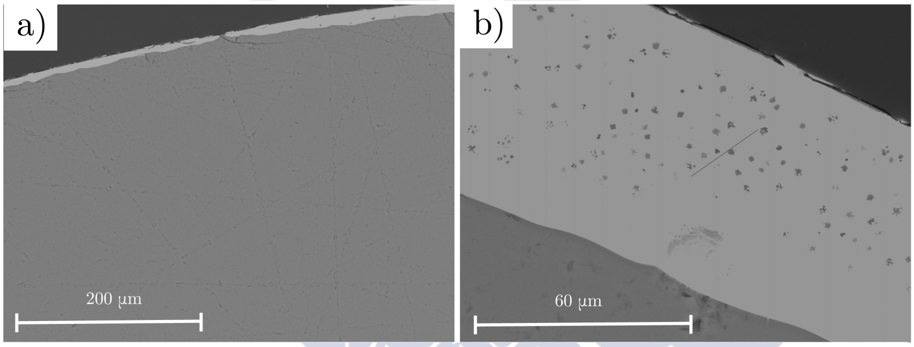

FIGURE 4.33: SEM micrographs obtained on a transverse cross section of $SiO_2$ rod coated with a suspension of $Er_2O_3$ in isopropyl alcohol. The laser treatment was performed with a $CO_2$ laser operating in Q-switch mode at 20 kHz and room temperature (see data corresponding to LZM1 in table 4.4).

Figures 4.36-4.39 show the cross sections SEM micrographs of samples treated under LZM2.1 and LZM2.2 process conditions (table 4.5). We have used glass rods of 1 and 2 mm of diameter as substrates; however, the treatment was only feasible for the 2 mm in diameter cylinder precursors given that the rods with diameter 1 mm resulted severely deformed under the laser action. The $CO_2$ laser was operated at 10.6 $\mu$m and 2 kW at ambient temperature for all samples. Consider figures 4.36a) and 4.36b), where SEM micrographs of the samples subject to LZM2.1 process are shown. In this instance two regions can

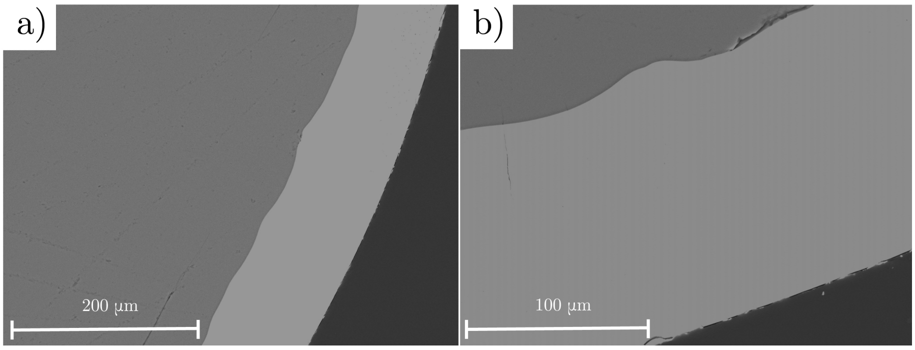

FIGURE 4.34: SEM micrographs obtained on a transverse cross section of $SiO_2$ rod coated with a suspension of $Yb_2O_3$ in isopropyl alcohol. The laser treatment was performed with a $CO_2$ laser operating in Q-switch mode at 20 kHz and room temperature (see data corresponding to LZM1 in table 4.4).

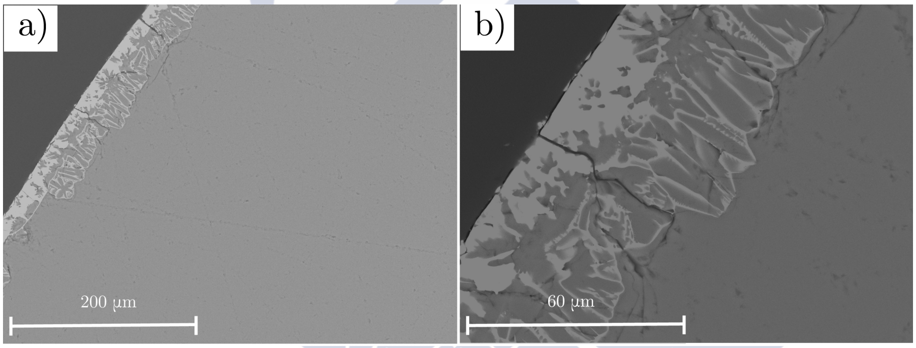

FIGURE 4.35: SEM micrographs obtained on a transverse cross section of $SiO_2$ rod coated with a suspension of $LiNbO_3$ in isopropyl alcohol. The laser treatment was performed with a $CO_2$ laser operating in Q-switch mode at 20 kHz and room temperature (see data corresponding to LZM1 in table 4.4).

be differentiated, the inner area corresponding to the glass rod substrate and the Dy-coating that has been deposited on the substrate. The Dy has not been incorporated to the $SiO_2$ rod as intended, but Si has been found in the coating which implies that part of Si of the substrate has migrated to the coating. Serious cracks appear on the sample, mostly due to sudden changes in temperature on the surface of the glass rods. On the other hand, gradual slight incorporation of Dy has been obtained applying LZM2.2 and surface cracks are practically inexistent. Such case is depicted in the figures 4.36c) and 4.36d).

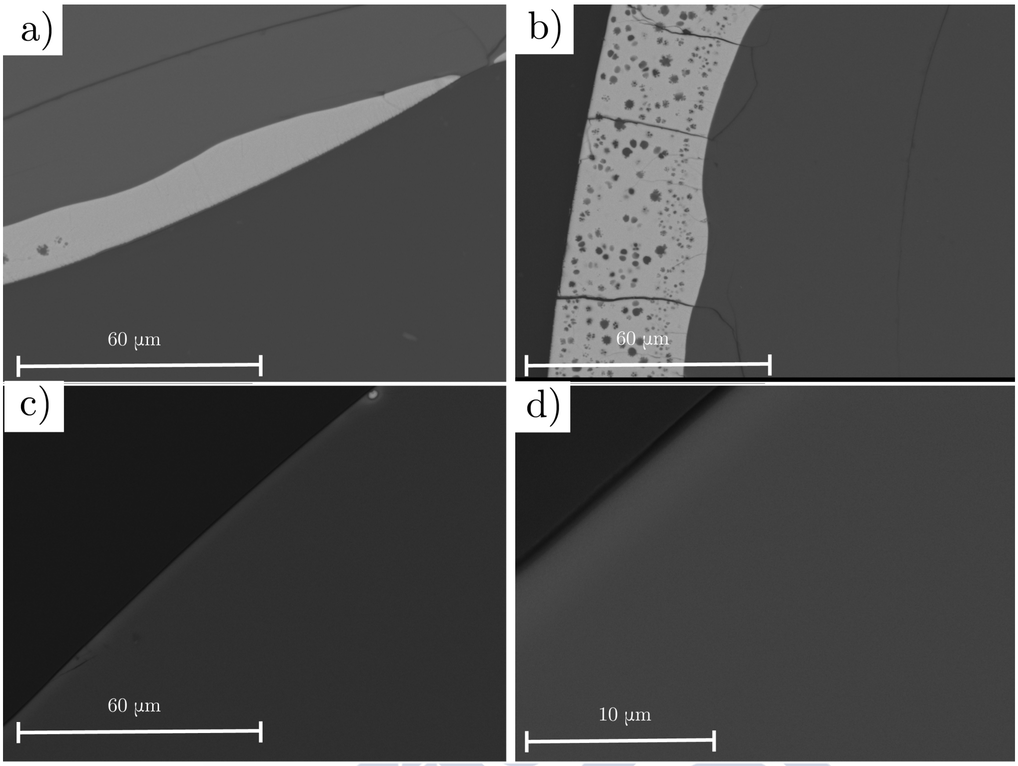

FIGURE 4.36: SEM micrographs obtained on a transverse cross section of $SiO_2$ rod coated with a suspension of $Dy_2O_3$ in isopropyl alcohol for: a), b) LZM2.1 treatment and c), d) LZM2.2 treatment. The sample processing was performed using a $CO_2$ laser with power fixed at 2 kW and room temperature (see data corresponding to LZM2 in table 4.5).

Similar results have been obtained for Er and Yb-coatings, as follows from figures 4.37 and 4.38. In both cases, a coating has been deposited on the precursor $SiO_2$ glass cylinder and compositional analysis reveals that diffusion of Si towards the coating took place. This effect is more pronounced for the erbium-coating case. The same tendency is observed for both LZM2.1 and LZM2.2 treatments. If the glass cylinder is coated with the erbium suspension a coating of thickness ca. 20 coating $\mu$m is achieved on either laser heat experiment, while when using the ytterbium dioxide suspension the coating obtained is approximately of 10 $\mu$m thick.

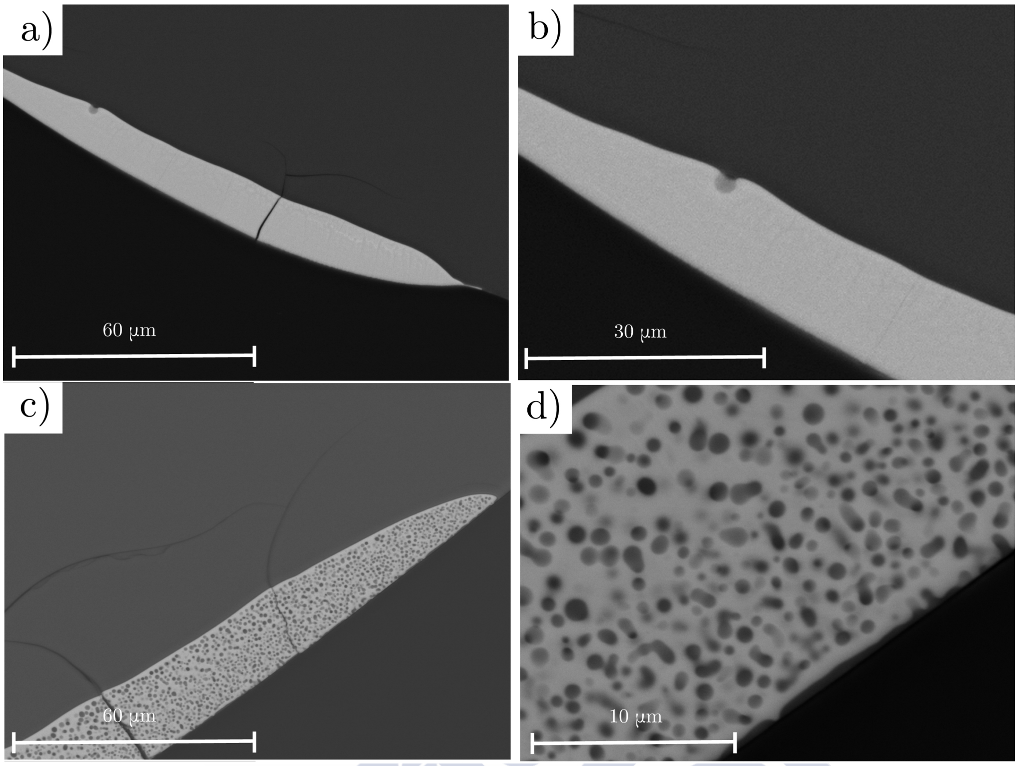

FIGURE 4.37: SEM micrographs obtained on a transverse cross section of $SiO_2$ rod coated with a suspension of $Er_2O_3$ in isopropyl alcohol for: a), b) LZM2.1 treatment and c), d) LZM2.2 treatment. The sample processing was performed using a $CO_2$ laser with power fixed at 2 kW and room temperature (see data corresponding to LZM2 in table 4.5).

On the other hand, the diffusion of $LiNbO_3$ in the $SiO_2$ rod substrate has been possible with LZM2 process, as shown in figure 4.39. For the less energetic treatment (LZM2.1), the dopant has penetrated in the substrate approximately 50 $\mu$m although the diffusion is not homogenous. This fact is reflected in figures 4.39a) and b). On the contrary, as can be seen from figures 4.39c) and d), for the LZM2.2 process a smooth diffusion of the dopant within the $SiO_2$ of ca. 17 $\mu$m has taken place. Cracks can be observed in both LZM2.1 and LZM2.2 treatments, although in the latter they have been reduced significantly.

SEM micrographs obtained for LZM3.6 is shown in figure 4.40. The parameters

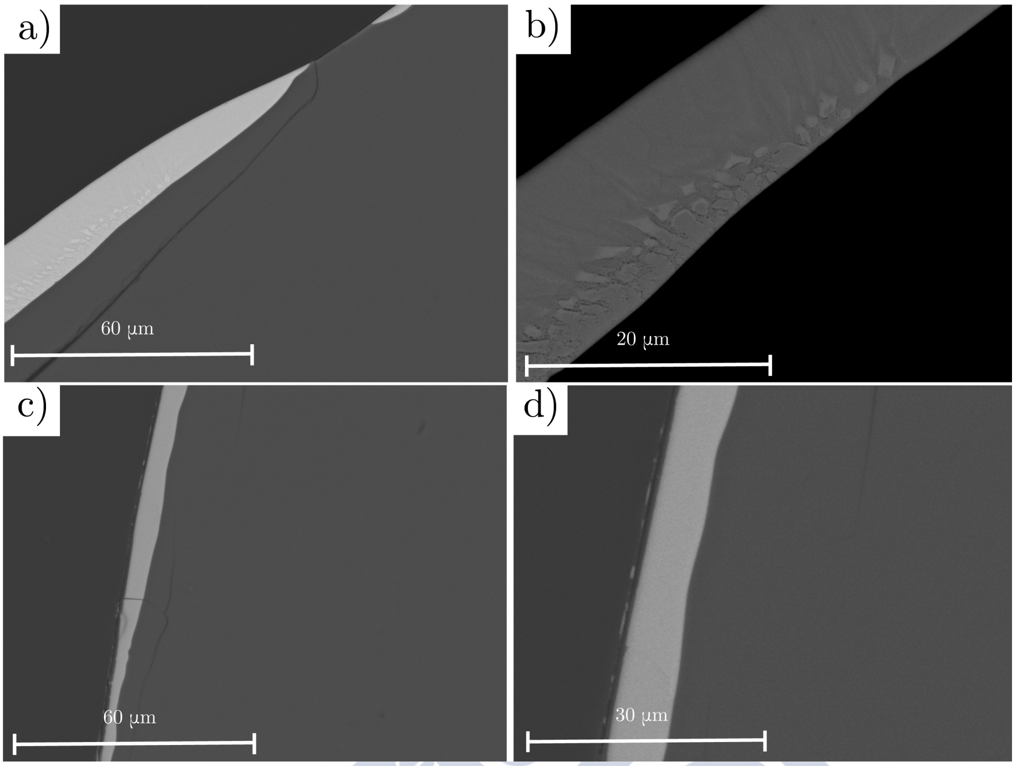

Figure 4.38: SEM micrographs obtained on a transverse cross section of $SiO_2$ rod coated with a suspension of $Yb_2O_3$ in isopropyl alcohol for: a), b) LZM2.1 treatment and c), d) LZM2.2 treatment. The sample processing was performed using a $CO_2$ laser with power fixed at 2 kW and room temperature (see data corresponding to LZM2 in table 4.5).

of the process can be seen in table 4.6. In this instance, $LiNbO_3$-coated $SiO_2$ glass rods were treated with the ROFIN-Sinar 350W SLAB-type $CO_2$ laser in Q-switched mode operating at 10.6 $\mu$m. The glass cylinder precursors were pre-heated at 120°C and laser treatment was also carried out at 120°C. Only the LZM3.6 results are shown as this turned out as the only treatment among all those performed that generated transparent samples. As can be observed from the figure, a crack-free material has been obtained and three regions can be distinguished: i) the outermost region of the glass rod; where homogeneous diffusion occurs; ii) a region with non-homogeneous diffusion; and iii) the unaffected by diffusion process core of the $SiO_2$ rod. The $LiNbO_3$ is diffused

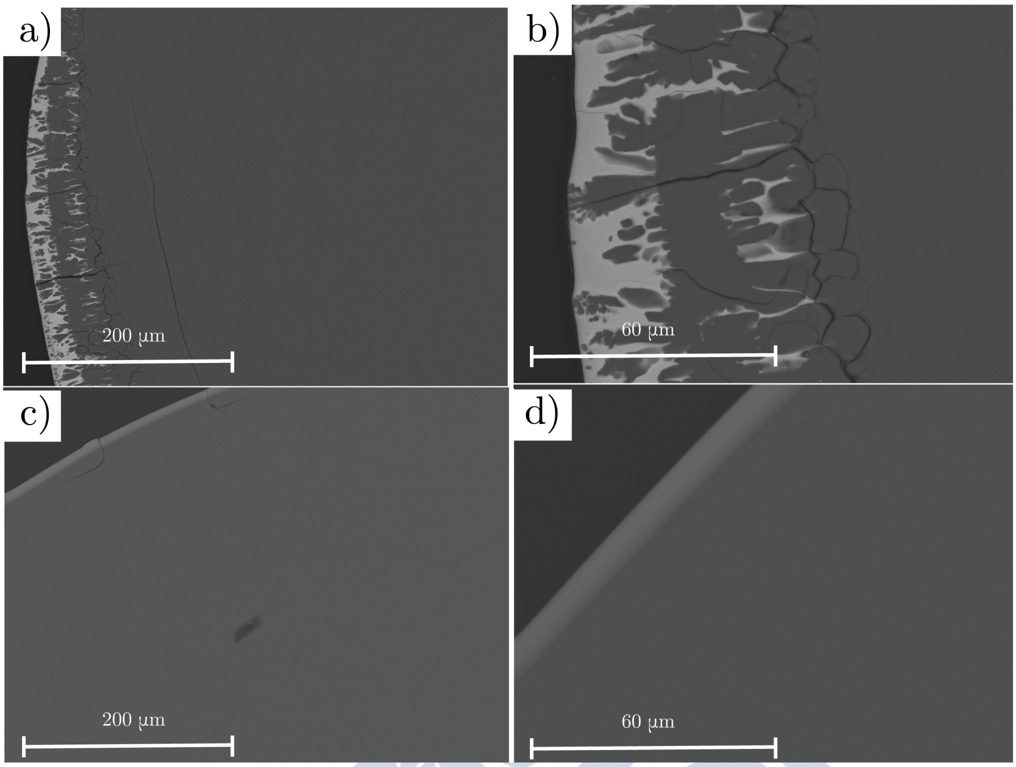

FIGURE 4.39: SEM micrographs obtained on a transverse cross section of $SiO_2$ rod coated with a suspension of $LiNbO_3$ in isopropyl alcohol for: a), b) LZM2.1 treatment and c), d) LZM2.2 treatment. The sample processing was performed using a continuos $CO_2$ laser with power fixed at 2 kW and room temperature (see data corresponding to LZM2 in table 4.5).

in an area of thickness ca. 10 $\mu$m.

#### 4.6.2.2 Spectral Ellipsometry results

The doped commercial silica rods were obtained by means of Spectral Ellipsometry in order to investigate changes in refractive index profile across their transverse section. The refractive index evolution with position along the radial distance in $SiO_2$ glass rods of diameter 4.6 mm treated with the processing parameters of LZM1 collected in table 4.4 are shown in figures 4.41-4.44. The refractive index is presented for $\lambda$ = 630 nm and $\lambda$ = 740 nm

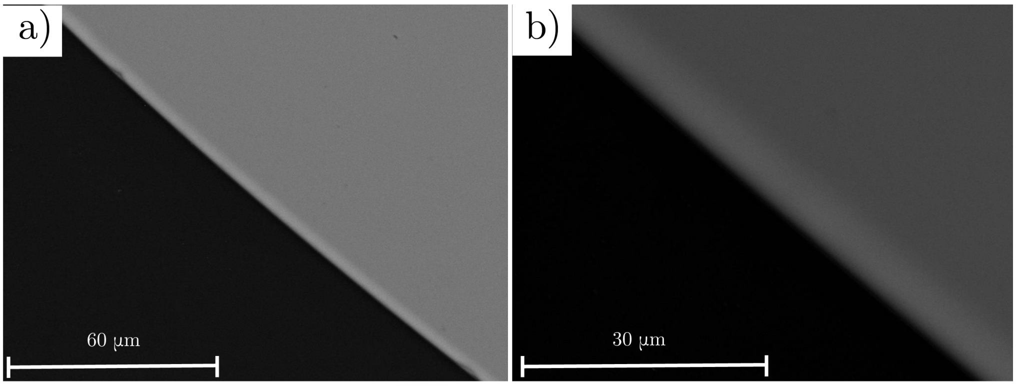

Figure 4.40: SEM micrographs obtained on a transverse cross section of $SiO_2$ rod coated with a suspension of $LiNbO_3$ in isopropyl alcohol. The laser treatment was performed with a $CO_2$ laser operating in Q-switch mode at 20 kHz. The glass cylinder precursors were pre-heated at 120°C (see data corresponding to LZM3 in table 4.6).

in the graphs labelled as a) and b), respectively. The obtained results suggest that a gradient of refractive index has been generated in the silica rods most likely due to laser action. This modification of the refractive index occurs in all the cases considered. According to the figures, the refractive index at the edges of the glass rods have increased with respect to the index at the core of the substrate. The measured refractive index at $\lambda = 740$ nm for dysprosium, erbium, ytterbium, and lithium niobate doping elements is shown in figures 4.41, 4.42, 4.43, and 4.44 with approximately 0.02, 0.014, 0.026 and 0.031 refractive index increase, respectively. The gradual index variation is more pronounced for the $LiNbO_3$-doped $SiO_2$ cylinder, where a higher ion diffusion was revealed with SEM/EDX characterization (see figure 4.35).

The results generated by SE are promising; nevertheless, more ellipsometric measurements must be performed in order to increase the accuracy of the final results comprising that the measurements should be repeated taking several independent acquisitions in each point, the use of a dispersion model to describe the raw data is advisable, the measurement should also be performed along distinct radial direction lines and a smaller measurement spot data can be considered to increase spatial resolution. Besides, the surface of the measured samples was not perfectly flat, therefore the polishing process must be optimized before new data acquisition.

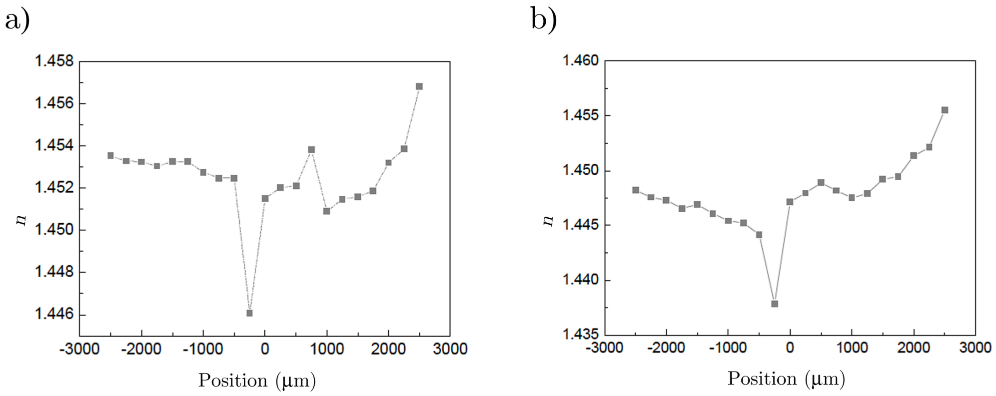

FIGURE 4.41: Refractive index for the Dy-doped silica rod at 630 nm (a) and 740 nm (b) for selected measurement positions of figure 4.16.

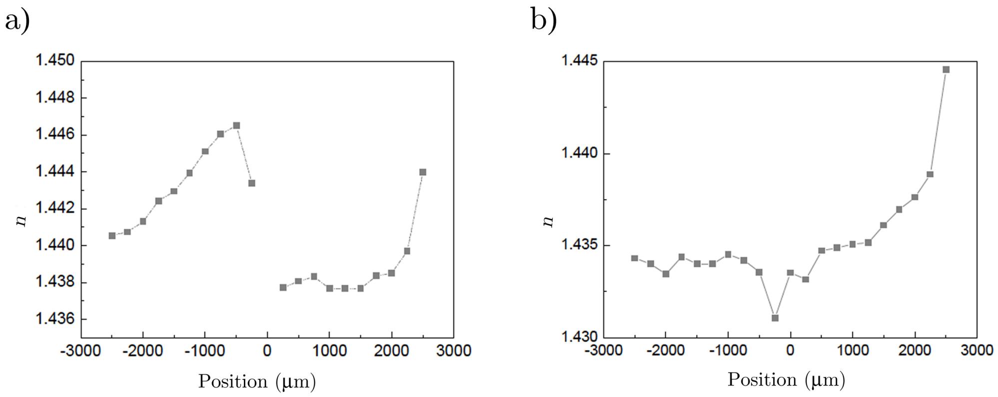

FIGURE 4.42: Refractive index for the Er-doped silica rod at 630 nm (a) and 740 nm (b) for selected measurement positions of figure 4.16.

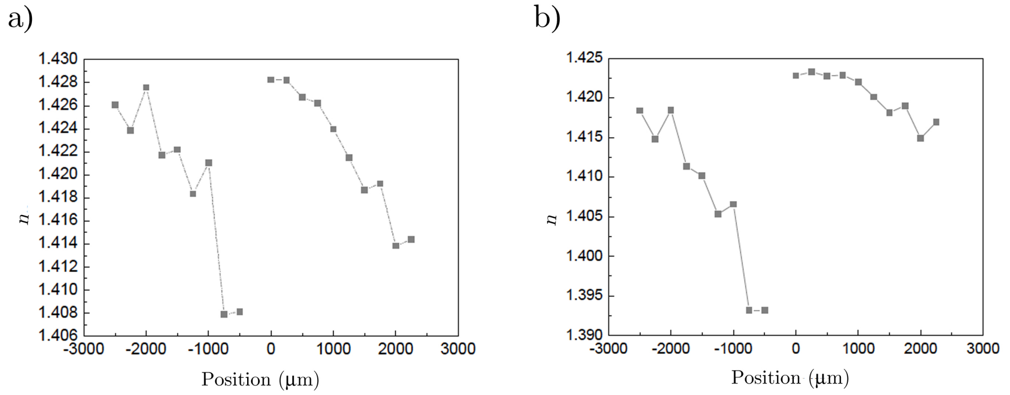

FIGURE 4.43: Refractive index for the Yb-doped silica rod at 630 nm (a) and 740 nm (b) for selected measurement positions of figure 4.16.

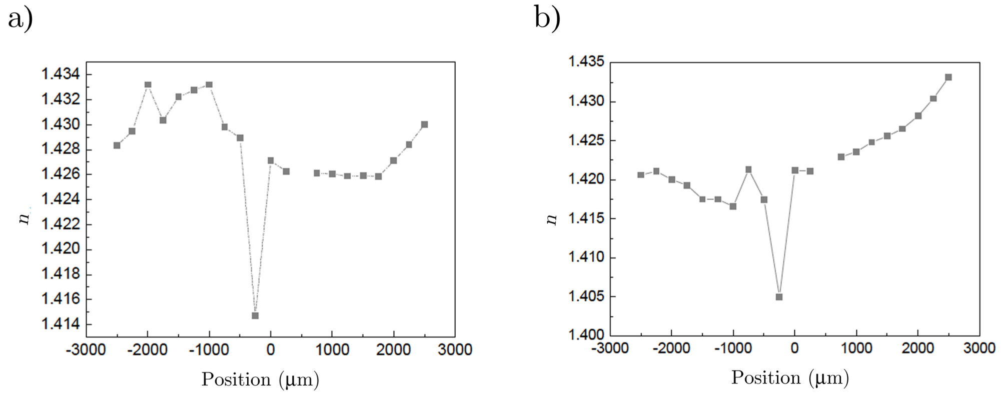

FIGURE 4.44: Refractive index for the $LiNbO_3$-doped silica rod at 630 nm (a) and 740 nm (b) for selected measurement positions of figure 4.16.

# Conclusions

In the present thesis the use of active GRadient-INdex media with gain or loss for the design and fabrication of external, compact laser beam shaping systems has been proposed. General conditions for Gaussian beam transformation through this kind of media have been obtained and particularized for two different refractive index profiles: a parabolic and a hyperbolic secant refractive index. Finally, two active GRIN media fabrication methods, sol-gel chemical route and laser zone melting technique, have been explored as an alternative to GRIN media conventional fabrication process. Conclusions derived from this work can be summarized as follows.

- Effects of gain or loss in an active material can be considered by using a complex refractive index instead of the real one. Active GRIN materials can be regarded as quadratic phase transformers with a Gaussian mask.
- Particular cases of Gaussian beam transformation such as uniform beam shaping, collimation and focusing can be studied by circle diagrams in the complex plane.
- The active GRIN media has the capability to tailor an input spherical Gaussian beam in the following ways: i) a beam with uniform irradiance distribution when the beam half-width tends to infinite at the output face of the material; ii) a plane Gaussian beam whether the radius of curvature at the output tends to infinite; iii) transforming the input spherical Gaussian beam into an uniform plane wavefront in case the

complex curvature is zero at the output and iv) the input Gaussian beam is turned into an output point source if infinite complex curvature is obtained. The main advantage of these beam shaper devices is their capability to provide amplification or attenuation on the Gaussian laser beam.

- For active GRIN medium with parabolic refractive index profile and an input Gaussian beam of $\lambda = 1064$ nm, laser beam shaping length is larger if the media presents gain and shorter for the case of on-axis loss.
- The influence of the input beam parameters on shaping length with a parabolic GRIN media was analyzed obtaining that the shaping length increase with wavelength and decrease with beam waist size and distance from the beam waist to the input face of the GRIN media.
- For HS active GRIN material larger shaping lengths than for parabolic active media are obtained.
- Both gain GRIN media (Parabolic and HS) can be used to reshape plane Gaussian beams into beams with a very flat irradiance profile choosing suitable parameters.
- For a practical case, and for the GRIN media with the following parameters: $a = 0.5$ mm, $n_{0R} = 1.57$, $n_{0I} = -10^{-5}$, $g_R = 0.31924$ mm$^{-1}$ and $g_I = 0.00072$ mm$^{-1}$ wider tolerance intervals are obtained for the parabolic beam shaper; however uniform beams with higher irradiance profiles can be achieved using the active HS beam shapers.

Regarding the fabrication techniques analyzed, we can conclude that

- An active GRIN material can be fabricated by sol-gel route as a multilayer material. The control on the complex refractive index can be accomplish by mainly varying the precursors nature, molar ratios, the use of modifying agents and synthesis temperature, among others.
- Sol-gel derived thin films might be a suitable candidate for active GRIN beam shaper devices due to its powerfulness and versatility for tailoring the characteristics of the films.

- Erbium and ytterbium doped silica-titania and silica films were prepared by sol-gel process, using the 70MTES/30TISP, 60MTES/40TEOS and TEOS sol systems. Film thickness varied with RE concentration thickness and increased linearly with increasing withdrawal rate at dip-coating process. The highest thickness values were achieved for larger dopant concentration. Additionally, the refractive index of the films decreased with RE concentration.

- As to the extinction coefficient $k$, a general tendency to increase with increasing doping concentration could be noticed, although the mechanisms of light loss in are worth original investigations. Porosity of the Er and Yb-doped silica-titania films increase with RE concentration.

- AFM images of the as-deposited and annealed films revealed smooth surfaces and the formation of porous granular structures where valleys, mountains and island clusters became larger as erbium concentration increases.

- Sample with 2.0 at.% erbium-doped silica-titania film showed noticeable photoluminescence emission under 980 nm excitation.

- For laser zone melting technique, results obtained indicate that axial and gradual introduction of dysprosium and lithium niobate were obtained, while erbium and ytterbium doping did not produce any noticeable diffusion within the glass substrate. On the contrary, Si diffusion took place in the erbium and ytterbium layers deposited on the substrate and densified by laser action. SEM studies also revealed that *in-situ* heating of the sample aids to avoid cracking during laser irradiation.

- The refractive index gradients obtained by means of spectroscopic ellipsometry were 0.02, 0.014, 0.026 and 0.031 for dysprosium, erbium, ytterbium and lithium niobate doping elements, respectively. Although these are promising results, at this stage of the research the analysis does not enable to determine the feasibility of LZM for preparation of active GRIN medium.

This work has opened some interesting future researching lines to be developed further.

- The theory outlined in this thesis as well as the design in Chapters 2 and 3 are restricted to the problem of producing circular flat-top beams for symmetrical laser beams (for example, fiber lasers, tunable Ti:Sapphire, Nd:YAG or $CO_2$ lasers) by active GRIN materials simply to keep the mathematical analysis as simple as possible. The rectangular beam shaping problem for asymmetrical laser beams (for example, excimer or diode laser) has the same conceptual base, and all the results here may readily be extended to the two dimensional problem.
- The design and tolerance analysis carried out in Chapter 3 can be extended to the rest of the optical functions that can be implemented with active GRIN materials, that is, focusing and collimation.
- This research may be the primary study which is done by applying sol-gel and LZM processes to active GRIN media fabrication. Therefore, their application feasibility is not yet studied enough. However, we suggest that these RE-doped sol-gel films have great potential in active GRIN materials development through this study. In this sense, more advanced research in regards to the type of dopants, synthesis of the sols and other processing conditions need to be accomplished as more variety of thickness, optical constant and luminescence studies are required for future beam shapers devices development.
- With the aim to improve the photoluminescence results obtained for the sol-gel derived samples, erbium and ytterbium-doped film deposited on silicon substrates for a wider range of dopant concentrations, sintered at 750 and 800°C and using $SiO_2$-$TiO_2$, $SiO_2$ and $TiO_2$ systems have been prepared during the development of this thesis. Their characterization is planned in the near future.
- The ellipsometric measurements of the samples prepared by LZM technique should be repeated to obtain more accurate data taking several

independent acquisitions in each point, using a dispersion model to describe the raw data, performing the measurements along distinct radial direction lines and considering a smaller measurement spot to increase spatial resolution. Another future task is the characterization of the samples prepared with the LZM2 and LZM3 treatments by Spectral Ellipsometry.

- During the development of this thesis, a third method for active GRIN materials fabrication has been explored in collaboration with GRINTECH, a company specialized in GRIN lenses manufacturing: the ion-exchange method. Results have shown that the ytterbium doping element influences the real part of the refractive index, and that the parabolic profile is maintained after the ion-exchange process. However, the extinction coefficient of the samples could not be measured due to the low spatial resolution of the ellipsometers used in relation to the aperture of the GRIN material. Within this context, experimental research must be extended to more doping elements to confirm the results and a reliable characterization method for the extinction coefficient must be used.

USC
UNIVERSIDADE
DE SANTIAGO
DE COMPOSTELA

# Appendix A

# Circle diagram for beam transformations

## A.1 Uniform beam shaping condition

The condition for uniform beam shaping by a parabolic-like active GRIN medium takes the form of

$$Im[n_0\dot{q}(d)q^*(d)] = 0 \Longrightarrow w(d) \to \infty \tag{A.1}$$

Considering the expressions for the position and the slope of the complex ray given by the complex matrix aquation (2.22) and that the complex curvature at the input face of the active GRIN material is given by equation (1.113), we can rewrite the condition for plane Gaussian beam as[1]

---

[1] To simplify the expressions the thickness dependence has been omitted.

$$
\begin{aligned}
& n_{0I}\left[\frac{|U|^2}{|n_0|^2} Re(H_a^* \dot{H}_a) + \frac{n_{0R}U_R + n_{0I}U_I}{|n_0|^2} Re(H_f^* \dot{H}_a + \dot{H}_f^* H_a) + \right. \\
& \left. + Re(H_f^* \dot{H}_f) + \frac{n_{0I}U_R - n_{0R}U_I}{|n_0|^2} Im(H_f^* \dot{H}_a + Re\dot{H}_f^* H_a)\right] + \\
& + n_{0R}\left[Im(H_f^* \dot{H}_f)\frac{|U|^2}{|n_0|^2} Im(H_a^* \dot{H}_a) + \frac{n_{0R}U_R + n_{0I}U_I}{|n_0|^2} Im(H_f^* \dot{H}_a - \dot{H}_f^* H_a) + \right. \\
& \left. + \frac{n_{0I}U_R - n_{0R}U_I}{|n_0|^2} Re(H_f^* H_a - H_f^* \dot{H}_a)\right] = 0
\end{aligned}
\tag{A.2}
$$

Readjusting this equation as function of the real ($U_R$) and imaginary ($U_I$) part of the complex curvature at the input plane we have that

$$
\begin{aligned}
& |n_0|^2 \frac{Im(n_0 H_f^* \dot{H}_f)}{Im(n_0 H_a^* \dot{H}_a)} + |U|^2 + \\
& + \frac{|n_0|^2 Im(H_f^* \dot{H}_a) - (n_{0R}^2 - n_{0I}^2) Im(\dot{H}_f^* H_a) + 2n_{0R}n_{0I} Re(\dot{H}_f^* H_a)}{Im(n_0 H_a^* \dot{H}_a)} U_R + \\
& + \frac{|n_0|^2 Re(H_f^* \dot{H}_a) - (n_{0R}^2 - n_{0I}^2) Re(\dot{H}_f^* H_a) - 2n_{0R}n_{0I} Im(\dot{H}_f^* H_a)}{Im(n_0 H_a^* \dot{H}_a)} U_I = 0
\end{aligned}
\tag{A.3}
$$

The above expression can be written in the form

$$
(U_R - C_R)^2 + (U_I - C_I)^2 = h^2 \Rightarrow U_R^2 + U_I^2 - 2U_R C_R - 2U_I C_I + C_R^2 + C_I^2 = h^2
\tag{A.4}
$$

by defining the center of the circumference $C(C_R, C_I)$ as

$$
\begin{aligned}
& C_R = -\frac{|n_0|^2 Im(H_f^* \dot{H}_a) - (n_{0R}^2 - n_{0I}^2) Im(\dot{H}_f^* H_a) + 2n_{0R}n_{0I} Re(\dot{H}_f^* H_a)}{2Im(n_0 H_a^* \dot{H}_a)} = \\
& = -\frac{|n_0|^2 Im(H_f^* \dot{H}_a) + Im(n_0^2 \dot{H}_f H_a^*)}{2Im(n_0 H_a^* \dot{H} a)} = -\frac{Im(n_0^2 \dot{H}_f H_a^*)}{2Im(n_0 H_a^* \dot{H} a)}
\end{aligned}
\tag{A.5}
$$

and

$$C_I = -\frac{|n_0|^2 Re(H_f^* H_a) - (n_{0R}^2 - n_{0I}^2) Re(\dot{H}_f^* H_a) - 2n_{0R} n_{0I} Im(\dot{H}_f^* H_a)}{2Im(n_0 H_a^* \dot{H}_a)} =$$
$$= -\frac{|n_0|^2 Re(H_f^* \dot{H}_a^*) - Re(n_0^2 \dot{H}_f H_a^*)}{2Im(n_0 H_a^* \dot{H} a)} = -\frac{|n_0 H_f|^2 - Re(n_0^2 \dot{H}_f H_a^*)}{2Im(n_0 H_a^* \dot{H} a)} \tag{A.6}$$

where we have used the relations listed in section A.3.

Therefore, comparing equations (A.3) and (A.4) we can obtain the radius $h$ of the circumference as

$$h^2 = C_R^2 + C_I^2 - |n_0|^2 \frac{4Im(n_0 H_f^* \dot{H}_a) Im(n_0 H_a^* \dot{H}_a)}{4Im^2(H_a^* \dot{H}_a)} \tag{A.7}$$

Substituting expressions for $C_R$ and $C_I$ and taking into account that

$$C_R^2 + C_I^2 =$$
$$= |n_0|^2 \frac{|n_0|^2 |H_f^*|^2 |\dot{H}_a|^2 + |n_0|^2 |\dot{H}_f|^2 |H_a^*|^2 - 2Re(n_0^2 H_f^* \dot{H}_f H_a^* \dot{H}_a)}{4Im^2(n_0 H_a^* \dot{H}_a)} \tag{A.8}$$

the radius $h$ is given by

$$h^2 = \frac{|n_0|^4}{4Im^2(H_a^* \dot{H}_a)} \tag{A.9}$$

## A.2 Plane Gaussian beam condition

An active GRIN media can turn an input spherical Gaussian beam into a plane Gaussian beam whether the following condition is fulfilled

$$Re[n_0 \dot{q}(d) q^*(d)] = 0 \Longrightarrow R(d) \to \infty \tag{A.10}$$

The center $C'(C'_R, C'_I)$ and the radius $h'$ of the circle corresponding to plane Gaussian beam transformation can be obtained doing a similar calculus to that carried out for the uniform beam condition. Hence, substituting the position and the slope of the complex ray in (A.10) we obtain that

$$\begin{aligned}
&n_{0R}\Bigg[\frac{|U|^2}{|n_0|^2}Re(H_a^*\dot{H}_a) + \frac{n_{0R}U_R + n_{0I}U_I}{|n_0|^2}Re(H_f^*\dot{H}_a + \dot{H}_f^*H_a) + \\
&+ Re(H_f^*\dot{H}_f) + \frac{n_{0I}U_R - n_{0R}U_I}{|n_0|^2}Im(H_f^*\dot{H}_a + \dot{H}_f^*H_a)\Bigg] + \\
&- n_{0I}\Bigg[Im(H_f^*\dot{H}_f)\frac{|U|^2}{|n_0|^2}Im(H_a^*\dot{H}_a) + \frac{n_{0R}U_R + n_{0I}U_I}{|n_0|^2}Im(H_f^*\dot{H}_a - \dot{H}_f^*H_a) + \\
&+ \frac{n_{0I}U_R - n_{0R}U_I}{|n_0|^2}Re(H_f^*H_a - H_f^*\dot{H}_a)\Bigg] = 0
\end{aligned} \tag{A.11}$$

Expressing this equation in terms of the real and imaginary parts of the complex curvature $U$

$$\begin{aligned}
&|n_0|^2\frac{Re(n_0H_f^*\dot{H}_f)}{Re(n_0H_a^*\dot{H}_a)} + |U|^2 + \\
&\frac{|n_0|^2Re(H_f^*\dot{H}_a) + (n_{0R}^2 - n_{0I}^2)Re(\dot{H}_f^*H_a) + 2n_{0R}n_{0I}Im(\dot{H}_f^*H_a)}{Re(n_0H_a^*\dot{H}_a)}U_R + \\
&- \frac{|n_0|^2Im(H_f^*\dot{H}_a) + (n_{0R}^2 - n_{0I}^2)Im(\dot{H}_f^*H_a) - 2n_{0R}n_{0I}Re(\dot{H}_f^*H_a)}{Re(n_0H_a^*\dot{H}_a)}U_I = 0
\end{aligned} \tag{A.12}$$

we can obtain the coordinates of the center of the circumference

$$\begin{aligned}
C'_R &= -\frac{|n_0|^2Re(H_f^*\dot{H}_a) + (n_{0R}^2 - n_{0I}^2)Re(\dot{H}_f^*H_a) + 2n_{0R}n_{0I}Im(\dot{H}_f^*H_a)}{2Re(n_0H_a^*\dot{H}_a)} = \\
&= -\frac{|n_0|^2Re(H_f^*\dot{H}_a) + Re(n_0^2\dot{H}_fH_a^*)}{2Re(n_0H_a^*\dot{H}_a)} = -\frac{|n_0H_f|^2 + Re(n_0^2\dot{H}_fH_a^*)}{2Re(n_0H_a^*\dot{H}_a)}
\end{aligned} \tag{A.13}$$

$$
\begin{aligned}
C'_I &= \frac{|n_0|^2 Im(H_f^* \dot{H}_a) + (n_{0R}^2 - n_{0I}^2) Im(\dot{H}_f^* H_a) - 2n_{0R}n_{0I} Re(\dot{H}_f^* H_a)}{2Re(n_0 H_a^* \dot{H}_a)} = \\
&= \frac{|n_0|^2 Im(H_f^* \dot{H}_a) - Im(n_0^2 \dot{H}_f H_a^*)}{2Re(n_0 H_a^* \dot{H}_a)} = -\frac{Im(n_0^2 \dot{H}_f H_a^*)}{2Re(n_0 H_a^* \dot{H}_a)}
\end{aligned}
\tag{A.14}
$$

The radius $h'$ can be determined as

$$
h'^2 = C_R'^2 + C_I'^2 - |n_0|^2 \frac{4Re(n_0 H_f^* \dot{H}_f) Re(n_0 H_a^* \dot{H}_a)}{4Re^2(n_0 H_a^* \dot{H}_a)}
\tag{A.15}
$$

where

$$
\begin{aligned}
&C_R'^2 + C_I'^2 = \\
&\quad = |n_0|^2 \frac{|n_0|^2 |H_f^*|^2 |\dot{H}_a|^2 + |n_0|^2 |\dot{H}_f|^2 |H_a^*|^2 - 2Re(n_0^2 H_f^* \dot{H}_f H_a^* \dot{H}_a)}{4Re^2(n_0 H_a^* \dot{H}_a)}
\end{aligned}
\tag{A.16}
$$

The radius of the circumference corresponding to plane Gaussian beam transformation is given by

$$
h'^2 = \frac{|n_0|^4}{4Re^2(n_0 H_a^* \dot{H}_a)}
\tag{A.17}
$$

## A.3 Useful relations

The following relations have been used to develop the mathematical background presented in this thesis.

$Re(ab) = Re(ab)^*$

$Re(ab^*) = Re(a)Re(b) + Im(a)Im(b) = Re(a^*b)$

$Re(ab) = Re(a)Re(b) - Im(a)Im(b)$

$Im(ab) = -Im(ab)^*$

$$Im(ab) = Re(a)Im(b) + Im(a)Re(b)$$
$$Im(ab^*) = Im(a)Re(b) - Re(a)Im(b) = -Im(ab)^*$$

$$Im[H_f^*(d)\dot{H}_a(d)] = 0$$
$$H_{fR}(z) = \dot{H}_{aR}(z)$$
$$H_{fI}(z) = \dot{H}_{aI}(z)$$

$$Im[H_f^*(z)\dot{H}_f(z)] = -Im[H_f(z)\dot{H}_f^*(z)] = H_{fR}(z)\dot{H}_{fI}(z) - \dot{H}_{fR}(z)H_{fI}(z)$$
$$Im[H_a^*(z)\dot{H}_a(z)] = -Im[H_a(z)\dot{H}_a^*(z)] = H_{aR}(z)\dot{H}_{aI}(z) - \dot{H}_{aR}(z)H_{aI}(z)$$
$$Im[H_f^*(z)\dot{H}_a(z)] = -Im[H_f(z)\dot{H}_a^*(z)] = H_{fR}(z)\dot{H}_{aI}(z) - \dot{H}_{fI}(z)H_{aR}(z)$$
$$Im[H_a^*(z)\dot{H}_f(z)] = -Im[H_a(z)\dot{H}_f^*(z)] = H_{aR}(z)\dot{H}_{fI}(z) + H_{aI}(z)\dot{H}_{fR}(z)$$
$$Im[H_a^*(z)\dot{H}_f(z)] + Im[H_a^*(z)\dot{H}_f(z)] = Im[H_f^*(z)\dot{H}_a^*(z) + \dot{H}_f(z)H_a^*(z)]$$
$$Re[\dot{H}_f^*(z)H_a^*(z)] = Re[\dot{H}_f^*(z)H_a(z)] = \dot{H}_{fR}(z)H_{aR}(z) + \dot{H}_{fI}(z)H_{aI}(z)$$
$$Re[H_f^*(z)\dot{H}_a^*(z)] = Re[H_f^*(z)\dot{H}_a(z)] = H_{fR}(z)\dot{H}_{aR}(z) + H_{fI}(z)\dot{H}_{aI}(z)$$
$$Re[\dot{H}_f^*(z)H_a^*(z)] - Re[H_f^*(z)\dot{H}_a^*(z)] = Re[\dot{H}_f^*(z)H_a^*(z) - H_f(z)\dot{H}_a^*(z)]$$
$$Re[H_f^*(z)\dot{H}_f^*(z)] = Re[H_f^*(z)\dot{H}_f^*(z)] = H_{fR}(z)\dot{H}_{fR}(z) + H_{fI}(z)\dot{H}_{fI}(z)$$
$$Re[H_a^*(z)\dot{H}_a^*(z)] = Re[H_a^*(z)\dot{H}_a^*(z)] = H_{aR}(z)\dot{H}_{aR}(z) + H_{aI}(z)\dot{H}_{aI}(z)$$
$$Re[H_f^*(z)\dot{H}_a(z)] = Re[H_f(z)\dot{H}_a^*(z)] = H_{fR}(z)\dot{H}_{aR}(z) + H_{fI}(z)\dot{H}_{aI}(z)$$
$$Re[\dot{H}_f^*(z)H_a(z)] = Re[\dot{H}_f(z)H_a^*(z)] = \dot{H}_{fR}(z)H_{aR}(z) + \dot{H}_{fI}^*(z)H_{aI}(z)$$
$$Re[\dot{H}_f^*(z)H_a(z)] + Re[\dot{H}_f^*(z)H_a^*(z)] = Re[H_f(z)\dot{H}_a^*(z) + \dot{H}_f^*(z)H_a(z)]$$
$$Im[\dot{H}_f(z)H_a^*(z)] = -Im[\dot{H}_f^*(z)H_a(z)] = \dot{H}_{fI}(z)H_{aR}(z) - \dot{H}_{fR}(z)H_{aI(z)}$$
$$Im[H_f(z)\dot{H}_a^*(z)] = -Im[H_f^*(z)\dot{H}_a(z)] = H_{fI}(z)\dot{H}_{aR}(z) - H_{fR}(z)\dot{H}_{aI}(z) =$$
$$0$$
$$Im[\dot{H}_f(z)H_a^*(z)] - Im[H_f(z)\dot{H}_a^*(z)] = Im[\dot{H}_f(z)H_a^*(z) - H_f(z)\dot{H}_a^*(z)]$$

# Appendix B

# Resumen

Desde que el primer láser fue puesto en funcionamiento en 1960 por Theodore Maiman, sus aplicaciones no han dejado de aumentar hasta hacer de él una herramienta fundamental en nuestros días. Los haces más simples producidos por una fuente láser son los conocidos como haces Gaussianos puros (modo TEM00). La obtención de haces láser con un perfil de irradiancia determinado es de crucial importancia para un gran número de aplicaciones, siendo una tecnología instrumental usada en experimentos básicos así como en procesos industriales que incluyen, entre otros, litografía de semiconductores, impresión láser, taladro en circuitos integrados, fotoablación en microelectrónica, procesado de materiales, almacenamiento óptico de datos, etc.. El proceso de redistribución del perfil de irradiancia para obtener un perfil adecuado que permita la optimización de una aplicación concreta se conoce como conformado de haz, del inglés *beam shaping.* El ejemplo más habitual de conformado de haces láser es la conversión de un haz de perfil Gaussiano en otro con amplitud y fase constantes. Estos haces uniformes, que presentan una distribución de irradiancia constante en un área especificada, son necesarios en muchas aplicaciones láser entre las que se incluyen el procesado de materiales, litografía, tratamientos médicos, bombeos para otros láseres de mayor potencia, etc. Las principales características que deben tener este tipo de dispositivos son una alta eficiencia y una buena capacidad a la hora de uniformizar la irradiancia del haz.

Los conformadores de haz han cobrado mucha importancia en los últimos años y se han desarrollado varias alternativas para la conversión de haces Gaussianos en haces uniformes. Los conformadores pueden dividirse en dos clases: conformadores intra-cavidad y extra-cavidad. Los dispositivos conformadores de tipo intra-cavidad generan un haz plano dentro de la propia cavidad del láser, mientras que los dispositivos extra-cavidad permiten el control de la irradiancia y la curvatura compleja de la salida de un láser, con el objetivo final de producir la uniformización de dicha salida. Hasta el momento se han propuesto numerosos dispositivos para producir la transformación de haces Gaussianos en otros con una distribución de irradiancia uniforme. Algunos ejemplos son filtros con perfiles absorbentes que varían radialmente, sistemas ópticos de revolución o anamórficos dióptricos y catóptricos y elementos difractivos como hologramas y óptica binaria. Los absorbentes están limitados por su modesta eficiencia y restringidos a láseres de bastante baja potencia. La óptica reflectora se usa para uniformización fuera de eje requiriendo diseños con superficies asimétricas y complicadas. La óptica difractiva es muy sensible a la variación de la longitud de onda y al desalineamiento. Sin embargo, la óptica refractiva produce uniformización eficiente con dispositivos coaxiales que minimizan los problemas de alineamiento y sensibilidad espectral. Los dispositivos conformadores de haz, excepto los absorbentes, se fabrican con elementos pasivos que producen una redistribución espacial de la irradiancia transformando un haz no uniforme en otro uniforme. Los absorbentes utilizan vidrios neutros de densidad variable o películas metálicas de transmitancia variable depositadas sobre substratos de vidrio que producen la uniformización de haces por absorción.

Dentro de este contexto, el trabajo de investigación que se recoge en esta tesis tiene como objetivo central el estudio fundamental y diseño de un nuevo tipo de conformadores de haz extra-cavidad realizados con materiales activos de GRadiente de INdice (GRIN). El término GRIN se refiere a materiales inhomogéneos en los que el índice de refracción varía punto a punto, mientras que cuando se habla de materiales activos se está refiriendo a materiales que son capaces de amplificar o atenuar un haz de radiación óptica o, lo que es lo mismo, a materiales con ganancia o pérdida. Los medios GRIN se encuentran comúnmente en la naturaleza, siendo los ejemplos más relevantes el cristalino del ojo y la atmósfera de la tierra. Cuando la luz se propaga en un medio GRIN sigue trayectorias curvas. El índice de refracción de estos medios puede ser seleccionado de tal manera que puede funcionar de la misma forma que elementos ópticos convencionales como lentes o prismas.

Este objetivo se considera como un blanco en la búsqueda de la condición de uniformización para la curvatura compleja del haz, de perfiles de haz con funciones específicas en microóptica y de ganancias o pérdidas en la irradiancia del haz conformado. Esto es, se pretende uniformizar haces Gaussianos controlando de forma activa la amplificación/reducción de irradiancia y la curvatura compleja del haz no uniforme para realizar funciones específicas en microóptica usando un solo componente óptico. El trabajo se ha centrado en conformado de haces láser de simetría circular (láseres de fibra, Nd:YAG, Nd:YVO$_4$, etc.) pero el estudio puede ser extendido fácilmente en un futuro a láseres cuyo haz de salida sea asimétrico y astigmático, tal y como como ocurre en los láseres de diodo.

La tesis está organizada en cuatro capítulos. En el Capítulo 1 se exponen la terminología y los principios básicos de propagación de la luz en medios inhomogéneos dentro del marco de la óptica geométrica para longitudes de onda muy pequeñas. A continuación, se proporciona una descripción general de la propagación en medios GRIN mediante una transformada lineal integral, para después particularizar el estudio de la propagación a medios con perfil de índice de refracción de tipo parabólico y de tipo secante hiperbólica.

El Capítulo 2 está dedicado al estudio de la propagación de haces Gaussianos en medios GRIN activos y a las diferentes transformaciones de las que pueden ser objeto. Los efectos de ganancia o pérdida en los materiales GRIN activos pueden ser tenidos en cuenta de una forma muy sencilla: substituyendo en las expresiones obtenidas para los medios GRIN pasivos del Capítulo 1 el valor del índice de refracción real por un índice de refracción complejo. Dependiendo del signo de la parte imaginaria de dicho índice de refracción ($n_I$) el medio tendrá ganancia ($n_I < 0$) o pérdida ($n_I > 0$). En este capítulo se analizaron los perfiles de índice de refracción de los medios GRIN activos descritos por un perfil de índice de tipo parabólico y secante hiperbólica. La secante hiperbólica es un caso muy interesante de medio inhomogéneo al ser un perfil más general que el parabólico, ya que la función parabólica puede considerarse como la primera aproximación del desarrollo en series de Taylor de la función secante hiperbólica, y porque la ecuación que rige la propagación de la luz puede ser resuelta de forma analítica sin precisar de ninguna aproximación. Además, el medio con perfil de tipo secante hiperbólica está libre de aberraciones para los rayos meridionales. Con este estudio ha sido posible determinar la influencia del índice de refracción complejo en el tipo de guiado de ambos medios y en los efectos de pérdida y ganancia. Además, se ha presentado el formalismo de la propagación de haces láser en medios GRIN activos considerados como transformadores cuadráticos de fase con máscara Gaussiana inducida. A partir del análisis de la propagación se han podido obtener las condiciones generales de transformación de haz que pueden llevar a cabo estos medios como una solución geométrica en el espacio 2D de la curvatura compleja del haz de entrada. La curvatura e irradiancia del haz transformado fue obtenida como función de los rayos axial y de campo, del perfil del índice de refracción y del espesor de los medios GRIN activos. Del análisis de las transformaciones se obtuvieron las condiciones para las que los medios pueden llevar a cabo las siguientes transformaciones de haz:

- Condición para la generación de haz uniforme, para la cual el Gaussiano esférico incidente es convertido en un frente esférico uniforme de irradiancia y curvatura real del frente emergente en función de los parámetros del medio y de los rayos axial y de campo. En este caso el medio GRIN actúa como un sistema conformador de haz con ganancia o pérdida, dependiendo del valor de la parte imaginaria del índice de refracción.

- Condición para la generación de haz plano Gaussiano, para la cual el haz Gaussiano esférico incidente es transformado en un haz Gaussiano plano. La irradiancia y la cintura del haz emergente fueron obtenidas en función de los parámetros del medio y de los rayos axial y de campo. En este caso el medio GRIN activo actúa como un sistema transformador Gaussiano esférico/plano.
- Condición para la colimación de haces, donde el medio actúa como un sistema colimador de haz transformando un haz esférico Gaussiano incidente en un frente plano uniforme.
- Condición de enfoque, donde el haz Gaussiano esférico incidente es convertido en un punto luminoso a la salida, comportándose el medio GRIN activo como un sistema colimador.

En el Capítulo 3 se ha aplicado el desarrollo teórico sobre la propagación de haces Gaussianos en medios GRIN activos, con perfil de índice de tipo parabólico y secante hiperbólica, al diseño de conformadores de haces uniformes mediante simulaciones desarrolladas con el software comercial MATLAB. Entre las principales ventajas del conformador objeto de esta tesis cabe destacar que comprende un único elemento, lo que minimiza su complejidad, y que permite atenuar o amplificar el perfil uniforme de irradiancia del láser. Se pueden obtener diferentes dispositivos conformadores, con distintas configuraciones modificando los parámetros de diseño del conformador. Así, se pueden obtener conformadores GRIN activos con distintas longitudes de conformado variando los parámetros correspondientes a la parte real e imaginaria del índice de refracción apertura y/o espesor del conformador. En este capítulo se han diseñado varios ejemplos prácticos de conformadores para un haz láser con longitud de onda 1064 nm y radio 0.45 mm utilizando un medio GRIN activo con perfil de tipo parabólico: i) con pérdida a lo largo del eje óptico y en los bordes, ii) con ganancia a lo largo del eje óptico y en los bordes, iii) con pérdida a lo largo del eje óptico y ganancia en los bordes y iv) con ganancia a lo largo del eje óptico y pérdida en los bordes. Para cada uno de dichos casos se ha analizado la evolución de los parámetros del haz incidente en el material, es decir, de la cintura y del radio de curvatura, y se ha determinado la longitud de conformado. El plano z en el medio activo donde la cintura tiende a infinito es aquel que verifica la condición de conformado, obteniéndose que el conformador con mayor espesor es el que corresponde al caso con ganancia a lo largo del eje óptico y en los bordes del medio. Además, se ha analizado la evolución de la irradiancia del haz en el medio. Por otro lado, se ha realizado un estudio para determinar la influencia de los parámetros del haz incidente en el diseño del conformador. De dicho estudio se ha obtenido que la distancia de conformado (o espesor que debe tener el medio GRIN activo para actuar como un conformador de haz uniforme) se incrementa para longitudes de onda más largas. Sin embargo, la distancia de conformado disminuye si el radio del haz y la distancia de éste a la cara de entrada del medio activo aumentan. En este mismo capítulo también se ha realizado un estudio comparativo de los perfiles de índice de refracción de un caso particular de medio GRIN activo con perfil de índice de refracción de tipo parabólico y otro medio con perfil de tipo secante hiperbólica. Tal y como se esperaba, tanto para la parte real del índice de refracción como para la imaginaria, ambos perfiles coinciden en la región paraxial y se separan a medida que se alejan de la misma. El estudio de la evolución de las partes real e imaginaria de los perfiles de índice de tipo parabólico y secante hiperbólica del medio GRIN activo para los distintos casos de pérdida y ganancia planteados en el trabajo han demostrado que la distancia a la que se separan los dos tipos de perfiles es la misma independientemente del caso considerado. Asimismo, se ha analizado la evolución del rayo complejo en ambos medios GRIN activos parabólico y secante hiperbólica en el caso de medios con ganancia y pérdida a lo largo de $z$. Lo que se ha observado en este caso es que los rayos asociados al haz Gaussiano de entrada no cruzan el eje óptico y que la amplitud de las oscilaciones no se mantiene constante a lo largo de la propagación en el medio debido a los efectos de ganancia y pérdida y que dicha amplitud decrece con la distancia de propagación. Es interesante hacer notar que la diferencia entre las trayectorias para el caso parabólico y el caso secante hiperbólica aumenta con la distancia de propagación en el material y es más pronunciada en los valles que en las crestas. En cuanto a lo que se refiere a la evolución de la cintura en el medio parabólico y en el secante hiperbólica, se ha determinado que la distancia de conformado es mayor para el segundo tanto en el caso de medio con ganancia en el eje y en los bordes como en el caso de pérdida en eje y ganancia en los bordes. Para finalizar este capítulo, se ha realizado un estudio de las tolerancias en espesor y en longitud de onda de dos conformadores con perfil de tipo parabólico y secante hiperbólica diseñados para transformar un haz incidente con longitud de onda igual a 575 nm y radio 0.45 mm en un haz con una distribución de irradiancia uniforme. Para evaluar la calidad de la uniformización del haz producido a la salida del medio se ha utilizado el valor cuadrático medio o RMS (del inglés *root mean square*). De dicho estudio se ha concluido que el conformador de tipo parabólico presenta una mayor tolerancia a la desviación de los valores de diseño.

En el Capítulo 4 se ha estudiado la viabilidad de fabricar materiales GRIN activos mediante la ruta química conocida como Sol-Gel y la técnica de Fusión Zonal por Láser (del inglés *Laser Zone Melting*, LZM). El proceso sol-gel se desarrolló hace más de 40 años como una alternativa tecnológica para la preparación de vidrios y materiales cerámicos a temperaturas considerablemente bajas. De forma general, el proceso sol-gel conlleva la evolución de redes inorgánicas a través de la formación de una suspensión coloidal (sol) y su gelificación para formar una red en una fase líquida continua (gel). Este método presenta numerosas ventajas frente a otros métodos de síntesis de vidrios y materiales cerámicos. La tecnología sol-gel se puede aplicar para obtener dispositivos de muy diversa naturaleza y prácticamente “a medida”, teniendo en cuenta principalmente los materiales precursores, ratios molares, solventes y catalizadores, concentraciones, ratio de hidrólisis y condiciones de deposición, entre otros parámetros involucrados en el proceso. Por otro lado, el método sol-gel permite la incorporación de tierras raras como el erbio y el iterbio, muy utilizados en el campo de la fotónica para obtener amplificación óptica. Uno de los objetivos de la parte experimental de la tesis consistía en preparar y caracterizar monocapas de los sistema $SiO_2$-$TiO_2$ y $SiO_2$ dopadas con distintos porcentajes de erbio (también de iterbio en el caso del sistema $SiO_2$-$TiO_2$) y sintetizadas por el método sol-gel. Con este primer estudio se obtuvieron los valores de las constantes ópticas (índice de refracción y coeficiente de extinción) y espesor de las capas. Así, el método sol-gel podría utilizarse para obtener materiales GRIN activos superponiendo capas donde cada una de ellas tenga un índice de refracción complejo tal que la estructura final esté caracterizada por un perfil de índice complejo y siguiendo una distribución de tipo parabólica. Las capas se depositaron sobre substratos de vidrio utilizando la técnica de inmersión conocida como dip-coating y posteriormente fueron sometidas a un tratamiento térmico (sinterizado). Las capas finas se caracterizaron usando Elipsometría Espectral para obtener el valor de su espesor y de las constantes ópticas. El espesor de las capas depende de la velocidad a la que el substrato es extraído del líquido, siendo mayor para velocidades de extracción más elevadas. Por otro lado, los valores de espesor más elevados se obtuvieron para las mayores concentraciones de dopante. Con los diferentes sistemas utilizados se consiguieron índices de refracción de 1.66, 1.33 y 1.44 (medidos para $\lambda = 633$ nm). Los resultados mostraron que el índice de refracción disminuye al aumentar la concentración de dopante, aumentando la porosidad de los mismos. Con respecto al coeficiente de extinción, podría decirse que se observa una tendencia general a aumentar con la concentración de dopante, aunque esto es algo que debe ser estudiado con mayor profundidad. La caracterización topográfica de las capas se realizó mediante Microscopía de Fuerzas Atómicas (del inglés *Atomic Force Microscopy*, AFM), donde se pudo observar que las capas obtenidas son poco rugosas y que este último parámetro se incrementa con la concentración de erbio utilizada. Por último, las capas mostraron fotoluminiscencia en el infrarrojo en torno a 1.54 $\mu$m, siendo la capa dopada con mayor concentración de erbio la que presentó un pico mayor de intensidad. Los tiempos de vida media medidos fueron prácticamente insignificantes, delatando la probable presencia de un exceso de impurezas OH en la capa final. El otro método que se ha explorado en este trabajo es el método de fusión zonal por láser. Esta técnica permite el procesado de materiales mediante la focalización de un haz láser de $CO_2$ al provocar gradientes de temperatura elevados en áreas relativamente pequeñas, promoviendo el fundido local del material en las proximidades del área tratada. En este trabajo se ha utilizado el LZM como primer ensayo experimental para la preparación de medios de gradiente de índice activos con geometría cilíndrica. Para ello, se depositaron distintos recubrimientos de compuestos inorgánicos ($Er_2O_3$, $Dy_2O_3$, $Yb_2O_3$ y $LiNbO_3$) mediante la técnica dip-coating sobre cilindros de $SiO_2$ de diferentes diámetros. Se aplicaron varios tratamientos láser en cada caso y la morfología y composición química de las muestras resultantes se caracterizaron con Microscopía Electrónica de Barrido combinada con análisis de energía dispersiva (SEM-EDX). Los resultados obtenidos muestran que se ha conseguido difusión del niobato de litio en todos los casos, siendo el proceso más eficiente aquel en el que el substrato se precalentó previamente a 120°C para evitar el choque térmico. Para los recubrimientos con erbio e iterbio se obtuvo una capa bien diferenciada depositada sobre el substrato, sin observarse que los dopantes se difundieran en el mismo; sin embargo, sí se observó en algunos casos que se produjo difusión del Si hacia la capa depositada. El análisis mediante Elipsometría Espectral de algunas de las muestras confirmó la generación de un gradiente de índice desde los bordes al centro del substrato de $SiO_2$ cilíndrico.

La memoria finaliza con las principales conclusiones que se han extraído de este tesis doctoral y se realiza una reflexión sobre las futuras líneas de investigación a las que la misma ha dado lugar.


USC
UNIVERSIDADE
DE SANTIAGO
DE COMPOSTELA

# Bibliography

[1] F. M. Dickey, S. Holswade, and D. L. Shealy, Eds., *Laser Beam Shaping Applications*. Boca Raton: CRC Press, 2005.

[2] W. B. Veldkamp and C. J. Kastner, "Beam profile shaping for laser radars that use detector arrays," *Applied Optics*, vol. 21, no. 2, pp. 345–356, 1982. [Online]. Available: http://ao.osa.org/abstract.cfm?URI=ao-21-2-345

[3] J. Cordingley, "Application of a binary diffractive optic for beam shaping in semiconductor processing by lasers," *Applied Optics*, vol. 32, no. 14, pp. 2538–2542, 1993. [Online]. Available: http://ao.osa.org/abstract.cfm?URI=ao-32-14-2538

[4] Y. Kato, K. Mima, N. Miyanaga, S. Arinaga, Y. Kitagawa, M. Nakatsuka, and C. Yamanaka, "Random phasing of high-power lasers for uniform target acceleration and plasma-instability suppression," *Physics Review Letters*, vol. 53, pp. 1057–1060, 1984. [Online]. Available: http://link.aps.org/doi/10.1103/PhysRevLett.53.1057

[5] H. P. Herzig, *Micro-Optics: Elements, Systems And Applications*. Rochester, New York: CRC Press, 1997.

[6] F. M. Dickey and S. C. Holswade, *Laser Beam Shaping: Theory and Techniques*. Rochester, New York: CRC Press, 2000.

[7] P. A. Bélanger and C. Paré, “Optical resonators using graded-phase mirrors,” *Optics Letters*, vol. 16, no. 14, pp. 1057–1059, 1991. [Online]. Available: http://ol.osa.org/abstract.cfm?URI=ol-16-14-1057

[8] C. Paré and P. Bélanger, “Custom laser resonators using graded-phase mirrors,” *IEEE Journal of Quantum Electronics*, vol. 28, no. 1, pp. 355–362, 1992.

[9] I. A. Litvin and A. Forbes, “Gaussian mode selection with intracavity diffractive optics,” *Optics Letters*, vol. 34, no. 19, pp. 2991–2993, 2009. [Online]. Available: http://ol.osa.org/abstract.cfm?URI=ol-34-19-2991

[10] I. A. Litvin and A. Forbes, “Intra–cavity flat–top beam generation,” *Optics Express*, vol. 17, no. 18, pp. 15 891–15 903, 2009. [Online]. Available: http://www.opticsexpress.org/abstract.cfm?URI=oe-17-18-15891

[11] F. M. Dickey, “Laser beam shaping,” *Optics and photonics news*, vol. 14, no. 4, pp. 30–35, 2003.

[12] D. L. Shealy and J. A. Hoffnagle, “Laser beam shaping profiles and propagation,” *Applied optics*, vol. 45, no. 21, pp. 5118–5131, 2006. [Online]. Available: http://ao.osa.org/abstract.cfm?URI=ao-45-21-5118

[13] R. J. Collier, C. B. Burckhardt, and L. H. Lin, *Optical Holography*. Academic Press, New York, 1971.

[14] C. S. Ih, “Absorption lens for producing uniform laser beams,” *Applied Optics*, vol. 11, no. 3, pp. 694–695, 1972. [Online]. Available: http://ao.osa.org/abstract.cfm?URI=ao-11-3-694

[15] D. A. B. Miller and S. D. Smith, “Variable attenuator for gaussian laser beams,” *Applied Optics*, vol. 17, no. 23, pp. 3804–3808,

1978. [Online]. Available: http://ao.osa.org/abstract.cfm?URI=ao-17-23-3804

[16] M. Quintanilla and A. M. de Frutos, “Holographic filter that transforms a gaussian into a uniform beam,” *Applied Optics*, vol. 20, no. 5, pp. 879–880, 1981. [Online]. Available: http://ao.osa.org/abstract.cfm?URI=ao-20-5-879

[17] N. C. Roberts, “Multilevel computer-generated holograms with separable phase functions for beam shaping,” *Applied Optics*, vol. 31, no. 17, pp. 3198–3200, 1992. [Online]. Available: http://ao.osa.org/abstract.cfm?URI=ao-31-17-3198

[18] S. K. Dew and R. R. Parsons, “Absorbing filter to flatten gaussian beams,” *Applied Optics*, vol. 31, no. 18, pp. 3416–3419, 1992. [Online]. Available: http://ao.osa.org/abstract.cfm?URI=ao-31-18-3416

[19] S. P. Chang, J.-M. Kuo, Y.-P. Lee, C.-M. Lu, and K.-J. Ling, “Transformation of gaussian to coherent uniform beams by inverse-gaussian transmittive filters,” *Applied Optics*, vol. 37, no. 4, pp. 747–752, 1998. [Online]. Available: http://ao.osa.org/abstract.cfm?URI=ao-37-4-747

[20] W. W. Simmons, G. W. Leppelmeier, and B. C. Johnson, “Optical beam shaping devices using polarization effects,” *Applied Optics*, vol. 13, no. 7, pp. 1629–1632, 1974. [Online]. Available: http://ao.osa.org/abstract.cfm?URI=ao-13-7-1629

[21] Y. Ohtsuka, Y. Arima, and Y. Imai, “Acoustooptic 2-d profile shaping of a gaussian laser beam,” *Applied Optics*, vol. 24, no. 17, pp. 2813–2819, 1985. [Online]. Available: http://ao.osa.org/abstract.cfm?URI=ao-24-17-2813

[22] Y.-H. Huang, S.-W. Ko, M.-S. Li, S.-C. Chu, and A. Y.-G. Fuh, “Modulation of shape and polarization of beam using a liquid crystal

q-plate that is fabricated via photo-alignment," *Optics Express*, vol. 21, no. 9, pp. 10 954–10 961, 2013. [Online]. Available: http://www.opticsexpress.org/abstract.cfm?URI=oe-21-9-10954

[23] S. L. Ream, "A convex beam integrator," *Laser Focus*, no. 15(11), pp. 68–71, 1979.

[24] R. Dubravko, "Irradiance redistribution of collimated radiation using a simple intensity redistributor," *Applied Optics*, vol. 29, no. 18, pp. 2675–2678, 1990. [Online]. Available: http://ao.osa.org/abstract.cfm?URI=ao-29-18-2675

[25] F. M. Dickey and B. D. O'Neil, "Multifaceted laser beam integrators: General formulation and design concepts," *Optical Engineering*, vol. 27, no. 11, pp. 271 199–271 199–, 1988. [Online]. Available: http://dx.doi.org/10.1117/12.7976799

[26] C. Li, J. Li, and A. Delmas, "An optical device to homogenize a laser beam," *Chinese Optics Letters*, vol. 3, no. 12, pp. 698–700, 2005. [Online]. Available: http://col.osa.org/abstract.cfm?URI=col-3-12-698

[27] S. Bollanti, P. D. Lazzaro, and D. Murra, "More about the light beam shaping by the integration method," *The European Physical Journal Applied Physics*, vol. 28, no. 2, pp. 179–186, 2004. [Online]. Available: http://www.epjap.org/10.1051/epjap:2004164

[28] E. T. Kana, S. Bollanti, P. D. Lazzaro, D. Murra, O. Bouba, and M. B. Onana, "Laser beam homogenization: Modeling and comparison with experimental results," *Optics Communications*, vol. 264, no. 1, pp. 187 – 192, 2006. [Online]. Available: http://www.sciencedirect.com/science/article/pii/S0030401806001374

[29] F. Wippermann, U.-D. Zeitner, P. Dannberg, A. Bräuer, and S. Sinzinger, "Beam homogenizers based on chirped microlens arrays," *Optics Express*, vol. 15, no. 10, pp. 6218–6231, 2007.

[Online]. Available: http://www.opticsexpress.org/abstract.cfm?URI=oe-15-10-6218

[30] Y. Kawamura, Y. Itagaki, K. Toyoda, and S.Namba, "A simple optical device for generating square flat-top intensity irradiation from a gaussian laser beam," *Optics Communications*, vol. 48, no. 1, pp. 44–46, 1983. [Online]. Available: http://www.sciencedirect.com/science/article/pii/0030401883902468

[31] R. J. Pressley, "Optical beam homogenizer," 1984, uS Patent 4,475,027. [Online]. Available: https://www.google.com/patents/US4475027

[32] X. Deng, X. Liang, Z. Chen, W. Yu, and R. Ma, "Uniform illumination of large targets using a lens array," *Applied optics*, vol. 25, no. 3, pp. 377–381, 1986. [Online]. Available: http://ao.osa.org/abstract.cfm?URI=ao-25-3-377

[33] G. Zheng, C. Du, C. Zhou, and C. Zheng, "Micrograting-array beam-shaping technique for asymmetrical laser beams," *Applied optics*, vol. 44, no. 17, pp. 3540–3544, 2005. [Online]. Available: http://ao.osa.org/abstract.cfm?URI=ao-44-17-3540

[34] W.-H. Lee, "Method for converting a gaussian laser beam into a uniform beam," *Optics Communications*, vol. 36, no. 6, pp. 469 – 471, 1981. [Online]. Available: http://www.sciencedirect.com/science/article/pii/0030401881901930

[35] W. B. Veldkamp, "Laser beam profile shaping with binary diffraction gratings," *Optics Communications*, vol. 38, no. 5, pp. 381 – 386, 1981. [Online]. Available: http://www.sciencedirect.com/science/article/pii/0030401881900717

[36] W. B. Veldkamp, "Laser beam profile shaping with interlaced binary diffraction gratings," *Applied Optics*, vol. 21, no. 17, pp.

3209–3212, 1982. [Online]. Available: http://ao.osa.org/abstract.cfm?URI=ao-21-17-3209

[37] L. A. Romero and F. M. Dickey, “Lossless laser beam shaping,” *Journal of the Optical Society of America A*, vol. 13, no. 4, pp. 751–760, 1996. [Online]. Available: http://josaa.osa.org/abstract.cfm?URI=josaa-13-4-751

[38] F. M. Dickey and S. C. Holswade, “Gaussian laser beam profile shaping,” *Optical Engineering*, vol. 35, no. 11, pp. 3285–3295, 1996. [Online]. Available: http://dx.doi.org/10.1117/1.601069

[39] J. A. Hoffnagle and C. M. Jefferson, “Design and performance of a refractive optical system that converts a Gaussian to a flattop beam,” *Applied Optics*, vol. 39, no. 30, pp. 5488–5499, 2000. [Online]. Available: http://ao.osa.org/abstract.cfm?URI=ao-39-30-5488

[40] D. Palima and J. Glückstad, “Gaussian to uniform intensity shaper based on generalized phase contrast,” *Optics Express*, vol. 16, no. 3, pp. 1507–1516, 2008. [Online]. Available: http://www.opticsexpress.org/abstract.cfm?URI=oe-16-3-1507

[41] S. Zhang, G. Neil, and M. Shinn, “Single-element laser beam shaper for uniform flat-top profiles,” *Optics Express*, vol. 11, no. 16, pp. 1942–1948, 2003. [Online]. Available: http://www.opticsexpress.org/abstract.cfm?URI=oe-11-16-1942

[42] C. C. Aleksoff, K. K. Ellis, and B. D. Neagle, “Holographic conversion of a gaussian beam to a near-field uniform beam,” *Optical Engineering*, vol. 30, no. 5, pp. 537–543, 1991. [Online]. Available: http://dx.doi.org/10.1117/12.55833

[43] M. Rossi and T. Hessler, “Stray-light effects of diffractive beam-shaping elements in optical microsystems,” *Applied Optics*, vol. 38, no. 14, pp. 3068–3076, 1999. [Online]. Available: http://ao.osa.org/abstract.cfm?URI=ao-38-14-3068

[44] S. Zhang, Q. Yang, and G. Lüpke, "Spatial beam shaping of ultrashort laser pulses: theory and experiment," *Applied Optics*, vol. 44, no. 27, pp. 5818–5823, 2005. [Online]. Available: http://ao.osa.org/abstract.cfm?URI=ao-44-27-5818

[45] J. Hahn, H. Kim, K. Choi, and B. Lee, "Real-time digital holographic beam-shaping system with a genetic feedback tuning loop," *Applied Optics*, vol. 45, no. 5, pp. 915–924, 2006. [Online]. Available: http://ao.osa.org/abstract.cfm?URI=ao-45-5-915

[46] J. H. McDermit and T. E. Horton, "Reflective optics for obtaining prescribed irradiative distributions from collimated sources," *Applied Optics*, vol. 13, no. 6, pp. 1444–1450, 1974. [Online]. Available: http://ao.osa.org/abstract.cfm?URI=ao-13-6-1444

[47] P. W. Scott and W. H. Southwell, "Reflective optics for irradiance redistribution of laser beams: design," *Applied Optics*, vol. 20, no. 9, pp. 1606–1610, 1981. [Online]. Available: http://ao.osa.org/abstract.cfm?URI=ao-20-9-1606

[48] P. H. Malyak, "Two-mirror unobscured optical system for reshaping the irradiance distribution of a laser beam," *Applied Optics*, vol. 31, no. 22, pp. 4377–4383, 1992. [Online]. Available: http://ao.osa.org/abstract.cfm?URI=ao-31-22-4377

[49] K. Nemoto, T. Fujii, N. Goto, H. Takino, T. Kobayashi, N. Shibata, K. Yamamura, and Y. Mori, "Laser beam intensity profile transformation with a fabricate dmirror," *Applied Optics*, vol. 36, no. 3, pp. 551–557, 1997. [Online]. Available: http://ao.osa.org/abstract.cfm?URI=ao-36-3-551

[50] Z. H. Yang and J. R. Leger, "Flattop mode shaping of a vertical cavity surface emitting laser using an external-cavity aspheric mirror," *Optics Express*, vol. 12, no. 22, pp. 5549–5555, 2004. [Online]. Available: http://www.opticsexpress.org/abstract.cfm?URI=oe-12-22-5549

[51] V. Oliker, "Optical design of freeform two-mirror beam-shaping systems," *Journal of the Optical Society of America. A*, vol. 24, no. 12, pp. 3741–3752, 2007. [Online]. Available: http://josaa.osa.org/abstract.cfm?URI=josaa-24-12-3741

[52] J. Liang, R. N. Kohn, M. F. Becker, and D. J. Heinzen, "High-precision laser beam shaping using a binary-amplitude spatial light modulator," *Applied Optics*, vol. 49, no. 8, pp. 1323–1330, 2010. [Online]. Available: http://ao.osa.org/abstract.cfm?URI=ao-49-8-1323

[53] B. R. Frieden, "Lossless conversion of a plane laser wave to a plane wave of uniform irradiance," *Applied Optics*, vol. 4, no. 11, pp. 1400–1403, 1965. [Online]. Available: http://ao.osa.org/abstract.cfm?URI=ao-4-11-1400

[54] D. Shafer, "Gaussian to flat-top intensity distributing lens," *Optics & Laser Technology*, vol. 14, no. 3, pp. 159 – 160, 1982. [Online]. Available: http://www.sciencedirect.com/science/article/pii/003039928290113X

[55] S. R. Jahan and M. A. Karim, "Refracting systems for gaussian-to-uniform beam transformations," *Optics & Laser Technology*, vol. 21, no. 1, pp. 27 – 30, 1989. [Online]. Available: http://www.sciencedirect.com/science/article/pii/003039928990008X

[56] M. Arif, M. M. Hossain, A. A. S. Awwal, and M. N. Islam, "Two-Element Refracting System for Annular Gaussian-to-Bessel Beam Transformation," *Applied Optics*, vol. 37, no. 19, pp. 4206–4209, 1998. [Online]. Available: http://ao.osa.org/abstract.cfm?URI=ao-37-19-4206

[57] D. W. Griffin, "Gaussian beam intensity flattener," *Optical Engineering*, vol. 37, no. 7, pp. 2185–2187, 1998. [Online]. Available: http://dx.doi.org/10.1117/1.601712

[58] D. L. Shealy, S.-H., and Chao, “Geometric optics-based design of laser beam shapers,” *Optical Engineering*, vol. 42, no. 11, pp. 3123–3138, 2003. [Online]. Available: http://dx.doi.org/10.1117/1.1617311

[59] C. Yang, R. Zhang, Q. Xu, and P. Ma, “Continuous phase plate for laser beam smoothing,” *Applied Optics*, vol. 47, no. 10, pp. 1465–1469, 2008. [Online]. Available: http://ao.osa.org/abstract.cfm?URI=ao-47-10-1465

[60] V. Oliker, “On design of free-form refractive beam shapers, sensitivity to figure error, and convexity of lenses,” *Journal of the Optical Society of America A*, vol. 25, no. 12, pp. 3067–3076, 2008. [Online]. Available: http://josaa.osa.org/abstract.cfm?URI=josaa-25-12-3067

[61] F. Duerr and H. Thienpont, “Refractive laser beam shaping by means of a functional differential equation based design approach,” *Optics Express*, vol. 22, no. 7, pp. 8001–8011, 2014. [Online]. Available: http://www.opticsexpress.org/abstract.cfm?URI=oe-22-7-8001

[62] A. G. A. J., G. J. B., and Trenholme, “Lens and mirror design via the principal surface,” *Applied Optics*, vol. 15, no. 10, pp. 2579–2582, 1976. [Online]. Available: http://ao.osa.org/abstract.cfm?URI=ao-15-10-2579

[63] N. Davidson, A. A. Friesem, and E. Hasman, “Reflective and refractive systems for general two-dimensional beam transformations,” *Applied Optics*, vol. 33, no. 5, pp. 815–820, 1994. [Online]. Available: http://ao.osa.org/abstract.cfm?URI=ao-33-5-815

[64] X. Gao, H. Ohashi, H. Okamoto, M. Takasaka, and K. Shinoda, “Beam-shaping technique for improving the beam quality of a high-power laser-diode stack,” *Optics Letters*, vol. 31, no. 11, pp.

1654–1656, 2006. [Online]. Available: http://ol.osa.org/abstract.cfm?URI=ol-31-11-1654

[65] C. Wang and D. L. Shealy, “Design of gradient-index lens systems for laser beam reshaping,” *Applied optics*, vol. 32, no. 25, pp. 4763–4769, 1993. [Online]. Available: http://ao.osa.org/abstract.cfm?URI=ao-32-25-4763

[66] S. Sinzinger, K.-H. Brenner, J. Moisel, T. Spick, and M. Testorf, “Astigmatic gradient-index elements for laser-diode collimation and beam shaping,” *Applied Optics*, vol. 34, no. 29, pp. 6626–6632, 1995. [Online]. Available: http://ao.osa.org/abstract.cfm?URI=ao-34-29-6626

[67] B. J. Koch, J. R. Leger, A. Gopinath, Z. Wang, and R. A. Morgan, “Single-mode vertical cavity surface emitting laser by graded-index lens spatial filtering,” *Applied Physics Letters*, vol. 70, no. 18, pp. 2359–2361, 1997. [Online]. Available: http://scitation.aip.org/content/aip/journal/apl/70/18/10.1063/1.118873

[68] A. V. Pfeil, B. Messerschmidt, V. Blümel, U. Possner, and T. Possner, “Making fast cylindrical gradient-index lenses diffraction limited by using a wave-front-correction element,” *Applied Optics*, vol. 37, no. 22, pp. 5211–5215, 1998. [Online]. Available: http://ao.osa.org/abstract.cfm?URI=ao-37-22-5211

[69] R. K. Luneburg, *Mathematical Theory of Optics*. Berkeley: University of California Press, 1964.

[70] E. W. Marchand, *Gradient Index Optics*. New York: Academic Press, 1978.

[71] H. Kogelnik, “On the propagation of gaussian beams of light through lenslike media including those with a loss or gain variation,” *Applied Optics*, vol. 4, no. 12, pp. 1562–1569, 1965. [Online]. Available: http://ao.osa.org/abstract.cfm?URI=ao-4-12-1562

[72] L. Casperson and A. Yariv, "The gaussian mode in optical resonators with a radial gain profile," *Applied Physics Letters*, vol. 12, no. 10, pp. 355–357, 1968. [Online]. Available: http://scitation.aip.org/content/aip/journal/apl/12/10/10.1063/1.1651851

[73] L. W. Casperson, "Beam modes in complex lenslike media and resonators," *Journal of the Optical Society of America*, vol. 66, no. 12, pp. 1373–1379, 1976. [Online]. Available: http://www.osapublishing.org/abstract.cfm?URI=josa-66-12-1373

[74] M. Nazarathy, A. Hardy, and J. Shamir, "Generalized mode propagation in first-order optical systems with loss or gain," *Journal of the Optical Society of America*, vol. 72, no. 10, pp. 1409–1420, 1982. [Online]. Available: http://www.osapublishing.org/abstract.cfm?URI=josa-72-10-1409

[75] R. Martínez-Herrero and P. M. Mejías, "Beam characterization through active media," *Optics Communications*, vol. 85, no. 2-3, pp. 162–166, 1991. [Online]. Available: http://www.sciencedirect.com/science/article/pii/003040189190387S

[76] C. Gomez-Reino, M. V. Perez, and C. Bao, *Gradient-Index Optics: Fundamentals and Applications.* Berlin Heidelberg: Springer Verlag, 2002.

[77] A. I. Gómez-Varela, M. T. Flores-Arias, C. Bao-Varela, X. de la Fuente, and C. Gómez-Reino., "Propagation of gaussian beams through active GRIN materials," *Journal of Physics: Conference Series*, vol. 274, no. 1, p. 012124, 2011. [Online]. Available: http://stacks.iop.org/1742-6596/274/i=1/a=012124

[78] C. Bao-Varela, A. I. Gómez-Varela, M. T. Flores-Arias, and C. Gomez-Reino, "Propagation in active GRIN materials: comparison between parabolic and hyperbolic secant complex refractive index profiles," in *Proc. SPIE 8001, International*

*Conference on Applications of Optics and Photonics*, M. F. Costa, Ed., 2011, pp. 80 012J–80 012J–8.

[79] A. Gómez-Varela, M. Flores-Arias, C. Bao-Varela, and C. Gómez-Reino, "Focusing, collimation and beam shaping by active GRIN rod lenses: Theory and simulation," *Optics and Lasers in Engineering*, vol. 50, no. 12, pp. 1706–1715, 2012. [Online]. Available: http://www.sciencedirect.com/science/article/pii/S0143816612002205

[80] A. I. Gómez-Varela, C. Bao-Varela, and M. T. Flores-Arias, "A tolerance analysis on design parameters of parabolic and hyperbolic secant active GRIN materials for laser beam shaping purposes," *Laser Physics*, vol. 24, no. 11, p. 115802, 2014. [Online]. Available: http://stacks.iop.org/1555-6611/24/i=11/a=115802

[81] A. Sharma, D. V. Kumar, and A. K. Ghatak, "Tracing rays through graded-index media: a new method," *Applied Optics*, vol. 21, no. 6, pp. 984–987, 1982. [Online]. Available: http://ao.osa.org/abstract.cfm?URI=ao-21-6-984

[82] K. Iga, Y. Kokubun, and M. Oikawa, *Fundamentals of Microoptics: Distributed-Index, Microlens, and Stacked Planar Optics.* Tokyo: Academic Press, 1984.

[83] J. A. Arnaud, *Beam and fiber optics.* New York, San Francisco, and London: Academic Press, 1976.

[84] M. Born, E. Wolf, A. B. Bhatia, P. C. Clemmow, D. Gabor, A. R. Stokes, A. M. Taylor, P. A. Wayman, and W. L. Wilcock, *Principles of Optics: Electromagnetic Theory of Propagation, Interference and Diffraction of Light.* Cambridge; New York: Cambridge University Press, 1999.

[85] A. E. Siegman, *Lasers.* Mill Valley, California: University Science Books, 1986.

[86] D. Marcuse, *Light transmission optics.* New York: Van Nostrand Reinhold, cop., 1989.

[87] M. C. T. B. E. A. Saleh and, *Fundamentals of photonics.* Hoboken, New Jersey: John Wiley & Sons, 2007.

[88] A. Yariv, *Optical Electronics.* New York: Holt McDougal, 1984.

[89] H. Kogelnik, "Imaging of optical modes – resonators with internal lenses," *Bell System Technical Journal*, no. 44, pp. 455–494, 1965.

[90] K. Halbach, "Matrix representation of gaussian optics," *American Journal of Physics*, vol. 32, no. 2, p. 90, 1964. [Online]. Available: http://scitation.aip.org/content/aapt/journal/ajp/32/2/10.1119/1.1970159

[91] L. W. Casperson, "Synthesis of gaussian beam optical systems," *Applied Optics*, vol. 20, no. 13, pp. 2243–2249, 1981. [Online]. Available: http://ao.osa.org/abstract.cfm?URI=ao-20-13-2243

[92] I. S. Gradshteyn and I. M. Ryzhik, *Table of Integrals, Series and Products.* New York: Academic Press, 1980.

[93] J. Sochacki and C. Gomez-Reino, "Nonfull-aperture Luneburg lenses: a novel solution," *Applied Optics*, vol. 24, no. 9, pp. 1371–1373, 1985. [Online]. Available: http://ao.osa.org/abstract.cfm?URI=ao-24-9-1371

[94] M. Sochacka, J. Sochacki, and C. Gómez-Reino, "Paraxial region index profiles of GRIN rods," *Applied Optics*, vol. 25, no. 1, pp. 142–145, 1986. [Online]. Available: http://ao.osa.org/abstract.cfm?URI=ao-25-1-142

[95] M. Nazarathy and J. Shamir, "First-order optics: operator representation for systems with loss or gain," *Journal of the Optical Society of America*, vol. 72, no. 10, pp. 1398–1408,

1982. [Online]. Available: http://www.osapublishing.org/abstract.cfm?URI=josa-72-10-1398

[96] M. Nazarathy and J. Shamir, "First-order optics–a canonical operator representation: lossless systems," *Journal of the Optical Society of America*, vol. 72, no. 3, pp. 356–364, 1982. [Online]. Available: http://www.osapublishing.org/abstract.cfm?URI=josa-72-3-356

[97] S. Abe and J. T. Sheridan, "Generalization of the fractional fourier transformation to an arbitrary linear lossless transformation an operator approach," *Journal of Physics A: Mathematical and General*, vol. 27, no. 12, p. 4179, 1994. [Online]. Available: http://stacks.iop.org/0305-4470/27/i=12/a=023

[98] S. Abe and J. T. Sheridan, "Optical operations on wave functions as the abelian subgroups of the special affine fourier transformation," *Optics Letters*, vol. 19, no. 22, pp. 1801–1803, 1994. [Online]. Available: http://ol.osa.org/abstract.cfm?URI=ol-19-22-1801

[99] S. Abe and J. T. Sheridan, "Almost-fourier and almost-fresnel transformations," *Optics Communications*, vol. 113, no. 4–6, pp. 385–388, 1995. [Online]. Available: http://www.sciencedirect.com/science/article/pii/003040189400521U

[100] A. W. Lohmann, "Image rotation, wigner rotation, and the fractional fourier transform," *Journal of the Optical Society of America A*, vol. 10, no. 10, pp. 2181–2186, 1993. [Online]. Available: http://josaa.osa.org/abstract.cfm?URI=josaa-10-10-2181

[101] C. Gomez-Reino, "GRIN optics and its application in optical connections," *International Journal of Optoelectronics*, vol. 7, pp. 607–680, 1992.

[102] G. Eichmann, "Quasi-geometric optics of media with inhomogeneous index of refraction," *Journal of the Optical Society of America*,

vol. 61, no. 2, pp. 161–168, 1971. [Online]. Available: http://www.osapublishing.org/abstract.cfm?URI=josa-61-2-161

[103] T. H. Maiman, "Stimulated optical radiation in ruby," *Nature*, vol. 187, no. 4736, pp. 493–494, 1960. [Online]. Available: http://www.nature.com/nature/journal/v187/n4736/abs/187493a0.html

[104] P. A. Bélanger, "Beam propagation and the ABCD ray matrices," *Optics Letters*, vol. 16, no. 4, pp. 196–198, 1991. [Online]. Available: http://ol.osa.org/abstract.cfm?URI=ol-16-4-196

[105] D. W. Hewak and J. W. Lit, "Solution deposited optical waveguide lens," *Applied Optics*, vol. 28, no. 19, pp. 4190–4198, 1989. [Online]. Available: http://ao.osa.org/abstract.cfm?URI=ao-28-19-4190

[106] X. Mao, S.-C. S. Lin, M. I. Lapsley, J. Shi, B. K. Juluri, and T. J. Huang, "Tunable liquid gradient refractive index (l-GRIN) lens with two degrees of freedom," *Lab on a Chip*, vol. 9, no. 14, pp. 2050–2058, 2009. [Online]. Available: http://dx.doi.org/10.1039/B822982A

[107] C. Bao, R. Srivastava, C. Gómez-Reino, and M. V. Pérez, "Gaussian beam propagation and imaging in hyperbolic secant profile media," *Pure and Applied Optics: Journal of the European Optical Society Part A*, vol. 5, no. 1, p. 15, 1996. [Online]. Available: http://stacks.iop.org/0963-9659/5/i=1/a=003

[108] C. Gómez-Reino and E. Larrea, "Paraxial imaging and transforming in a medium with gradient-index: transmittance function," *Applied Optics*, vol. 21, no. 23, pp. 4271–4275, 1982. [Online]. Available: http://ao.osa.org/abstract.cfm?URI=ao-21-23-4271

[109] T. Li, "Dual forms of the gaussian beam chart," *Applied Optics*, vol. 3, no. 11, pp. 1315–1317, 1964. [Online]. Available: http://ao.osa.org/abstract.cfm?URI=ao-3-11-1315

[110] Newport Corporation, "Refractive beam shapers," accessed October 5, 2015. [Online]. Available: http://www.newport.com/Refractive-Beam-Shapers/315393/1033/info.aspx

[111] D. T. Moore, "Gradient-index optics: a review," *Applied Optics*, vol. 19, no. 7, pp. 1035–1038, 1980. [Online]. Available: http://ao.osa.org/abstract.cfm?URI=ao-19-7-1035

[112] P. Sinai, "Correction of optical aberrations by neutron irradiation," *Applied Optics*, vol. 10, no. 1, pp. 99–104, 1971. [Online]. Available: http://ao.osa.org/abstract.cfm?URI=ao-10-1-99

[113] M. A. Pickering, R. L. Taylor, and D. T. Moore, "Gradient infrared optical material prepared by a chemical vapor deposition process," *Applied Optics*, vol. 25, no. 19, pp. 3364–3372, 1986. [Online]. Available: http://ao.osa.org/abstract.cfm?URI=ao-25-19-3364

[114] Y. S. A., Tagaya, and Y. Koike, "Application of polymer graded-index materials for aberration correction of progressive addition lenses," in *Proceedings of SPIE*, vol. 7213, 2009, pp. 72 130L–72 130L–9. [Online]. Available: http://dx.doi.org/10.1117/12.808451

[115] S. Ohmi, H. Sakai, Y. Asahara, S. Nakayama, Y. Yoneda, and T. Izumitani, "Gradient-index rod lens made by a double ion-exchange process," *Applied Optics*, vol. 27, no. 3, pp. 496–499, 1988. [Online]. Available: http://ao.osa.org/abstract.cfm?URI=ao-27-3-496

[116] A. J. Visconti and J. L. Bentley, "Fabrication of large-diameter radial gradient-index lenses by ion exchange of $Na^+$ for $Li^+$ in titania silicate glass," *Optical Engineering*, vol. 52, no. 11, pp. 112 103–112 103, 2013. [Online]. Available: http://dx.doi.org/10.1117/1.OE.52.11.112103

[117] L. C. Klein, *Sol-Gel technology for thin films, fibers, preforms, electronics, and specialty shapes.* Park Ridge, New Jersey, U.S.A.: Noyes Publications, 1988.

[118] M. Yamane, A. Yasumori, M. Iwasaki, and K. Hayashi, "Graded index materials by the sol-gel process," in *Proceedings of SPIE 1328, Sol-Gel Optics*, vol. 1328, 1990, pp. 133–144. [Online]. Available: http://dx.doi.org/10.1117/12.22553

[119] M. Laczka, J. N. D., Wegrzynek, and M. Wychowaniec, "GRIN glasses prepared by sol-gel method," in *Proc. SPIE 2943*, 2011, pp. 95–104. [Online]. Available: http://dx.doi.org/10.1117/12.255522

[120] F. Rey-García, C. Gómez-Reino, M. T. Flores-Arias, G. F. D. L. Fuente, A. Durán, and Y. Castro, "Sol-gel coatings: An alternative route for producing planar optical waveguides," *Thin Solid Films*, vol. 519, no. 22, pp. 7982–7986, 2011. [Online]. Available: http://www.sciencedirect.com/science/article/pii/S0040609011011990

[121] S. M. Attia, J. Wang, G. Wu, J. Shen, and J. Ma, "Review on Sol-Gel Derived Coatings: Process, Techniques and Optical Applications," *Journal of Materials Science & Technology*, vol. 18, no. 3, pp. 211–218, 2002. [Online]. Available: http://caod.oriprobe.com/articles/4730208/Review_on_Sol_Gel_Derived_Coatings_Process__Techniques_and_Optical_App.htm

[122] E. M. Yeatman and M. M. Ahmad, "Sol-gel fabrication of rare-earth doped photonic components," *Journal of Sol-Gel Science and Technology*, vol. 11, no. 19, pp. 231–236, 2000. [Online]. Available: http://dx.doi.org/10.1023/A%3A1008792423076

[123] R. R. Gonçalves and Y. Messaddeq, "Erbium-activated silica-zirconia planar waveguides prepared by sol-gel route," *Thin Solid Films*, vol. 516, no. 10, pp. 3094–3097, 2008. [Online]. Available: http://www.sciencedirect.com/science/article/pii/S0040609007013399

[124] Y. Qiao, N. Da, D. Chen, W. Ma, Q. Zhou, and J. Qiu, “Spectroscopic properties of Nd$^{3+}$, Yb$^{3+}$-doped and Nd$^{3+}$–Yb$^{3+}$-codoped high silica glass,” *Journal of Materials Science*, vol. 44, no. 15, pp. 4026–4030, 2009. [Online]. Available: http://link.springer.com/article/10.1007/s10853-009-3558-9

[125] R. M. Almeida and A. C. Marques, “Rare earth-doped photonic crystals via sol-gel,” *Journal of Materials Science: Materials in Electronics*, vol. 20, no. 1, pp. 307–311, 2009. [Online]. Available: http://dx.doi.org/10.1007/s10854-008-9596-2

[126] I. de Francisco V. V., Lennikov, J. A. Bea, A. Vegas, J. B. Carda, and G. F. de la Fuente, “In-situ laser synthesis of rare earth aluminate coatings in the system Ln-Al-O (Ln = Y, Gd),” *Solid State Sciences*, vol. 13, no. 9, pp. 1813–1819, 2011. [Online]. Available: http://linkinghub.elsevier.com/retrieve/pii/S1293255811002329

[127] V. V. Lennikov, P. E. Kazin, Y. D. Tretyakov, and G. F. de la Fuente, “Laser Zone Melting and Texture Formation in MgO-doped $Bi_{2.03}Sr_{1.93}Ca_{1.07}Cu_{2.05}O_{8+\partial}$,” *Zeitschrift für anorganische und allgemeine Chemie*, vol. 630, no. 13-14, pp. 2337–2342, 2004. [Online]. Available: http://onlinelibrary.wiley.com/doi/10.1002/zaac.200400311/abstract

[128] F. Rey-García, “Planar waveguides obtained on commercial glass substrates by sol-gel and laser irradiation methods,” Ph.D. dissertation, Area of Optics, Department of Applied Physics at University of Santiago de Compostela, Spain, 2012. [Online]. Available: http://hdl.handle.net/10347/4043

[129] C. J. Brinker and G. W. Scherer, *Sol-gel Science: The Physics and Chemistry of Sol-gel Processing.* San Diego: Academic Press, 1990.

[130] R. Reisfeld, “New materials for nonlinear optics,” in *Optical and Electronic Phenomena in Sol-Gel Glasses and Modern Application*,

ser. Structure and Bonding. Springer Berlin Heidelberg, 1996, no. 85, pp. 99–147. [Online]. Available: http://link.springer.com/chapter/10.1007/BFb0111489

[131] R. Reisfeld, "Sol-gel technology for optoelectronic systems," *SPIE Newsroom*, 2006. [Online]. Available: http://www.spie.org/x8530.xml

[132] A. Baz, H. E. Hamzaoui, I. Fsaifes, G. Bouwmans, M. Bouazaoui, and L. Bigot, "A pure silica ytterbium-doped sol-gel-based fiber laser," *Laser Physics Letters*, vol. 10, no. 5, p. 055106, 2013. [Online]. Available: http://stacks.iop.org/1612-202X/10/i=5/a=055106

[133] D. L. Meixner and P. N. Dyer, "Influence of Sol-Gel Synthesis Parameters on the Microstructure of Particulate Silica Xerogels," *Journal of Sol-Gel Science and Technology*, vol. 14, no. 3, pp. 223–232, 1999. [Online]. Available: http://link.springer.com/article/10.1023/A%3A1008774827602

[134] M. Yamane, J. B. Caldwell, and D. T. Moore, "Preparation of Gradient-Index Glass Rods by the Sol-Gel Process," in *Symposium H – Better Ceramics Through Chemistry II*, ser. MRS Online Proceedings Library, vol. 73, 1986. [Online]. Available: http://journals.cambridge.org/article_S1946427400553809

[135] T. M. Che, J. B. Caldwell, and R. M. Mininni, "Sol-gel derived gradient index optical materials," in *Proceedings of SPIE 1328, Sol-Gel Optics 1328*, vol. 1328, 1990, pp. 145–159. [Online]. Available: http://dx.doi.org/10.1117/12.22554

[136] K. Shiro, "Sol-gel derived r-GRIN doped-silica lenses," in *Proceedings of SPIE 1328, Sol-Gel Optics*, 1990, pp. 160–166. [Online]. Available: http://dx.doi.org/10.1117/12.22555

[137] M. Ebelmen, *Comptes Rendus Acad. Sci. Fr.*, vol. 21, p. 502, 1845.

[138] L. L. Hench and J. K. West, “The Sol-Gel process,” *Chemical Reviews*, vol. 90, pp. 33–72, 1990. [Online]. Available: http://pubs.acs.org/doi/abs/10.1021/cr00099a003?journalCode=chreay

[139] L. C. Klein, *Sol-Gel Optics: Processing and Applications*. Massachusetts: Springer Science & Business Media, 1994.

[140] D. Levy and M. Zayat, *The Sol-Gel Handbook: Synthesis, Characterization and Applications, 3-Volume Set*. Weinheim, Germany: John Wiley & Sons, 2015.

[141] C. J. Brinker, G. C. Frye, A. J. Hurd, and C. S. Ashley, “Fundamentals of sol-gel dip coating,” *Thin Solid Films*, vol. 201, no. 1, pp. 97 – 108, 1991. [Online]. Available: http://www.sciencedirect.com/science/article/pii/004060909190158T

[142] L. D. Landau and B. G. Levich, “Dragging of a Liquid by a Moving Plate,” *Acta Physicochim.*, vol. 17, 1942.

[143] Wikimedia Commons, “Details of Sol-Gel dip coating process,” accessed October 10, 2015. [Online]. Available: https://commons.wikimedia.org/wiki/File:SolGel_DipCoating2.jpg

[144] M. A. Aegerter and M. Mennig, *Sol-Gel Technologies for Glass Producers and Users*. New York: Springer Science & Business Media, 2004.

[145] H. G. Floch, P. F. Belleville, and P. M. Pegon, “Sol-gel optical coatings for lasers II,” *American Ceramic Society Bulletin*, vol. 74, pp. 60–63, 1995. [Online]. Available: http://dx.doi.org/10.1007/BF00486334

[146] P. F. Belleville, H. G. Floch, and M. Berger, “Sol-gel optical coatings processed by the ‘laminar flow coating’ technique,” in *Proceedings of SPIE*, vol. 1758, 1992, pp. 40–47. [Online]. Available: http://dx.doi.org/10.1117/12.131998

[147] I. M.Thomas, “Preparation of dielectric highly reflective (hr) mirrors from colloidal oxide suspensions containing organic polymer binders,” in *Proc. SPIE*, vol. 2288, 1994, pp. 50–55. [Online]. Available: http://dx.doi.org/10.1117/12.188987

[148] J. A. Britten, “A simple theory for the entrained film thickness during meniscus coating,” *Chemical Engineering Communications*, vol. 120, pp. 59–71, 1993.

[149] H.-C. Cha, Y.-C. Huang, F.-H. Hsu, C.-M. Chuang, D.-H. Lu, C.-W. Chou, C.-Y. Chen, and C.-S. Tsao, “Performance improvement of large-area roll-to-roll slot-die-coated inverted polymer solar cell by tailoring electron transport layer,” *Solar Energy Materials and Solar Cells*, vol. 130, pp. 191–198, 2014. [Online]. Available: http://www.sciencedirect.com/science/article/pii/S0927024814003535

[150] A. Larrea, G. F. D. la Fuente, R. I. Merino, and V. M. Orera, “$ZrO_2$-$Al_2O_3$ eutectic plates produced by laser zone melting,” *Journal of the European Ceramic Society*, vol. 22, no. 2, pp. 191–198, 2002. [Online]. Available: http://www.sciencedirect.com/science/article/pii/S0955221901002795

[151] M. Mora, C. López-Gascón, L. A. Angurel, and G. F. de la Fuente, “The influence of support temperature on Bi-2212 monoliths textured by diode laser zone melting,” *Superconductor Science and Technology*, vol. 17, p. 1329, 2004. [Online]. Available: http://iopscience.iop.org/0953-2048/17/11/015

[152] L. A. Angurel, J. C. Díez, and G. F. de la Fuente, “Laser Induced Cylindrical Zone Melting of $Bi_2Sr_2CaCu_2O_{8+\delta}$ Superconductors,” *Zeitschrift für anorganische und allgemeine Chemie*, vol. 635, no. 12, pp. 1767–1772, 2009. [Online]. Available: http://onlinelibrary.wiley.com/doi/10.1002/zaac.200900267/abstract

[153] L. C. Estepa and G. F. de la Fuente, “Continuous furnace with coupled laser for the surface treatment of materials,” 2012, US Patent

8,278,589. [Online]. Available: http://www.google.com/patents/US8278589

[154] R. Aroz, V. Lennikov, R. Cases, M. L. Sanjuán, G. F. de la Fuente, and E. Muñoz, "Laser synthesis and luminescence properties of $SrAl_2O_4$:$Eu^{2+}$, $Dy^{3+}$ phosphors," *Journal of the European Ceramic Society*, vol. 32, no. 16, pp. 4363–4369, 2012. [Online]. Available: http://www.sciencedirect.com/science/article/pii/S0955221912003731

[155] H. G. Rubahn, *Laser Applications in Surface Science and Technology.* New York: John Wiley & Sons, 1999.

[156] W. Duley, *$CO_2$ Lasers Effects and Applications.* New York, San Francisco, London: Elsevier, 2012.

[157] W. M. Steen, *Laser Material Processing.* London, England: Springer Science & Business Media, 2003.

[158] A. J. Ikushima, T. Fujiwara, and K. Saito, "Silica glass: A material for photonics," *Journal of Applied Physics*, vol. 88, no. 3, pp. 1201–1213, 2000. [Online]. Available: http://scitation.aip.org/content/aip/journal/jap/88/3/10.1063/1.373805

[159] M. Yamane and Y. Asahara, *Glasses for Photonics.* Cambridge: Cambridge University Press, 2000.

[160] M. J. F. Digonnet, *Rare-Earth-Doped Fiber Lasers and Amplifiers, Revised and Expanded.* New York: CRC Press, 2001.

[161] N. V. Kiritchenko, L. V. Kotov, M. A. Melkumov, M. E. Likhachev, M. M. Bubnov, M. V. Yashkov, A. Y. Laptev, and A. N. Guryanov, "Effect of ytterbium co-doping on erbium clustering in silica-doped glass," *Laser Physics*, vol. 25, no. 2, p. 025102, 2015. [Online]. Available: http://stacks.iop.org/1555-6611/25/i=2/a=025102

[162] V. P. Gapontsev, S. M. Matitsin, A. A. Isineev, and V. B. Kravchenko, "Erbium glass lasers and their applications," *Optics & Laser Technology*, vol. 14, no. 4, pp. 189–196, 1982. [Online]. Available: http://www.sciencedirect.com/science/article/pii/0030399282900950

[163] M. J. Weber, "Science and technology of laser glass," *Journal of Non-Crystalline Solids*, vol. 123, no. 1-3, pp. 208–222, 1990. [Online]. Available: http://www.sciencedirect.com/science/article/pii/002230939090786L

[164] X. Han, G. Cao, T. Pratum, D. T. Schwartz, and B. Lutz, "Synthesis and properties of $Er^{3+}$-doped silica glass by sol-gel processing with organic complexation," *Journal of Materials Science*, vol. 36, no. 4, pp. 985–993, 2001. [Online]. Available: http://link.springer.com/article/10.1023/A%3A1004836225856

[165] D. Moutonnet, R. Chaplain, M. Gauneau, Y. Pelous, and J. L. Rehspringer, "Realization and characterization of Er and Yb glasses obtained by the sol-gel method," *Materials Science and Engineering: B*, vol. 9, no. 4, pp. 455–457, 1991. [Online]. Available: http://www.sciencedirect.com/science/article/pii/0921510791900724

[166] L. H. Slooff, M. J. A. de Dood, A. van Blaaderen, and A. Polman, "Effects of heat treatment and concentration on the luminescence properties of erbium-doped silica sol-gel films," *Journal of Non-Crystalline Solids*, vol. 296, no. 3, pp. 158 – 164, 2001. [Online]. Available: http://www.sciencedirect.com/science/article/pii/S0022309301009036

[167] S. Abedrabbo, B. Lahlouh, S. Shet, A. Fiory, and N. Ravindra, "Spin-Coated Erbium-Doped Silica Sol-Gel Films on Silicon," *arXiv:1202.0777 [cond-mat, physics:physics]*, 2012, arXiv: 1202.0777. [Online]. Available: http://arxiv.org/abs/1202.0777

[168] G. C. Righini and M. Ferrari, "Photoluminescence of Rare-Earth-Doped Glasses," *Rivista del Nuovo Cimento*, vol. 556282, no. 12, 2005. [Online]. Available: http://www.sif.it/riviste/ncr/econtents/2005/028/12/article/0

[169] H. K. Juwhari, M. H. Kailani, B. I. Lahlouh, S. A. Abedrabbo, K. A. Saleh, and W. White, "Infrared photoluminescence of sol-gel spin-coated films of rare-earth activated lanthanum silicate," *Materials Letters*, vol. 87, pp. 80 – 83, 2012. [Online]. Available: http://www.sciencedirect.com/science/article/pii/S0167577X12010841

[170] G. C. Righini, S. Pelli, M. Ferrari, C. Armellini, L. Zampedri, C. Tosello, S. Ronchin, R. Rolli, E. Moser, M. Montagna, A. Chiasera, and S. J. L. Ribeiro, "Er-doped silica-based waveguides prepared by different techniques: RF-sputtering, sol-gel and ion-exchange," *Optical and Quantum Electronics*, vol. 34, no. 12, pp. 1151–1166, 2002. [Online]. Available: http://link.springer.com/article/10.1023/A%3A1021338906917

[171] W. Huang and R. R. A. Syms, "Sol-Gel Silica-on-Silicon Buried-Channel EDWAs," *Journal of Lightwave Technology*, vol. 21, no. 5, p. 1339, 2003. [Online]. Available: http://www.osapublishing.org/abstract.cfm?uri=jlt-21-5-1339

[172] A. G. Okhrimchuk, L. N. Butvina, E. M. Dianov, I. A. Shestakova, N. V. Lichkova, V. N. Zagorodnev, and A. V. Shestakov, "A new dysprosium laser : 5.5-$\mu$m oscillation in the Dy$^{3+}$:RbPb$_2$cl$_5$ crystal at room temperature," in *European Conference on Lasers and Electro-Optics, 2007 and the International Quantum Electronics Conference. CLEOE-IQEC 2007*, 2007, pp. 1–1.

[173] S. R. Bowman, S. O'Connor, and N. J. Condon, "Diode pumped yellow dysprosium lasers," *Optics Express*, vol. 20, no. 12, p. 12906, 2012. [Online]. Available: https://www.osapublishing.org/oe/abstract.cfm?uri=oe-20-12-12906

[174] R. Jing, C. Dan-Ping, Y. Guang, X. Yin-Sheng, Z. Hui-Dan, and C. Guo-Rong, “Near Infrared Broadband Emission from Bismuth-Dysprosium Codoped Chalcohalide Glasses,” *Chinese Physics Letters*, vol. 24, no. 7, p. 1958, 2007. [Online]. Available: http://stacks.iop.org/0256-307X/24/i=7/a=047

[175] M. Lawrence, “Lithium niobate integrated optics,” *Reports on Progress in Physics*, vol. 56, no. 3, p. 363, 1993. [Online]. Available: http://stacks.iop.org/0034-4885/56/i=3/a=001

[176] L. Arizmendi, “Photonic applications of lithium niobate crystals,” *Physica Status Solidi (a)*, vol. 201, no. 2, pp. 253–283, 2004. [Online]. Available: http://dx.doi.org/10.1002/pssa.200303911

[177] W. Sohler, H. Hu, R. Ricken, V. Quiring, C. Vannahme, H. Herrmann, D. Büchter, S. Reza, W. Grundkötter, S. Orlov, H. Suche, R. Nouroozi, and Y. Min, “Integrated optical devices in lithium niobate,” *Optics Photonics News*, vol. 19, no. 1, pp. 24–31, 2008. [Online]. Available: http://www.osa-opn.org/abstract.cfm?URI=opn-19-1-24

[178] P. Rabiei, J. Ma, S. Khan, J. Chiles, and S. Fathpour, “Heterogeneous lithium niobate photonics on silicon substrates,” *Optics Express*, vol. 21, pp. 25 573–25 581, 2013. [Online]. Available: http://www.opticsexpress.org/abstract.cfm?URI=oe-21-21-25573

[179] R. M. A. Azzam and N. M. Bashara, *Ellipsometry and polarized light*. Amsterdam; New York; Oxford: North-Holland, 1977.

[180] H. G. Tompkins and E. A. Irene, *Handbook of Ellipsometry*. Springer Berlin Heidelberg, 2005.

[181] H. Fujiwara, *Spectroscopic Ellipsometry: Principles and Applications*. Tokio: Wiley, 2007.

[182] K. Vedam, "Spectroscopic ellipsometry: a historical overview," *Thin Solid Films*, vol. 313-314, pp. 1–9, 1998. [Online]. Available: http://www.sciencedirect.com/science/article/pii/S0040609097007621

[183] B. J. Gibbons, M. E. Hawley, S. Trolier-McKinstry, and D. G. Schlom, "Real-time spectroscopic ellipsometry as a characterization tool for oxide molecular beam epitaxy," *Journal of Vacuum Science & Technology A*, vol. 19, no. 2, pp. 584–590, 2001. [Online]. Available: http://scitation.aip.org/content/avs/journal/jvsta/19/2/10.1116/1.1351054

[184] L. R. Dahal, J. Li, J. A. Stoke, Z. Huang, A. Shan, A. S. Ferlauto, C. R. Wronski, R. W. Collins, and N. J. Podraza, "Applications of real-time and mapping spectroscopic ellipsometry for process development and optimization in hydrogenated silicon thin-film photovoltaics technology," *Solar Energy Materials and Solar Cells*, vol. 129, pp. 32–56, 2014. [Online]. Available: http://www.sciencedirect.com/science/article/pii/S0927024814000452

[185] P. Eaton and P. West, *Atomic Force Microscopy*. Oxford; New York: Oxford University Press, 2010.

[186] N. A. Geisse, "AFM and combined optical techniques," *Materials Today*, vol. 12, no. 7-8, pp. 40–45, 2009. [Online]. Available: http://www.sciencedirect.com/science/article/pii/S1369702109702019

[187] R. Kassies, K. O. van der Werf, A. Lenferink, C. N. Hunter, J. D. Olsen, V. Subramaniam, and C. Otto, "Combined AFM and confocal fluorescence microscope for applications in bio-nanotechnology," *Journal of Microscopy*, vol. 217, no. Pt 1, pp. 109–116, 2005.

[188] A. B. Mathur, G. A. Truskey, and W. M. Reichert, "Atomic force and total internal reflection fluorescence microscopy for the study of force transmission in endothelial cells," *Biophysical Journal*, vol. 78, no. 4, pp. 1725–1735, 2000. [Online]. Available: http://www.ncbi.nlm.nih.gov/pmc/articles/PMC1300769/

[189] D. Hu, M. Micic, N. Klymyshyn, Y. D. Suh, and H. P. Lu, "Correlated topographic and spectroscopic imaging beyond diffraction limit by atomic force microscopy metallic tip-enhanced near-field fluorescence lifetime microscopy," *Review of Scientific Instruments*, vol. 74, no. 7, pp. 3347–3355, 2000. [Online]. Available: http://scitation.aip.org/content/aip/journal/rsi/74/7/10.1063/1.1581359

[190] F. Dubreuil, N. Elsner, and A. Fery, "Elastic properties of polyelectrolyte capsules studied by atomic-force microscopy and RICM," *The European Physical Journal E*, vol. 12, no. 2, pp. 215–221, 2003. [Online]. Available: http://link.springer.com/article/10.1140/epje/i2003-10056-0

[191] C. Picart, B. Senger, K. Sengupta, F. Dubreuil, and A. Fery, "Measuring mechanical properties of polyelectrolyte multilayer thin films: Novel methods based on AFM and optical techniques," *Colloids and Surfaces A: Physicochemical and Engineering Aspects*, vol. 303, no. 1-2, pp. 30 – 36, 2007. [Online]. Available: http://www.sciencedirect.com/science/article/pii/S0927775707001264

[192] J. V. Chacko, C. Canale, B. Harke, and A. Diaspro, "Sub-diffraction nano manipulation using STED AFM," *PLoS ONE*, vol. 8, no. 6, p. e66608, 2013. [Online]. Available: http://dx.doi.org/10.1371%2Fjournal.pone.0066608

[193] J. Yu, J. Yuan, X. Zhang, J. Liu, and F. XiaoHong, "Nanoscale imaging with an integrated system combining stimulated emission depletion microscope and atomic force microscope," *Chinese Science Bulletin*, vol. 58, no. 33, pp. 4045–4050, 2013. [Online]. Available: http://link.springer.com/article/10.1007/s11434-013-6011-z

[194] A. Monserrate, S. Casado, and C. Flors, "Correlative atomic force microscopy and localization-based super-resolution microscopy: Revealing labelling and image reconstruction artefacts,"

*ChemPhysChem*, vol. 15, no. 4, pp. 647–650, 2014. [Online]. Available: http://dx.doi.org/10.1002/cphc.201300853

[195] D. R. Vij, Ed., *Luminescence of Solids.* Boston, MA: Springer US, 1998. [Online]. Available: http://link.springer.com/10.1007/978-1-4615-5361-8

[196] R. Egerton, *Physical Principles of Electron Microscopy: An Introduction to TEM, SEM, and AEM.* New York: Springer Science & Business Media, 2006.

[197] S. Amelinckx, D. van Dyck, J. van Landuyt, and G. van Tendeloo, *Electron Microscopy: Principles and Fundamentals.* Weinheim, Germany: Wiley-VCH Verlag GmbH, 2008.

[198] Accessed October 15, 2015. [Online]. Available: http://serc.carleton.edu/research_education/geochemsheets/techniques/SEM.html

[199] Research Group Electrochemical & Surface Engineering – Vrije Universiteit Brussel, accessed October 15, 2015. [Online]. Available: http://www.surfgroup.be/semedx

[200] S.-Y. Kuo and W.-F. Hsieh, "Structural and optical properties of erbium-doped Ba0.7Sr0.3TiO3 thin films," *Journal of Vacuum Science Technology*, vol. 23, pp. 768–772, 2005. [Online]. Available: http://adsabs.harvard.edu/abs/2005JVST...23..768K

[201] S. Bruynooghe, A. Chabli, F. Bertin, F. Pierre, and G. Leflem, "Preparation and characterization of $Nd^{3+}$ and $Er^{3+}$-doped silica sol-gel coatings by Rutherford backscattering spectroscopy and spectroscopic ellipsometry," *Journal of Materials Research*, vol. 12, no. 10, pp. 2779–2783, 1997. [Online]. Available: http://journals.cambridge.org/article_S0884291400041650

[202] M. R. Baklanov, K. P. Mogilnikov, V. G. Polovinkin, and F. N. Dultsev, "Determination of pore size distribution in thin films by

ellipsometric porosimetry," *Journal of Vacuum Science & Technology B*, vol. 18, no. 3, pp. 1385–1391, 2000. [Online]. Available: http://scitation.aip.org/content/avs/journal/jvstb/18/3/10.1116/1.591390

[203] E. Skoczek, J. Jaglarz, and P. Karasinsk, "Ellipsometric and Spectrophotometric Investigations of Porous Silica Thin Films Produced by Sol-Gel Method," *Acta Physica Polonica A*, vol. 120, no. 4, pp. 732–735, 2011. [Online]. Available: http://psjd.icm.edu.pl/psjd/element/bwmeta1.element.bwnjournal-article-appv120n436kz

[204] X. Orignac, D. Barbier, X. . M. Du, R. M. Almeida, and O. M. E. Yeatman, "Sol-gel silica/titania-on-silicon Er/Yb-doped waveguides for optical amplification at 1.5 $\mu$m," *Optical Materials*, vol. 12, no. 1, pp. 1–18, 1999. [Online]. Available: http://www.sciencedirect.com/science/article/pii/S0925346798000767

[205] N. V. Gaponenko, A. V. Mudryi, O. V. Sergeev, V. E. Borisenko, E. A. Stepanova, A. S. Baran, A. I. Rat'ko, J. C. Pivin, and J. F. McGilp, "Erbium luminescence in sol-gel derived oxide glass films," *Spectrochimica Acta Part A: Molecular and Biomolecular Spectroscopy*, vol. 54, no. 13, pp. 2177 – 2182, 1998. [Online]. Available: http://www.sciencedirect.com/science/article/pii/S1386142598001358